ABSTRACT

Title of Dissertation: THE DETECTION AND MODELING OF MULTINONSTATIONARITY FOR ACCURATE ASSESSMENT OF LONG-TERM HYDROLOGIC RISK

Kristin L. Gilroy, Doctor of Philosophy, 2011

Dissertation Directed By: Dr. Richard H. McCuen
Department of Civil and Environmental Engineering

Climate change and urbanization are nonstationary factors that influence hydrologic data, which results in the concept of multinonstationarity in hydrologic data. Methods to deal with important aspects of multinonstationarity do not exist. Currently, a statistical method to detect multinonstationarity in a hydrologic time series is needed. Likewise, flood mitigation methods, such as infrastructure designs and the national flood insurance policy, are based on the assumption of stationarity and, therefore, may not provide expected levels of protection in a nonstationary environment. The goal of this study was to provide a method to detect and model multinonstationarity in hydrologic data, as well as to assess the change in risk associated with multinonstationarity. A statistical test was developed to identify multiple change points within a time series, which is necessary to achieve optimum modeling accuracy for hydrologic data in a nonstationary environment. A procedure was developed to incorporate multinonstationarity into the existing flood frequency analysis method based on two nonstationary factors: urbanization and climate change. Finally, a flood risk assessment

was conducted in which the risks as well as the performance of a flood mitigation system were compared for stationary and multinonstationary environments.

The results showed that the incorporation of multinonstationarity into the current flood frequency analysis creates a noticeable difference in the magnitude of floods for the same return period as well as the associated risk. Based on the developed method, engineers and policy makers can begin to analyze the hydrologic and risk sensitivity of communities to nonstationarity. If the sensitivities of the system are understood, the factors, such as urbanization and emissions rates that influence climate change, can potentially be controlled to mitigate the consequences. Therefore, while many uncertainties exist in regards to the future conditions of these nonstationary factors, through methods such as those proposed in this study, the range of possibilities will be better understood and lead to more informed decisions to mitigate future risks.

THE DETECTION OF MODELING OF MULTINONSTATIONARITY FOR ACCURATE ASSESSMENT OF LONG-TERM HYDROLOGIC RISK

by

Kristin L. Gilroy

Dissertation submitted to the Faculty of the Graduate School of the
University of Maryland, College Park in partial fulfillment
of the requirements for the degree of
Doctor of Philosophy
2011

Advisory Committee:

Dr. Richard H. McCuen, Chair
Dr. Kaye Brubaker
Dr. Gerry Galloway
Dr. Lewis E. Link
Dr. Adel Shirmohammadi

ProQuest LLC.
789 East Eisenhower Parkway
P.O. Box 1346
Ann Arbor, MI 48106 - 1346

Acknowledgements

I would like to thank the professors and mentors who have inspired me throughout my academic career and to pursue my PhD in water resources engineering. I am incredibly grateful to Dr. Richard H. McCuen for his many years of encouragement and guidance. I would also like to thank Dr. Kaye L. Brubaker, Dr. Gerry Galloway, and Dr. Lewis E. Link for their assistance throughout the completion of my dissertation.

Finally, I would like to thank my parents. This great, personal accomplishment would not have been possible without their never ending love and support.

Table of Contents

Figures

Tables

1 Introduction

1.1 Problem Statement

Recent extreme events such as Hurricane Katrina and the Midwest Floods of 2008 have brought attention to the effects of flooding and the need for flood protection. Current design standards and policies, such as the National Flood Insurance Policy, are based upon the estimated magnitude of the 100-year flood event, determined by a flood frequency analysis. Flood frequency analyses are conducted in an attempt to predict the likelihood of a flood of a specific magnitude occurring. Current methods to conduct flood frequency analyses assume flood event stationarity and independence. Stationarity implies that the probability of the occurrence of a 100-year flood in a given year will not change over time. However, recent extreme events as well as considerable research suggest that our climate is nonstationary. Likewise, changes in land cover, which influence runoff, have been occurring throughout the past century and will continue to increase as people relocate to urban areas. Changes in both of these variables may change the statistics of flood records and, therefore, the accuracy of flood frequency estimates. Milly et al. (2009) state that stationarity is no longer an applicable assumption for water-resource risk assessment and planning. Existing methods must be updated in order to adapt to the uncertainties that will exist in a changing environment.

1.2 Climate Change

Scientists suggest that climate change is a main source of nonstationarity. Caused by factors such as an increase in the concentrations of greenhouse gases in the atmosphere, climate change increases downwelling infrared radiation and, therefore, surface temperatures. This influences the hydrologic cycle, as much of the surface

moisture is evaporated by the increased heating at the surface (Trenberth1999). Increased temperatures and water vapor in the atmosphere will increase the transport of water vapor from areas of divergence to areas of convergence. The result is global changes in precipitation, particularly increases in the intertropical convergence zones and subpolar and polar regions and decreases in the subtropics. North America and Europe will experience patterns of both moistening and drying with much uncertainty existing at the boundaries (IPCC 2007).

In addition to mean precipitation increases, the change in extreme events in the changing climates is important. Many studies have been conducted in an attempt to predict the changes expected in extreme precipitation both globally and regionally. For example, Karl and Knight (1998) detected a 10% increase in precipitation across the contiguous United States. They found this increase to occur mainly in the heavy to extreme precipitation events, implying that the increase is disproportionate across the precipitation distribution. Barnet et al. (2006) showed that the global average frequency of extremely wet days is expected to double in response to doubled atmospheric CO_2 conditions. Semenov and Bengtsson (2002) determined that the mean precipitation intensity will increase significantly in response to increased atmospheric greenhouse gas concentrations, with an increase of about 20% in the eastern United States for the twenty-first century. Likewise, the frequency of wet days exceeding the 90^{th} percentile is expected to increase globally, with an increase of about 30% in the eastern United States for the twenty-first century (Semenov and Bengtsson 2002). Based on the A1B greenhouse gas emissions scenario, the IPCC (2007) predicts that the fraction of extreme wet seasons in a set time period is expected to increase by 97 to 100% regionally

throughout North America from 1980-2000 to 2080-2100, in which an extreme wet season is defined by the wettest year in the 1980-2000 control period and the fraction of years exceeding this magnitude in the 2080-2100 time period is considered the percent increase. These studies imply changes in extreme precipitation events are presently occurring on a global scale as well as regionally in the United States.

As stated in the IPCC (2007) and suggested in aforementioned studies, climate change causes nonstationarity in physical processes. Thus, the statistical distributions of precipitation are changing over time. As runoff is directly dependant on precipitation, nonstationarity in the precipitation distribution will result in changes to flood frequency as well.

1.3 Urbanization

In addition to a changing climate, landuse changes occur over time, which influence the watershed response to precipitation events. Theobald et al. (2009) predicted that the impervious surface cover in the conterminous United States will increase from 83,749 km^2 in 2000 to 111,070 km^2 in 2030. Likewise, they predict 8.5% of all watersheds in the United States will be stressed and degraded due to impervious cover by 2030. Increased urbanization results in reduced infiltration capabilities. For example, a studied conducted by Kauffman et al. (2009) showed that increases in impervious area in Delaware resulted in decreases in dry weather baseflow, suggesting that decreased infiltration capacities are limiting groundwater recharge. Limited infiltration results in an increase in and rerouting of surface runoff. Because of this, the post-urbanization watershed runoff that would result from a precipitation event will differ from and most likely be greater than the pre-urbanization watershed runoff resulting from the same

event. Beighley et al. (2009) found that varying the source of impervious area data and, therefore, the amount of impervious area in a hydrologic model resulted in noticeable differences in the simulated peak discharge value ranging from the 2-yr to the 100-yr flood. Therefore, while climate change is influencing the precipitation intensity and frequency, urbanization and other land use changes are affecting the runoff resulting from the changing precipitation events.

1.4 Detection of Nonstationarity

While the effects of nonstationarity are clear, detecting trends in rainfall and runoff data are difficult. Graphical analyses are a common form of trend detection in data analysis; however, dominance of random variation often makes it difficult to identify systematic changes or trends from such graphs (McCuen 2003). Many statistical tests are available to detect trends in data where random variation greatly influences individual sample points. However, the power of such tests is influenced by the length of data records available and assumptions specific to the test such as distribution type.

In the case of climate change or urbanization, trends may not exist throughout the entire data set. For example, urbanization may only occur during a ten-year time period and then stabilize while climate change may only affect the latter portion of the flood record. The location within a time series in which the statistical characteristics may change as a result of outside factors such as environmental changes is defined as a change point (Reeves et al. 2007). Knowledge of change points within a hydrologic time series is beneficial in order to provide accurate hydrologic models. For example, assume that a noticeable trend occurs in a mean annual discharge time series and is modeled through linear regression. The time series spans the entire 20th century; however, the rate of land

development rapidly increased in the middle of the 20th century, which resulted in a significant increase in mean annual discharge. If linear regression is applied to the entire time series, then the effect of urbanization will be underestimated. Likewise, if the zoning laws were implemented in the latter portion of the 20th century, which resulted in the stabilization of the previously increasing effects of urbanization, then the extrapolation of the fitted linear model will result in overprediction of future runoff. The knowledge of the change points at which urbanization both began and then ceased to influence the mean annual discharge would enable the modeler to better model the hydrologic time series.

While the importance of the identification of change points is apparent, currently a statistical test to detect multiple change points in time based on multinonstationarity does not exist. Reeves et al. (2007) discuss the statistical tests that are currently available; however, they state that the existing tests all assume that at most, one change point exists within the time series analyzed. Therefore, detection of trends influenced by nonstationarity is constrained by the limitations of existing statistical tests and behavior of the predictor variables.

1.5 Effect of Nonstationarity on Flood Frequency Analyses

In addition to the importance of the detection of nonstationarity within hydrologic data, methods to model the effects of nonstationarity are needed. Flood frequency analyses are used as a method of estimating the probability of the occurrence of a particular flood magnitude. The current method for conducting a flood frequency analysis, recommended by the U.S. Water Resources Council in Bulletin 17B (Interagency 1982), assumes that the peak discharge data analyzed are stationary and

independent (McCuen 2005). Based on the expected changes in climate and land development, the existing method proposed to conduct a flood frequency analysis will be inapplicable under future nonstationary conditions.

Flood frequency estimates are a primary basis upon which floodplain management measures and the National Flood Insurance Program are based (Olsen 2006). For example, the 100-yr storm is an accepted criterion upon which floodplain management decisions are based. In a nonstationary world, the magnitude of the 100-yr event will be changing, most likely increasing, year-to-year. Therefore, a new design criterion may be necessary for future floodplain management designs. Without knowledge of the change in flood frequencies with nonstationarity, current approaches to floodplain management may be inefficient as their effectiveness may decrease while flood frequencies increase.

Research has attempted to develop a frequency analysis method that accounts for nonstationarity for both precipitation and flooding events. Khaliq et al. (2006) recommend incorporating covariates into parameters of distributions in a precipitation frequency analyses. Katz et al. (2002) applied the covariate approach using sea level pressure and seasonal Darwin pressure as covariates in prediction parameters for precipitation and peak flow distributions, respectively, at different locations. Villarini et al. (2009a) and Villarini et al. (2009b) used the Generalized Additive Models for Location, Scale, and Shape (GAMLSS) to model the time variant flood parameters. Cunderlik and Ouarda (2006) and Leclerc and Ouarda (2007) modeled the first two moments of multiple flood series as a function of time to develop a nonstationary regional flood frequency analysis method that can be applied at ungauged sites.

While these nonstationarity studies begin to provide solutions to the issue of nonstationarity, many limitations still exist. Existing flood frequency studies do not account for both land use change and climate change when varying the flood frequency distribution parameters. Likewise, most studies use time as the only variable, which assumes that the change that occurs is temporally and spatially stationary. Improvements to these proposed nonstationary methods are necessary to ensure that the most accurate estimate of future flood conditions is available. The inability to adapt the existing flood frequency method to multinonstationary conditions may result in a decrease in the expected level of protection for both structural and non-structural mitigation systems that are dependent on the estimates of flood magnitudes provided by flood frequency analyses.

1.6 Effects of Nonstationarity on Risk Analyses

The inability to statistically detect multinonstationarity and adjust flood frequency analyses for nonstationarity influences the assessment of risk associated with current flood frequency estimates. Risk can be defined as the product of the probability of the occurrence of an event and the consequences associated with the event. The consequences, such as property damage and loss of life, are dependent on the defined hazard. For example, the hazard associated with flooding would reflect the depth and velocity of the flood. As the magnitude of the hazard increases, the consequences will likely increase.

The goal of a risk analysis, as defined by Moser et al. (2009), is to evaluate risk and then consider the monetary and non-monetary costs and benefits involved in the implementation of risk mitigation methods. The risk analysis process consists of risk

assessment, risk management, and risk communication. The risk assessment process is dependent on the accurate assessment of the hazard and resulting consequences. Potential options to mitigate the estimated risk are considered through risk management. Risk communication includes the discussion between the parties involved in each of the risk assessment and management processes as well as additional stakeholders.

With the existence of nonstationarity, it is likely that the flood hazard associated with a selected probability of occurrence will be underestimated. For example, a flood frequency analysis based on stationary conditions will likely underestimate the 100-yr flood because the effects of the climate change and urbanization are not taken into account. Therefore, the hazard associated with the 100-yr return period, or a 1% chance of occurrence in any given year, will be underestimated. As a result, the consequences associated with the event will also be underestimated. If the consequences associated with a selected event are underestimated, it will be difficult to provide effective options to mitigate the risk. Therefore, it is necessary for nonstationarity to be implemented into risk analyses to ensure that policy makers and engineers are making well-informed decisions in an uncertain environment.

1.7 Research Goals and Objectives

In order to better evaluate flood risk in a multinonstationary environment of the future, better methods to detect and model nonstationarity in flood frequency patterns are needed as well as an approach to risk assessment in a nonstationary environment. Therefore, the goals of this research were to (1) develop a statistical method to detect multinonstationarity within a time series, (2) provide a method to conduct a multinonstationary flood frequency analysis that accounts for the effects of urbanization

and climate change, and (3) perform a nonstationary assessment of hydrologic risk. This goal was achieved through the following objectives:

- Develop a statistical procedure to aid in the detection of multinonstationarity
- Develop a model that estimates future flow forecasts based on varying climate change and urbanization conditions
- Develop an adjustment method to adjust measured annual maximum flood records to climate change and urbanization conditions at the design year of interest
- Apply method to project beyond existing data records for multiple design years and design scenarios
- Develop a multinonstationary flood frequency analysis based on the adjusted peak discharge records
- Demonstrate risk assessment in a multinonstationary environment and compare results to risk assessments of flood frequency analyses that assume stationarity

Through this research, engineers will have new methods to detect, model, and assess nonstationarity for hydrologic data. As a result, the range of potential future flood risks will be better understood. Scenario-based changes in flood frequency over time can be analyzed to determine the necessary approaches to mitigate flood risk. Additionally, the availability of such information may have an impact on future policies regarding climate change, such as CO_2 emissions and urbanization. Policy makers and engineers will be able to make better informed decisions about future actions in order to reduce the negative effects of flooding. Variations of the method developed will aid in understanding the effects of multiple variables on future conditions in other nonstationary environments.

2 Literature Review

2.1 Climate Change

2.1.1 Introduction

The IPCC Fourth Assessment Report: Climate Change 2007 defines climate change as "the state of the climate that can be identified (e.g. using statistical tests) by changes in the mean and/or variability of its properties and that persists for an extended period, typically decades or longer". While changes show spatial variation, general observed global changes over the past century include a decrease in the frequency of cold events while warm events have increased in frequency; heavy precipitation events have increased in frequency; and sea level has risen at many sites worldwide in the past half century (IPCC 2007).

A changing climate can have a significant influence on the hydrologic cycle. Changes in temperature influence evaporation demands and soil moisture conditions. Temperature also influences snowmelt both in time of occurrence and amount. Changes in precipitation influence soil moisture conditions as well as runoff quantities. And changes in runoff quantity influence streamflow as well as water table levels replenished by infiltrated rainfall (McCuen 2005). Numerous studies have been conducted to project the future changes in the climate both on a global and regional scale and those effects on the hydrologic cycle. A summary of the processes involved in a changing climate, observed and projected changes from the IPCC, and general circulation models and emissions scenarios is provided herein. Additional studies are then discussed in regards to precipitation, streamflow, and temperature in a nonstationary future.

2.1.2 Global and Regional Observed Climate Changes from the 20th Century

Observed records of climate indices such as temperature and precipitation suggest that statistical changes have occurred, both globally and regionally. In many instances, the rate of change has increased throughout the past century. The estimated increase in global land surface temperature from 1850 to 2005 is 0.54 degrees Celsius per decade with an uncertainty of plus or minus 0.015 degrees. From 1901 to 2005, estimates of warming increased ranging from 0.68 to 0.084 degrees Celsius per decade with uncertainties of 0.024 and 0.021, respectively. From 1979 to 2005, this rate increased again with estimates ranging from 0.188 to 0.315 degrees Celsius per decade with uncertainties equal to 0.069 and 0.088, respectively. These observations suggest that the rate of change of the Earth's surface temperature has increased throughout the past century. Regionally, warming has been statistically significant in most of globe with a few exceptions over the past century (Trenberth et al. 2007).

The urban heat island effect suggests that urban areas experience greater warming and climate change effects than neighboring areas. However, these changes depend on local and seasonal climatic factors such as wind and cloud cover (Trenberth et al. 2007). Additionally, the detected effects of urbanization on climate change appear to be lower than temperature trends on a decadal and longer time scale (Jones et al. 1990; Peterson et al. 1999). Additionally, areas with the greatest socioeconomic development have also been significantly influenced by atmospheric circulation changes which cause warming. This makes it difficult to conclude that warming was caused by urbanization. The IPCC 2007 assessment included an uncertainty equal to 0.006 and 0.002 degrees Celsius for land and combined land and ocean temperature estimates since 1900 to account for the urban heat island effect (Trenberth et al. 2007).

Changes in atmospheric moisture, precipitation, and atmospheric circulation have accompanied increases in temperature. However, measurement errors make it difficult to accurately report changes in precipitation and record lengths are generally shorter and less abundant than those for temperature. Therefore, significant variation exists in the estimates of global mean annual precipitation changes. However, regional trends have been reported. In the higher latitudes, ranging from 30 to 85 degrees north, increasing trends in annual precipitation range from 6 to 8% from 1900 to 2005. In North America and Canada, precipitation has increased from 1900 to 2005 with the exception of the South West United States and parts of Mexico. Most of South America has experienced an increase in precipitation except Chile and Western portions of the continent. Australia has also experienced an upward trend in precipitation; however, this trend is most likely due to two wet periods during the 1970's and 1990's. Southwest Australia has experienced a decreasing trend since 1975. Western Africa and Sahel precipitation records show the greatest decreasing trend. India has experienced a 20% increase in precipitation over the entire 20th century; however, a decrease has occurred since 1979. In Eurasia, the majority of locations have experienced an increase rather than a decrease in precipitation. Snowfall has also been affected by increasing temperatures, with many high latitude areas experiencing a shift from snow to rain. Overall, much uncertainty in trends, regional patterns, and data limitations make it difficult to assess general changes in precipitation patterns with climate change (Trenberth et al. 2007).

While increased temperatures are expected to affect precipitation, a consistent correlation between the two variables does not exist. In North America and Europe, warmer seasons show a negative correlation between temperature and precipitation, with

warmer summers experiencing less rainfall than cooler summers. In latitudes above 40 degrees, a positive correlation exists during winter months due to an increased water holding capacity with temperature. When ocean conditions are a driving force of the atmosphere, such as during El Nino events, temperature and precipitation are positively correlated. Other regional variations have been observed in the relationship between precipitation and temperature, which suggests that the relationship is influenced by additional factors (Trenberth et al. 2007).

2.1.3 Climate Change, Drivers, and Uncertainties

Climate is influenced by changes to the Earth's radiation balance. 30% of solar radiation is reflected back to space from the atmosphere, with 2/3 of this reflected radiation due to clouds and particles such as aerosols and 1/3 due to areas, such as snow, ice, and desert, with light-colored surfaces. The remaining energy from the sun is absorbed by the Earth's surface. To maintain an energy balance, the Earth emits longwave radiation back to space. However, greenhouse gases in the atmosphere trap a portion of this energy and warm the Earth's surface. This process is known as the natural greenhouse gas effect, with carbon dioxide and water vapor as the most influential greenhouse gases. Cloud cover also can have a greenhouse gas effect, but this effect is outweighed by the cooling effect clouds have through reflecting incoming solar radiation back to space. Energy is also released from the Earth's surface through evaporation. As water vapor from evaporation condenses into clouds, the energy is released as latent heat, which influences atmospheric circulation and, therefore, ocean circulation (Le Treut 2007).

Changes to any of the following components will alter the Earth's radiation balance: (1) incoming solar radiation; (2) solar radiation levels reflected back to space; and (3) longwave radiation from the Earth to space. The reflection of incoming solar radiation is influenced by changes in cloud cover, aerosols and other atmospheric particles, and land cover. Changes in longwave radiation from the Earth to space are affected by changes in atmospheric GHG concentrations. This enhances the greenhouse gas effect (Le Treut 2007).

GHGs and aerosols affect the radiative forcing, or changes in the energy balance, within the Earth's atmosphere. Positive and negative radiative forcings have warming and cooling effects on the global climate, respectively, thus causing climate change. In general, GHGs have a positive radiative forcing while aerosols have a negative radiative forcing. Feedback cycles, such as water vapor, carbon, and cloud patterns, also influence climate change; however, much uncertainty remains in the modeling of feedback cycles (IPCC 2007). These effects are summarized in Figure 1-1 provided by the IPCC Fourth Assessment Report: Climate Change 2007 (Le Treut et al. 2007).

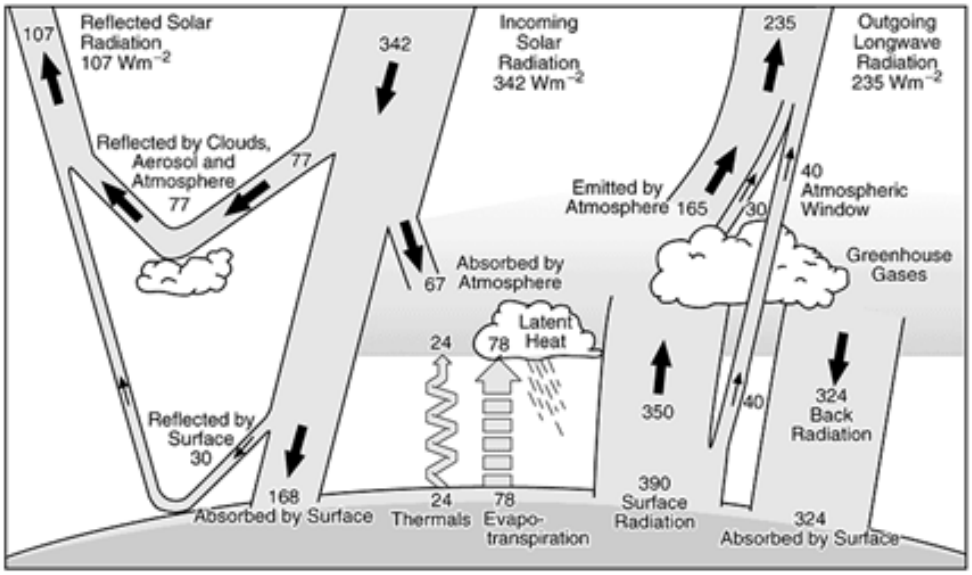

Figure 2-1. The Earth's Annual and Global Mean Energy Balance provided by the IPCC Fourth Assessment Report: Climate Change 2007 (Le Treut et al. (2007)

The IPCC Fourth Assessment Report: Climate Change 2007 states that it is extremely unlikely that global climate changes over the past half century occurred without external forcings and very likely that anthropogenic factors played a role. As previously explained, external forcings of climate change include greenhouse gases (GHGs) and aerosols. While some GHGs and aerosols are the result of natural causes, anthropogenic factors cause increases in CO_2, methane (CH_4), nitrous oxide (N_2O), and halocarbons, each with a long lifespan in the atmosphere although the lifespan varies with each GHG. Increases in GHG emissions result in increases in atmospheric concentrations. Anthropogenic factors also release aerosols into the atmosphere (IPCC 2007).

2.1.4 Climate Change Effects on Hydrologic Cycle

As changes in radiative forcings influence temperature, evaporation processes are directly affected as well. Therefore, warming will potentially increase the occurrence of droughts. Additionally, the moisture holding capacity of the atmosphere increases as temperatures increase. For every 1 degree Celsius increase in temperature, the increase in moisture holding capacity is estimated at 7% by the Clausius-Claperyon relationship (Trenberth et al. 2007). While mean precipitation is constrained by the energy budget of the atmosphere, extreme events are affected by the moisture availability (Allan and Ingram 2002). Therefore, a warmer climate is expected to increase moisture availability and increase storm intensity, even if the mean annual precipitation remains unchanged. A warmer climate will likely be at risk of more droughts during periods without precipitation but greater evaporation rates and more floods as a result of heavier precipitation events (Trenberth et al. 2007).

While the general effects of a warmer climate on the hydrologic cycle are understood, many uncertainties exist and make it difficult to project changes in regional and global mean and extreme precipitation events. The regional existence of aerosols can influence temperature and evaporation, therefore, precipitation. Atmospheric circulation patterns also influence precipitation patterns. Examples include El Nino and the North Atlantic Oscillation. Additionally, increases in temperature in colder climates will influence snowfall and snowpack. The expected result is a shift from winter snow events to rain events and reduced availability of water resources from snowmelt in the spring and summer (Trenberth et al. 2007). Finally, data limitations and significant regional differences have made it difficult to detect observed trends in precipitation throughout the past century (Huntington 2006).

2.1.5 General Circulation Models Forcings and Uncertainties

General Circulation Models (GCMs) have been developed in an attempt to better understand and predict changes in climate. The main forcing agents for GCMs in the IPCC report include greenhouse gas emissions and aerosols, while some models include other factors such as the effects of land cover on surface albedo. Physical and chemical processes are simulated to determine the resulting atmospheric concentrations, radiative forcings, and finally, climate response throughout each of the IPCC emissions scenarios, which will be discussed in Section 2.1.7. Within these sequential calculations exists a carbon feedback cycle. The carbon feedback cycle refers to the reduction in the efficiency of anthropogenic CO_2 absorption by the Earth system. As a result, the atmospheric CO_2 concentration is increased at a faster rate. Therefore, greater reductions in CO_2 emissions will be required to attain a stabilization of atmospheric concentrations. Much uncertainty exists, however, in the modeling of the carbon feedback cycle. Figure 2-2, provided by the IPCC Fourth Assessment Report: Climate Change 2007 (Meehl et al. 2007), shows the transition steps from climate model forcing agents to the climate response as well as the uncertainties involved in each step. Other uncertainties involved in the climate model compiled in the IPCC include variations of forcing agents used by individual modeling groups as well as the indirect effects of aerosols modeled in each GCM (Meehl et al. 2007).

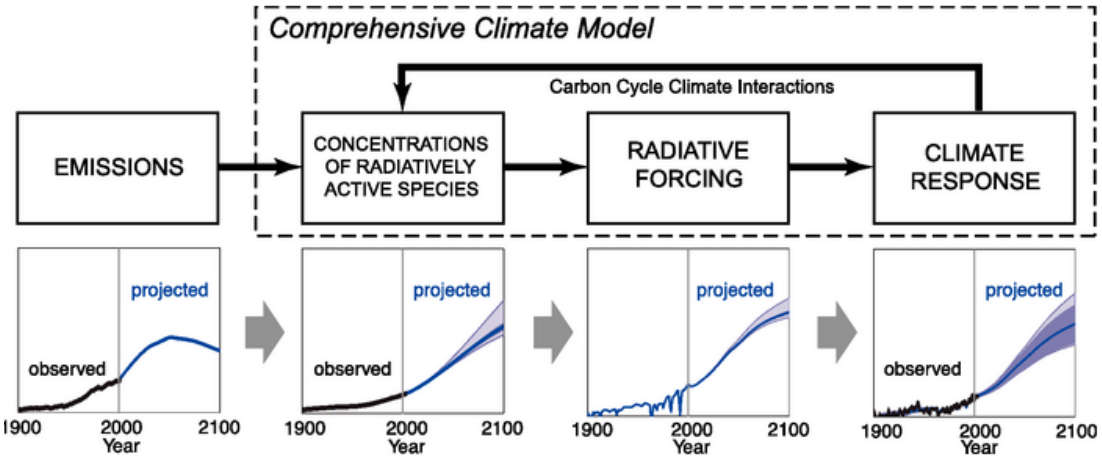

Figure 2-2. Uncertainties with Climate Models provided by the IPCC Fourth Assessment Report: Climate Change 2007 (Meehl et al. 2007)

In addition to uncertainties in the climate models, Overpeck et al. (2011) discuss the need for more accessible and understandable climate data. Existing knowledge of the climate system processes is based on observed and simulated data. This data is used by scientists as well as resource managers and policy makers to aid in decision making. This wide use enforces the need for more accessible climate data. Uncertainties in observed data exist based on changes in observation methods. Additionally, not all records are available digitally. Paleoclimatic data must be made more available as they provide insights into climate before observation instruments were available. Space borne instruments are a useful data source but require advancements as the life span is only a few years and they need advanced data processing techniques. The third type of climate data available is model-reanalyses, which are based on simulated data from global or regional forecast models using observed data for a specified period. Improvements to this type of data include the addition of more diverse observational data and longer time scales. The final data type available is outputs from numerical climate model simulations. The World Climate Research Program (WRCP) created the Coupled Model

Intercomparison Project (CMIP), which compiles and makes available climate projections from 16 international modeling groups for research and analysis. The availability of the data beyond the physical climate science research communities has enabled other research communities to incorporate projected climate changes in decision making. As advancements in modeling continue, the availability of climate data is expected to increase. Climate scientists face the challenge of making climate data both more available and understandable by other research communities.

2.1.6 Climate Responses

The output of the comprehensive climate model shown in Figure 2-2 is the climate response. Climate response includes changes in temperature, both mean and extreme; changes in precipitation, both mean and extreme; snow and ice cover; carbon cycle feedback; sea level rise and pressure; El Nino; monsoons; tropical cyclones; and other climatic events.

2.1.7 Emissions Scenarios for IPCC Studies

The IPCC Special Report on Emissions Scenarios (SRES) (2000) provided emissions scenarios to be used in the IPCC Third and Fourth Assessment Reports. The scenarios considered potential changes in the driving forces of climate change, which include changes in population, the economy, technology, land use, and energy, and their effects on greenhouse gases. Four different families of scenarios were developed to represent different combinations of projections for the driving forces: A1, A2, B1, and B2 (IPCC 2000).

The B2 family assumes regional solutions will exist for sustainability issues for the economy, society, and environment. The family consists of moderate population

growth and economic development with a slower and more varied technological change than the A1 and B1 families. The B1 family represents the fast shifting of economic structures towards a service and information economy with a focus on global solutions to sustainability issues. The A2 family represents a heterogeneous world with slow economic development and technological change, but fast population growth. The A1 family provides fast population growth that then declines in the middle of the 21st century as well as rapid economic growth and more efficient technology. The A1 family provides three additional scenario groups that vary based on their characterization of alternative developments of energy. The A1F scenario group projects a fossil fuel intensive future; A1B a balanced future; and A1T a predominantly non-fossil fuel future. In total, 40 scenarios were developed for the four families (IPCC 2000).

The emissions rates for greenhouse gases, SO_2, and ozone precursor emissions for each of the six scenario groups are shown in Table 2-1, provided by the IPCC SRES (2000). The rates for the illustrative scenarios are shown in bold with the range across all 40 scenarios in the family shown in parentheses. The carbon dioxide emissions rates that result from energy and industry changes for each of the four families are shown in Figure 2-3 and the rates that result from land-use change are shown in Figure 2-4. The bold lines represent the illustrative scenarios while the remaining lines represent the remaining 34 scenarios within the four groups. Also shown are the ranges provided by additional sources. The A1 family provides a range of emissions scenarios that span all four families, with the A1F providing the greatest rates, A1B moderate rates and AIT the lowest emissions rates. A2 provides the highest emission rates, B2 provides moderate emissions rates, and B1 provides low emissions rates. It is important to keep in mind that

these scenarios do not encompass every possible future emission scenario. Likewise, each scenario is assumed equally likely to occur (IPCC 2000).

Table 2-1. Summary of Greenhouse Gas, SO2, and Ozone Precursor Emissions in 1990, 2020, 2050, and 2100 as well as Cumulative CO2 Emissions provided by IPCC (2000).

Family			A1			A2	B1	B2
Scenario group		1990	A1FI	A1B	A1T	A2	B1	B2
Carbon dioxide, fossil fuels (GtC/ yr)		6						
	2020		**11.2** (10.7-14.3)	**12.1** (8.7-14.7)	**10** (9.8-10.0)	**11** (10.3-11.0)	**10** (8.2-13.2)	**9** (8.8-10.2)
	2050		**23.1** (20.6-26.8)	**16** (12.7-25.7)	**12.3** (11.4-12.3)	**16.5** (15.1-16.5)	**11.7** (8.5-17.5)	**11.2** (11.2-15.0)
	2100		**30.3** (30.3-36.8)	**13.1** (13.1-17.9)	**4.3** (4.3-8.6)	**28.9** (28.2-28.9)	**5.2** (3.3-7.9)	**13.8** (13.8-18.6)
CO_2, land use (GtC/ yr)		1.1						
	2020		**1.5** (0.3- 1.8)	**0.5** (0.3- 1.6)	**0.3** (0.3- 1.7)	**1.2** (1.1- 1.2)	**0.6** (0.0- 1.3)	**0** (0.0- 1.1)
	2050		**0.8** (0.0- 0.8)	**0.4** (0.0- 1.0)	**0** (- 0.2- 0.0)	**0.9** (0.8- 0.9)	**-0.4** (-0.7- 0.8)	**-0.2** (-0.2- 1.2)
	2100		**-2.1** (- 2.1- 0.0)	**0.4** (- 2.0- 2.2)	**0** (0.0- 0.1)	**0.2** (0.0- 0.2)	**-1** (- 2.6-0.1)	**-0.5** (- 0.5- 1.2)
Cumulative CO_2, fossil fuels (GtC)	1990-2100		**2128** (2096-2478)	**1437** (1220-1989)	**1038** (1038-1051)	**1773** (1651-1773)	**989** (794-1306)	**1160** (1160-1448)
Cumulative CO_2, land use (GtC)	1990-2100		**61** (31- 61)	**62** (31- 84)	**31** (31- 62)	**89** (81- 89)	**-6** (- 22- 84)	**4** (4- 125)
Cumulative CO_2, total (GtC)	1990-2100		**2189** (2127-2538)	**1499** (1301-2073)	**1068** (1068-1113)	**1862** (1732-1862)	**983** (772-1390)	**1164** (1164-1573)
Sulfur dioxide, (MtS/ yr)		70.9						
	2020		**87** (60- 134)	**100** (62- 117)	**60** (60- 101)	**100** (80- 100)	**75** (52- 112)	**61** (61- 78)
	2050		**81** (64- 139)	**64** (47- 64)	**40** (40- 64)	**105** (104- 105)	**69** (29- 69)	**56** (44- 56)

Family			A1			A2	B1	B2
Scenario group		1990	A1FI	A1B	A1T	A2	B1	B2
	2100		**40** (27- 83)	**28** (28- 47)	**20** (20- 27)	**60** (60- 69)	**25** (11- 25)	**48** (33- 48)
Methane, ($MtCH_4$ /yr)		310						
	2020		**416** (416- 479)	**421** (406- 444)	**415** (415- 466)	**424** (418- 424)	**377** (377- 430)	**384** (384- 391)
	2050		**630** (511- 630)	**452** (452- 636)	**500** (492- 500)	**598** (598- 671)	**359** (359- 546)	**505** (482- 505)
	2100		**735** (289- 735)	**289** (289- 535)	**274** (274- 291)	**889** (889-1069)	**236** (236- 561)	**597** (465- 597)
Nitrous oxide, (MtN/ yr)		6.7						
	2020		**9.3** (6.1- 9.3)	**7.2** (6.1- 9.6)	**6.1** (6.1- 7.8)	**9.6** (6.3- 9.6)	**8.1** (5.8- 9.5)	**6.1** (6.1- 11.5)
	2050		**14.5** (6.3- 14.5)	**7.4** (6.3- 13.8)	**6.1** (6.1- 6.7)	**12** (6.8- 12.0)	**8.3** (5.6- 14.8)	**6.3** (6.3- 13.2)
	2100		**16.6** (5.9- 16.6)	**7** (5.8- 15.6)	**5.4** (4.8- 5.4)	**16.5** (8.1- 16.5)	**5.7** (5.3- 20.2)	**6.9** (6.9- 18.1)
CFC/ HFC/ HCFC (MtC equiv./ y) [b]		1672						
	2020		**337**	**337**	**337**	292	291	299
	2050		**566**	**566**	**566**	312	338	346
	2100		**614**	**614**	**614**	753	299	649
PFC, (MtC equiv./ yr) [b]		32						
	2020		**42.7**	**42.7**	**42.7**	50.9	31.7	54.8
	2050		**88.7**	**88.7**	**88.7**	92.2	42.2	106.6
	2100		**115.3**	**115.3**	**115.3**	178.4	44.9	121.3
SF_6 , (MtC equiv./ yr) [b]		37.7						
	2020		**47.8**	**47.8**	**47.8**	63.5	37.4	54.7
	2050		**119.2**	**119.2**	**119.2**	104	67.9	79.2
	2100		**94.6**	**94.6**	**94.6**	164.6	42.6	69
CO, (MtCO/ yr)		879						
	2020		**1204** (1123- 1552)	**1032** (1032- 1248)	**1147** (1147- 1160)	**1075** (1075- 1100)	**751** (751- 1162)	**1022** (941- 1022)
	2050		**2159** (1619- 2307)	**1214** (1214- 1925)	**1770** (1244- 1770)	**1428** (1428- 1585)	**471** (471- 1470)	**319** (1180- 1319)
	2100		**2570**	**1663**	**2077**	**2326**	**363**	**2002**

Family			A1			A2	B1	B2
Scenario group		1990	A1FI	A1B	A1T	A2	B1	B2
			(2298-3766)	(1663-2532)	(1520-2077)	(2325-2646)	(363-1871)	(1487-2002)
NMVOC, (Mt/ yr)		139						
	2020		**192** (178- 230)	**222** (194- 222)	**190** (188- 190)	**179** (179- 204)	**140** (140- 193)	**180** (179- 180)
	2050		**322** (256- 322)	**279** (259- 301)	**241** (206- 241)	**225** (225- 242)	**116** (116- 237)	**217** (197- 217)
	2100		**420** (167- 484)	**194** (137- 552)	**128** (114- 128)	**342** (311- 342)	**87** (58- 349)	**170** (130- 170)
NOx , (MtN/ yr)		30.9						
	2020		**50** (46- 51)	**46** (46- 66)	**46** (46- 49)	**50** (47- 50)	**40** (38- 59)	**43** (38- 43)
	2050		**95** (49- 95)	**48** (48- 100)	**61** (49- 61)	**71** (66- 71)	**39** (39- 72)	**55** (42- 55)
	2100		**110** (40- 151)	**40** (40- 77)	**28** (28- 40)	**109** (109- 110)	**19** (16- 35)	**61** (34- 61)

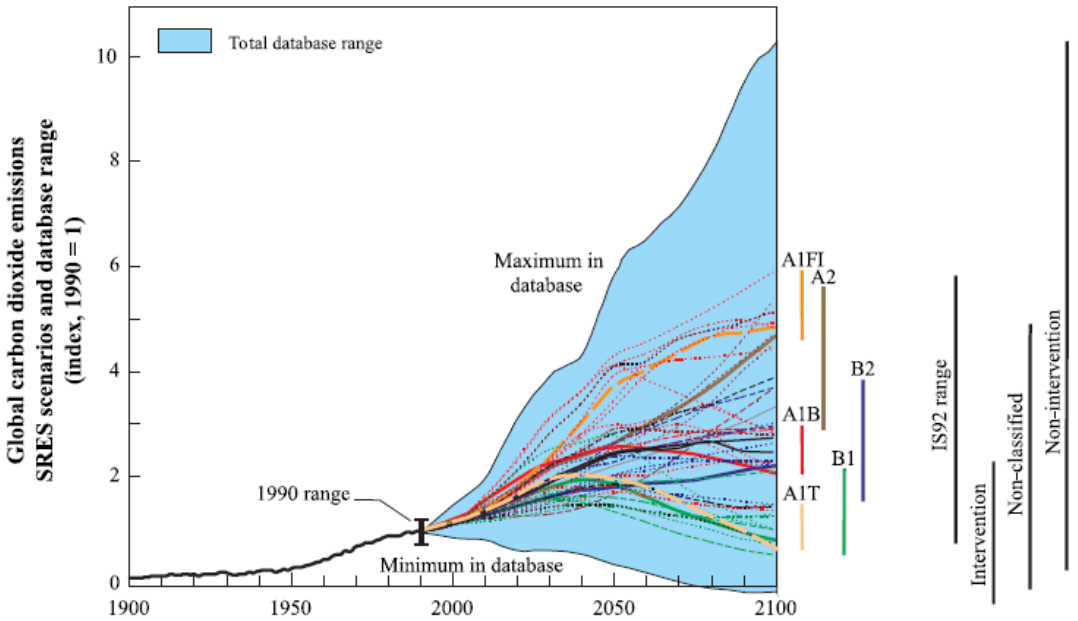

Figure 2-3. Global CO2 Emissions Related to Energy and Industry from 1900 to 2100 for the 40 SRES scenarios provided by IPCC (2000).

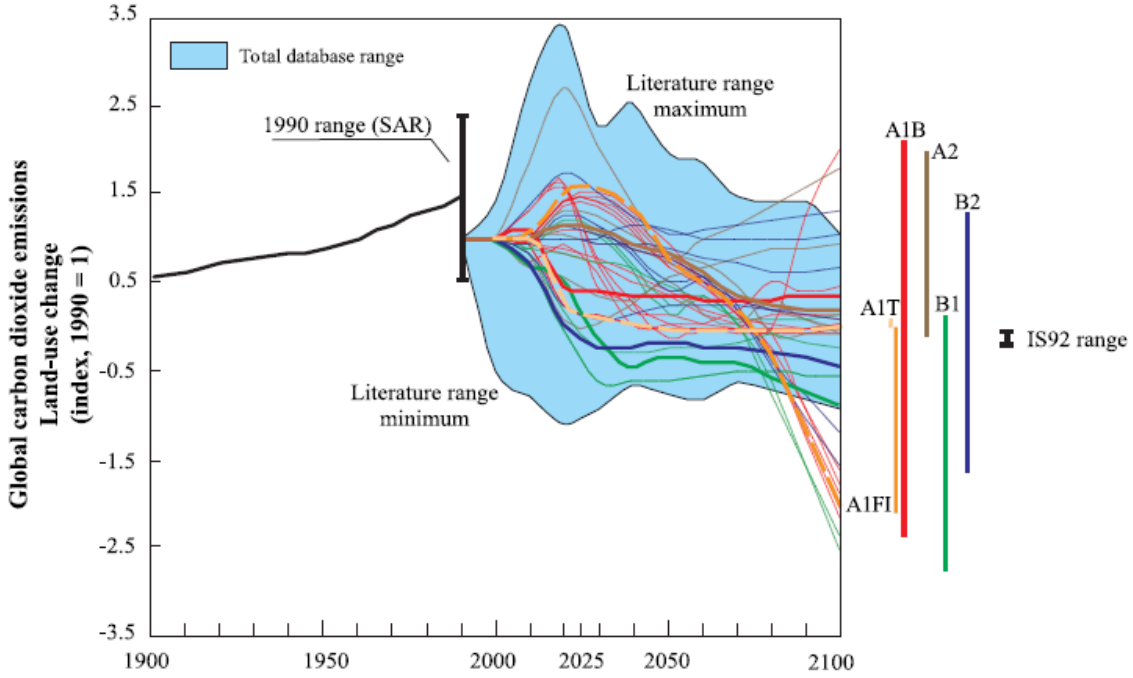

Figure 2-4. Global CO2 Emissions Related to Land-Use Changes from 1900 to 2100 for the 40 SRES scenarios provided by IPCC (2000).

In addition to emission rates, the IPCC SRES (2000) provides CO2 atmospheric concentration for each family. It is important to consider concentrations because scenarios that experience stabilization in emission rates can still result in high carbon dioxide atmospheric concentrations based on the previous emission rates. For example, despite A1B providing lower emission rates than A2 in Figure 2-5 in the year 2100, the range of the projected CO2 atmospheric concentration for A1B encompasses that projected for A2 in 2100, with projections both above and below those for A2. Therefore, assumptions in regards to the effects of each scenario on climate change in the 21st century should not be based solely on emissions rates, but concentrations as well.

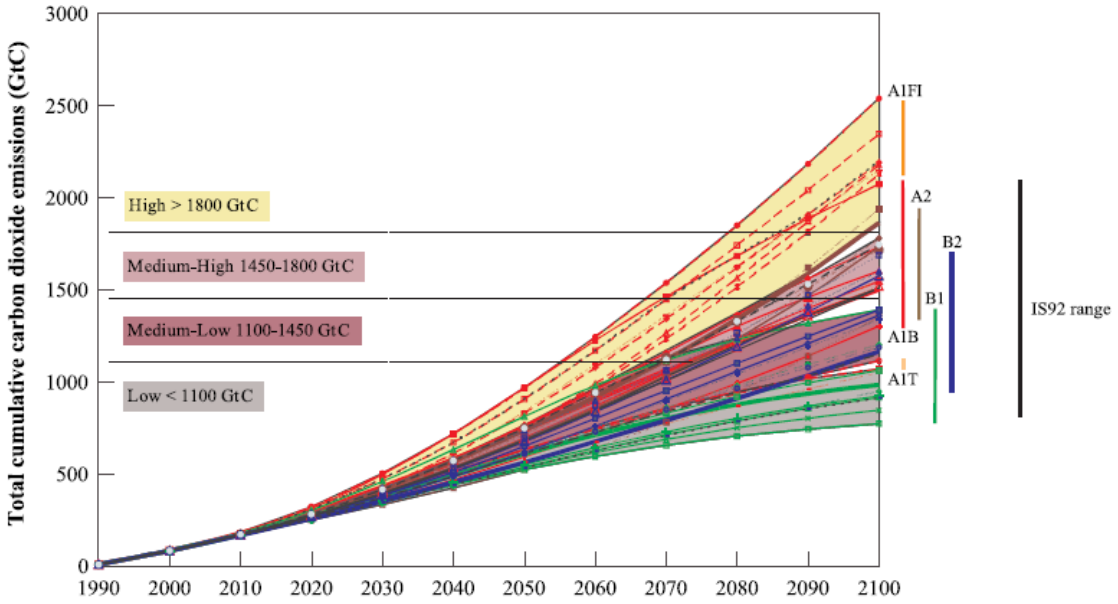

Figure 2-5. Total Global Cumulative CO2 Emmissions (GtC) from 1990 to 2100 for the 40 SRES Scenarios provided by IPCC (2000).

2.1.8 IPCC Global Climate Projections

The ensemble of GCMs included in the IPCC Fourth Assessment Report (2007) projects continued warming and increased annual mean precipitation for each of the three emissions scenarios. The multi-model ensemble mean projects an increase in temperature of 3.13, 2.65, and 1.79 degrees Celsius from the 1980-1999 base period to the 2080-2099 projection period. The committed scenario, in which atmospheric concentrations do not increase, is still projected to cause a 0.56 degrees Celsius increase. In each of the scenarios, the global mean precipitation is expected to increase, with the extreme events increasing by a greater percentage than the mean. Relative to the increase in mean precipitation from 1980 to 1999, the mean annual precipitation is expected to increase by 1.4% per degree Celsius increase for scenario A2.

2.1.9 IPCC Regional Climate Projections for North America

Average regional climate projections from climate model simulations suggest that the effects of climate change will vary throughout North America. Along the western, southern, and eastern continental edges of North America, the ensemble mean annual temperature of the MMD models increases by 2-3 degrees Celsius from the 1980 to 1999 period to the 2080 to 2099 period. In the northern regions, annual mean temperature increases as great as 5 degrees Celsius are expected. These projections vary between models. However, all of the models in the IPCC projected at least a 2 degrees Celsius increase over North America. Based on the mean of the PCMDI model simulations, annual precipitation is expected to increase by 20% throughout North America with an exception of the South-West where decreases in annual precipitation are expected. Some of the increases in precipitation are expected to be offset by an increase in evaporation (Christensen et al. 2007).

2.1.10 Climate Change Studies: Changes to Precipitation

Karl et al. (1998) assessed the trends in observed precipitation at 182 stations across the contiguous United States from 1910-1996. For stations missing data, a gamma function was fitted to each year and missing data were simulated based on the distribution. Additional data sets were used as a cross-reference for the results. Spatial averages were taken for nine regions of the United States to determine the change in precipitation for each region and nationally, both annually and seasonally. The data were assessed to determine trends in precipitation as well as the contribution of frequency and intensity changes to these trends. The results showed a precipitation increase of 10% across the contiguous United States, the greatest occurring in the spring and fall and least

in the winter. The annual trend remained stable among the different data sets; however, the seasonal trends varied as much as 4% per century. An increase in event frequency contributes to 87% of the increase in the total precipitation. One-third of the increase in frequency is attributed to the heavy and extreme precipitation categories or the 90th percentile and greater.

Karl et al. (2005) analyzed 30 to 80 years of historical records of high-frequency temperature and precipitation data from Australia, China, the Former Soviet Union, and the United States. The results showed a decrease in day-to-day temperature variation in the Northern hemisphere, but mixed trends in Australia. A significant increase was not detected. Only 18 of the 96 annual trends were positive. A nonparametric approach was used to assess the precipitation trends. The results showed that the United States experienced an increase in extreme precipitation events in all but the southeast and far west and a decrease in light and moderate events. These increases were predominantly in the spring and summer. A trend in the total precipitation was not found.

Wilby and Wigley (2002) assessed the changes in the precipitation shape and scale parameters of the two-parameter gamma distribution as a result of future climate change. Two General Circulation models were used to predict future changes: HADCM2 and CSM. The models were forced by estimated historical and projected future anthropogenic factors. Both models project much larger changes in the scale parameter than the shape parameter. Model differences existed in the patterns of change at regional scales for the parameters, but not at the area-averaged continental scale. This suggests the models differ in sensitivity to factors at the regional scale. Both models projected a

small increase in winter wet days and small decrease in summer wet days. An increase in total precipitation that was the results of extreme and heavy events was also projected.

Cubasch et al. (1995) simulated three 20-year periods based on the following scenarios: (1) present day CO_2 levels; (2) doubling of CO_2; and (3) tripling of CO_2 using a T42 atmosphere model. The annual temperature and precipitation cycle over IPCC regions were analyzed. The temperature simulations had much greater accuracy than the precipitation simulations based on observed data. Precipitation amounts were underpredicted and did not show a clear signal of change in amount; however, the rainfall intensity did shift with more high intensity and fewer low intensity storms in each season. Cubasch et al. (1995) found a negative correlation between temperature and precipitation.

Dore (2005) summarized literature findings that pertain to climate change and the effects on global precipitation patterns. The summary suggested an increase in precipitation variance everywhere. A 2% increase in global precipitation has occurred throughout the twentieth century. While this increase is statistically significant, it is not spatially nor temporally uniform. Wet areas are becoming wetter, while dry areas are becoming drier. Precipitation is increasing at higher latitudes and decreasing in China, Australia, and Small Island States in the Pacific, while the variance is increasing at the equator.

Hayhoe et al. (2007) observed past and future changes in the Northeast of many climate change components including temperature, rainfall, drought, snow cover, soil moisture, and streamflow using nine GCMs to reproduce observed changes in these indicators as well as project future changes. B1, A2, and A1F1 emissions scenarios from the IPCC were analyzed. The results showed much uncertainty surrounding simulated

trends in precipitation. The average simulated annual trend equaled 0.7 +/- 3 mm/decade for the past century and 7 +/- 18 mm/decade for the years 1970-2000. The models proved to be more accurate in simulating winter trends than summer trends. Future projections from all models suggested an increase in winter but not summer precipitation, with a range from 12-30% increase in winter and 2% decrease to zero change in summer months depending on the emissions scenario. The simulated annual increase in precipitation ranged from 7-14% depending on the emissions scenario. Temperature was expected to increase by the year 2100 for every scenario, ranging from 2.9 to 5.3 degrees Celsius. Temperature driven trends such as seasonal warming, greater spring streamflows, extended growing seasons and early blooming, less snow cover, and an increase in droughts and low flows are expected to increase. These trends proved to be more sensitive to the A2 and A1F1 scenarios than to the B1 scenario.

Kharin and Zwiers (2000) analyzed the changes in extreme temperature, precipitation, and wind speed using the GCM from the Canadian Centre for Climate Modeling and Analysis. The IPCC 1992 Scenario A2 was used to determine changes in CO_2 and surface albedo over the period of study, 1900-2100. Extremes were analyzed in three 21-yr periods centered around the years 1985, 2050, and 2090. The simulated daily data was fit to a Generalized Extreme Value (GEV) distribution using L-moments and then return period values were calculated by inverting the fitted GEV distributions. The results showed a global increase in extreme precipitation. For the 20-year return period, the global average increase from 1985-2050 and 1985-2100 in 24-hour precipitation was 6.9 mm/day and 12.2 mm/day, respectively. The increases in annual mean precipitation during the same time periods were 1% and 4%, respectively. A relation between the

changes in the maximum and minimum temperature and the changes in the mean screen temperature, soil moisture, and snow and ice cover was found. Modest changes were determined in extreme wind speed over the extratropics.

Hennessy et al. (1997) analyzed the changes in precipitation based on an equilibrium doubling of CO_2 using the UKH1 and CSIRO9 global climate models. The existing $C0_2$ scenario in the UKH1 model equaled 326 ppm while the CSIRO9 model equaled 323 ppm. The UKH1 suggested a 3.5 degree Celsius increase in temperature and 9% increase in global average precipitation, while the CSIRO9 suggested a 4.8 degree Celsius increase in temperature and an 11% increase in global average precipitation. Regionally, more intense convective events are expected in middle and low latitudes, while events will remain nonconvective but increase in intensity in high latitudes. In the United States, Europe, Australia, and India, events with return periods greater than or equal to 1-year will increase by 10-25%. For a given precipitation intensity, the return period is expected to decrease on average by a factor ranging from 2 to 5.

Kharin et al. (2006) analyzed potential future changes in temperature and precipitation extremes using multiple global coupled climate models and the SRES B1, A1B, and A2 emissions scenarios. Changes were recorded from the time period of 1980-2000 to two different future time periods: (1) 2046-2065 and (2) 2081-2100. An extreme event was defined as the 20-year return period or greater. The study showed that relative changes are expected to be greater in extreme precipitation rather than mean precipitation changes. Return periods will be reduced everywhere as a result of these scenarios except for a few sub-tropical regions. For the 20-yr return period, the study suggests a 6% change in the 24-hour precipitation depth for every degree Kelvin change in temperature.

Groisman et al. (2004) analyzed changes in intense precipitation over land due to increases in greenhouse gas emissions. Projections from three GCM simulations for the 20th and 21st centuries with increasing greenhouse gas emissions were also analyzed. Intense precipitation events were defined as the top 0.3% of daily precipitation events. The results showed an increase in heavy precipitation in mid-latitudes in the past 50-100 years. Model projections suggested future increases in heavy precipitation events as well.

Semenov and Bengtsson (2002) analyzed changes in the mean daily precipitation, precipitation intensity, wet day frequency, and gamma distribution parameters based on increasing greenhouse gas concentrations in the atmosphere from the 20th to the 21st century. The coupled atmosphere-ocean general circulation model ECHAM4/OPYC3 was used to conduct the analysis and the IS92a "business as usual" scenario was used as a forcing. Trends observed from 1900-1900 increased in magnitude significantly during the 21st century. Over all land territories, the mean precipitation intensity and scale parameter increased in the 21st century. The number of wet days decreased everywhere but in the high northern latitudes. The mean precipitation changes varied regionally. In the eastern United States, the increase in mean precipitation was greater than the interdecadal variation and the increase in precipitation intensity showed a clear positive trend of about 20%. The number of wet days exceeding the 90th percentile increased significantly by about 30%.

Nichols et al. (2002) analyzed summer and non-summer precipitation data from 1956 to 1996 for the USAD-ARS Walnut Gulch Experimental Watershed for trends. The data were categorized by the number of events, the event precipitation depth, the 30-minute event intensity, and the event duration. Linear regression was used to determine

trends of seasonal precipitation statistics including minimum, maximum, mean, and variance. The results showed an annual increase in precipitation, most likely resulting from an increase in the frequency of the precipitation in the non-summer months. While the frequency increased, the other three criteria did not increase in the non-summer months. For the summer precipitation records, the frequency of events increased, but the average precipitation per event decreased.

2.1.11 Climate Change Studies: Changes to Streamflow

Dai et al. (2009) assessed the streamflow from 925 of the largest rivers in the world. Historical monthly streamflow data from 1949 to 2004 was used. The results showed that only one-third of the top 200 rivers analyzed showed statistically significant trends. The majority of this one-third showed negative trends. The time series showed large multiyear variations, and the significance of the trends were sensitive to the time period used. The model was able to assess most of the trends without incorporating direct human influences, suggesting that the affects of human activities on yearly streamflow for many large rivers is likely small in comparison to natural climate change. Among the top 20 rivers, Dai et al. (2009) reported an observed linear trend in the mean annual streamflow (km^3/yr) ranging from -3.95 to 1.82 (km^3/yr^2), with the greatest value for the Mississippi River.

Labat et al. (2004) developed a statistical wavelet-based method to reconstruct monthly discharges of 221 of the world's largest rivers. This data were then assessed to determine the affects of climate change on the hydrologic cycle and the influence on global and continental runoff in the past century. Linear regression was used to determine a trend between temperature and runoff. Analyses were conducted for two

reference periods: 1900-1975 and 1925-1994. The first reference period coincides with an additional study. The results showed a more rapid increase by a factor of 3 for the second reference period compared to the first reference period. Overall, the results showed a 4% increase in global runoff for every 1 degree Celsius increase in temperature. At a regional scale, runoff in North American rivers was most sensitive to climate change. However, it is difficult to determine between anthropogenic and natural causes.

Lins et al. (2005) assessed trends in streamflow data from 1940-1999 in the United States based on data from 435 stream gauging stations. The nonparametric Mann-Kendall test was used. Results showed an increasing trend in discharge in low to moderate ranges in the central 2/3 of the United States. The trend was less significant in the Eastern United States. Few trends were observed in annual maximum flow and a systematic shift in the timing of the annual minimum, median, or maximum flow was not detected.

Milly et al. (2005) assessed the affects of climate change on streamflow in the twentieth and twenty-first centuries. Twelve climate models found to have the lowest error for analyses based on simulations for observed data in 165 river basins were used to project streamflow data for the twenty-first century. The results showed an increase between 10 and 40% in runoff in high latitudes of North America and a decrease in mid-latitude Western North America by 2050. The results were based on average annual flows.

Milly et al. (2002) used streamflow measures and numerical simulations of anthropogenic effects of greenhouse gases and other anthropogenic factors to explore the risks of floods exceeding the 100-yr level with changing climate. The analysis focused

on 29 large basin facilities with data spanning at least 30 years. The Log Pearsons type III distribution and the method of moments were used to fit the annual maximum monthly mean flows and determine the 100-yr flood from the fitted distribution. Out of the 2066 station years assessed, the 100-yr flood was exceeded 21 times, with 16 of these events occurring in the second half of the record. This had a 1.3% probability of occurring based on a binomial distribution and the assumption that the events were independent. A significant change for lower return periods did not exist; however, the 200-yr flood had a significant increase. Milly et al. (2002) tested the hypothesis that radiatively forced climate change was a source of increasing flood risk with a 300-yr 'idealized CO2 quadrupling' experiment in which the mean CO2 concentration increased by 1% until the starting concentration was quadrupled. The results of this experiment showed a change in the annual mean discharge but not much change in the monthly maximum discharge. The 100-yr flood was exceeded more frequently in all but one basin. In half of the basins, the frequency of the control flood increased to a 12-yr return period as a result of radiatively forced climate change.

Burn and Elnur (2001) conducted a study to determine the hydrologic impacts of climate change in Canada by quantifying trends in hydrologic variables and their relationship with trends in meteorological variables. They assessed a spatial distribution between catchments that do and do not show trends. They adopted a systematic approach for detecting trends: (1) choose variables: low flow, average flow, high flow, timing, and duration; (2) choose stations; (3) use Mann-Kendall to check for trends; and (5) determine the significance of a detected trend using a permutation procedure. Cross correlation and serial correlation were considered. The results showed spatial and

temporal differences. Spatial differences were based on changes in climate with location and temporal changes were based on non-uniform meteorological variables. Trends and patterns for the hydrologic and meteorological variables showed similarities.

Hamlet and Lettenmaier (2007) analyzed the changes in flood risk within the Western United States as a result of climate change, both on a century- and interannual-scale. The study also analyzed the increased variation in precipitation since the 1970's. Detrended temperature data from the beginning and end of the 20th century temperature were used as input to the variable infiltration capacity hydrologic model. The results suggest that the increasing trend of one degree Celsius per century may be related to the changes in flood risk within the area. Most of the temperature changes are the result of mid-winter warming. Hamlet and Lettenmaier found that neither warm rain-dominant basins nor cold river basins experienced an increase in flood risk. However, transient intermediate basins experienced a variety of effects and were influenced by additional factors, such as antecedent snow and drainage area during storms. A relationship existed between the basin scale and the absolute value of the flood risk change; however, basic scale did not influence the relationship between mid-winter temperatures and flood risk. The study also suggests that flood risk changes are related to increased variation in precipitation. The greatest changes in food risk show a relationship with the Pacific Decadal Oscillation and El Nino Southern Oscillation, suggesting that interannual as well as century-scale climate changes must be considered.

Jha et al. (2006) analyzed the potential effects of climate change on streamflow in the Upper Mississippi River Basin. The Soil and Water Assessment Tool model was used to predict streamflow based on six AOGCM climate change scenarios. Each

scenario assumed a doubling of the atmospheric carbon dioxide concentration of 660 ppmv. Climate data inputs were based on 111 weather stations in and around the watershed. Landuse, soil, and topography input data were retrieved from the Better Assessment Science Integrating Point and Nonpoint Sources (BASINS) Package Version 3. The model was calibrated using USGS streamflow data from a gauge located on the Mississippi River. The results showed that over the 20-year simulation period, the six AOGCM climate change scenarios provided a change in annual streamflow ranging from -6 to 51%. These results suggest much uncertainty in climate change projections for the Upper Mississippi River Basin region.

Frey et al. (2010) studied the impacts of climate change on storm surge flooding in Corpus Christi, Texas. Climate factors considered included sea level rise and hurricane intensification. Future climate change conditions were based on three carbon dioxide doubling sensitivities: (1) cool, (2) average, and (3) warm and three IPCC carbon dioxide equivalent emissions scenarios: (1) AIFI, (2) AIB, and (3) B1. Physically based numerical models were used to predict hurricane winds and the resulting waves, surges, and morphological changes of the coastline. Models were then used to determine the resulting flooding and effects on population and infrastructure. The procedure was applied to three hurricanes: (1) Bret, (2) Beulah, and (3) a version of Carla. The results suggested an increase in flood water elevations in Corpus Christi ranging from 0.4 to 1.9 meters by the 2080's depending on the hurricane. The expected increases in economic damages range from $270-1,100 million for a variation of Hurricane Carla, $100-390 million for Hurricane Beulah, and $30-280 million for Hurricane Bret by the 2080's.

These results emphasize the consequences of ignoring the effects of climate change on flooding.

Xiong and Guo (2004) analyzed annual discharge series of the Yangtze River for abrupt and gradual change. The analyses were conducted for time series from 1882-2001. The Mann-Kendall and Spearman's Rho trend tests, both nonparametric tests, and a linear regression and t-test were used to assess gradual trends in the annual maximum, minimum, and mean of the time series discharges. A Bayesian model and the Monte Carlo Markov Chain sampling method were used for the single change-point or the abrupt change detection analysis of the mean levels in the time series. The results for the trend test showed that at a 5% significance level, the annual maximum flood series did not show a significant trend, while the annual mean and minimum flood series showed a decreasing trend. The results for the abrupt change analysis showed that in the past 120 years, the mean of both the annual minimum and mean discharges decreased. The analyses also showed that the trend term and abrupt change term were very closely related.

Douglas et al. (2000) used a spatially averaged Kendal's S trend test to analyze trends in floods and low flows in the United States over the past 30 years, as well as the past 50 years. With spatially correlated sites eliminated from the study, a trend in floods did not exist at the 5% level; however, a trend in low flows did exist in the Midwest and in the smaller regions of Ohio, North Central US, and the Upper Midwest. Ignoring the spatial correlation of regional streamflow resulted in more significant trends in both categories. Dougles et al. (2000) attributed the increase in low flows to the increase in precipitation observed in the Midwest.

Nijssen et al. (2001) used a macroscale hydrological model and a parameter transfer calibration method to predict river runoff in different climate zones. The transfer method involved calibrating parameters for nine large river basins and transferring the calibrated values within similar climate zones. The transfer calibration method did not reduce the bias or the root-mean-square-error for discharge predictions of individual basins, but did for the total of all basin predictions. Transferring the parameters globally caused an increase in precipitation and evapotranspiration prediction compared to a previous uncalibrated prediction.

Charlton et al. (2006) assessed the impact of climate change on surface runoff in Ireland. Patterns of runoff under baseline and future climate scenarios were simulated using the rainfall-runoff model, HYSIM, and analyzed for annual and seasonal changes. Data output from the HadCM3 Global Climate Model were used as a driver for the HYSIM model. Climate scenarios for two future time periods: 2041-2070 and 2061-2090, were assessed and changes in the annual and seasonal runoff were examined. The results showed a decrease in annual runoff for both climate scenarios, with the exception of a slight increase in a limited part of the Northwest. Summer runoff decreased in all areas of Ireland. Winter runoff increased in the west. It is assumed that the increase in winter runoff may lead to increases in magnitude and frequency of flooding, while the decreases in the summer may result in an increased frequency and duration of low flows.

Mareuil et al. (2007) assessed the effects of climate change on the frequency and severity of floods in the Chateauguay River Basin in Quebec, Canada. Output from three global climate models (GCMs) was combined with a stochastic weather generator and used to develop current and future climate scenarios. The current and future time periods

ranged from 1960-1990 and 2040-2060, respectively. These different climate scenarios were input into hydrologic modeling experiments to determine the effects of climate change on the frequency and severity of flood events during spring snowmelt and summer through fall storms. Storm return periods that range from 2 to 500 years were considered.

The results for the spring runoff events showed that two of the three GCM derived climate series had a statistically significant decrease. For the summer through fall runoff events, one GCM derived climate series had a statistically significant decrease while one showed a statistically significant decrease for only the higher return periods. The third GCM derived climate series did not show a statistically significant change in the spring or the summer-fall runoff events. Uncertainties related to the study and the models used were discussed.

Muzik (2002) assessed the effects of climate change on flood frequencies in a subalpine watershed in the Rocky Mountains of Alberta, Canada. A first-order analysis was conducted in which rainfall intensity changes were considered to have the most significant effect on future floods. Two scenarios based on changes in the parameters of the Gumbel distribution for rainfall were used in the study. The first was a 25% increase in both the mean and standard deviation and the second was a 50% increase in the standard deviation. Rainfall increase estimates were based on a literature review, transposition of southern climates, and general circulation model projections. The results showed that up to the 50-year return period, the first scenario resulted in much greater changes in flood discharges than the second scenario; the discharge values for the two scenarios converge at the 500-year return period; and scenario 2 did not have a significant

effect on storms less than a 2-year return period. The 100-yr peak flow is projected to increase by 40.9% and 35.3% for scenarios 1 and 2, respectively. These results suggest that even small to moderate rainfall intensity increases that are predicted to occur from climate change may have a significant effect on flooding.

Knowles and Cayan (2002) conducted a study to determine the effects of temperature increases on the Sacramento/San Joaquin Watershed and the San Francisco estuary. The Bay-Delta Watershed Model was used to predict delta outflows for the following scenarios: (1) temperatures from 1965-1987; (2) projected temperatures for 2030; (3) projected temperatures for 2060; and (4) projected temperatures for 2090. The outflow model predictions for each future scenario were compared to the outflow model predictions for the years 1965-1987. The differences between the future and previous time periods were added to existing outflow data for the 1965-1987 time period to develop four sets of outflows based on existing data and projected increases. The Uncles-Peterson (U-P) estuarine model was used to simulate estuary processes. The results show that by 2090, temperature increases will have caused a decrease of about 50% in the watershed's total April snowpack. This is projected to effect outflows from the watershed by increasing runoff peaks before April and decreased flows caused by snow-melt after April. The historical annual flow volume is projected to decreasing by about 20% by 2090 for both regions as a result of the decreased April-July runoff.

Maurer et al. (2010) analyzed the changes in projected streamflow for three Sierra Nevada rivers based on climate projections. Projections based on the SRES A2 and SRES B1 emissions scenarios for 11 GCMs were retrieved from the WRCP's CMIP3 multi-model data set. These projected data sets were then downscaled and used as input

into two hydrologic models: Sacramento Soil Moisture Accounting Model and the variable infiltration capacity model. The hydrologic models contained difference in regards to the computational, time steps, the calibration techniques, and the spatial extent. The results showed that despite differences within the models, both produced similar changes in monthly streamflow; however, differences existed in extreme flows. The results also showed a shift in runoff from spring to winter. As winter temperatures increase, more snowfall becomes rainfall. Therefore, streamflow increases in the winter and decreases in the spring due to less snowmelt.

Wegel (2011) analyzed observed floods on the Delaware River for different record lengths to determine. The Gumbel extreme value distribution was applied to the observed data for different record lengths to determine the change in return periods for varying time periods. The results showed that the length of the record influences the estimate return periods for a given flood.

2.1.12 Climate Change Studies: Changes to both Precipitation and Streamflow

Lettenmaier (1994) et al. statistically analyzed spatial patterns of average temperature, average daily temperature range, precipitation, and streamflow in the United States from 1948-88. Results showed an increase in autumn precipitation in the central United States; a streamflow increase from November to April in half of the stations, particularly in the north-central United States; and a statistically significant positive relationship between precipitation and temperature in roughly 2/3 of the sites. They noted that changes in streamflow may be the result of factors in addition to climate change.

Douville et al. (2002) studied the effect of increasing greenhouse gas emissions and aerosols on the hydrologic cycle. Changes in precipitation over two time periods: 1970-2000 and 2070-2100 were compared based on simulations from a coupled atmosphere-ocean climate model of the Centre National de Recherches Meteorologiques. The SRES-2 scenario was used to determine changes in CO_2, CH_4, N_20, CFC-11, and CFC-12 emissions. Effects on the hydrologic cycle were also simulated, and the simulated runoff converted to riverflow using a linear routing method. The results suggested an increase in precipitation throughout the 21st century with the exception of the subtropics and mid-latitude continents. The increase is suggested to be a result of a decrease in the water vapour cycling rate, which results in a greater water holding capacity of the atmosphere in warmer climates. Other factors included changes in moisture convergence in mid-latitudes and a decrease in precipitation efficiency, particularly in summer in the Northern Hemisphere mid-latitudes. Trends in simulated riverflow over recent decades were fairly consistent with the observed data; however, combined trends simulated for the 20th and 21st century differed from those found in just the 20th century, which implied that simply extrapolating observed trends should not be practiced. Biases in the regional hydrologic analysis revealed the need for downscaling techniques.

Milliman et al. (2008) assessed the global and regional trends of discharge from 137 rivers based on discharge and precipitation records from 1951-2000. To determine the effect of climate on changes in discharge, precipitation records from this time period were also assessed. The results showed that a global discharge trend did not exist as the cumulative discharge for the 137 rivers did not change; however, regional trends did

exist. Ninety-seven rivers showed a change of 10% in discharge. Of the rivers showing a trend, the majority with a positive trend were located in the Americas while negative trends were associated with arid and semi-arid regions in Africa, Asia, and Australia. Coinciding with the river discharge results, precipitation did not show a global trend but did show a significant regional trend. Milliman et al. (2008) determined whether climatic or anthropogenic factors were the key component that affects river discharges. They classified each river as 'normal', 'deficit', or 'excess' rivers depending on the factors that influence the river discharge. Normal river discharge is driven primarily by changes in precipitation as both experienced an increasing or decreasing trend; deficit river implied an increasing or neutral change in precipitation and a decreasing change in river discharge; excess river implied an increasing trend in river discharge and a decreasing trend in precipitation. In North America, the Mississippi River was classified as a normal river while rivers in Colorado were classified as deficit rivers.

Groisman et al. (2001) outlined the changes in the precipitation and snow cover the United States to determine their effects on high streamflow. Both regional and national trends were assessed. Seasonal and annual precipitation changes as well as one-day and multi-day heavy precipitation were assessed. For streamflow, the months of maximum mean streamflow and the preceding month for each region were the focus of the analyses. The standardized time series for nine United States regions were averaged for the streamflow data. For national trends, it was found that systematic increases in precipitation should cause an increase in streamflow over the United States assuming changes in evapotranspiration or watershed management do not occur. Regional trends included a fairly close relationship between heavy precipitation and high streamflow

events in months of maximum streamflow in regions of the eastern United States. In the western United States, the earlier occurrence of snow melt is believed to influence the relationship between heavy precipitation and high streamflows. Data for the central United States were not available to draw conclusions regarding this relationship.

Fekete et al. (2003) assessed uncertainties of six monthly precipitation data sets and the effects of resulting runoff predictions due to these uncertainties. The results suggested that in wet regions, the error in the precipitation was equal to the error in the predicted runoff because precipitation exceeds evaporation; in semi-dry regions, the runoff error was greater than the precipitation error because runoff-generation is a nonlinear function; and in arid regions, precipitation did not provide runoff because precipitation does not produce runoff.

Lettenmaier et al. (1994) analyzed average monthly temperature, precipitation, streamflow, and daily temperature range for trends for the continental United States from 1948-88. The data for the analysis came from 1036 stations from the historical climatology network and 1009 stations from a streamgage network. The nonparametric Mann-Kendall test and Seasonal Kendall test were used to detect trends and a slope method was used to determine the magnitude of the trends. The results showed an increase in the March temperature at almost half of the stations. Precipitation increased in the fall in a quarter of the stations, mainly in the central United States. Increases in streamflow in almost half the stations from November to April were detected, with the greatest trend occurring in the north-central United States. A second part of the study evaluated relative changes in variables, particularly in regards to streamflow. A bivariate test was used. The results showed that trends in streamflow were not always consistent

with changes in climatic variables, suggesting that water management effects may have played a role.

Using data from the past century, the USGS National Streamflow Information Program conducted a study of trends in the water budget of the Upper Mississippi. Human influences such as agricultural irrigation and evaporation of water from surface reservoirs were cited. Likewise, climatic influences such as changes in precipitation and evapotranspiration processes were explained. A 2.1 %/decade increase in precipitation was reported for the Mississippi River Basin that resulted in a 4.5%/decade increase in Mississippi River discharges. The report also recognized the existence of natural variability within the data records.

2.1.13 Climate Change Studies: Changes to Temperature

Davis et al. (2010) provide a breakdown of CO_2 emissions from existing energy and transportation infrastructure by the industry sector as well as by country/regions. They also provide lower, middle, and upper estimates of the resulting cumulative atmospheric CO_2 and temperature change for 2060 assuming CO_2 emitting infrastructure is not expanded. They predicted a resulting warming of 1.3 degrees Celsius above pre-industrial warming.

Meehl et al. (2006) used the Community Climate System Model Version 3 (CCSM3), a global coupled climate model, to simulate three scenarios: (1) twentieth century climate; (2) simulations of three scenarios to 2100 based on emissions scenarios from the IPCC; and (3) scenarios of stabilized greenhouse gas concentrations. The results for global averages showed that, even if emissions are stabilized, significant warming and sea level rise will be experienced. The temperature showed signs of

leveling off for stabilized scenarios while the sea level rise continued to increase. This increase did not account for melt from ice sheets and glaciers. The high northern latitudes and land areas are predicted to experience the greatest warming.

Kiehl (2011) used historical observations rather than climate models to discuss the potential warming due to increased carbon dioxide. Kiehl (2011) states that the Earth's CO_2 concentrations are increasing to rates that have not existed in 30-100 million years, at which time the Earth's climate was extremely warm compared to current conditions. In addition, historical data implies that the Earth's sensitivity to CO_2 radiative forcings may be greater than projected by climate models. Based on these observations, it is possible that the Earth will experience climate conditions never experienced by the human species at a faster rate than projected by current climate models.

The effect of clouds on the climate is one of the greatest uncertainties in understanding climate change. Some studies suggest that warming will influence clouds and counter the effects of greenhouse gases; however, computer models suggest that cloud changes will enhance warming. Andrew Dessler of Texas A & M University analyzed the effect of cooling and warming from La Nina and El Nino, respectively, on clouds. Dessler found that on the time scale analyzed, clouds did not counter the greenhouse gas warming effect. He found a small positive feedback, which would suggest warming, but could not eliminate the possibility of a small negative feedback as well. Regardless, the results did not support the possibility of a large negative feedback, which would result in cooling (Kerr 2010).

Kerr (2009) reports that the loss from ice sheets in Greenland and Antarctica have accelerated in the past seven years. The results were based on measurements from the Gravity Recovery and Climate Experience (GRACE) satellite missions. This contradicts results that the shrinking of the southeastern Greenland glaciers had slowed. The inability to extrapolate these short term findings into the future is emphasized.

Kaufman et al. (2009) analyzed warming and cooling trends in the Arctic for the past 2000 years. They compiled available climate records from above 60 degrees north with record lengths greater than 1,000 years at annual to decadal time periods. Data from 23 sites that contained paleoclimatic records based on lake sediment, glacier ice, and tree rings were analyzed. The data was compiled based on 10-yr mean temperatures and standardized relative to the reference period 980 to 1800. Kaufman et al. (2009) found that a cooling trend occurred from 1 C.E. to 1900 C.E. The twentieth century, however, showed an increasing trend including four of the five warmest decades occurring between 1950 and 2000.

Despite projections by the IPCC for warming of 0.2 degrees Celsius from 1999 through 2008, the past decade showed a flat trend. The Hadley Centre group used climate models to try to quantify the likelihood of a decade long warming pause. 700 years of 20th century climate data were simulated based on 10 modeling runs. The century long warming equaled 2 degrees Celsius as expected. However, within the 700 years, 17 independent 10-yr time period experienced trends resembling the past decade. Scientists explain that this is the result of natural variability. Models did not suggest pauses greater than 15 years, which suggest that warming will continue in the next few years.

2.1.14 Climate Change Engineering

Hegerl and Solomon (2009) discussed the risks involved in climate engineering. Geoengineering solutions aim to counteract the effects of climate change and remain a controversial topic among climate scientists. One criticism is that studies focus too much on how to counteract warming without evaluating additional risks involved. A need exists for emphasis on both benefits and risk of geoengineering. For example, one solution is to reduce increasing incoming solar radiation by increasing atmospheric reflecting particles or positioning reflective mirrors beyond the atmosphere. This would provide a quick solution to warming; however, risks can be analyzed through the effects of volcanic eruptions in the past, which caused massive cooling followed by drought due to the decrease in evaporation. Models have captured changes in precipitation in the 20thcentury due to greenhouse gases; however, the magnitude of these changes has been underestimated. This suggests that an external forcing may be missing that influences precipitation. Therefore, methods that only target warming may have additional effects on the climate. Until these processes are fully understood, emphasis on the risk as well as the benefits of geoengineering must be made.

2.2 Landuse Change Studies

2.2.1 Introduction

As population increases and technology advances, changes in land use will continue to occur. Land cover has a significant impact on the velocity and quantity of runoff within a watershed. Variables accounting for land cover or landuse exist in the Manning's Equation, the SCS Method, and the Rational Method as the Manning's roughness coefficient, the curve number, and the runoff coefficient, respectively

(McCuen 2005). Therefore, it is reasonable to assume that as land cover or land use changes in a watershed, the characteristics of runoff would change as well. Research exploring the effects of land use change, particularly in regards to agricultural and urbanization changes, on runoff characteristics will be discussed herein.

2.2.2 Urbanization Land use Changes

Bronstert et al. (2002) discussed the effects of land-use and climate change on storm runoff generation. They discussed the possible effects of climate change and landuse change on storm water runoff, models that showed the hydrologic responses to these changes, and two studies conducted in Germany. The first and second case studies showed the effects of climate change and land-use changes, respectively, on storm runoff production in catchments in Germany. The land use case study analyzed the hydrologic effect of potential future land use scenarios using the hydrologic model WaSiM-ETH. Urbanization was the main focus of the land use analysis. The results showed that land use had a greater influence on flooding caused by high rainfall intensities than low rainfall intensities.

The United States Geological Survey (USGS) developed a regression equation to predict peak discharge rates for urbanization that results in an impervious area of 15% or greater (Sauer et al. 1981). The equation depends on factors such as the impervious cover and the rural peak discharge for the area. Values of the rural peak discharge for a specific return period of interest are available for all locations through the USGS.

The USGS conducted a nationwide study to develop a method of predicting urban peak discharge at ungauged site (Sauer et al. 1983). 269 gauged basins in 31 states were used to design regression equations for the 2-yr, 5-yr, 10-yr, 25-yr, 50-yr, 100-yr, and

500-yr flows. Three models were developed, two consisting of seven independent parameters and one consisting of three independent parameters. The seven parameter models included basin development factor, impervious area (%), drainage area, slope, rainfall intensity, basin lag time, and lake or reservoir storage depending on the model. The three parameter model consisted of rural discharge, basin development factor, and drainage area. The three models provided unbiased estimates of flood frequency with a standard error of regression ranging from +/- 37% for the 5-yr flood and +/- 49% for the 500-yr flood.

Moglen and Shivers (2006) developed a method to adjust rural peak discharge values to urbanized conditions. The method can be applied nationally based on seven available models, each varying in complexity and input parameters. The Null Model is the simplest model and requires only rural peak discharge as an input. The Simple Impervious Model consists of moderate complexity and requires the rural peak discharge as well as the percent impervious area within the watershed. The Simple Population Density Model consists of the same structure as the simple impervious; however, population density is used as an indicator of impervious area. The Imperviousness Distribution model has moderate to high complexity and contains an additional input variable, the 10th and 90th percentile of urbanized are within the watershed. This variable represents the level of homogeneity within the watershed. Likewise, the Population Density Distribution model requires the 10th and 90th percentile of population density within the watershed. The final models are the Scaled Impervious and Scaled Population Density Models. These models take into account the argument that the

effect of impervious area on runoff is not linear, and includes a scaled value of the input parameters, either impervious area or population density.

Moglen and Shivers (2006) applied each of these models to watersheds throughout the United States and analyzed the goodness-of-fit and physical rationality of each. The results showed that different models performed the best based on the coefficient of determination and standard error ratio based on the return period analyzed. The Impervious and Population Density Distribution Models perform slightly better overall, with the impervious model providing slightly better predictions than the density model. However, the variation in goodness-of-fit values ranged from 0.779 to 0.909 for the coefficient of determination and 0.257 to 0.48 for the standard error ratio. This suggests that each model performs well based on the goodness-of-fit statistics. Analysis of the parameters, however, suggests that the population density models, with the exception of the density distribution model, contain non-rational trends in one or more of the model exponents. Therefore, the Population Density and Impervious Area Distribution Models provide the best predictions based on physical rationality and goodness-of-fit.

De Roo et al. (2003) used the LISFLOOD catchment model to determine the effects of flood defense methods and landuse change on flooding in the Oder basin, covering parts of the Czech Republic, Poland, and Germany. The model was calibrated and validated for the flood events of 1977, 1985, and 1997. The study showed that the measures of flood defense proposed by the International Oder Commission significantly improve and reduce flood risk. The model showed that reforestation reduces flood peaks, while future urbanization causes a slight increase in peak discharge. However, the

authors noted that the data used to simulate the model had higher amounts of rainfall in more rural and mountain areas as opposed to urban areas. Therefore, if higher rainfall amounts occurred over urban areas, the effect of urbanization can be assumed to be greater.

Todd et al. (2007) conducted a study to establish the relationship between land use change, climate, and watershed hydrology in the area of Indianapolis, Indiana. Historical precipitation and streamflow data were assessed for significant trends. The Mann-Kendall Rank Correlation Test was used to detect and determine the significance of any trends. A hydrologic model was also used to predict surface and subsurface water flows for multiple historical land use scenarios. The results did not show a statistically significant increasing trend in precipitation; however, a significant trend for streamflow and baseflow did exist. This would suggest that land use changes as opposed to climate changes over time are influencing watershed hydrology in the Indianapolis area. However, the hydrologic modeling approach did not show the same effects of land use changes. Using land use data from the years 1940 and 2000, the model resulted in a slight increase in baseflow, a decrease in runoff, and a decrease in evaporation over time.

Beighley et al. (2009) analyzed the effects of impervious area estimation methods on simulated peak discharge. Two data estimation methods were used: (1) high resolution aerial photographs and (2) medium resolution satellite data. The results showed that the different methods resulted in a difference in peak discharge estimates of 16% and 9% for the 2-year and 100-yr storm, respectively, at the watershed scale for the Mission Creek watershed in Santa Barbara, California. At the model unit scale, these

differences increased to over 41 and 21%, respectively. This suggests the sensitivity of peak discharge to impervious area.

Glick (2009) analyzed the effects of impervious cover on stormwater quality and quantity at 38 stormwater monitoring stations in Austin, Texas. The results showed a relationship between impervious cover and mean concentration of pollutants with a correlation coefficient equal to 0.75.

Kauffman et al. (2009) analyzed nineteen watersheds near the University of Delaware campus with impervious areas ranging from 3 to 44% to determine the effects of urbanization. They found that a relationship exists between impervious area and dry weather stream baseflow. This suggested that increased impervious area reduces infiltration capabilities, thus reducing groundwater recharge.

Hundecha and Bardossy (2004) analyzed the effects of land use change using a conceptual rainfall-runoff model. Model parameters were calibrated regionally based on land use, soil type, catchment size, and topographic structure. Regional parameter values were then transferred to a catchment scale for each individual basin. Results suggested that urbanization causes an increase in summer peak discharge values and a small increase in winter peak discharge values. Afforestation causes a decrease in both peak and total runoff volume.

Endreny et al. (2009) analyzed the effects of impervious area on hydrologic model parameters and compared the use of NLCD land use data with road-enhanced NLCD land use data. 704 watersheds in New York were analyzed under impervious area conditions of 1992 and then of 2001. The results showed that the road enhanced data provided a significant increase in impervious area in both 1992 and 2001, resulting in an

increase in hydrologic parameters, including the curve number, runoff coefficients, and event mean concentration based pollutant loads. These findings suggested that impervious roadways have a significant impact on hydrologic measures and road enhanced NLCD should replace original NLCD data.

Moscrip and Montgomery (1997) analyzed six lower order streams in the Puget lowlands in Washington regarding the effects of urbanization from 1940-1950 to 1980-1990. The urbanization records and flood frequencies for each basin were retrieved. The discharge records for each basin were separated into pre- and post-urbanization time periods. Two of the basins were used as control basins, as they did not show significant changes in land use. The results showed that the basins experiencing urbanization changes also experienced shifts in flood frequency, whereas the control basins did not show any changes in flood frequency. The 10-year flood shifted between the 1-year and 4-year flood within the basins experiencing urbanization. A decline in salmon abundance was also observed in the urban basins. The results of this study suggested that urbanization causes decline in salmon as well as changes in flood frequency.

Konrad et al. (2005) analyzed the influence of urbanization on interannual streamflow patterns in 16 streams in the Puget lowlands of Washington. They used the following metrics to analyze the data: (1) fraction of time that streamflow is greater than the mean (T_{Qmean}); (2) the annual peak streamflow coefficient of variation (CV_{AMF}); and (3) the fraction of time that discharge is greater than the 0.5-year flood ($T_{0.5}$). Urbanization was measured based on the road density within the watersheds using geographic information systems. The results suggest a relationship between streamflow and urban development, as road density had a significant positive relationship with

$Q_{0.5}$and Q_{AMF}, but not the mean discharge or the duration for which a flow is exceeded. The annual peak discharge contained less variation in streams within urban watersheds. The study also analyzed the effects on channel form and stability. The results show that models to predict channel width had the lowest standard error when based on Q_{mean} and Q_{10}, suggesting a strong relationship. Analysis of $T_{0.5}$ suggests that urban areas experience a brief duration of frequent high flows. An inverse relationship existed between streambed stability during the 0.5-year flood and the $T_{0.5,}$ suggesting that urban streams experience an increase in streambed disturbance.

Mejia and Moglen (2009) analyzed the relationship between the spatial patterns of urban development and flood conditions through an optimization approach. The objective functions in the optimization approach represented the following different spatial patterns: (1) clustered development at most downstream locations in watershed; (2) development distributed uniformly in watershed; (3) clustered development at upstream headwater locations; and (4) clustered development at downstream locations with low density development throughout the watershed. The aggregate impervious area in Option 4 was kept below an optimized policy threshold to explore the effect of implementing such a threshold. The results showed that option 1 reduced flood peaks throughout the entire stream network. In option 2, all locations within the stream network experienced the same hydrologic effects due to the even distribution of urbanization. Option 3 had the most negative hydrologic effects on the watershed. The results for Option 4 suggested that implementing an aggregate imperviousness policy threshold may be beneficial in reducing the effects of urbanization.

Reed (1990) analyzed the watershed of Valley Creek at the Schuylkill River to assess the effects of land use changes on flood frequency and hydrograph characteristics. Five phases of the watershed conditions were defined and discussed. Phase 1 consisted of a heavily forested watershed with high soil infiltration and subsurface processes that dominated the surface runoff. The peak was lower and flooding occurred less frequently than under existing conditions. As a result, the stream channel was not as wide or deep as today. This phase was estimated to have occurred in the 1600's. Phase 5, occurring in the 1990's, was classified as poor watershed conditions. Forest exists only in the least productive soils and steep slopes. Woodlands and agriculture land use have decreased the most compared to other land use types since 1970. Reed (1990) used the SCS TR-55 method to simulated the five phases and compare the hydrologic characteristics of the watershed. The results showed that peaks doubled over the 300-yrs with land use changes. The increased peak resulted in an impaired fluvial system.

McCuen and Thomas (1990) explained methods to estimate urban flood frequency when assumptions of independence and stationarity are not valid. The methods explained are as follows: (1) the use of statistical tests to select a homogenous period of record; (2) determination and removal of peak discharge trends, followed by the application of a frequency analysis to the residuals; (3) adjust the annual peak discharge to homogeneous conditions based on an urbanization index; and (4) use a calibrated watershed model and climatic data to simulate a homogeneous series of data. The four methods were applied to an urban watershed in Louisville, Kentucky. The results showed that each of the four methods provided comparable estimates for the 100-yr flood.

2.2.3 Agricultural Land use Changes

Fitzpatrick et al. (1999) used geomorphic field techniques and hydrologic modeling to assess the effect of land use changes resulting from human actions since the 1870's on flooding and sedimentation in North Fish Creek in Wisconsin. The HEC-1 rainfall/runoff model was used to conduct the hydrologic modeling analysis. The land use scenarios were modeled including pre-settlement conditions of forested land cover, peak agricultural conditions occurring in the mid 1920's to the mid 1930's, and current land cover conditions. The results show that when agricultural activities were at a maximum, in the 1920's and 1930's, the peak flows that occur on an average of 2-year intervals were predicted to be three times greater than pre-settlement conditions. Under current land cover conditions, flood peaks of storms that occur at two-year intervals were predicted to be twice as great as pre-settlement conditions. Sediment loads during the maximum agricultural conditions were 2.5 and up to 5 times greater than under current and pre-settlement land cover conditions, respectively. This suggests that land cover has an effect on flooding and sedimentation, while afforestation practices may decrease flood peaks and, therefore, decrease erosion and sedimentation.

Moussa et al. (2002) analyzed the human influence on flooding in regards to agricultural practices such as tillage practices and ditch networks. It was assumed that tillage influences infiltration rates while ditch networks affect the transport of water from the agricultural field the catchment outlet, both influencing flooding. The spatially distributed hydrologic model, MHYDAS, was developed and tested on the farmed catchment of Roujan in Southern France. Three flooding events were simulated: (1) 30

April 1993; (2) 31 August 1994; and (3) 30 September 1994. The water table levels were high during the spring and fall flooding event and low during the summer flooding event.

For the tillage practice analysis, three scenarios were assessed: (1) all vineyard fields are non-tilled; (2) all vineyard fields are tilled; and (3) all fields, vineyards, and other land uses are freshly tilled. The results showed that for all three flooding events, the freshly tilled scenario had the greatest reduction in the value of the peak discharge but not the timing. In the summer flood event, the major hydrologic process was the flow from the ditch to the groundwater, which is expected considering the low water table.

For the ditch network analysis, a man-made ditch network was compared to drainage based on a digital elevation match. For the three flood events, the man-made ditch network accelerated the runoff by causing concentrated flow and lacking natural obstacles. Also, when the water table was lower than the ditch network, much of the runoff produced at the field scale was infiltrated into the groundwater.

2.2.4 Hydraulic Geometry Relationships

Hydraulic geometry relationships have been developed that relate watershed characteristics to stream channel geometry. Bankfull flow is defined as an event that fills a channel to the active floodplain elevation, which influences channel dimensions. Sweet and Geratz (2003) analyzed the bankfull hydraulic geometry relationships for the North Carolina's Coastal Plains. Channel dimensions were collected based on cross-sectional and longitudinal survey data from streams. Power models were fit to relate drainage area to bankfull discharge as well as cross-sectional area, width, and mean depth of a channel. Likewise, Dunn and Leopold (1978) developed graphical relationships between bankfull

flows versus drainage area for channels in Pennsylvania and Wyoming in addition to graphical relationships between bankfull flows and channel velocity, depth, and width.

2.3 Trend Detection Methods

Radziejewski and Kundsewica (2004) assessed the necessary strength and length for change in data to be detected statistically as a trend. Generated data for river flow records lacking trends were used and altered to contain gradual and abrupt trends. The performance of different tests was compared: Mann-Kendall, Spearman's Rank correlation, Normal Scores Linear Regression, Distribution-Free CUSUM, and Cumulative Deviations applied to normal scores. The results showed that neither weak changes nor changes over a short time period can be detected.

Strupczeqksi et al. (2001) reviewed the use of statistics of extremes in hydrology and characteristics of hydrological extremes. They focused on climate-related issues such as variability and change. Recent developments in statistics of extremes were introduced such as the point process model that combined the block maxima and the point-over-threshold method; estimation techniques were compared. Trends in hydrologic extremes as a result of global warming were also discussed.

Yue and Pilon (2004) used Monte Carlo simulation to compare the power of the following statistical tests in determining the significance of linear and nonlinear monotonic trends: (1) parametric t-test, (2) non-parametric Mann-Kendall test, (3) Boot-strap based slope test, and (4) bootstrap-based MK test. The results showed that the slope based tests, t-test and BS-slope test, were equally powerful and the rank based tests, Mann-Kendall and bootstrap-based MK test, were equally powerful. The slope tests were slightly more powerful for normally distributed data and the rank tests were slightly more

powerful for non-normally distributed data. The power of the test was slightly sensitive to the shape of the trend.

Frei and Schar (2000) developed a methodology to assess frequency trends in rare and extreme weather events using the binomial distribution and logistic regression method for trend estimating and testing. They determined the detection probability, which was a quantitative estimation of the Type II error, based on Monte Carlo-simulated surrogate records. The detection probability was a function of record length, average return period, and magnitude of trend. The method was applied to data in Switzerland. The results showed difficulty in detecting frequency trends of rare events and the importance of long records of data.

Khaliq et al. (2009) assessed the results of trend detection methods in the presence of serial and cross correlation. They reviewed methods of trend detection, including Mann-Kendall, Spearman Rank correlation, Sen's slope, and the least squares regression. The first two methods are rank based while the latter two are slope based methods. Methods addressing the effects of cross and serial correlation were introduced. The study used annual mean daily flows of Canadian River basins. The results showed that ignoring the presence of cross and serial correlation can cause in erroneous results.

Zhang et al. (2004) compared methods of detecting significant linear trends in extreme values using Monte Carlo simulations. For the Monte Carlo simulations, precipitation data that contained pre-determined trends were simulated. The simulated frequency of precipitation in each year was based on the normal distribution, while the precipitation depths were based on the exponential distribution to develop extreme data. The results showed that the ordinary least squares test to be the least reliable. Kendall's

tau-based method was more powerful than the OLS method, but the advantage decreased as the sample size decreased. The Generalized Linear Regression Method in the GEV distribution was more powerful than OLS and Kendall's tau-based method, but it was better when only estimating one parameter. The r-largest method was consistently better than both the OLS and Kendall method, and improved upon the GEV method when more than one extreme per annual block was used.

Kundzewicz et al. (2004) provided guidance regarding methods of detecting changes in hydrological time series. They discussed suitable data sets, statistical tests, exploratory analysis, and interpretation of results for change detection in hydrological records. Methods of trend detection discussed included distribution free methods as well as resampling and bootstrap methods for data. They suggested a greater use of distribution-free methods because hydrological data are often non-normal and contain seasonal and serial correlations. They also recommended resampling techniques because they require few data assumptions and are flexible, robust, and powerful. The need to examine external evidence to determine if changes are caused by land use, climate, or other changes in area was also emphasized.

Yue et al. (2002) used Monte Carlo simulation to explore the power of the Mann-Kendall and Spearman's rho tests in detecting monotonic trends. The tests were applied to annual maximum daily streamflow data from 20 pristine basins in Ontario, Canada. The results suggest that the power of the tests increase with an increase in the magnitude of the trend and sample size and decrease with an increase in the amount of variation within the time series. The power is also influenced by properties of the data such as the distribution and skewness. The tests had similar levels of power in detecting trends.

Statistical tests for the detection of change points within a time series are also important in hydrologic and climate data. Change points in time series can be defined as the time at which the statistical characteristics of the data change. Reeves et al. (2007) provides a summary of the existing change point detection methods where the time series contains a single change point. Table 2-2, provided from Reeves et al. (2007), shows the hierarchy of regression models that can be tested using the existing change point detection tests and methods. Models 1 and 2 suggest that a change point does not exist. Models 3 through 5 suggest that a change point does exist. Model 3 consists of a change in mean for a zero slope model; Model 4 consists of a change in mean with a non-zero slope; and Model 5 consists of both a change in mean and slope at the change point location.

Table 2-2. Hierarchy of Models Provided by Reeves et al. (2007) in which c Denotes the Change Point Location.

Model 1	$Y_t=\mu$	$+\varepsilon_t$
Model 2	$Y_t=\mu + \beta t$	$+\varepsilon_t$
Model 3	$Y_t=\mu + \Delta I(t>c)$	$+\varepsilon_t$
Model 4	$Y_t= \mu + \beta_1 t + \Delta I(t>c)$	$+\varepsilon_t$
Model 5	$Y_t= \mu + \beta_1 t + \Delta I(t>c)+ \beta_2 t*I(t>c)$	$+\varepsilon_t$

.

Table 2-3 shows the single change point test statistics explained and compared by Reeves et al. (2007). Each test statistic depends on the assumption that at most, only one change point exists within a time series. Additionally, many tests assume that the residuals are independent and identically and normally distributed. For each statistical test, the null hypothesis determines which model Table 2-3 is tested.

Table 2-3. Existing Single Change Point Detection Tests.

Test	Ho	Ha	Test Statistic	Assumptions
Standard Normal Homogeneity (SNH)	Zt ~ N(0,1), 1<=t<=n	Z t~ N (μ_1,0), 1<=t<=c Zt ~ N (μ_2,0), c+1<=t<=n where c = change point location	T_0=max(T_C), 1<=c<n with T_C=c* $\overline{Z_1^2}$ + (n-c)*$\overline{Z_2^2}$ Where $\bar{Z}_1=\frac{1}{c}\sum_{i=1}^{c} Z_i$ and $\bar{Z}_2=\frac{1}{n-c}\sum_{i=c+1}^{n} Z_i$ where $Z_t = \frac{y_t-\bar{y}}{s}$	1) At most one change point within the time series 2) Standardization produces normal variables with unit variance
Nonparametric Standard Normal Homogenity (NPW)	$\mu_1 = \mu_2$	$\mu_1 \neq \mu_2$	W_{max} = max(W_C) 1<=c<=n where $W_c=12\frac{[\sum_{i=1}^{c} r_t - c*(n+1)/2]^2}{c(n-1)(n+1)}$ where c = change point location and r is the rank of the t^{th} element in the series	1) At most one change point within the time series
Two-Phase Regression Model (Hinkley 1969, 1971)	$\mu_1 = \mu_2$	$\mu_1 \neq \mu_2$	F_{max} = max(F_C) 1<=c<n where $F_C=\frac{(SSE_0-SSE_A)/2}{SSE_A/(n-4)} \sim F_{2,n-4}$ where SSE_0 and SSE_A are the sume of the squared errors under H_0 and H_A, respectively, and the following model: $Y_t=\begin{cases} \mu_1+\beta_1 x_1+\varepsilon_t, 1\le t\le c \\ \mu_1+\beta_2 x_2+\varepsilon_t, c+1\le t\le n \end{cases}$ where x_1<=x_2<=…..<=x_n and where c = change point location	1) At most one change point within the time series 2) Errors, ε_t, are zero mean, independentand identically, normally distributed
Revised Two-Phase Regression Model (Lund and Reeves 2002) (LR)	$\mu_1 = \mu_2$ $and \beta_1 = \beta_2$	$\mu_1 \neq \mu_2$ and/or $\beta_1 \neq \beta_2$	F_{max} = max(F_C) 1<=c<n where $F_C=\frac{(SSE_0-SSE_A)/2}{SSE_A/(n-4)} \sim F_{2,n-4}$ where SSE_0 and SSE_A are the sume of the squared errors under H_0 and H_A, respectively, and the following model: $Y_t=\begin{cases} \mu_1+\beta_1 x_1+\varepsilon_t, 1\le t\le c \\ \mu_2+\beta_2 x_2+\varepsilon_t, c+1\le t\le n \end{cases}$ where x_1<=x_2<=…..<=$x_{n\ and}$ where c = change point location	1) At most one change point within the time series 2) Errors, ε_t, are zero mean, independentand identically, normally distributed
Two-Phase Regressin with Common Trend Wang (2003) (XLW)	$\mu_1 = \mu_2$	$\mu_1 \neq \mu_2$	F_{max} = max(F_C) 1<=c<n where $F_C=\frac{(SSE_0-SSE_A)/2}{SSE_A/(n-3)} \sim F_{2,n-3}$ where SSE_0 and SSE_A are the sume of the squared errors under H_0 and H_A, respectively, and the following model: $Y_t=\begin{cases} \mu_1+\beta_t x_1+\varepsilon_t, 1\le t\le c \\ \mu_2+\beta_t x_2+\varepsilon_t, c+1\le t\le n \end{cases}$ where x_1<=x_2<=…..<=$x_{n\ and}$ where c = change point location	1) At most one change point within the time series 2) Errors, ε_t, are zero mean, independentand identically, normally distributed 3) Does not allow trend shifts at change point time

In addition to the individual test statistics, Reeves et al. (2007) discussed hierarchical methods for the detection of change points within a time series. Within these methods, the appropriate model from Table 2-2 is selected and then the location of the change point is determined. The Modified Vincent Method is a hierarchical method that tests the residuals from Models 1 through 5 based on the Durbin-Watson test. If the residuals are determined to be adequate, a change point location is then estimated based on the c that minimizes the SSE. Two additional methods to select the appropriate model within a hierarchal method are the Akaike's Information Criteria (AIC) and the Sawa's Baye's criteria (SBC). The idea behind these methods is to penalize the addition of excessive model parameters.

Reeves et al. (2007) found the AIC and SBC approaches both have the potential for high Type-I errors depending on the model selected. For model 3 in Table 2-2, SNH and NPW were found to be the most powerful test statistics when the assumptions were met. However, both tests failed to accurately detect change points located at the beginning or end of a series. The performance of the XLW, LR, and GNL methods varied depending on the model of the data based on Table 2-2.

Reeves et al. (2007) recommend future research in the development of change point tests. They suggest the development of more powerful nonparametric procedures to eliminate the requirement for independence and normality of the residuals. Additionally, they emphasize the need for a test to detect multiple change points within a time series. While common practice is to locate one change point and then analyze the remainder of the time series for an additional change point, Reeves et al. (2007) state that this will lead

to inaccurate detection of change points because the results for the detection of the first change point will be heavily biased by the existence of additional change points.

2.4 Frequency Analysis Methods

2.4.1 Introduction

Flood frequency analyses are used as a method of estimating the probability of a particular flood magnitude occurring in order to plan accordingly. The statistical distribution most commonly used in flood frequency analyses in the United States is the Log-Pearson Type III distribution. It is recommended by the U.S. Water Resources Council in Bulletin 17B (Interagency 1982). The analysis procedure is as follows: (1) create a time series of the logarithms of the annual maximum flood series value, Y_i; (2) Calculate the mean, $\overline{Y}$, the standard deviation, S_y, and the standardized skew, g, of the logarithms; (3) select values of exceedance probability for the analysis and obtain the corresponding standardized variate, K, values that are provided in table form; and (4) for the exceedance probabilities selected, calculate the LP3 curve values as follows: $Y=\overline{Y}+K*S_y$. Then plot the values and the exceedance probabilities to develop the flood frequency curve. The computed discharges can be determined by taking the antilog of the values on the curve (McCuen 2005).

Many variations of the flood frequency method proposed by Bulletin 17B have been proposed. Stedinger and Griffis (2008) discussed the need for updates in Bulletin 17B's method that include the following: (1) improved methods to estimate a regional skew; (2) methods to incorporate historic data; (3) a consistent treatment of outliers; (4) methods to assess statistical uncertainties in estimates; (5) incorporation of generated flood records based on precipitation records and watershed models into flood frequency

analyses; (6) incorporation of simulations of reservoir system performance and regulated flows; and (7) development of distributions for very extreme floods. In addition to the improvements suggested by Stedinger and Griffis (2008), alternative distributions have also been considered. Additionally, methods for a flood frequency analysis for nonstationary conditions are being developed, as the Bulletin 17B method for assumes stationarity of the data. A sampling of studies that suggest deviations from the Bulletin 17B approach to flood frequency analyses will be discussed herein.

2.4.2 Frequency Distributions

The generalized extreme value distribution (GEV) is a popular choice for representing extreme hydrologic data. Data can converge to one of three GEV distributions: Type I, Type II, or Type III. The cumulative distribution function for the GEV distribution is as follows:

$$F(x) = \exp\left\{-\left[1 - \frac{\mathrm{K}(x-\xi)}{\alpha}\right]^{1/\mathrm{K}}\right\} \qquad \text{for K} \neq 0 \qquad \text{Eq. 2-1}$$

with ξ = location parameter, α = scale parameter, and K = shape parameter. A positive shape parameter results in a Type III distribution with a finite upper bound and thinner tail. A negative shape parameter results in a Type II distribution and a thicker tail (Stedinger et al. 1993). In the estimation of maximum values in hydrology, the Type III distribution is not practical, as it is bounded from above (Koutsoyiannis 2004). The Gumbel or Type I distribution is attained when the shape parameter equals zero and has the following distribution:

$$F(x) = \exp\left\{-\exp\left[-\frac{(x-\xi)}{\alpha}\right]\right\}. \qquad \text{for K} = 0 \qquad \text{Eq. 2-2}$$

The distribution resembles the Gumbel distribution when the magnitude of the shape parameter is less than 0.3 (Stedinger et al. 1993).

Wilks (1993) compared the performance of the following probability distributions in representing annual extreme and partial duration precipitation data: (1) Beta-P; (2) Beta-k; (3) Revfeim distribution; (4) Generalized gamma distribution; (5) Generalized Pareto distribution; (6) Generalized Extreme Value distribution; (7) Transnormal distribution; (8) Three-parameter lognormal distribution; and (9) Gumbel distribution. The Maximum Likelihood method was used to fit the parameters. The parameters were estimated using the Levenberg-Marquardt method, a generalization of the Newton-Raphson algorithm. The degree of fit was determined in the right tail using quantile-quantile plots. The boot-strap method was also used. The results showed that the Beta-P distribution was almost unbiased for the quantile extrapolations and had a small variance for partial duration data. The 3-parameter lognormal performed well for partial duration, but the right tail was inferior to the Beta-P. The Beta-K was best for annual extremes but inferior to the Beta-P for partial duration data.

De Michele et al. (2008) evaluated the critical design storm (CDS) considering the possibility of non-stationarity in Italy. Two data lengths assessed were: (1) past 30 years starting at different times and (2) past 90 years. The CDS was computed by fitting the annual maxima of the daily rainfall with each of the following extreme value distributions: (1) General Extreme Value Distribution (GEV); (2) Gumbel Distribution (EV1); (3) Frechet Distribution (EV2); and (4) Log-Normal Distribution (LN2). Parameter estimation was conducted using L-Moments. The Anderson-Darling and Kolmogorov-Smirnoff goodness-of-fit tests were used to assess the ability of model to fit

observed data. The results showed that the GEV, Gumbel, and LN2 were all a satisfactory fit and met a 95% confidence level while the Frechet did not. An increasing tendency of the CDS was less noticeable when the entire data set was used, while shorter time spans showed an increase in CDS starting around 1940. To account for the presence of nonstationarity, they suggested increasing the estimated value of the CDS for design.

While additional distributions have proved to be a good representation of hydrologic data, Stedinger and Griffis (2008) support the use of the LP3 distribution for flood frequency analyses. They argue that the differences in quantile estimators that results from other extreme value distributions is less than the uncertainties associated with the actual estimations. They suggest that the use of a reasonable distribution, such as the LP3 distribution, is sufficient and emphasis should be placed on improvements in fitting the distribution based on expansions in the knowledge of flood processes and regional patterns.

2.4.3 Regional Analyses

Koutsoyiannis (2004) analyzed 169 rainfall records throughout Europe and North America to determine regional characteristics of the GEV distribution. Koutsoyiannis (2004) discussed the difficulty in estimating the shape parameter with sample sizes as great as 100 years or more due to sampling variation and estimation bias. The results showed that the Type II GEV distribution is the best representation of hydrologic extremes and a constant shape parameter value of 0.15 represents the rainfall distributions in both Europe and North America. Note that the notation used by Koutsoyiannis differs from that explained by Stedinger et al. (1993) and a positive shape parameter represents a Type II distribution.

Javelle et al. (2001) used Flood-Duration-Frequency (QdF) Analysis to develop a statistical model that provides a more complete description of a basin's flood regime. The model is similar to the Intensity-Duration-Frequency method (IDF) but uses a minimal amount of parameters. The study analyzed 158 stream gauges from basins in Quebec and Ontario, Canada. The QdF model proved to be robust and independent of geography or climate. The Index-Flood (IF) method was then generalized to develop a regionalized QdF model used for fixed non-contiguous homogeneous regions. Javelle et al. (2001) determined that neighborhood approaches are more efficient. The results showed that regression is a main source of error for both methods in estimating flood indices. The authors suggested testing the model for more sophisticated methods for delineating homogeneous regions or determining significant physiographic characters.

Groupe de recherché en hydrologie statistique (GREYHS) (1996) reviewed different techniques for forming homogeneous regions as well as different methods of regional flood estimation in order to estimate floods at sites with little or no data available. Techniques used to determine homogeneous regions included: (1) region of influence; (2) canonical correlation analysis; (3) correspondence analysis and ascending hierarchical clustering; and (4) L-moments. Flood frequency analysis methods included: (1) GEV/PWM index flood procedure; (2) regional non-parametric analysis; (3) regional flood estimation by peaks-over-threshold methods based on direct multiple regression, the GP/POT index flood procedure, and the EXP/POT index flood procedure; (4) regional L-moment analysis; and (5) the regional estimation of floods by regression methods. Approaches in comparing these methods must be developed.

Castellarin et al. (2000) used Monte Carlo simulation to assess the performance of four hydrological similarity measures when used to form homogeneous pooling groups for a regional flood frequency analysis. The effectiveness of a pooled frequency analysis depends on the homogeneity of the group and the target size. The following measures for forming homogeneous pooling groups were used: (1) seasonality of hydrological extreme events, (2) measures of frequency of rainfall extremes and permeability, (3) daily rainfall L-statistics, and (4) daily rainfall and permeability. The pooling group consisting of the whole area of study was used as a reference condition. The results showed that all of the pooling groups based on similarity measures performed better than the whole area of study. The seasonality of hydrological extreme events pooling measurement performed the best. The first and second similarity measures overestimated while the third and fourth measures underestimated the true flow quantiles.

2.4.4 Nonstationarity

Khaliq et al. (2006) conducted a review of frequency analysis methods and their assumptions of independence and stationarity. They addressed the issue of climate change affecting these assumptions and reviewed existing approaches to this issue. Methods for removing serial dependence in order to satisfy the assumption of independence were reviewed including the decorrelation approach, the Lettenmaier technique, and the probability density estimation by wavelets and kernels. Approaches reviewed addressing non-stationarity include the r-largest model, the peaks-over-threshold (POT) method, covariates and time-varying moments, quantile regression method, local likelihood, and pooled flood frequency analysis. Future recommendations were also discussed.

Cunderlik and Ouarda (2006) defined components in a nonstationary flood-duration-frequency model. Time dependent model parameters were identified on a regional basis. The model assumes temporally and spatially constant nonstationarity. The model can be used to estimate future flood quantiles. The model was applied to a hydrologically homogeneous region in Quebec, Canada. The results showed that significant bias in flood quantiles will exist if nonstationarity is ignored.

Villarini et al. (2009) developed a flood frequency analysis framework based on the Generalized Additive Models for Location, Scale, and Shape Parameters (GAMLSS). GAMLSS is a tool for modeling time series under nonstationary conditions and can describes the variability of the moments of the annual maximum peak discharge by modeling the parameters of the distribution as a function of time through cubic splines. The method was applied to annual maximum peak discharge records for Little Sugar Creek in Charlotte, North Carolina. The results showed that range of the 100-yr flood discharge value throughout an 83 record as well as the vast increase in the return period of the flood determined to be the 100-yr flood in 1957. Villarini et al. (2009) suggest that alternative definitions of return period be developed for non-stationarity scenarios.

El Adlouni et al. (2007) developed an estimation method for the use of the GEV distribution for quantile estimation in the presence of nonstationarity. They assumed parameters are time-dependent or dependent on other covariates. Parameter estimation was done with generalized maximum likelihood estimation method instead of the maximum likelihood estimation method (common method); covariates were incorporated into parameters with GML. They note that it is important to take into consideration additional information such as historical and regional information to define prior

distribution. The Monte Carlo Markov Chains method was used for estimator calculations in the case of the GML method. They conducted a simulation study to compare the performances of GML (integrates the prior information on the shape parameter) and ML methods using: stationary GEV model; nonstationary case with a linear dependence to the location parameter on covariates; nonstationary case with quadratic dependence on covariates; and nonstationary case with linear dependence in both location and scale parameters. The covariates used included time and the Southern Oscillation Index (SOI). The results showed that the GLM performed better than ML for the studied cases with respect to bias and the root mean squared error. They recommended the following research for the future: develop a distribution that depends on more than one covariate; focus on other statistical distributions and different nonstationarity structures such as trends in the variance of the series (scale parameter); and development of a new framework for risk assessment in the case of nonstationarity.

Villarini et al. (2009) analyzed nonstationarity in the annual peak discharge records from 50 stations in the United States. Trends in flood peaks and abrupt changes in the mean or variance were explored over time using the Mann-Kendall, Spearman, Pearson, and Generalized Additive Models for location, scale, and shape (GAMLSS). GAMLSS accounts for abrupt changes and trends in the parameters of a distribution function. Four scenarios were explored using GAMLSS: (1) a stationary model; (2) the mean varied linearly as a function of time; (3) the variance varied linearly as a function of time; (4) both the variance and the mean varied as a function of time. The results showed that it was difficult to prove nonstationarity despite the significant landuse changes that occurred over time.

Leclerc and Ouarda (2007) explored a method of conducting a regional flood frequency analysis (FFA) that accounts for non-stationarity in ungauged sites. Canonical correlation analysis (CCA) was conducted to define a hydrologic neighborhood of the ungauged site based on meteorological and drainage basin characteristics. The GEV distribution was used to calculate the 5- and 100-yr flood quantiles for the hydrologic neighborhoods based on three different models: (1) stationary moments; (2) nonstationary with first moment varying linearly as a function of time; (3) nonstationary with first moment varying quadratically as a function of time. The time variant flood quantiles were then regressed on the following variables: (1) basin drainage area; (2) gauging station latitude and longitude; (3) mean total winter/spring precipitation; and (4) mean winter/spring maximum air temperature. These equations were verified with gauged watersheds but can then be applied to ungauged watersheds based on the hydrologic neighborhood. The analysis was conducted on river flow gauging stations located in southeastern Canada and northeastern United States. The results showed that multiple regression based on 2 to 4 predictor variables provided efficient estimates with RMSE of 38.2 and 60.8% for the 5-yr and 100-yr, respectively, while the use of canonical correlation analysis to define the hydrologic neighborhood did not improve these estimates. This is most likely due to the small number of sites available for the hydrologic neighborhood.

Raff et al. (2009) developed a method to estimate future flood frequencies using the CMIP3 monthly precipitation data combined with a rainfall-runoff model. The rainfall-runoff model required precipitation in 6-hour time increments; therefore, Raff et al. (2009) retrieved daily precipitation data from the CMIP3 data. Then, they randomly

sampled rainfall depths from a 6-hour time period in the observed data record which were scaled by the ratio of the projected monthly rainfall depth to the observed monthly rainfall depth. A scale constant was applied to ensure that the aggregate precipitation equaled that of the projected time period. The method of sampling 6-hour data records was divided into four categories: hot-wet, hot-dry, cold-wet, and cold-dry based on the median temperature and precipitation in the observed months. This was to ensure that scaling was done in a physically rational manner based on the characteristics of the month analyzed. Raff et al. (2009) then calculated flood frequency curves based on the observed and projected runoff depths and the Log Pearson 3 distribution. Nonstationarity was accounted for based on the concept of 'Look ahead' time periods. Frequency analyses were applied to various time periods considered to have stationary climate conditions. The following time periods were analyzed: (1) current conditions; (2) 2011-2040; (3) 2041-2070; and (4) 2071-2099.

Kwon et al. (2011) used a weather state-based, stochastic multivariate model based on seasonal precipitation rates projected through a regional climate model to simulate and project daily precipitation under climate change conditions for the A2 emissions scenario. The simulated precipitation was input into the Sacramento Soil Moisture Accounting precipitation –runoff model and the Bayesian Markov Chain Monte Carlo scheme was applied to provide an estimate of uncertainties associated with the resulting peak discharge projections. The approach was applied to the Soyang Dam in South Korea. Kwon et al. (2011) compared the design floods that were projected for 2045 based on the projected data from 2030-2060 and the design flood for 1985 based on observed data from (1970-2000). The results suggested that flood events with return

periods greater than 50-yrs experienced a 10% increase in magnitude. However, uncertainties increased with the return period.

Kwon et al. (2008) used a Hierarchical Bayesian Analysis to analyze multiple factors that affect extreme flood events in Montana, which include sea surface temperature (SST), predicted GCM precipitation data, climate indices, and snowpack depth. The climate information was implemented to update estimates of parameter values for the Gumbel distribution, which was used represent annual maximum flood data. The Markov Chain Monte Carlo algorithm was used to then estimate the flood risk prediction parameters. The Bayesian extreme value distribution model was then used to estimate the 100-yr flood from 1930 to 2005. The results showed a statistically significant link between the peak discharge and the SST indices, snowpack depth, and GCM seasonal precipitation data, which suggests that climate indicators can be used to predict flood risk.

Villarini et al. (2010) used the Generalized Additive Models in Location, Scale and Shape (GAMLSS) to assess nonstationarity in seasonal rainfall and temperature from in Rome. Covariate analyses were then conducted based on the Atlantic Multidecadal Oscillation, North Atlantic Oscillation, and Mediterranean Index. Five two parameter extreme value distributions were analyzed, which included the Gamma, Gumbel, logistic, lognormal, Weibull distributions. The results showed that the Mediterranean Index was a statistically significant predict-tor regardless of the season and the North Atlantic Oscillation was a statistically significant predictor for the winter season.

Renard et al. (2006) used a Bayesian framework to account for nonstationarity in extreme events. Three probabilistic models were demonstrated: (1) stationary, (2) step

change, and (3) linear trend. Four extreme value distributions were discussed: (1) exponential, (2) generalized Pareto, (3) Gumbel, and (4) GEV. Regional prior knowledge was used to develop prior distributions and posterior distributions were developed. Frequency analyses were developed for peak-over-threshold extreme events, which take into account uncertainty in both the prior and posterior distributions.

Sivapalan and Samual (2009) provided a nonstationary approach to risk assessment for flood structures. The risk of failure over a design life was defined based on the following equation:

$$R(n, q_p) = 1 - \prod_{m=1}^{n}[1 - P_m^{jm}(Q \geq q_p)] \quad \text{Eq. 2-1}$$

where n = expected life of a design project, m corresponds to the sequential year over the design life, j_m=climate state of the year m, $P_m^{jm}(Q>=q_p)$ = probability that the annual maximum flood, Q, is greater than or equal to q_p in the year under the climate state. This equation was applied to three catchments in Australia based on climate states from pre-1970 climate and post-1970 climate. Possible future evolution of the climate states was randomly generated based on a Markov Chain Model and then a rainfall-runoff model was applied. The results showed a reduction in risk of failure over a design life for Perth, Australia, due to a drier climate in the post-1970 scenario. In each of the three analyses, the design flood decreases as the acceptable level of risk increases.

2.5 Risk Assessment

Risk is defined as a combination of the probability and consequences associated with an event. Policies are often based upon the risk associated for a given return period,

particularly the 100-yr flood. The analysis of risk and the importance of accurate flood frequency estimates will be discussed herein

Moser et al. (2009) define the risk analysis process as the evaluation of risk followed by the consideration of the monetary and non-monetary costs and benefits involved in the implementation of risk mitigation methods. Risk analysis consists of three components: (1) risk assessment; (2) risk management; and (3) risk communication. Risk assessment is considered to be the technical component of a risk analysis, in which the risk is quantified. This includes identification and characterization of the hazard, assessment of the exposure, and estimation of the risk. Risk management considers environmental, social, cultural, ethical, political and legal factors to analyzed potential options to mitigate the assessed risk. Finally, risk communication is the ongoing communication between the two components to ensure that both parties are well informed. Moser et al. discuss the implementation of risk analysis within the U.S. Army Corp of Engineers.

The Interagency Performance Evaluation Task Force, established by the U.S. Ary Corps of Engineers (USACE), analyzed the New Orleans and Southern Louisiana Hurricane Protection System following Hurricane Katrina (USACE 2009). The analysis consisted of a risk assessment for both pre- and post-Hurricane Katrina conditions based on flood mitigation methods and the distribution of the population and property. Within the report, risk was calculated based on the product of the vulnerability of flooding and the consequences that would result.

The vulnerability of flooding is comprised of the definition of the hazard and the probability of the occurrence as well as the system performance. The hazard is defined as

the event or condition that can result in negative consequences. For example, in the assessment of a hurricane, the hazard would include the surge and wave conditions caused by the hurricane. The system performance, which can be considered a reliability analysis, refers to how structural components of the hazard mitigation system will withstand the hazard. For example, system performance would include the level at which levees, floodwalls, or gates will withstand flooding that may result from a hurricane. The vulnerability of flooding of an area combines both the likelihood of the occurrence of the hazard and the system performance during the event.

The consequences are defined by the potential loss of life and property damage that results from the event. Historical data was used to develop flood-depth versus damage relationships to assess property damage from the defined hazard. Census data and evacuation plans were used as input to a simulation model to estimate the loss of life. Finally, the consequences for the defined hazard were multiplied by the probability of occurrence to estimate the risk.

The United States Corps Army of Engineers (2006) provided guidance for flood damage reduction studies. The report discusses the shift from sensitivity analyses to risk analyses in project development. Risk analyses take into account both the risk and uncertainty in multiple aspects of an investment project. Decisions can be made based on better knowledge of risks and costs within a project. The report defines risk as the likelihood of a flood event with undesirable consequences occurring in an area. Uncertainty refers to the imprecision of knowledge about technical and economical parameters and functions involved in the project plan. Uncertainty exists in planning and design variables due to errors in sampling, measurement, estimating, and forecasting as

well as the inability to accurately model physical processes with mathematical equations. Parameters within the project are described in terms of probability distributions to account for uncertainties. The regulation describes requirements for risk analyses to be used for flood reduction studies. The goal of the regulation is develop a method in which all key variables, parameters, and components within the study are represented as a probabilistic analysis. Requirements include a feasibility report, general design memorandum, and general evaluation reports. Focus should be on those variables that have a significant impact on the study outcome. Minimum variables required include: (1) a stage-damage function for economic analysis; (2) discharge corresponding to exceedance probabilities for hydrologic studies; (3) conveyance roughness and cross-section geometry for hydraulic studies; and (4) structural and geotechnical performance of existing structures. The use of a full range of floods, not just the Standard Project Flood (SPF), is required to evaluate project alternatives. Risk analysis must quantify the flood protection performance of all alternatives within the final recommendation at all scales and residual risk must also be considered. The National Economic Development plan must be used for a cost-benefit analysis. And local sponsors and residents must understand the tradeoffs between engineering performance, economic performance, and project costs.

Purdy (2010) discusses International Organization of Standardization's (ISO) progress in standardizing risk management, including vocabulary, performance criteria, a method of identifying, analyzing, evaluating, and treating risk, and guidance for integrating the method into decision making. The group consisted of nominated experts from 28 countries and specialist organizations. ISO defined risk as the effect of

uncertainty on objectives. Uncertainty was defined as the result of internal and external factors that may interfere with or aid in achieving the objectives. Risk treatment was considered the act of changing the probability and degree of both negative and positive consequences in order to increase the project benefits. ISO defined performance criteria to ensure effective risk management. First, risk management must create and protect value. It must be a part of all organizational processes as well as decision making. The method must address uncertainties as well as human and cultural factors. The method must be systematic, structured, timely, and tailored as well as used the best available information. It must also be transparent and inclusive as well as dynamic, iterative, and responsive to change. Finally, the method must promote continuous improvement within the organization. ISO also defined a process for risk management. The method is based on multiple steps, all of which require iteration between both the steps and the processes of communication and consultation as well as monitoring and reviewing. Communication and consultation involve internal and external stakeholders. Monitoring and reviewing are necessary as existing risks change and new risks occur. The steps include first establishing the context of the project. Second, completing a risk assessment, involving risk identification, analysis and evaluation. Risk assessment is followed by risk treatment. Finally, the process must be implemented into the organizational decision making process.

Burby (2006) discusses the growing trend in flood losses over the past century. They argue that poor policy planning is to blame, both at the federal and local levels. They define two paradoxes: the safe development and the local government paradox. The safe development paradox is based on the attempt of federal policy to reduce losses

through structural mitigation and building codes as well as disaster relief; however, the result has been an increase in development in vulnerable areas. The local government paradox states that the avoidance of disaster losses is not a priority for local officials. Burby (2006) argues that the most efficient approach to mitigate losses and, therefore, risk is the requirement of local governments to restrict development in vulnerable areas.

Godschalk (2006) explains a nonstationary approach to risk assessment based on a method known as the 'Buildout Analysis'. A buildout analysis analyzes the effects of future landuse patterns on a watershed to aid in the evaluation of potential consequences and, therefore, potential alternative for future growth. Many communities have conducted buildout analyses to encourage the wise use of floodplains to mitigate the vulnerability and, therefore, the risk associated with flooding. Successful Buildout Analyses have been conducted in Mecklenberg County, North Carolina, and the state of Massachusetts.

Blais et al. (2006) analyzed whether existing floodplain management techniques required by the NFIP address changing conditions in the watershed. They analyzed the consequences (both losses and benefits) involved in the management of future conditions. Qualitative and quantitative assessments were conducted through interviews and a risk assessment, respectively. Damages to current and future inventory for the existing and future 100-yr floodplain were analyzed. The results showed an increase in damages from flooding that would results from future development within the watershed. The costs associated with managing future floodplain conditions were determined negligible in comparison to the potential consequences. Blais et al. (2006) recommend that

communities manage future conditions within the watershed in order to mitigate the risk of flooding.

The Federal Emergency Management Agency (FEMA) developed the HAZUS software program to provide loss estimates for wind, flood, and earthquake events on a regional basis. The flood model is expected to assist in flood risk mitigation, response, and recovery preparedness by providing local, state, and regional officials as well as consultants with regional risk estimates. The methodology consists of two basic analyses: (1) Potential Earth Science Hazards and (2) Damage Analysis. For the flood model, the potential earth science hazard analysis characterizes the riverine or coastal inundation and velocity based on the frequency and discharge of the event and ground elevation of the study region. The expected loss estimate accounts for both structural and economic factors. The loss estimates are based on vulnerability curves developed from the hazard analysis.

The program consists of three levels of complexity which vary based on the input required by the user and the level of analysis conducted within the program. The higher the level, the more sophisticated the loss estimate will be. Level one requires minimal effort by the user and the loss estimates are based on default data within the HAZUS program. The user is required to specify the study region and input the topographic data for the region. Levels 2 and 3 require more extensive inventory data and hazard information from the user.

The default data within the HAZUS program assesses damage to the general building stock within the United States as well as national data for essential facilities such as police stations, high potential loss facilities such as stormwater management

structures, transportation and lifeline systems, agriculture, vehicles, and demographics. This information is available on the census block level for the flood model.

In addition to the assessment of the hazard, the HAZUS program also provides the ability to incorporate a flood warning into the scenario in order to mitigate losses. The risk reduction based on a flood warning is estimated based on the U.S. Army Corps of Engineers approach which uses the "Day" curves.

Uncertainties exist within the estimated economic and structural losses. The use of national data as a representation of a regional analysis creates uncertainties. The level of inputs provided by the user aids in the reduction of these uncertainties. The program does not currently provide uncertainty estimates. Therefore, results should be used with caution.

3 Development of Method to Detect Multinonstationarity

3.1 Introduction

Many statistical tests have been developed to detect different types of change within a data series. Popular statistical tests to determine whether or not the data are correlated or that a gradual trend exists include the Kendall Tau test, the ANOVA test, and the Spearman-Conley test. The Two-sample t-test and the Mann-Whitney, however, test for an abrupt change in the mean rather than a gradual trend. In addition to the variation within the null hypothesis, different tests require different assumptions to be applied to a data set. For example, the Kendall Tau test, ANOVA test, and the two-sample t-test are each parametric tests, which means that certain distribution assumptions are required to ensure the full power of the test. The Spearman-Conley test and Mann-Whitney test are each non-parametric tests, which means they do not require distribution assumptions for the data. While the Kendall Tau test is a parametric test, it also can be categorized as a rank-based test along with the Spearman-Conley and Mann-Whitney tests.

While high power in detecting secular trends is important, it is also important that statistical tests are sensitive to partial trends. Nonstationary factors, such as climate change and urbanization, have and will continue to influence hydrologic data. As a result, many climate change and urbanization time series contain partial duration trends. For example, temperature data might be available for the past century; however, many records only show noticeable increases in temperature starting in the 1970's. Likewise, urbanization often occurs over a short period of time and then slows down. Therefore, results of statistical tests can be misinterpreted if the entire time series is analyzed rather than the period of time during which climate change and urbanization occur.

Partial duration trends can be detected through statistical tests on change points within the data, where change points are defined as discontinuities in a time series as the result of outside factors such as environmental changes (Reeves et al. 2007). However, few tests currently exist to identify change points in data series. Reeves et al. (2007) explained and compared existing change point tests including the standard normal homogeneity (SNH) test, the nonparametric SNH test, two-phase regression of Wang (2003), TPR of Lund and Reeves (2002), method of Vincent (1998), Akaike's information criteria, Sawa's Bayes criteria, as well as a method developed within the study. However, Reeves et al. (2007) emphasized that these tests assume that at most, one change point exists within a data series examined. Wang and Feng (2004) proposed a semi-hierarchical splitting algorithm for the detection of multiple change points; however, an actual test does not currently exist to detect multiple change points within a time series. Additionally, time series differ from a random variable because the predictor variable has a uniform rather than a normal distribution. Therefore, most existing tests do not apply to time series. Therefore, the goal of Objective 1 was to develop a test to identify both the location and significance of multiple change points in a time series. The theory development and results will be discussed herein.

3.2 Development of Change Point Test

In a nonstationary environment, outside factors, such as changes in watershed characteristics, will influence the statistical characteristics of a time series. In some cases, an outside factor may influence the data during a portion of the time series and then stop. For example, urbanization may occur only over a period of two decades within a 60-year time period. This would result in the occurrence of two change points within

the time series: (1) the time at which urbanization begins and (2) the time at which urbanization ends. In the event of multinonstationarity, multiple factors will have influenced the data over all or parts of the series, which will also result in multiple change points within the time series. These change points could occur simultaneously or at independent times within the time series. Therefore, regardless of the number of nonstationary factors that influence the time series, multiple change points may exist within a time series.

The addition of a nonstationary factor would result in a change in the slope of the data. This change could consist of an increase, decrease, or stabilization of the data. With this in mind, the first approach attempted in this study for the development of a change point test was to adjust the Kendall Tau test. The Kendall Tau test is a powerful statistical test to detect a monotonically increasing or decreasing trend in the data. The Kendall Tau test was adjusted in two ways in an attempt to develop a test to detect change points in a time series. First, the Kendall Tau test was systematically applied to sub-samples within the data and the test statistic equaled the sum of the resulting Z-statistics. Second, the Kendall Tau test was systematically applied to sub-samples within the data and the test statistic equaled the greatest difference between the resulting Z-statistics. The results showed that the Kendall Tau test was not sensitive to partial duration trends and, therefore, change points within the data. Appendix A explains the methodology and results for this approach.

The second approach was developed based on the following relationship between the slope and correlation coefficient:

$$b = r*\frac{S_y}{S_x} \qquad \text{Eq. 3-1}$$

in which 'b' = the slope coefficient, 'r' = the correlation coefficient, S_x= the standard deviation of the predictor variable (time), and S_y= the standard deviation of the criterion variable. This relationship can be solved for the correlation coefficient as follows:

$$r = b * \frac{S_x}{S_y} \quad \text{Eq. 3-2.}$$

Therefore, the correlation coefficient is directly related to the slope and variation within the data and is representative of a change in the time series.

The Fisher's 'Z' transformation converts the sample correlation coefficient to a normally distributed Z-value based on the following equation:

$$Z = \frac{1}{2}\ln\left(\frac{1+r}{1-r}\right) \quad \text{Eq. 3-3.}$$

Therefore, if a sample affected by multinonstationarity was divided into multiple sub-samples, and the Z-values were calculated for the data within each sub-sample, the variation between the Z-values would be the greatest when the sub-samples are divided at the location in which the changes in the data occurred. This theory was used in the development of the following test statistic based on the variance of the calculated Z-values:

$$T = \sum_{i=1}^{m}(n_i - 3) * {Z_i}^2 - \frac{\left(\sum_{i=1}^{m}(n_i-3)*Z_i\right)^2}{\sum_{i=1}^{m}(n_i-3)} \quad \text{Eq. 3-4}$$

where m = the number of sub-samples; n = the sample size for each sub-sample i; and Z = the Z-value calculated in Eq. (3) for each sub-sample. The test statistic would be applied systematically to sub-samples within a time series and the sub-samples that provide the largest calculated T-statistic would reflect the change point locations within the time series. Based on this test statistic, the null hypothesis states that a change point does not exist within the time series. Likewise, the alternative hypothesis states that a

change point does exist within the time series. The null hypothesis can be tested for multiple change points using the test statistic.

3.3 Development of critical values

The first step to assess the developed test statistic was to determine the critical values. Under the assumption of normally distributed random variables, the T-statistic follows a chi-square distribution; however, time series differ from a general data set in that the predictor variable is not a random variable because it is uniformly rather than normally distributed. The predictor variable is a sequence of integer values. Therefore, the chi-square distribution could not be used to determine critical values for the change point T- statistic. Instead, critical values were determined through simulation.

Data were simulated for 5,000 samples of varying sizes based on the null hypothesis that a change point does not exist. The T-statistic was systematically applied to varying sub-samples within the time series. Then, the maximum calculated T-statistic was stored for each simulation. The 5,000 stored T-statistics were then ranked, and the test statistics in the 90^{th}, 95^{th}, 99^{th}, and 99.5^{th} percentiles were stored as the critical values for the 10%, 5%, 1%, and 0.5% level of significance, respectively. The T-statistics within these percentiles represent a Type I error, in which the null hypothesis is rejected when a change point does not exist.

This method was repeated for time series based on different correlation coefficients (i.e., different trends). Since the distribution of the correlation coefficient changes with the value of the coefficient, the critical values showed slight variation based on the correlation coefficients analyzed. Therefore, a power model was fit to the critical

values as a function of the individual correlation coefficients calculated for each sub-sample within the test. The following functional form was fit to the critical values:

$$CV = A*param^B \quad \text{Eq. 3-5}$$

in which CV = critical value, A and B and defined in Table 3-1 for the 10%, 5%, 1%, and 0.5% levels of significance, and param is defined by the following equation:

$$param = \frac{\sum_i^m n_i r_i}{\sum_i^m n_i} \quad \text{Eq. 3-6}$$

where 'i' designates the sub-sample, m = number of sub-samples, n = sub-sample size, and r = correlation coefficient for sub-sample.

Table 3-1. Coefficients for Critical Value Power Model.

Alpha	0.50%	1%	2.50%	5%	10%
A	11.9522	10.662	8.794	7.514	5.974
B	0.16835	0.1809	0.1832	0.1989	0.207

3.4 Verification of Critical Values

The critical values were verified through simulation. Multiple analyses were conducted in which 1,000 samples were simulated with a sample size of 120 divided into three even sub-samples, a mean of 1,000, and a standard deviation of 50. Each analysis consisted of three parts, one null hypothesis scenario and two alternative hypothesis scenarios. Then, a different correlation coefficient was applied to each sub-sample. For example, the first analysis tested a correlation coefficient of 0.9. For the null hypothesis scenario, data within each sub-sample was simulated based on the following equation:

$$y_i = \bar{y} + r_i \frac{S_y}{S_{xi}} * (x_i - \bar{x}) + z * S_y * \sqrt{1 - r_i^2} \quad \text{Eq. 3-7}$$

where z is a randomly generated number based on the normal distribution with a mean of zero and standard deviation of one and r_i equals 0.9 for each sub-sample. The alternative hypothesis scenario consisted of data simulated based on the same equation for each sub-sample, but $r_1 = 0.9$, $r_2 = 0$, and $r_3 = 0.9$. The different r-values for each sub-sample will result in two statistically significant change points within the data, as a difference in R^2 greater than 5% is considered statistically significant. The second alternative hypothesis scenario consisted of $r_1 = 0$, $r_2 = 0.9$, and$r_3 = 0.9$. This would provide one statistically significant change point within the simulated time series. This analysis was conducted for r = 0.9, r = 0.7, r = 0.5, and r= 0.3. The resulting test statistic and critical values were calculated and are shown in Table 3-2.

The results show that for the null hypothesis scenarios, the null hypothesis is accepted, as expected, regardless of the correlation coefficient analyzed. The alternative hypothesis scenarios result in the rejection of the null hypothesis for all levels of significance for the scenarios with r = 0.7 and 0.9. The null hypothesis is rejected for the 10% level of significance for r = 0.5. The null hypothesis is accepted for r = 0.3, which is understandable considering this corresponds to an R^2 value of only 0.09. These results imply that the critical values result in the appropriate test conclusions for samples that contain change points.

Table 3-2. Verification of Critical Values for Sample-Size N= 120; Sub-Sample Sizes: n1=40, n2=40, n3=40; Standard Deviation = 50; and Y □=1000.

				Level of Significance				
R1	R2	R3	T	0.5	1	2.5	5	10
0.9	0.9	0.9	1.122	11.742	10.461	8.626	7.358	5.845
0.9	0	0.9	46.861	10.967	9.721	8.008	6.788	5.375

				Level of Significance				
R1	R2	R3	T	0.5	1	2.5	5	10
0	0.9	0.9	46.855	10.967	9.721	8.008	6.788	5.375
0.7	0.7	0.7	1.500	11.256	9.996	8.238	6.999	5.549
0.7	0	0.7	15.495	10.513	9.289	7.648	6.457	5.102
0	0.7	0.7	15.080	10.513	9.289	7.648	6.457	5.102
0.5	0.5	0.5	1.822	10.636	9.406	7.745	6.5463	5.176
0.5	0	0.5	5.893	9.934	8.740	7.191	6.039	4.759
0	0.5	0.5	5.783	9.934	8.740	7.191	6.039	4.759
0.3	0.3	0.3	1.775	9.759	8.575	7.053	5.914	4.656
0.3	0	0.3	2.284	9.115	7.969	6.548	5.456	4.281
0	0.3	0.3	2.284	9.115	7.969	6.548	5.456	4.281

The analyses were repeated for a standard deviation of 250 to determine the sensitivity of test statistic to variation within the data. The results are shown Table 3-3. The results suggest that the critical values perform just as effectively, regardless of the increase in variation within the data.

Table 3-3. Verification of Critical Values for Sample-Size N= 120; Sub-Sample Sizes: n1=40, n2=40, n3=40; Standard Deviation = 250; and Y □=1000.

				Level of Significance				
R1	**R2**	**R3**	**T**	**0.5**	**1**	**2.5**	**5**	**10**
0.9	0.9	0.9	1.1725	11.7421	10.4607	8.6259	7.3582	5.8451
0.9	0	0.9	47.0124	10.9673	9.7209	8.0084	6.7881	5.3746
0	0.9	0.9	46.6437	10.9673	9.7209	8.0084	6.7881	5.3746
0.7	0.7	0.7	1.4585	11.2556	9.9958	8.2377	6.9994	5.5488
0.7	0	0.7	13.9499	10.5130	9.2889	7.648	6.4571	5.1021
0	0.7	0.7	15.1872	10.5130	9.2889	7.648	6.4571	5.1021
0.5	0.5	0.5	1.7316	10.6358	9.4055	7.7453	6.5463	5.1755
0.5	0	0.5	6.0423	9.9340	8.7403	7.1908	6.0391	4.7588
0	0.5	0.5	6.0215	9.9340	8.7403	7.1908	6.0391	4.7588
0.3	0.3	0.3	1.7083	9.7594	8.5753	7.0533	5.9139	4.6562
0.3	0	0.3	2.2697	9.1154	7.9688	6.5484	5.4556	4.2813
0	0.3	0.3	2.3323	9.1154	7.9688	6.5484	5.4556	4.2813

For the final analysis, the sensitivity of the critical values to uneven sub-samples was tested. The data were simulated based on the same method previously described; however, the sample was divided into sub-samples of 30, 60, and 30 data values. The results are shown in Table 3-4. The results suggest that the test performs equally as well for uneven sub-samples as with even sample sizes.

Table 3-4. Verification of Critical Values for Sample-Size N= 120; Sub-Sample Sizes: n1=30, n2=60, n3=30; Standard Deviation = 250; and Y □=1000.

				Level of Significance				
R1	**R2**	**R3**	**T**	**0.5**	**1**	**2.5**	**5**	**10**
0.9	0.9	0.9	1.2301	11.7421	10.4607	8.6259	7.3582	5.8451
0.9	0	0.9	54.9257	10.4488	9.2279	7.5972	6.4105	5.0638
0	0.9	0.9	37.651	11.1869	9.9302	8.183	6.949	5.5072
0.7	0.7	0.7	1.4733	11.2556	9.9958	8.2377	6.9994	5.5488
0.7	0	0.7	18.1145	10.0159	8.8178	7.2554	6.098	4.8071
0	0.7	0.7	12.1805	10.7235	9.4889	7.8148	6.6101	5.228
0.5	0.5	0.5	1.8096	10.6358	9.4055	7.7453	6.5463	5.1755
0.5	0	0.5	6.889	9.4644	8.2971	6.8216	5.7032	4.4837
0	0.5	0.5	4.7856	10.133	8.9285	7.3477	6.1822	4.8763
0.3	0.3	0.3	1.7426	9.7594	8.5753	7.0533	5.9139	4.6562
0.3	0	0.3	2.8011	8.6845	7.5647	6.2122	5.1522	4.0338
0	0.3	0.3	1.8865	9.298	8.1405	6.6912	5.585	4.387

3.5 Verification of Test Statistic

The test statistic was then verified using simulated data. Samples were simulated with the following characteristics: (1) slope = 1; (2) mean = 1,000; and standard error = 0.1. The data consisted of two change points. The first sub-sample contained zero slope, the second sub-sample contained the designated slope, and the third sub-sample a zero slope in the third sub-sample.

Multiple analyses were conducted in which two change points were simulated within the data. Each analysis consisted of a different combination of total sample size

and change point locations. Then, the sample was divided systematically into sub-samples and the test statistic was calculated for each test statistic. The maximum test statistic was then determined, and the associated change point locations as well as the critical values were stored. Table 3-5 shows the results for each analysis conducted. The results suggest that the test statistic detects the change point location within plus or minus one of the actual simulated change point location. Likewise, the calculated T-statistics suggest very significant change points in the data.

Table 3-5. Detected Change Point Locations and T-Statistics for Slope = 1 and Se = 0.1.

	Simulated Change Point Location		Detected Change Point Location			
n	**1**	**2**	**1**	**2**	**CV alpha = 1%**	**T-Statistic**
200	40	80	39	81	9.7937	881.3416
	40	120	39	121	10.339	1688.1
	60	100	59	101	9.935	864.81
	60	140	59	140	10.622	1649.9
150	30	60	29	61	9.748	608.88
	30	90	29	91	10.444	1140.2
	45	75	44	76	10.178	590.73
	45	105	45	106	10.415	1128.7
100	20	40	20	41	9.5541	321.5
	20	60	20	60	10.822	601.32
	30	50	29	51	9.5176	347.97
	30	70	29	71	10.471	653.84

Figure 3-1 shows the response surface as the test statistic is systematically applied for different sub-samples and, therefore, change points. The response surface is for a sample size of 200 and change points located at 60 and 140. The response surface suggests that as the change point location tested nears the actual change point location,

the test statistic value increases, which would be expected. Likewise, as the change point locations tested deviates from the actual change point locations, the calculated test statistic decreases. This suggests that the theory behind the test statistic performs as expected.

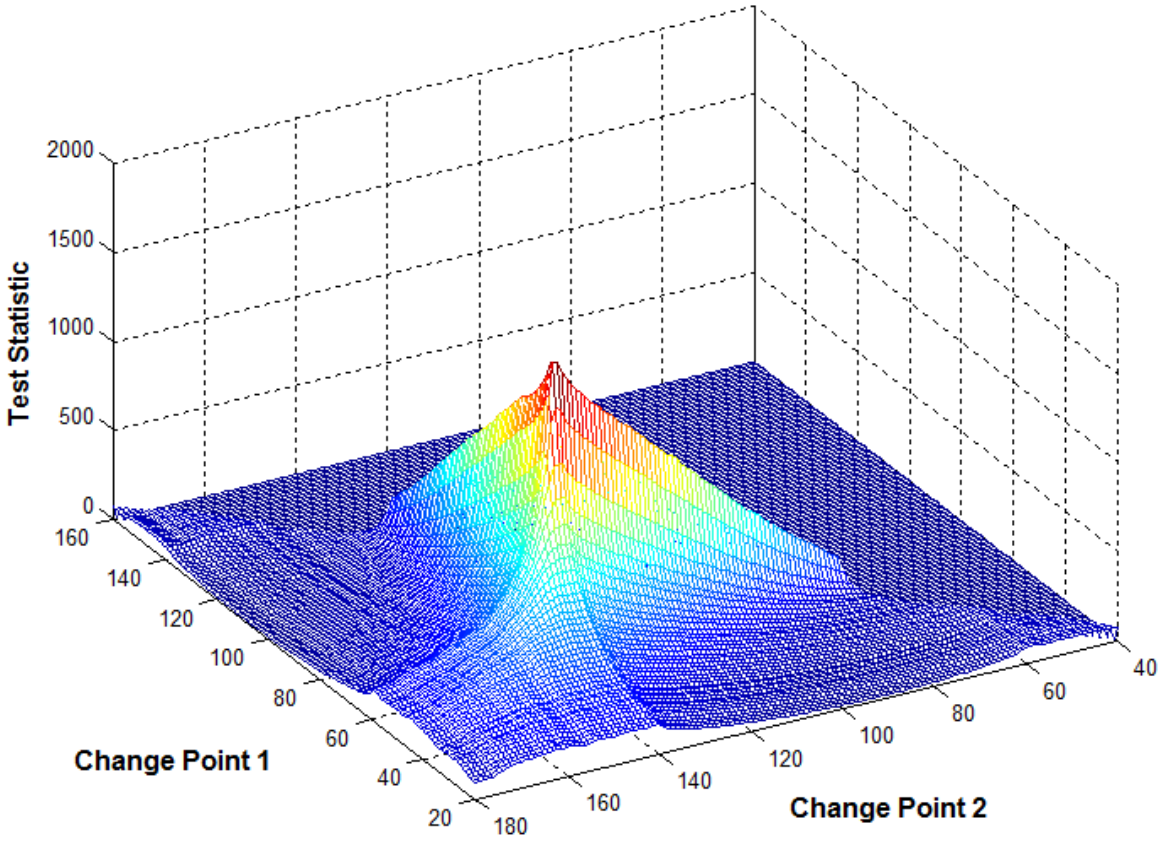

Figure 3-1. Response Surface of Test Statistic for a Sample Size Equal to 200, and Change Points Located at 60 and 140.

Two additional analyses were conducted in which the slopes within the second sub-sample were decreased from to 0.5 and then 0.1. The purpose was to test the sensitivity of the test statistic the ratio of the standard error to the standard deviation. Decreasing the slope will increase the standard error ratio. The results are shown in Tables 3-6 and 3-7 for the slopes of 0.5 and 0.1, respectively.

Table 3-6. Detected Change Point Locations and T-Statistics for Slope = 0.5 and Se = 0.1.

	Simulated Change Point Location		Detected Change Point Location			
n	1	2	1	2	CV alpha = 1%	T
200	40	80	39	81	9.3379	668.55
	40	120	39	119	10.38	1349.7
	60	100	59	101	9.4811	724.81
	60	140	61	141	10.263	1333.8
150	30	60	29	61	9.6327	544.99
	30	90	29	89	10.557	865.31
	45	75	44	76	9.7238	453.63
	45	105	45	106	10.362	887.93
100	20	40	20	41	9.8183	206.78
	20	60	20	61	10.439	487.58
	30	50	29	51	9.5798	239.87
	30	70	29	71	10.689	520.97

Table 3-7. Detected Change Point Locations and T-Statistics for Slope = 0.1 and Se = 0.1.

	Simulated Change Point Location		Detected Change Point Location			
n	1	2	1	2	CV alpha = 1%	T
200	40	80	38	83	9.9143	367.72
	40	120	38	123	10.755	623.03
	60	100	59	101	9.7304	372.53
	60	140	57	137	10.392	723.33
150	30	60	26	65	9.7365	194.38
	30	90	28	93	10.56	473.15
	45	75	42	76	9.533	216.07
	45	105	43	106	10.589	441.97
100	20	40	20	43	9.4272	135.71
	20	60	20	58	10.26	192.45
	30	50	25	55	10.228	108.88

	Simulated Change Point Location		Detected Change Point Location			
n	1	2	1	2	CV alpha = 1%	T
	30	70	26	68	10.446	207.28

It is apparent from Tables 3-6 and 3-7 that the test is sensitive to the random variation within the data. While the change points detected are very close to the actual change points, it appears that the test statistic consistently underestimates the first change point and overestimates the second change point. The response surface is shown in Figure 3-2 for the analysis consisting of a sample size of 200 and change points located at 60 and 140 and slope equal to 0.1. Compared to Figure 3-1, it is apparent that the response surface in Figure 3-2 is flatter near the actual change point locations. This suggests that as the difference in the slopes and, therefore, the correlation coefficients of the sub-samples decrease, the difference between the test statistic values calculated for each potential change point location decreases as well. This is expected, as it is more difficult to reject the null hypothesis for any trend detection test as random variation increase or the magnitude of the trend decreases.

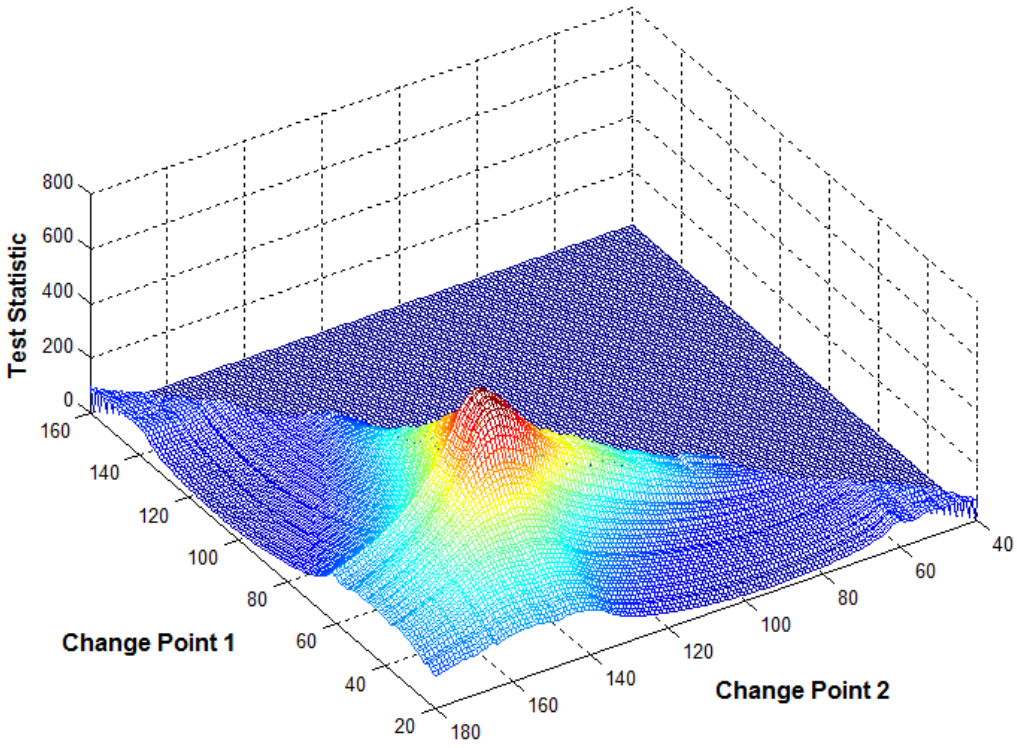

Figure 3-2. Response Surface of Test Statistic for a Sample Size Equal to 200, Slope Equal to 0.1, and Change Points Located at 60 and 140.

It is clear from the response surfaces that the test statistics for potential change point locations within the vicinity of the simulated change point locations provide nearly equal and statistically significant test statistic values. The critical values for the individual test statistics were analyzed for each combination of potential change point locations to determine whether a relationship exists between the test statistic and the critical value. In the event that the critical value calculated for the different sub-sample increases as the test statistic increases, the test statistic at the actual change point location may be more statistically significant even if another location provides a larger test statistic value.

The analysis region was limited to the change point locations that encompassed both the simulated and calculated breakpoints of the sample. The calculated test statistic

and critical values for the region of analysis are shown in Tables 3-8 and 3-9, respectively. The maximum test statistic and the test statistic for the actual change point locations are highlighted. Likewise, the critical values associated with the two change point locations are highlighted in Table 3-8. While the change point locations of 57 and 145 provide the greater test statistic, it is apparent from Table 3-8 that the critical value is also larger but not significantly. This is because the critical values are sensitive to the correlation coefficients of the individual sub-samples. This suggests that the maximum test statistic may not be the best indicator of the change point locations, but rather the rejection probability associated with the test statistic at each change point location may be a better indication of the actual change points.

Table 3-8. Test Statistic Values for Analysis Region for Sample Size Equal to 200, Slope equal to 0.1, and Change Points Located at 60 and 140.

	Change Point 2					
Change Point 1	**140**	**141**	**142**	**143**	**144**	**145**
57	702.79	702.29	712.55	730.45	720.71	730.96
58	679.67	683.65	683.27	693.55	711.37	701.96
59	699.87	688.77	693.23	692.83	703.31	721.39
60	679.54	689.14	678.54	683.2	683.14	693.77
61	657.96	677.7	687.52	677.57	682.67	683.02
62	632.64	656.7	676.53	686.54	677.11	682.64

Table 3-9. Critical Values at the 5% Level of Significance for Analysis Region for Sample Size Equal to 200, Slope equal to 0.1, and Change Points Located at 60 and 140.

	Change Point 2					
Change Point 1	**140**	**141**	**142**	**143**	**144**	**145**
57	6.4952	6.5338	6.5368	6.5099	6.518	6.4886
58	6.4988	6.5327	6.5704	6.5733	6.5471	6.555
59	6.3672	6.457	6.4918	6.5305	6.5335	6.5066

	Change Point 2					
Change Point 1	**140**	**141**	**142**	**143**	**144**	**145**
60	6.3519	6.3618	6.4519	6.4867	6.5256	6.5286
61	6.3417	6.2966	6.3069	6.4001	6.436	6.4761
62	6.3591	6.2885	6.2418	6.2525	6.3488	6.386

3.6 Conclusions

The results of this study suggest that theory behind the test statistic developed accurately detects multiple change points within a time series. However, limitations do exist with the application of this test statistic. The current method selects the maximum test statistic calculated based on a systematic application of the test statistic to potential change points within a time series. A more accurate approach would be to calculate the rejection probabilities associated with the test statistics calculated at each potential change point location. Based on these results, it is recommended that future research be conducted in which the distribution of the critical values is determined. This would enable the rejection probability to be calculated for every test statistic, rather than only the 10%, 5%, 2.5%, and 1% levels of significance.

The development of a statistical test to detect multiple change points within a time series improves the state of the art in change point detection. Currently, a change point test that can detect more than one change point within a time series is not available (Reeves et al. 2007). The detection of multiple change points will become increasingly important as multinonstationarity continues to influence hydrologic data. Knowledge of change point locations will aid in the optimal modeling of hydrologic data as well as other time series that are influenced by multiple factors.

4 Development of Climate Change and Urbanization Adjustment Factor

4.1 Introduction

Climate change scenarios are based on the assumption of significant temporal increases in greenhouse gas emissions during the twenty-first century leading to changes in temperature and preciptation. As a greater percentage of the population settles in urban areas, urbanization scenarios indicate significant temporal increases in imperviousness during the twenty-first century. Each of these factors will influence the hydrologic cycle and, therefore, flood risk. The goal of Objective 3 is to develop a method to adjust annual maximum flood data to climate change and urbanization conditions at a design year. The adjusted time series can then be used to conduct a flood frequency analysis. The return periods of floods under future climate change and urbanization conditions can then be estimated. The development of each component will be discussed in detail herein.

4.2 Development of Multinonstationarity Model

To develop a multinonstationarity model, the individual effects of each variable, climate change and urbanization, on flooding were considered. The first step was to determine whether the method should adjust peak discharge values simultaneously or individually for urbanization and climate change. For an individual approach, physical reasoning would be necessary to support the sequential order in which adjustments are made. Therefore, a review of the influence of each component on the hydrologic cycle was conducted.

In Chapter 2, the effects of climate change were discussed based on the IPCC findings as well as individual studies. The studies show a global increase in temperature

in response to increases in greenhouse gas emissions. An increase in the water-holding capacity of the Earth's atmosphere accompanies and an increase in evaporation accompany an increase in temperature (Trenberth 1999). The increase in atmospheric moisture content is expected to enhance precipitation and snowfall rates (Karl et al. 1995). More intense rainfall events will result in more runoff and greater floods. It can be assumed that evaporation will not play a role during the occurrence of precipitation events and, therefore, increased evaporation rates will only mitigate flooding through the reduction of antecedent moisture conditions during rainless time periods. Therefore, the main effect of climate change on flood risk is the change in precipitation patterns with increased greenhouse gas concentrations.

Many studies have shown the effects of urbanization on flooding. Changes in land cover involved in urbanization tend to decrease infiltration capabilities of the watershed and therefore, alter runoff characteristics. This leads to increases in runoff. While theories regarding the "heat island effect" of urbanization exist, the potential effects of urbanization on climate change and, therefore, precipitation were ignored for this study. Therefore, the urbanization effect considered in this study is the increase in runoff that results from a lower infiltration amounts, faster runoff times, and reduced surface storage such as depression and interception storages.

Based on the individual effects of climate change and urbanization on the hydrologic cycle, it was determined that the adjustment method should include individual components to consider each factor separately. The main effect of climate change on flood risk results from the change in precipitation patterns, while the main effect of urbanization results from the change in runoff caused by a precipitation event. Therefore,

the structure of the adjustment model was developed to account first for climate change and second for urbanization in order to follow the sequence of the physical processes influenced by each factor.

Figure 4-1 provides a diagram of the adjustment model structure. The model includes three components: (1) a climate change adjustment method for an observed 24-hour precipitation event based on a climate change scenario; (2) the conversion of the design and observed year rainfall event to a peak runoff event; and (3) an urbanization adjustment method for the resulting design and observed year peak runoff events based on the design and observed year urbanization conditions, respectively. Note that in each component, an estimated value for both the observed year and design year are calculated. The final adjustment factor developed through the model is a ratio of the estimated design and observed year peak discharge for the respective climate and urbanization conditions. This ratio is then multiplied by the observed peak discharge value from the original time series. The development of each of the three components within this model will be discussed herein.

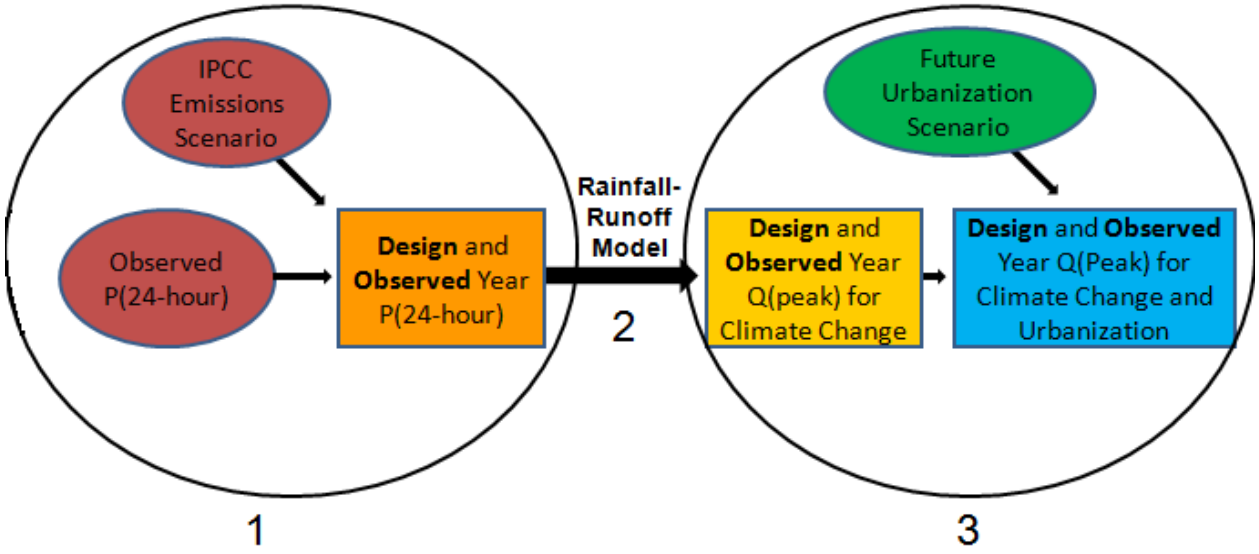

Figure 4-1. Diagram of Climate Change and Urbanization Adjustment Method Structure.

4.3 Development of Climate Change Adjustment Method

The climate change adjustment method required a physically rational approach to transform an observed 24-hour rainfall event to future climate change conditions. The goal was to estimate the expected change in heavy rainfall intensity over time for a specified climate change scenario and then apply the estimated change to the observed precipitation record. As stated in Chapter 2, many uncertainties still exist within GCM climate response predictions. Despite these uncertainties, GCMs currently provide the best physical estimate of future climate changes based on realistic future emissions scenarios. Therefore, the climate change adjustment method was developed using the precipitation data compiled based on IPCC emission scenarios through the World Climate Research Programme's (WRCP's) Coupled Model Intercomparison Projection phase 3.

4.3.1 Retrieval of GCM Data

The World Climate Research Programme's (WCRP's) Coupled Model Intercomparison Project phase 3 (CMIP3) multi-model dataset consists of climate model output from past, present, and future climate simulations from multiple GCMs. Output variables are available for 3-hourly, daily, and monthly time periods depending on the model and variable. The data are provided for rectilinear latitude-longitude grids, with the resolution varying for each model (Meehl et al. 2007).

The CMIP3 multi-model dataset provides climate simulations based on different emissions scenarios. Each participating modeling group was required to provide a twentieth century simulation (20C3M) as well as additional scenarios for varying emissions projections. For this study, simulated precipitation data were analyzed for the SRES A2, A1B, and B1 scenarios, which represent low, medium, and high emission rates, respectively (Meehl et al 2007). The 20C3M experiment was conducted from the year 1850 to 2000 and used observed greenhouse gas emissions. SRES A2, A1B, and B2 were conducted from the year 2000 to at minimum, the year 2100. Each of these experiments used the end of the 20C3M run as the initial conditions and used the greenhouse gas emissions projected for the specified climate change scenario (Mehl et al. 2007) (See Chapter 2 for further explanation of emissions scenarios).

Daily precipitation data were retrieved for this study from the CMIP3 multi-model dataset. Precipitation flux was provided with the units $kg/m^2/s$ and included both liquid and solid phases. The density of water equals 1 gram per cubic centimeter. Therefore, 1 kilogram of water equals 1000 cm^3. This volume distributed over 1 m^2 equals 1 mm. Therefore, precipitation flux was converted to a daily depth (mm/day) by

multiplying the variable by 86,400 seconds/day (http://www.narccap.ucar.edu/data/data-tables.html).

The precipitation data were retrieved from the CSIRO Mark 3.5 GCM because this model provided daily precipitation values for every decade in the twentieth and twenty-first century, rather than just the four decades specified in the CMIP3 requirements. The grid resolution of the CSIRO Mark 3.5 model was 192 x 96 and the vertical resolution was 18.

To retrieve precipitation data from the CSIRO model, the latitude and longitude coordinates for an area of interest were required. The GCM outputs represent the precipitation within the latitudinal and longitudinal bounds that define each grid cell. The study area selected included the states of Maryland, Virginia, and Delaware to ensure the developed method would be applicable to multiple watersheds and still account for regional precipitation patterns. The region excluded mountain ranges in the western part of Virginia as the physical processes would likely be different from those of the remainder of the region. This exclusion does not limit the anlayses. The grid coordinates from which precipitation data were retrieved for the three emissions scenarios are listed in Table 4-1 and the grids as well as the defined study region are shown in Figure 4-2.

Table 4-1. Latitude and Longitude Bounds for Grids 1 through 12 from the CSIRO Mark 3.5 GCM.

Grid	1	2	3	4	5	6	7	8	9	10	11	12
Lat. (N)	35.4	37.3	41.0	35.4	37.3	41.0	35.4	37.3	41.0	35.4	37.3	41.0
	37.3	39.1	39.1	37.3	39.1	39.1	37.3	39.1	39.1	37.3	39.1	39.1
Long. (W)	81.5	81.5	81.5	79.6	79.6	79.6	77.8	77.8	77.8	75.9	75.9	75.9
	79.6	79.6	79.6	77.8	77.8	77.8	75.9	75.9	75.9	74.0	74.0	74.0

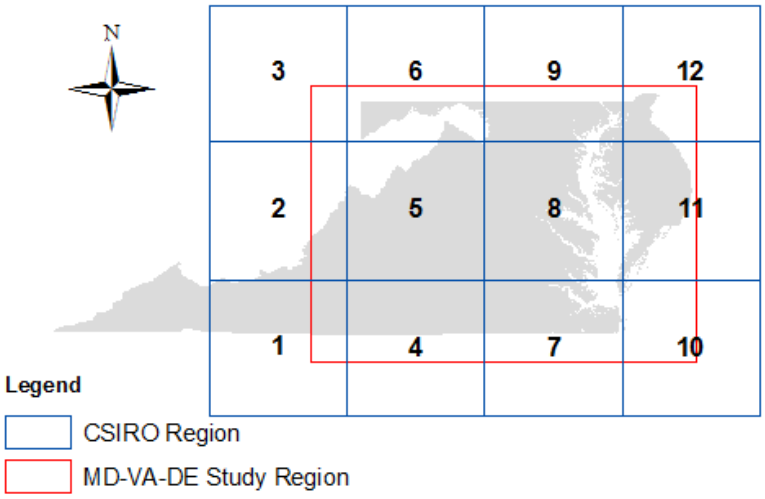

Figure 4-2. CSIRO Model Grids within Study Region for Precipitation Data

4.3.2 Development of Annual Maximum 24-hr Precipitation Time Series

Daily precipitation flux data were downloaded from the CSIRO model for each of the 12 grids and the three specified emissions scenarios from 2001 to 2100, as well as the 20C3M scenario from 1901-2000. The precipitation data were converted to depths (in./day). Next, the annual maximum 24-hr precipitation event was identified and stored for each data set. The 20C3M scenario, representative of the twentieth century, was then combined with each of the three emissions scenarios to provide three time series from 1901 to 2100 based on twentieth century emissions and the twenty-first century scenarios: A2, A1B, and B1. The annual maximum 24-hr precipitation time series for the 12 CSIRO cells are shown in Figures 4-3, 4-4, and 4-5 for the A2, A1B, and B1 emissions scenarios, respectively.

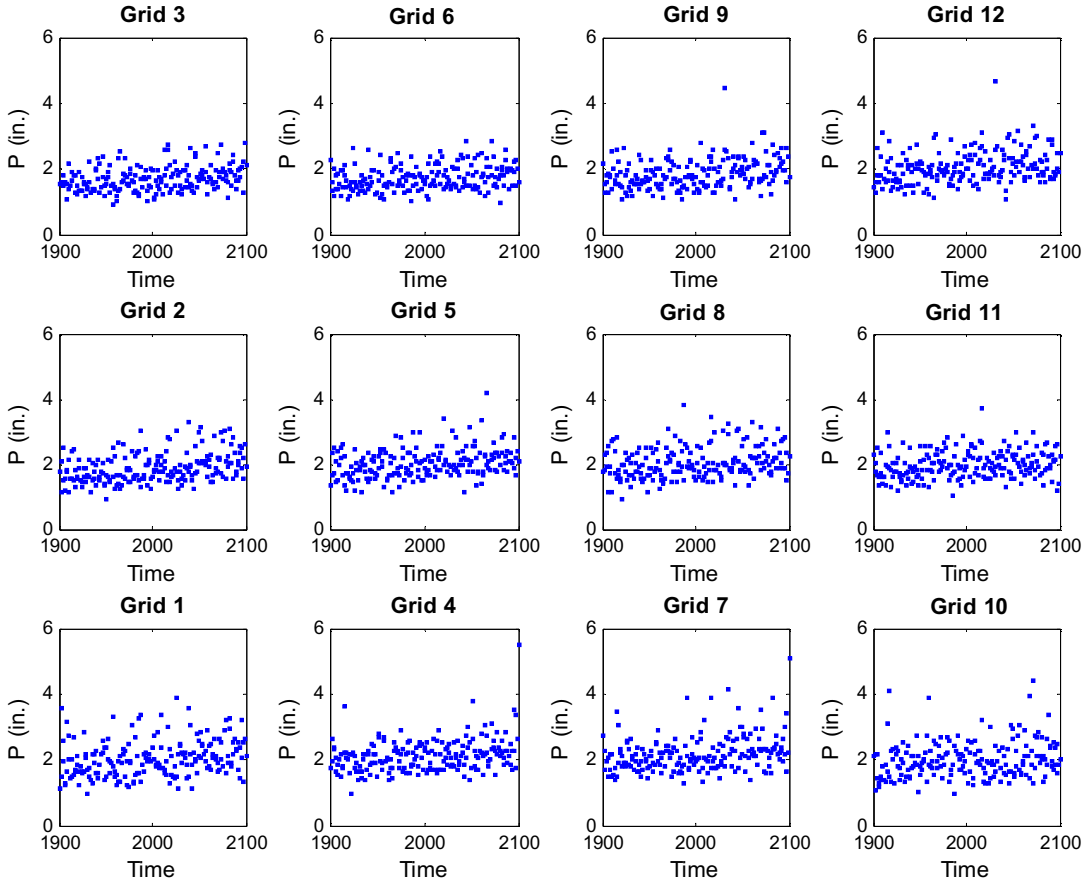

Figure 4-3. Annual Maximum 24-hr Precipitation Time Series for the SRES A2.

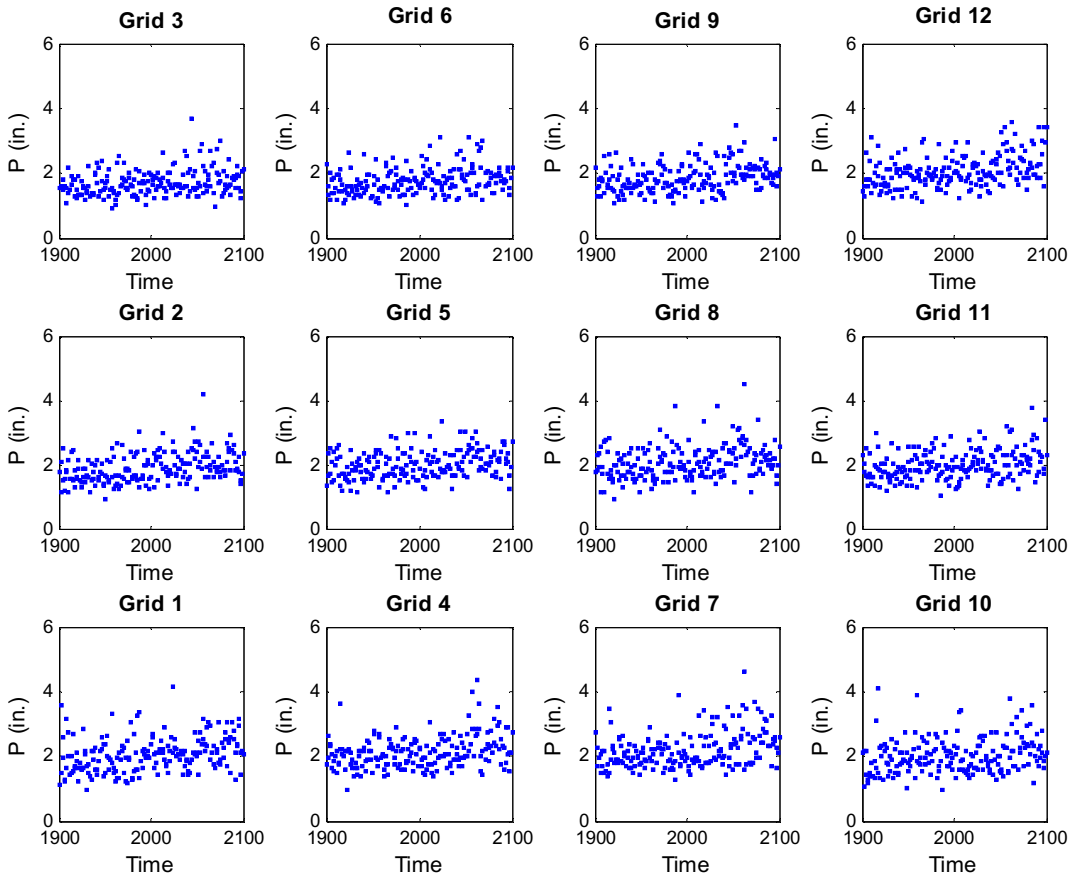

Figure 4-4. Annual Maximum 24-hr Precipitation Time Series for the SRES A1B.

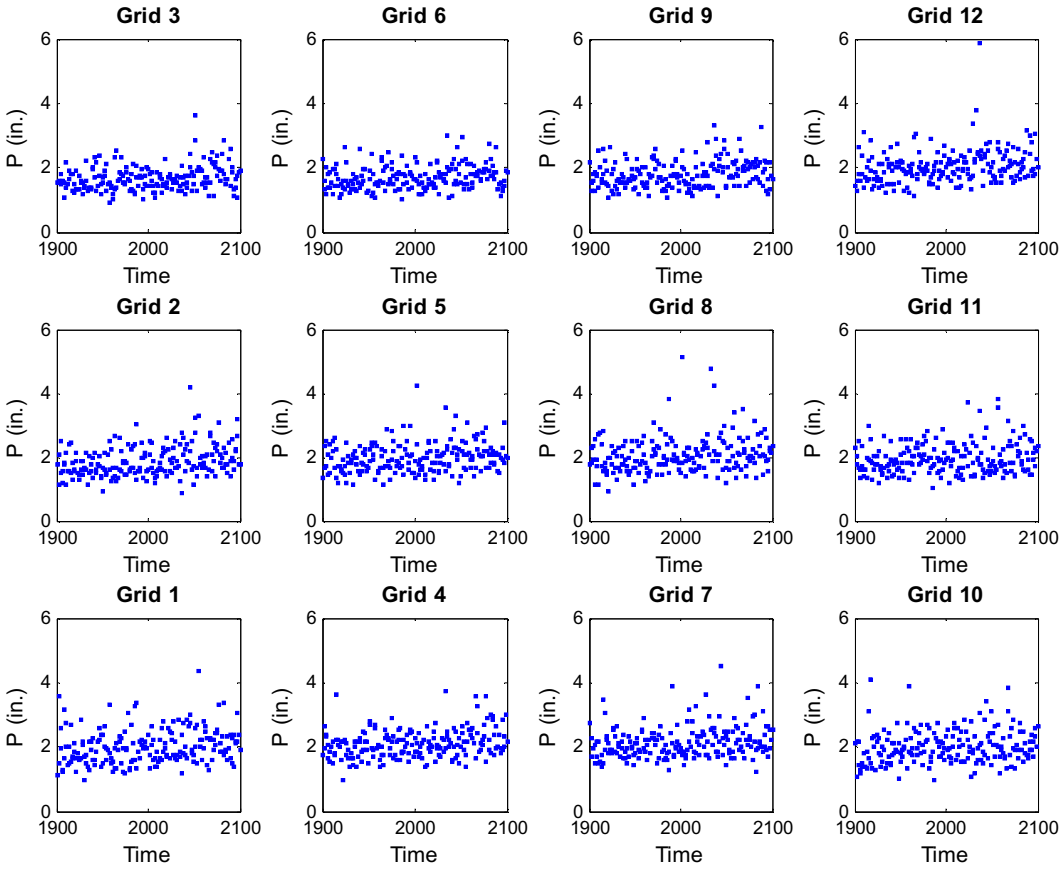

Figure 4-5. Annual Maximum 24-hr Precipitation Time Series for the SRES B1.

4.3.3 Selection of Annual Maximum Precipitation Distribution

With the annual maximum preciptiation time series available for each of the three emissions scenarios, the next step was to select the appropriate distribution upon which to analyze the changes in precipitation characteristics. Based on previous precipitation studies (Kharin and Zwiers 2005; Koutsoyiannis 2004; Martins and Stedinger 2000), the general extreme value (GEV) distribution was selected (see Chapter 2 for a descripition of the GEV distribution).

The GEV distribution uses three parameters, the location, scale, and shape parameters. As described in Chapter 2, the shape parameter denotes whether the data represent a Type I, II, or III distribution, with the Type II distribution being the most common for hydrologic data. While some studies represent the Type II distribution with a negative shape parameter and the Type III with a positive shape parameter, the opposite notation has been selected for this study. Therefore, a positive shape parameter will represent the Type II distribution. This notation was also adopted by Kharin and Zwiers (2005) and Koutsoyiannis (2004) and is also the notation applied in Matlab, the software program used in this research to conduct the GEV analysis.

The Kolmogorv-Smirnov One-Sample (KS-1) test was applied to each of the 36 annual maximum precipitation time series to ensure that the GEV distribution was representative of the data. To develop the null hypothesis for each of the analyses, the GEV parameters needed to be calculated; however, each data set consists of non-stationary precipitation data, as they represent changes in climate from the twentieth to the twenty-first century. Therefore, GEV parameters calculated from the entire data set would be inaccurate because the parameter values change throughout the 200 years. Therefore, a method developed by Kharin and Zwiers (2005) was applied in which the GEV parameters were calculated within 51-yr windows throughout each 200-yr time series. The parameter value that was calculated within any 51-yr time period was assigned to the middle year within the 51-yr window. The method of maximum likelihood was used to calculate the parameter values. Kharin and Zwiers (2005) and Semenov and Bengtsson (2002) discuss the advantages of using the method of maximum likelihood rather than the method of moments. The result was 36 time series (three

emissions scenarios for each of the 12 grids) comprised of 149 parameter values for each of the three GEV parameters.

To conduct the KS-1 test, the median parameter values from the 51-yr window analysis were selected to represent the population distribution, with the assumption that these values would provide the least deviation from the parameters during any given time period within the precipitation time series. Therefore, the null hypothesis for each analysis stated that the precipitation data record represents a population that follows the GEV distribution with the parameters defined as the median shape, scale, and location parameter for each of the 36 time series. The median GEV parameter values for the 12 grids are shown in Tables4-2, 4-3, and 4-4 for the A2, A1B, and B1 emissions scenarios, as well as the resulting test statistic from the KS-1 Test.

For a sample size equal to 200, the critical value for the KS-1 test is 0.115 for the 1% level of significance. Therefore, the null hypothesis is accepted for each of the 12 CSIRO grids and each of the emissions scenarios at the 1% level of significance. This implies that the GEV distribution is a good representation of the annual maximum precipitation for each emissions scenario.

Table 4-2. Median GEV Parameter Values from the 51-yr Window Analysis and KS-1 Test Statistic for the A2 Scenario.

Grid	1	2	3	4	5	6	7	8	9	10	11	12
KS-1 Test	0.044	0.045	0.061	0.059	0.051	0.082	0.075	0.047	0.111	0.044	0.077	0.057
Location	1.79	1.67	1.51	1.94	1.85	1.58	1.92	1.82	1.60	1.78	1.85	1.86
Scale	0.43	0.33	0.31	0.35	0.36	0.31	0.36	0.38	0.32	0.42	0.36	0.38
Shape	-0.03	0.00	-0.07	-0.15	-0.08	-0.09	-0.02	0.01	-0.05	-0.06	-0.13	-0.06

Table 4-3. Median GEV Parameter Values from the 51-yr Window Analysis and KS-1 Test Statistic for the A1B Scenario.

Grid	1	2	3	4	5	6	7	8	9	10	11	12
KS-1 Test	0.089	0.088	0.060	0.080	0.060	0.070	0.093	0.066	0.064	0.041	0.042	0.061
Location	1.86	1.75	1.54	1.90	1.80	1.61	1.91	1.82	1.64	1.77	1.80	1.84
Scale	0.40	0.36	0.30	0.36	0.36	0.32	0.34	0.40	0.34	0.41	0.38	0.38
Shape	-0.02	-0.07	-0.07	-0.13	-0.11	-0.02	0.01	-0.04	-0.10	-0.04	-0.16	-0.12

Table 4-4. Median GEV Parameter Values from the 51-yr Window Analysis and KS-1 Test Statistic for the B1 Scenario.

Grid	1	2	3	4	5	6	7	8	9	10	11	12
KS-1 Test	0.050	0.055	0.048	0.042	0.067	0.047	0.024	0.045	0.092	0.058	0.044	0.034
Location	1.77	1.65	1.49	1.90	1.75	1.52	1.92	1.82	1.57	1.82	1.72	1.82
Scale	0.40	0.35	0.30	0.36	0.37	0.30	0.35	0.40	0.32	0.42	0.36	0.37
Shape	-0.01	-0.04	-0.10	-0.10	-0.09	-0.06	0.03	0.08	-0.07	-0.09	-0.01	-0.05

4.3.4 Analysis of Change in GEV Parameters

The next step was to analyze the change in the GEV parameters as function of time and the emissions scenario. The time series of the location, scale, and shape parameters for each of the 12 grids and 3 emissions scenarios were analyzed. Then, the temporal change in each parameter was modeled. Model selection and fitting criteria for each parameter and emissions scenario will be explained herein, followed by discussions of the calibrated models.

4.3.4.1 Model Selection

The selection of the appropriate functional form is necessary to ensure that extrapolation from the beginning of the twentieth century and to the end of the twenty-first century provides rational estimates. Model selection for each GEV parameter time series was based on an initial graphical analysis as well as physical rationality. First, each GEV parameter time series was plotted versus time and the rate of change was

analyzed throughout the time series. An appropriate model was then selected based on these observations. For example, an exponential function was selected for a parameter time series in which the rate of change increased with time or a logistic function was selected for a parameter time series in which the rate of change increased and then decreased with time.

The initial model selection was then analyzed for physical rationality. The expected changes in the precipitation distribution parameters are unknown; however, assumptions can be made based on existing studies and trends in the emissions scenarios themselves. Studies suggest that heavy precipitation events will increase in magnitude while moderate events decrease in frequency in the Eastern United States. Every event in an annual maximum precipitation time series can be considered a heavy precipitation event. Therefore, increases in the magnitude of heavy precipitation events should be reflected in changes in the location, scale, or shape parameters. An increase in the location parameter would shift the precipitation distribution upwards and increase the storm magnitude for every return period. An increase in the scale parameter affects the spread of the distribution, which enhances precipitation extremes. Changes in the shape parameter influence the tail of the distribution, which also influences extreme events. Kharin and Zwier (2005) analyzed the global GEV parameters for precipitation and conclude that the location and scale parameters increased and the shape parameter experienced an insignificant decrease. The magnitude of these changes varied regionally. Based on these analyses, it can be assumed that the location and scale parameter will most likely increase with climate change and the model selected should account for this increase.

Emissions scenarios were also analyzed to provide additional information in regards to the expected changes in the GEV parameters for each emissions scenario. The emissions scenarios analyzed in this study (A2, A1B, and B1) change nonlinearly throughout the twenty-first century (see Chapter 2 for more details). Therefore, the precipitation distribution parameters most likely will not follow a linear model. Likewise, emission rates for the A2 and A1B scenarios are expected to increase throughout the twenty-first century while rates for the B1 scenario are expected to stabilize in the twenty-first century. Therefore, it is likely that the precipitation distribution parameters will follow similar trends. While emission rates most likely do not directly affect the precipitation distribution parameters, the rate of increase of emissions for each scenario should be considered in the selection of a model structure for parameter and scenario.

4.3.4.2 Model Coefficient Fitting Criteria

Once the model structure was selected, the coefficients were initially fit based on numerical optimization. Then, the coefficients were subjectively adjusted where necessary to ensure that they provided rational models for the twentieth and twenty-first century for each emissions scenario. For example, calculation of parameter values within set window lengths results in a loss of data values at the beginning and end of the sample. Therefore, the developed models needed to be extrapolated both backwards and forwards and the extrapolated models were assessed for rationality. Unfortunately, little information is available to provide constraints for extrapolation to the year 2100; however, verification was conducted at the end of the entire analysis to determine whether precipitation projections that result from the final models coincided with other

studies. For the twentieth century, the models would most likely be more stable than the twenty-first century because the emissions rates were more stable than rates projected for the twenty-first century. Therefore, the models were adjusted to ensure that extrapolating to the beginning of the twentieth century did not result in an irrational decrease in the parameter value.

In addition to the assessment of model rationality in extrapolation, it was necessary that the models for the three emissions scenarios provide the same GEV parameters for the twentieth century. The emission rates in the twentieth century are based on observed as opposed to projected values for the twenty-first century, and changes in the emissions scenarios do not exist until the year 2000. Therefore, the emissions rates for the preceding years should provide the same GEV parameters and, therefore, the same precipitation distribution.

Two issues arise that make it difficult to provide the same parameter values for the twentieth century for each of the three emission scenarios. First, the parameter values designated to a year after 1976 will be influenced by precipitation events after the year 2000, based on the 51-yr window within which GEV parameters are calculated. The emissions scenarios, however, begin to diverge starting in the year 2000. Therefore, despite the emissions scenarios being the same from 1900 to 2000, the GEV parameters will differ slightly at the end of the twentieth century for the three emission scenarios as they are influenced by events from the different scenarios. Second, if the model structure selected for a GEV parameter for the A2 scenario differs from that of the B1 scenario, it will be difficult to provide an exact fit for the three emissions scenarios in the twentieth century without a composite model, which can result in irrational model fits. Therefore,

final adjustments were made to the statistical model coefficients for each GEV parameter and emissions scenario to ensure that the differences between scenarios in the twentieth century parameter values were minimal.

Physical rationality was also ensured by comparing the parameter values to GEV parameters based on observed precipitation data within the MD-DE-VA region. Annual maximum precipitation data were retrieved from 32 rain gauges, and the GEV parameters for each precipitation record were calculated. The parameter values were then compared to ensure that magnitude of both the simulated GCM precipitation data and the observed regional precipitation data were similar. Necessary adjustments were made when the magnitudes differed significantly.

4.3.4.3 Location Parameter

For the annual maximum precipitation, the time series based on a 51-yr window length for the location parameter provided parameter values from 1926 to 2074. Values are lost at each end of the series as is characteristic of moving average filtering. Values of the median, mean, 25th percentile, and 75th percentile of the parameter values calculated for each of the 12 grids were computed. The results are shown in Figures 4-6, 4-7, and 4-8 for the A2, A1B, and B1 emissions scenario, respectively.

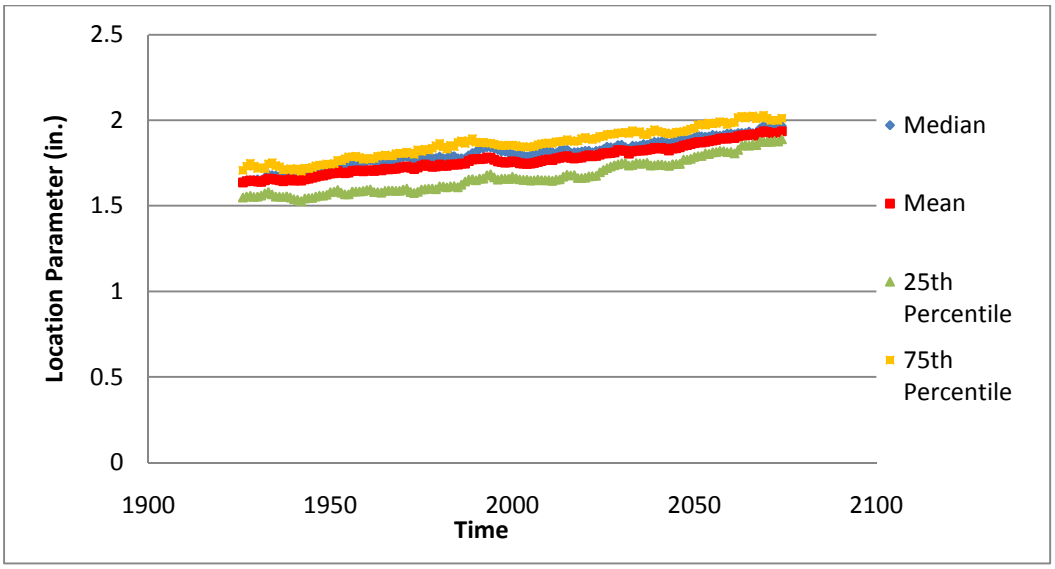

Figure 4-6. Median, Mean, 25th Percentile, and 75th Percentile of Location Parameters for the 12 CSIRO Grid Cells from 1926 to 2074 for the A2 Scenario.

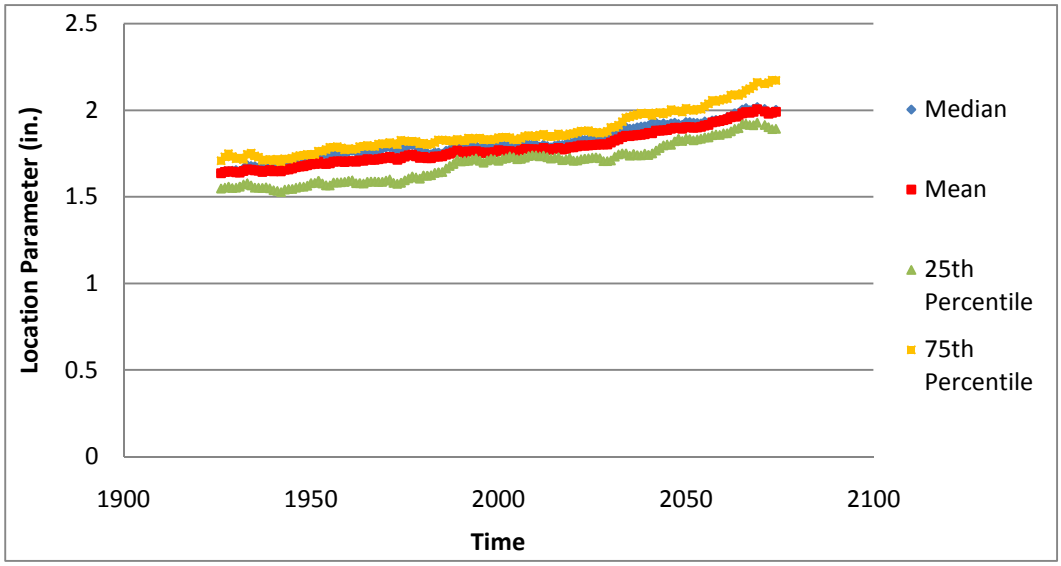

Figure 4-7. Median, Mean, 25th Percentile, and 75th Percentile of Location Parameters for the 12 CSIRO Grid Cells from 1926 to 2074 for the AB1 Scenario.

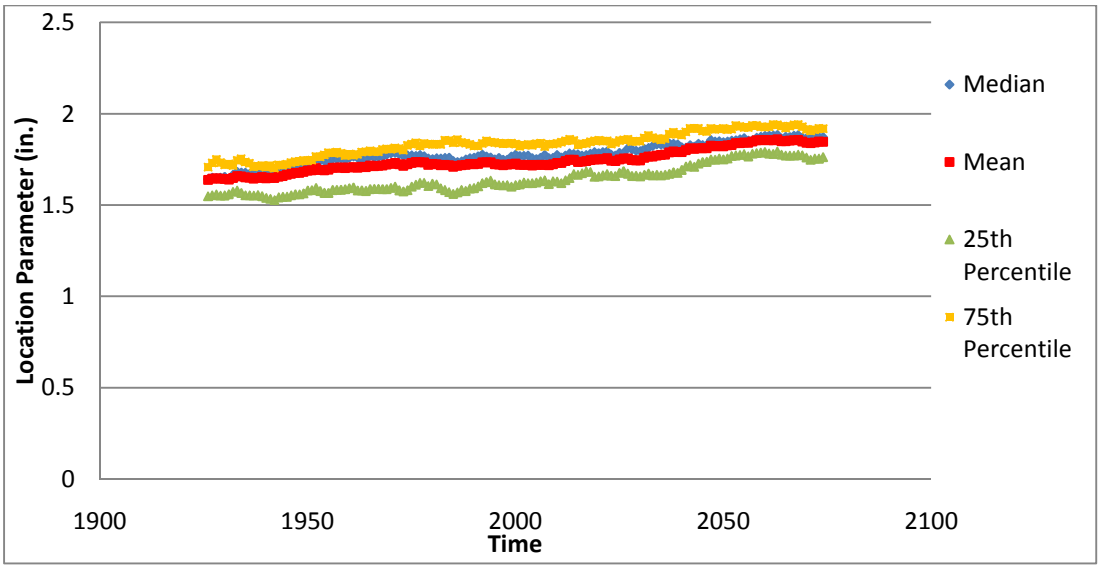

Figure 4-8. Median, Mean, 25th Percentile, and 75th Percentile of Location Parameters for the 12 CSIRO Grid Cells from 1926 to 2074 for the B1 Scenario.

Model Selection. A graphical analysis was conducted for each of the three scenarios to select the appropriate model structure. The rate of change of both the A2 and A1B location parameters appears to increase with time, which suggests that both parameter time series follow an exponential function. This function form was compared to the globally averaged GEV parameters as a function of time developed by Kharin and Zwiers (2005) for the A2 scenario and shown in Figure 4-9. Kharin and Zwiers (2005) also found an exponential trend in the global location parameter. Based on the GEV parameter graphs and verification by the globally averaged parameters, the following exponential model was fit to the location parameters for the A2 and A1B emissions scenarios:

$$y = C_1 + C_2 * e^{C3(x-C4)} \qquad \text{Eq. 4-1.}$$

with the coefficient values fit based on numerical optimization and adjusted for physical rationality.

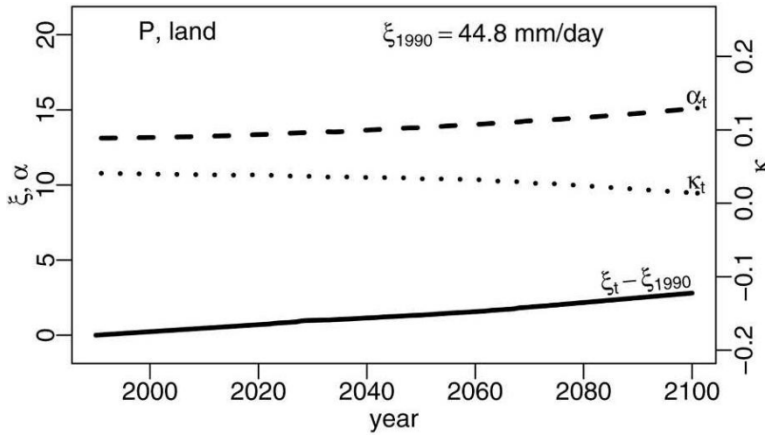

Figure 4-9. Rate of Change of the Shape (Ƙ), Scale (α), and Location (ξ) GEV Parameters as a Function of Time for the Global Land Precipitation Distribution for the A2 emissions scenario provided by Kharin and Zwiers (2005).

For scenario B1, however, the location parameter time series suggests that the rate of increase in the parameter values begins to decrease towards the end of the twenty-first century (see Figure 4-8). This coincides with the emissions rate reduction towards the end of the twenty-first century for the B1 emissions scenario (see Chapter 2). Therefore, the exponential model used for the A2 and A1B scenarios is not applicable. However, the twentieth century portion of the model needs to be consistent for the three scenarios because the twentieth century emissions rates are based on measured data regardless of the twenty-first century emissions rates.

Based on these observations, a composite model was selected for the location parameter for the B1 scenario. A slowly increasing exponential function was selected for the twentieth century followed by an exponential decay function for the twenty-first function. The composite model form is as follows:

$$y = C_1 + C_2 * e^{C3(x-C4)} \qquad \text{for } t <= t_c \qquad \text{Eq. 4-2}$$

$$y = C_5 + \frac{C_6}{1+C_7 e^{C8(x-C9)}} \qquad \text{for } t>t_c \qquad \text{Eq. 4-3}$$

with the coefficient values calibrated through numerical optimization and then adjusted for physical rationality.

Calibration of the Parameter Models. For each of the three emissions scenarios, the time series of the mean location parameter values for the 12 grids were fitted for the selected models. The model coefficients were first determined based on numerical optimization to ensure a least squares fit. Then, as previously discussed, the coefficient values were adjusted slightly to ensure that the twentieth century values were extrapolated at a rational rate. Final adjustments were also made to minimize the difference between the functions during the twentieth century to ensure that similar precipitation distributions would result regardless of the emissions scenario being analyzed. The coefficient values defined for the location parameter as well as the goodness-of-fit statistics are shown in Table 4-5 for scenarios A2, A1B, and B1. Figures 4-10, 4-11, and 4-12 show the fitted functions for the A2, A1B, and B1 scenarios, respectively.

Table 4-5. Fitted Coefficient Values for Location Parameter Models.

Emissions scenario	Coefficient values		Goodness-of-fit	
A2	C1	1.55	Se	0.013
	C2	0.1115	Se/Sy	0.165
	C3	0.0085	e	-0.001
	C4	1928.186	e/y	0
A1B	C1	1.525	Se	0.017
	C2	0.1315	Se/Sy	0.171
	C3	1926.008	e	0.006
	C4	-1.388	e/y	0.003
B1	C1	1.55	Se	0.026

Emissions scenario	Coefficient values		Goodness-of-fit	
	C2	0.1115	**Se/Sy**	0.417
	C3	0.00852	**e**	0.016
	C4	2.186	**e/y**	0.009
	C5	1.227		
	C6	1.2		
	C7	1.7		
	C8	0.005		
	C9	13.4		

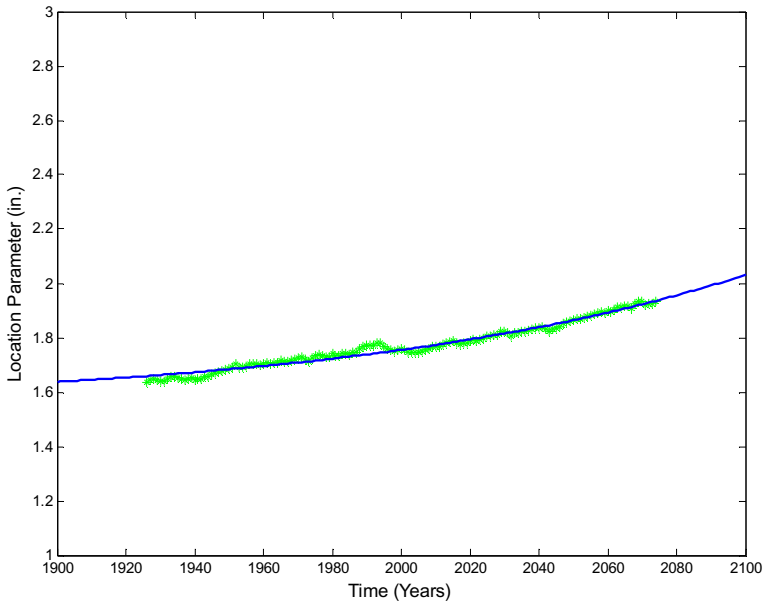

Figure 4-10. Location Parameter Model for the CSIRO Precipitation Data for SRES A2.

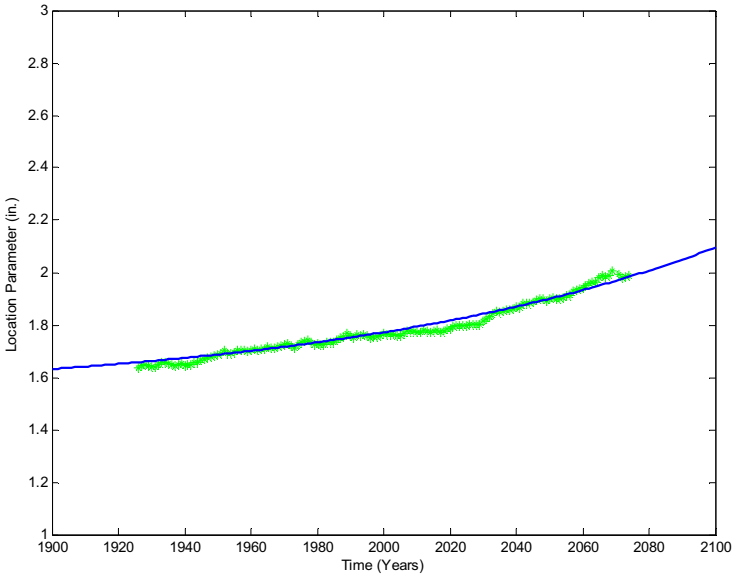

Figure 4-11. Location Parameter Model for the CSIRO Precipitation Data for SRES A1B.

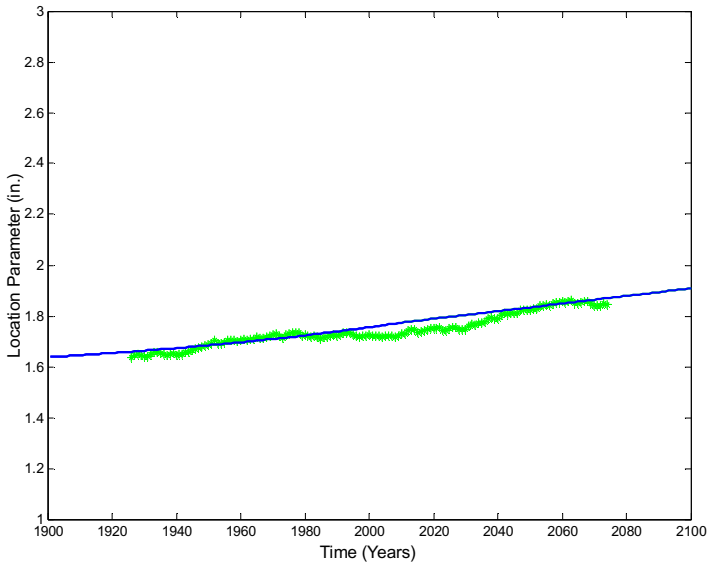

Figure 4-12. Location Parameter Model for the CSIRO Precipitation Data for SRES B1.

Goodness-of-fit. The relative biases for the adjusted models equaled 0, 0.003, and 0.009 for the A2, A1B, and B1 scenarios, respectively. Generally, the relative biases of less than 3% to 5% are not meaningful and certainly not statistically significant. The slight bias is the result of local biases within the data that are visible in Figures 4-10, 4-11, and 4-12. This is most likely the result of calculating parameter values from small sample sizes. The smaller the sample, the greater influence individual events will have on the calculated parmeter value. This may create high and low points within the time series and, therefore, the local biases in the model. Even with the adjustments for physical rationality, the models provide low bias with a few local biases within the time series for each scenario.

The ratio between the standard error and standard deviation for the A2, A1B, and B1 scenarios equal 0.165, 0.171, and 0.417, respectively. This implies that the models provide significantly better predications of the location parameter than the mean for each scenario. While the models for scenarios A2 and A1B provide ratios with relatively the same magnitude, B1 provides a ratio that is almost three times greater. Based on Figure 4-12, it appears that the total variation within the location parameter time series for the B1 scenario is less than that of the A2 and A1B scenario. Likewise, the B1 model experiences a greater local bias in the middle of the time series than the other scenarios. Both of these factors most likely contribute to the greater ratio between the standard error and standard deviation.

The goodness-of-fit statistics suggest that the location parameter models developed for each emissions scenarios provide a good estimate of the calculated location parameters. The models follow nonlinear trends, with A1B and A2 increasing throughout

the entire time series and B1 stabilizing in the 21 century. Both of these model characteristics were hypothesized based on previous studies and the rate of change of each emissions scenario.

4.3.4.4 Scale Parameter

As with the location parameter for each emissions scenario, the time series developed using the sliding windows method for the scale parameter consisted of values from the year 1926 to 2074. The time series of the median, mean, 25th percentile, and 75th percentile of the scale parameter for the 12 grids are shown in Figures 4-13, 4-14, and 4-15 for the A2, A1B, and B1 emisions scenarios, respectively. While the location parameter showed a smooth and slightly increasing exponential trend (see Figures 4-6, 4-7 and 4-8), the scale parameter (see Figures 4-13, 4-14, and 4-15) shows obvious peaks and low points throughout the time series that may reflect the fact that the second moment is more variable than the first moment. Therefore, before the model structure was selected, the scale parameter time series were analyzed to determine the cause of the local high and low points.

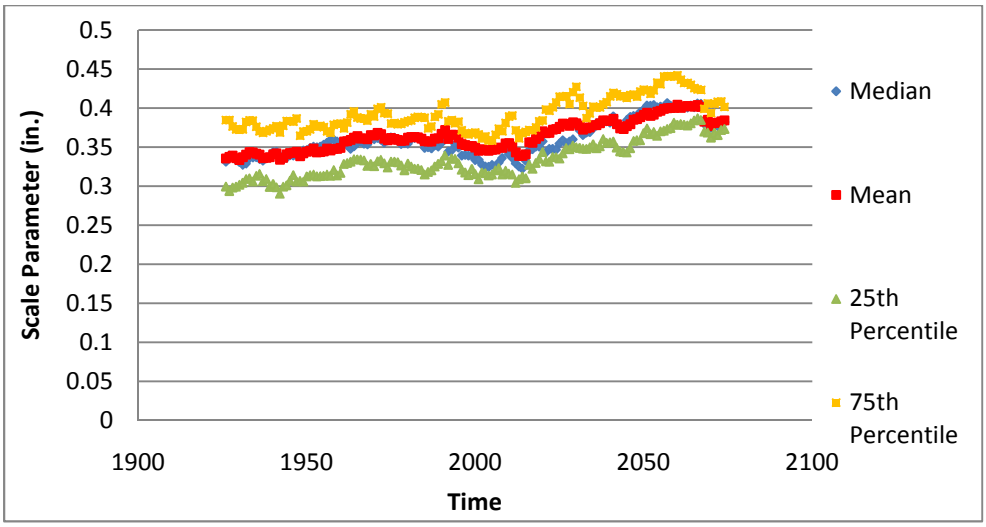

Figure 4-13. Median, Mean, 25th Percentile, and 75th Percentile of Scale Parameters for the 12 CSIRO Grid Cells for the A2 Scenario.

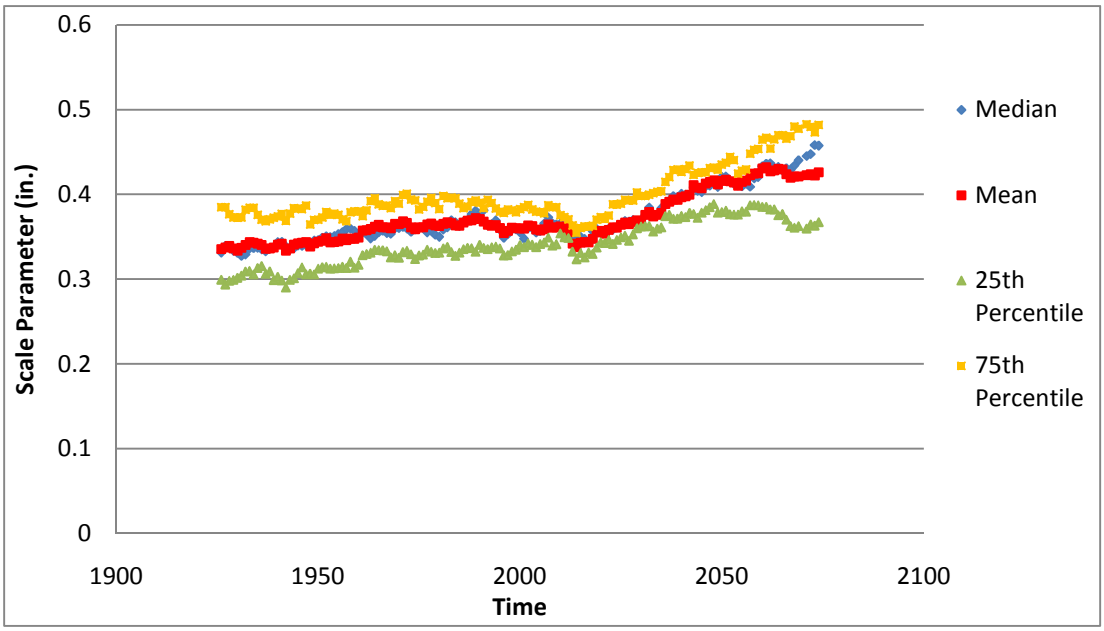

Figure 4-14. Median, Mean, 25th Percentile, and 75th Percentile of Scale Parameters for the 12 CSIRO Grid Cells for the A1B Scenario.

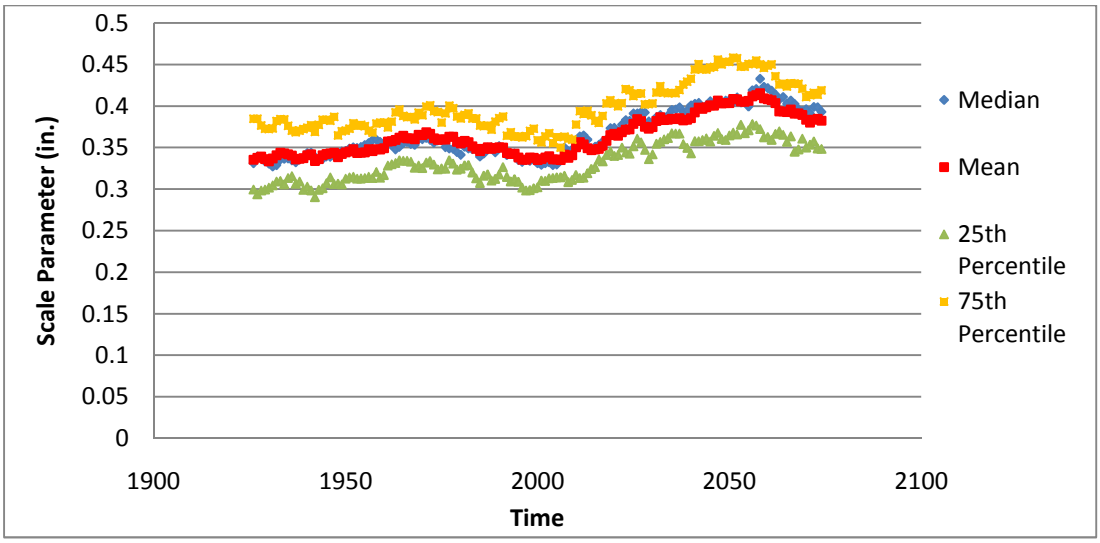

Figure 4-15. Median, Mean, 25th Percentile, and 75th Percentile of Scale Parameters for the 12 CSIRO Grid Cells for the B1 Scenario.

Analysis of the Scale Parameter. Figure 4-16 shows an example of irrational increases and decreases that occur in Grids 1 and 2 for the A2 scenario. In an attempt to determine the cause of each individual increase and decrease, the annual maximum precipitation data for Grids 1 and 2 were analyzed. Table 4-6 provides the precipitation events for Grid 1 that are two standard deviations or greater than the mean precipitation in the A2 annual maximum precipitation time series. These events are considered heavy precipitation events in this time series, and would most likely have the greatest influence on the scale parameter, which is a measure of the spread of the data. Table 4-6 also shows the window of scale parameters that would be influenced by each heavy precipitation event, based on the 51-yr time span. For example, a precipitation event that occurred in the year 2000 would influence the GEV parameters designated from the years 1975 to 2025 because the event would be included in the 51-yr window that surrounds each of these years.

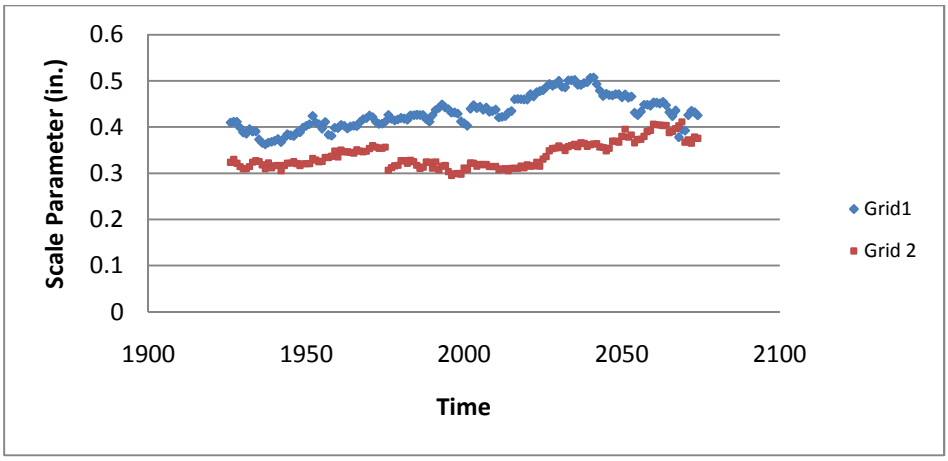

Figure 4-16. Scale Parameter for Grids 1 and 2 for SRES A2.

In Grid 1, the scale parameter experiences a lowpoint at 1937 followed by a steady increase and peak from 2030 to 2041. The time series experiences an abrupt decrease from 2068 to 2070 that is followed by an increase from 2071 to 2074. Based on the occurrence of heavy precipitation events, the high point of the scale parameter series that occurs at the beginning of the time series is influenced by large events in 1903 and 1909, with 1903 being one of the three greatest precipitation events shown in Table 4-6. The low point in the late 1930's, however, is only influenced by the heavy precipitation event in 1958. From 1960 to 2040, the scale parameter is influenced by a minimum of two heavy precipitation events for any given year, with the occurrence of two of the three greatest events in Table 4-6 in years 2026 and 2039. From 2065 to 2070, the scale parameter is only influenced by events that occurred in the years 2078 and 2083, both of which are in the lowest four precipitation depths in Table 4-6. Finally, the heavy precipitation event in the year 2095 influences the scale parameter at the year 2070, at which point the graph of the scale parameter experiences a final peak. Based on these

observations, it is apparent that the scale parameter is sensitive to the peak events within the time series, which is expected for a parameter representative of the spread in the data.

Table 4-6. Heavy Precipitation Events in Grid 2 for SRES A2.

Year	1903	1909	1958	1985	1987	2010	2026	2039	2078	2083	2095
Window Effected	1900-1928	1900-1934	1933-1983	1960-2010	1962-2012	1985-2035	2001-2051	2014-2064	2053-2100	2058-2100	2070-2100
P (in.)	3.60	3.16	3.34	3.28	3.38	3.39	3.86	3.59	3.22	3.29	3.19

Another concern was the dramatic drop that occurs from 1975 to 1976in the scale parameter for Grid 2. Analysis of the heavy precipitation events within the annual maximum time series for the Grid 1 and SRES A2, shown in Table 4-7, does not suggest a significant shift in heavy events that might influence the scale parameter during this time period. However, the entire annual maximum precipitation time series, shown in Figure 4-17, shows that a potential low outlier occurred in the year 1950. This low value would influence the scale parameters calculated from the year 1925 to 1975; however, the value of the 1950 event would not influence the 1976 scale value, which experienced a significant drop from the 1975 value. The omissions of the 1950 value would greatly reduce the variation which is reflected in the smaller scale value.

Table 4-7. Heavy Precipitation Events in Grid 1 for SRES A2.

Year	1987	2017	2026	2039	2049	2051	2066	2073	2077	2083	2086
Window Effected	1962-2012	1992-2042	2001-2051	2014-2064	2024-2074	2026-2076	2041-2091	2048-2098	2052-2100	2058-2100	2061-2100
P (in.)	3.04	2.80	3.03	3.31	2.99	3.11	2.87	2.98	3.03	3.06	2.82

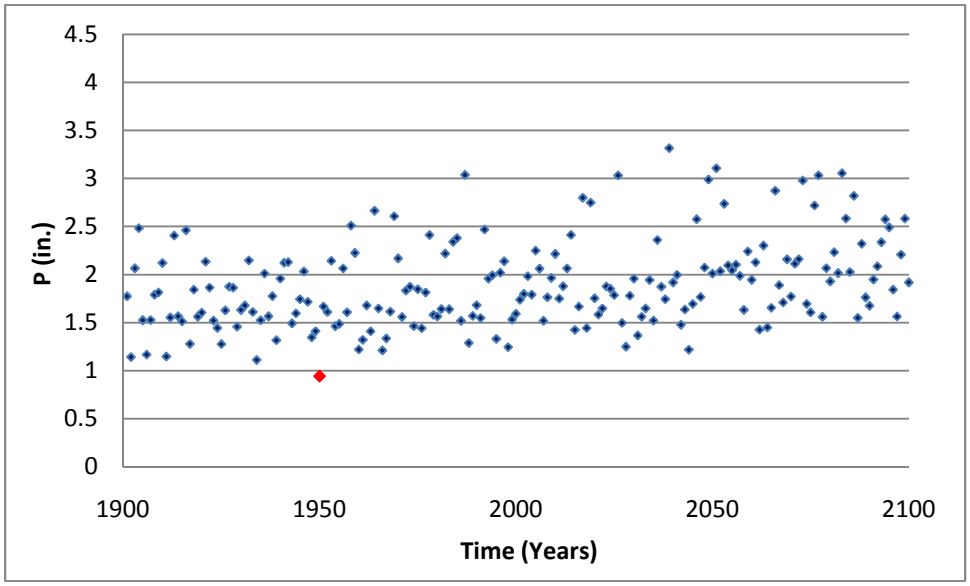

Figure 4-17. Annual Maximum Precipitation (in.) for Grid 2, SRES A2.

The 1950 precipitation event was removed to determine whether or not a single event within a 51-yr window could have such a significant influence on the scale parameter. The resulting scale parameter time series is shown in Figure 4-18. If compared to the original Grid 2 scale parameter time series shown in Figure 4-16, it is apparent that the abrupt decrease in the scale parameter is eliminated with the removal of 1950 low outlier. Therefore, both low and high preciptation outliers have a significant influence on the scale parameter.

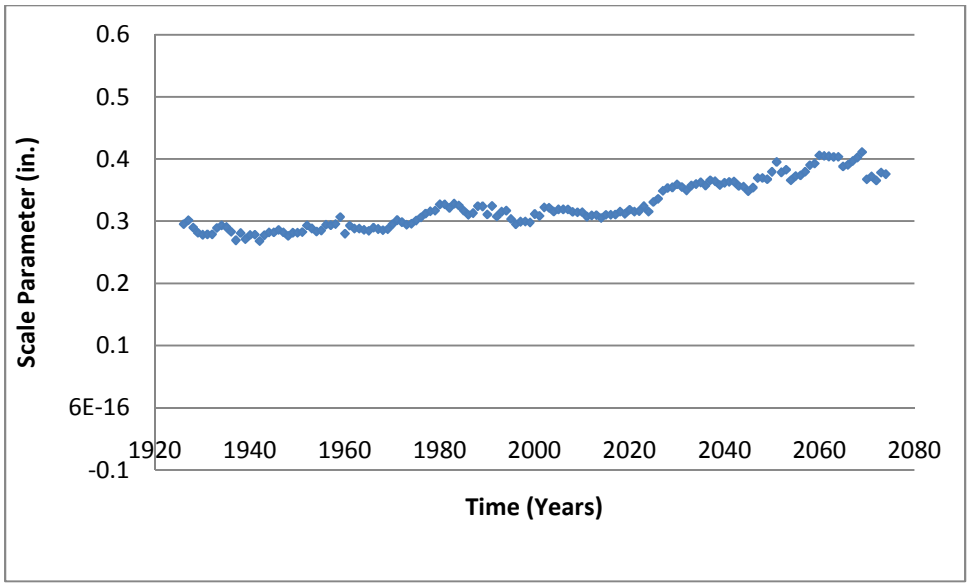

Figure 4-18. Scale Parameter Time Series for Grid 2, SRES A2 with Low Outlier in 1950 Eliminated.

Based on the effects of individual events on the scale parameter, the 51-yr window time period was increased to 71-yr windows to reduce the influence of individual precipitation events on the scale parameter without completely eliminating the trend that exists. The comparison between the window lengths for the scale parameter is shown in Figure 4-19. The 71-yr window smooths out the irrational peaks and low points within the time series; however, the overall trend remains, with a scale parameter value near 0.35 in the twentieth century, an increasing trend throughout the twenty-first century, and a value of 0.4 around 2060. Therefore, the 71-yr window length was selected to analyze the change in the scale parameter for each of the three emissions scenarios as shown in Figures 4-20, 4-21, and 4-22.

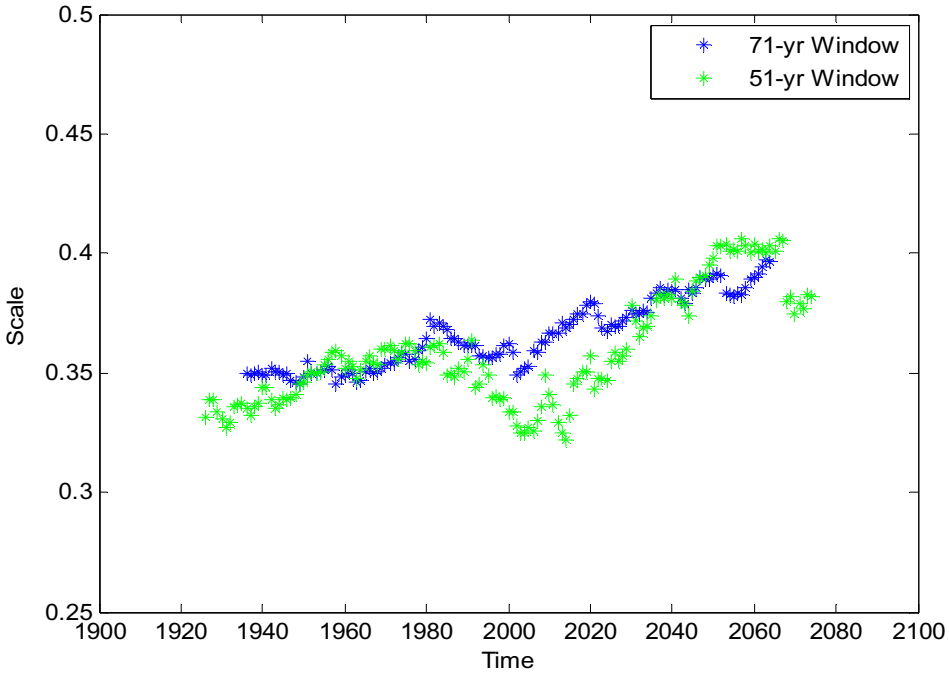

Figure 4-19. Comparison of the 51-yr and 71-yr Window Length in Calculating the Scale Parameter for SRES A2 based on the mean of the CSIRO 12 Grids.

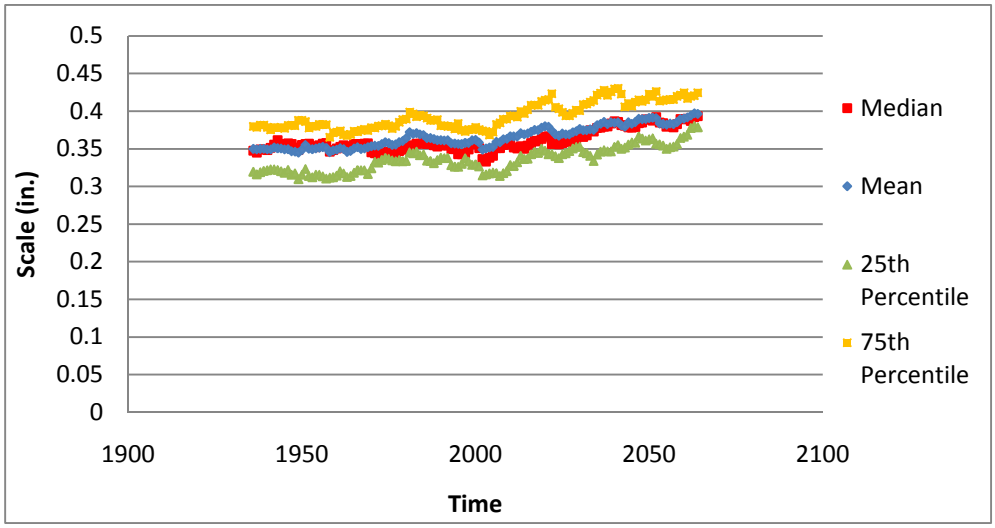

Figure 4-20. Median, Mean, 25th Percentile, and 75th Percentile of Scale Parameters for the 12 CSIRO Grid Cells from 1936 to 2064 for the A2 Scenario.

.

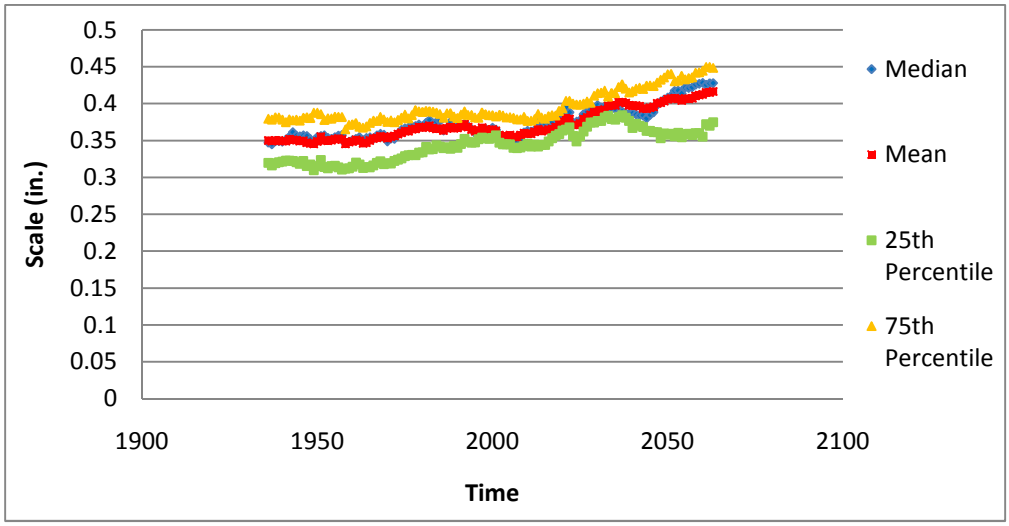

Figure 4-21. Median, Mean, 25th Percentile, and 75th Percentile of Scale Parameters for the 12 CSIRO Grid Cells from 1936 to 2064 for the A1B Scenario.

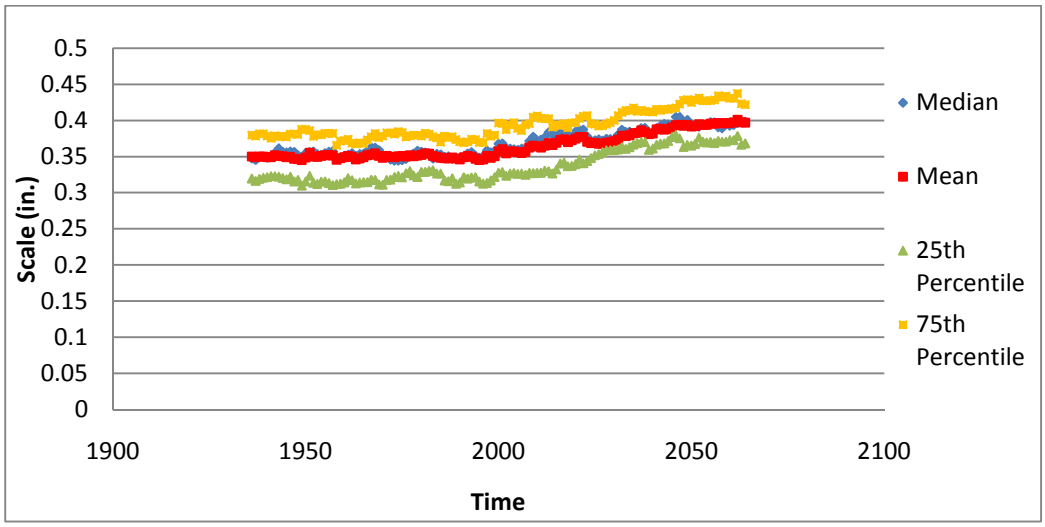

Figure 4-22. Median, Mean, 25th Percentile, and 75th Percentile of Scale.

Model Selection and Calibration. The scale parameter time series calculated based on a 71-yr window were then analyzed to determine the best model to represent the parameter values as a function of time. Similar to the location parameter, the scale

parameter for both the A2 and A1B scenarios appear to follow an exponential function as the rate of change increases with time. The scale parameter appears to have greater curvature than the locaiton parameter for both scenarios. Kharin and Zwiers (2005) found a similar functional form to represent the global scale parameter as shown in Figure 4-9 for the A2 scenario. Therefore, the following function was fit to the scale parameter for both the A2 and A1B scenarios:

$$y = C_1 + C_2 * e^{C3(x-C4)} \quad \text{Eq. 4-4.}$$

The coefficients were calibrated using numerical optimzation and then adjusted for physical rationality.

As with the location parameter, the scale parameter model for the B1 scenario differs from the A1B and A2 scenarios. The rate of change of the scale parameter appears to increase with time in the first portion of the time series and then decrease with time during the end of the twenty-first century. This again coincides with the reduction in the rate of change for emissions in the twenty-first century for the B1 scenario. Based on this observation, an exponential decay function was fit based on the following model

$$y = C_1 + \frac{C_2}{1+C_3 e^{C4(x-C5)}} \quad \text{Eq. 4-5.}$$

The model coefficient values were calibrated using numerical optimization and then adjusted for physical rationality. The fitted coefficient values are shown in Table 4-8 and the final models are shown in Figures 4-23, 4-24, and 4-25.

Table 4-8. Calibrated Coefficients for Scale Parameter Models

Emissions scenarios	Coefficient values		Goodness-of-fit	
A2	**C1**	0.34	**Se**	0.007
	C2	0.006	**Se/Sy**	0.48

	C3	0.017	**e**	-0.005
	C4	1936.86	**e/y**	-0.012
A1B	**C1**	0.34	**Se**	0.007
	C2	0.00637	**Se/Sy**	0.334
	C3	0.0197	**e**	-0.003
	C4	1936.84	**e/y**	-0.008
B1	**C1**	0.345	**Se**	0.01
	C2	0.065	**Se/Sy**	0.493
	C3	3	**e**	-0.007
	C4	0.045	**e/y**	-0.02
	C5	70		

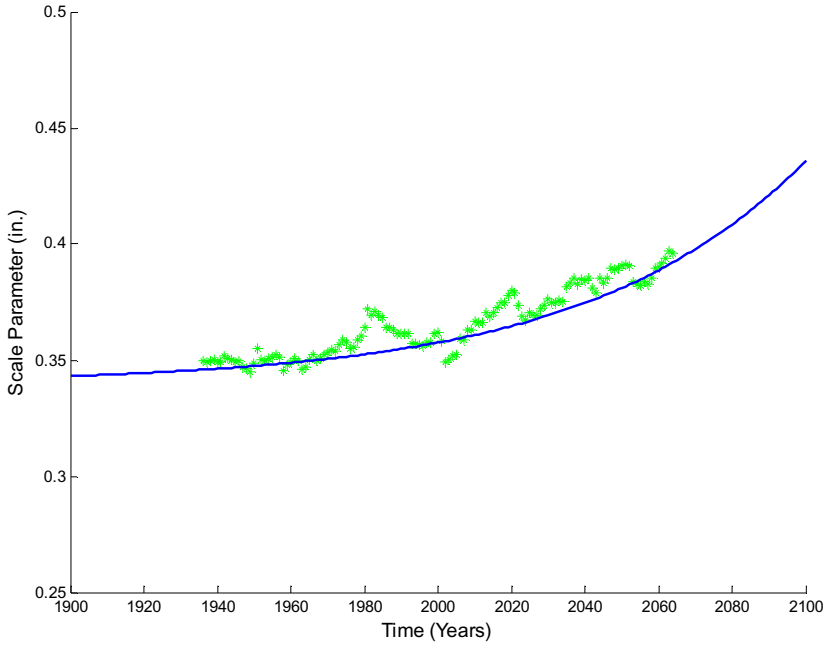

Figure 4-23. Scale Parameter Model for CSIRO Precipitation Data for SRES A2.

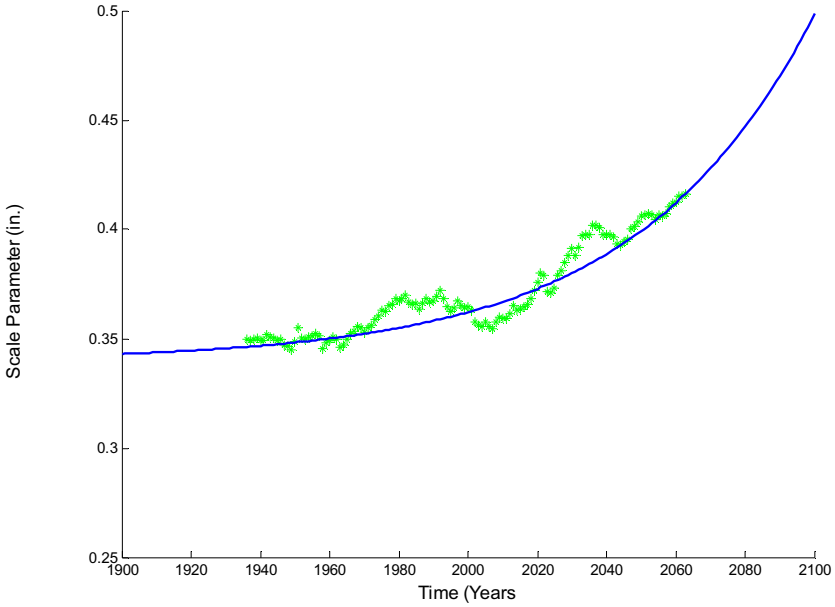

Figure 4-24. Scale Parameter Model for CSIRO Precipitation Data for SRES A1B.

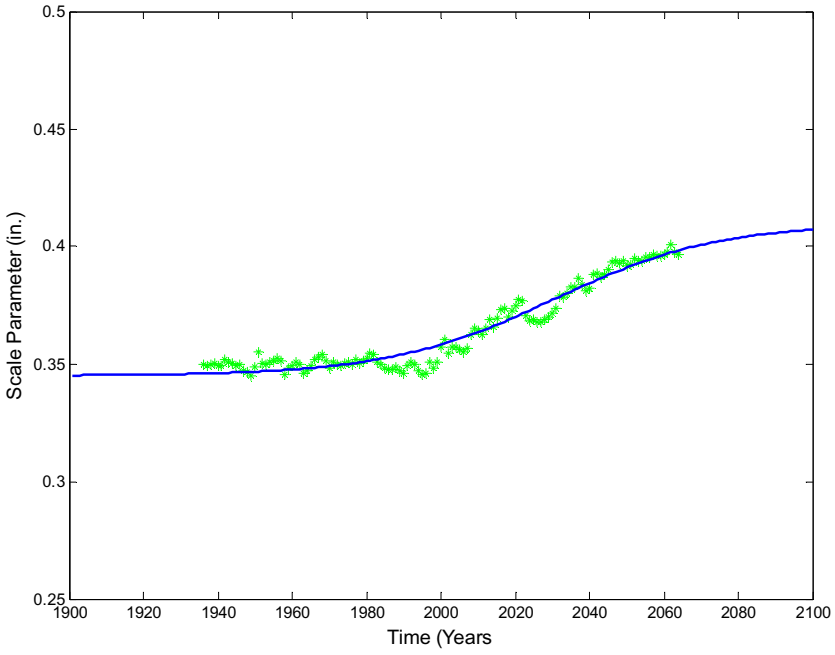

Figure 4-25. Scale Parameter Model for CSIRO Precipitation Data for SRES B1.

Goodness-of-Fit. As with the location parameter, the model coefficients for the scale parameter were calibrated with numerical optimization and then adjusted for physical rationality. The relative bias for scenarios A2, A1B, and B1 equaled -0.012, -0.008, and -0.02, respectively. Based on Figures 4-23, 4-24, and 4-25, the negative relative bias results from the few high points in the calculated scale parameter values. Analysis of the window length showed that these high points result from the calculation of the second moment of the data based on small sample sizes. This allows the scale parameter to be influenced by individual events within the time series. Therefore, it is reasonable that the models provide local biases due to the data rather than the models selected for the scale parameter.

The ratio between the standard error and the standard deviation equaled 0.48, 0.33, and 0.49 for the A2, A1B, and B1 scenarios, respectively. These values suggest that each of the models provided a statistically significant improvement in the estimation of the scale parameter compared to the mean of the data. The values are higher than the location parameter models, which is expected due to the increased variation within the time series data, as previously discussed.

The goodness of fit suggests that the calibrated models provide a good estimate of the scale parameter for the A2, A1B, and B1 scenarios. In addition, the nonlinear, increasing model structure for the A2 and A1B scenarios meet the hypothesis based on previous studies and the emissions scenarios. Likewise, the increasing and then decreasing model structure for the B1 scenario is expected based on the stabilization of emissions in the twenty-first century for the B1 scenario. Therefore, the developed scale

parameter models provide a good statistical fit and meet the specified physically rationality requirements.

4.3.4.5 Shape Parameter

Next, the shape parameter time series for each emissions scenario were analyzed. Figures 4-26, 4-27, and 4-28 show the shape parameter calculated within 51-yr windows for the A2, A1B, and B2 scenarios, respectively. It is apparent from the figures that the shape parameter calculated within 51-yr windows suggests an irrational sinusoidal shape. Therefore, further anaysis was conducted to determine the cause of the variation in the shape parameter data.

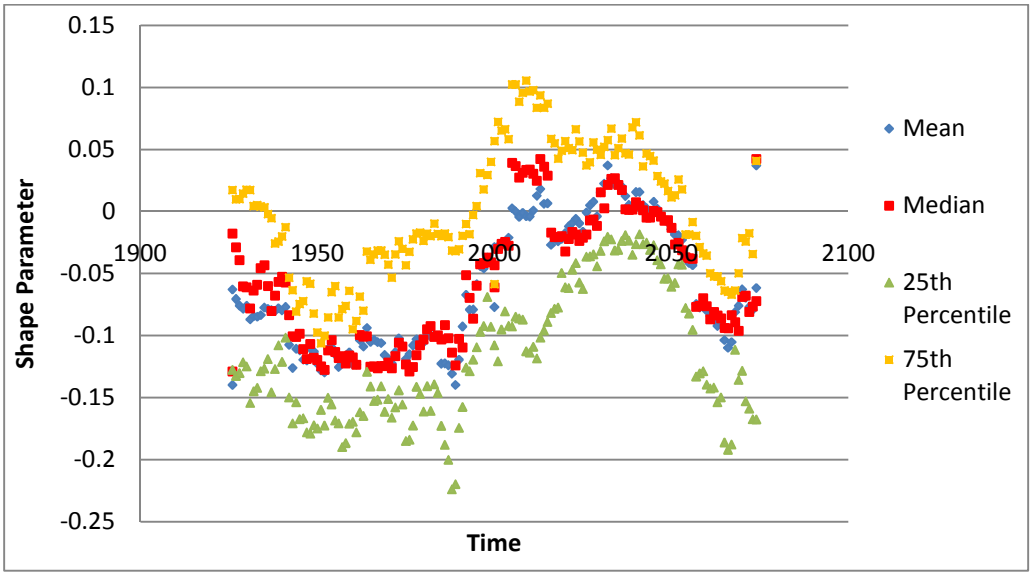

Figure 4-26. Median, Mean, 25th Percentile, and 75th Percentile of Shape Parameters for the 12 CSIRO Grid Cells from 1926 to 2074 for the A2 Scenario.

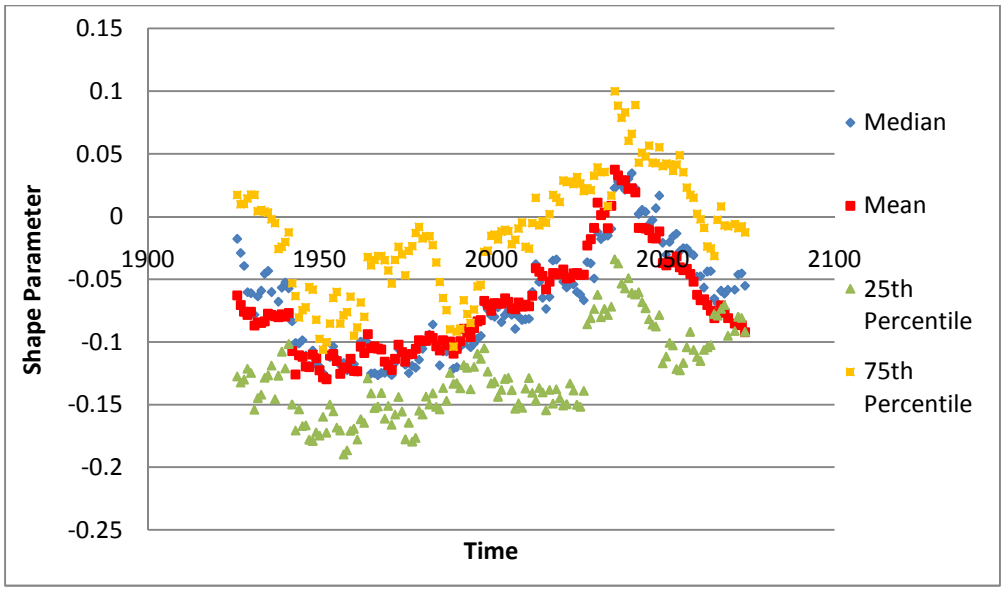

Figure 4-27. Median, Mean, 25th Percentile, and 75th Percentile of Shape Parameters for the 12 CSIRO Grid Cells from 1926 to 2074 for the A1B Scenario.

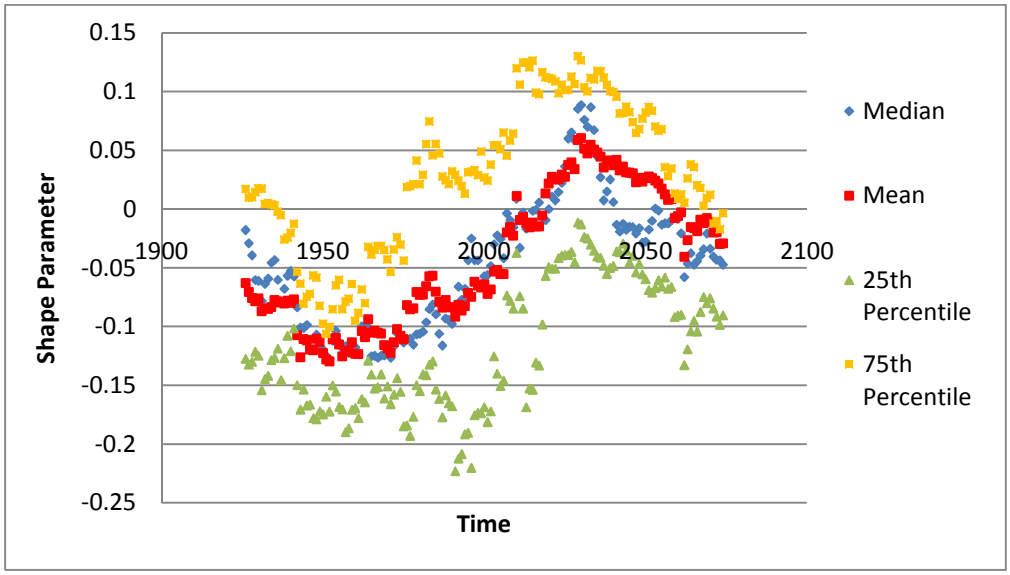

Figure 4-28. Median, Mean, 25th Percentile, and 75th Percentile of Shape Parameters for the 12 CSIRO Grid Cells from 1926 to 2074 for the B1 Scenario.

Based on the scale parameter analysis, it was assumed that this was a result of the sensitivity of the shape parameter to individual precipitation events. As with the scale parameter analysis, the window length was increased to 71-yrs and the results are shown in Figure 4-29. It is apparent that the increase in window length begins to smooth the

change in the parameter value, but the sinusoidal trend is still apparent. Therefore, the window length was increased to 91-yrs and 111-yrs and the results are shown in Figures 4-30 and 4-31, respectively.

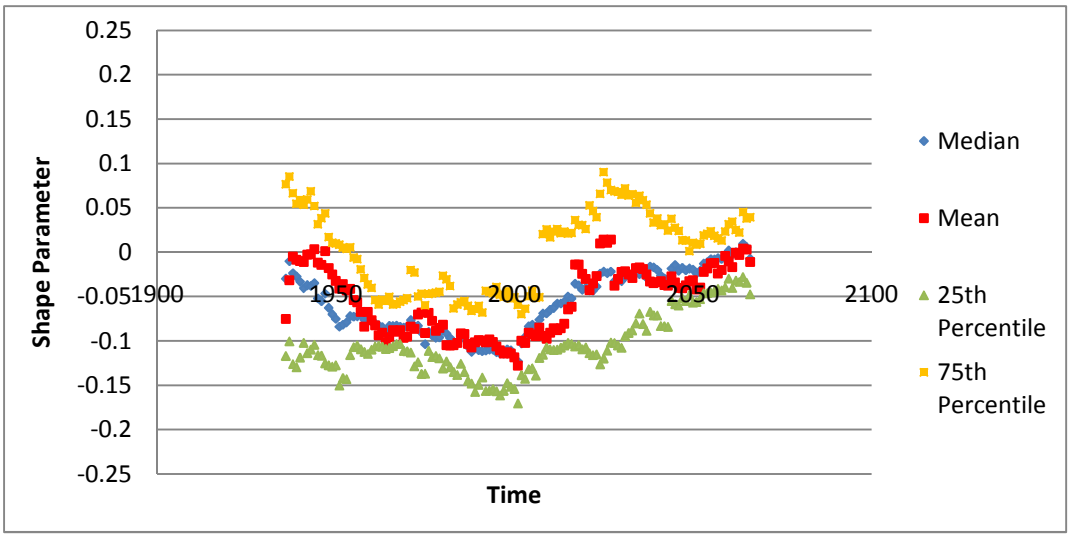

Figure 4-29. Shape Parameter as a Function of Time Calculated within 71-yr Windows.

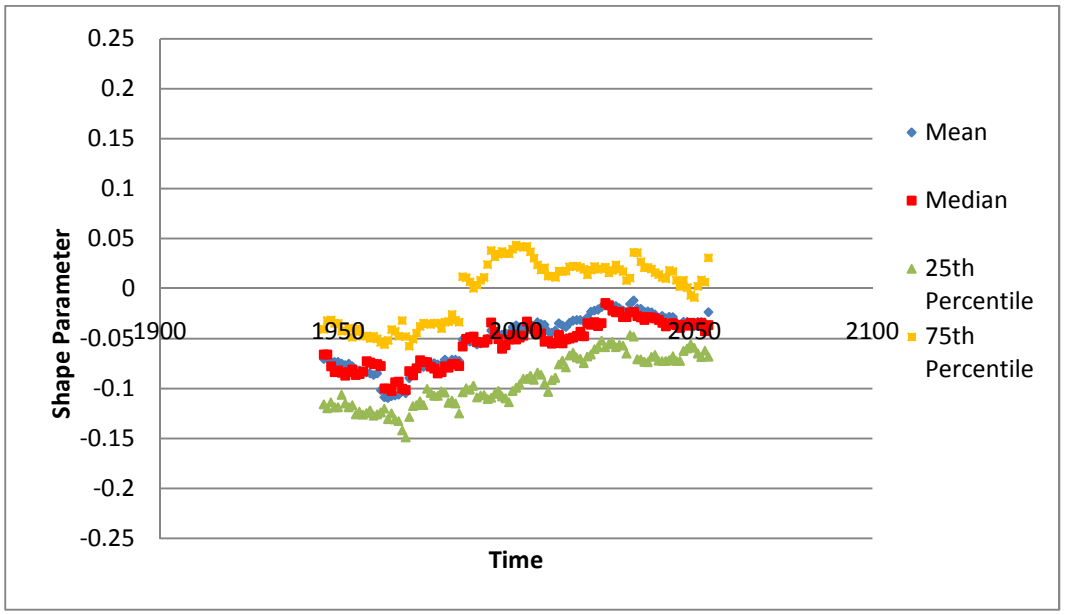

Figure 4-30. Shape Parameter as a Function of Time Calculated within 91-yr Windows.

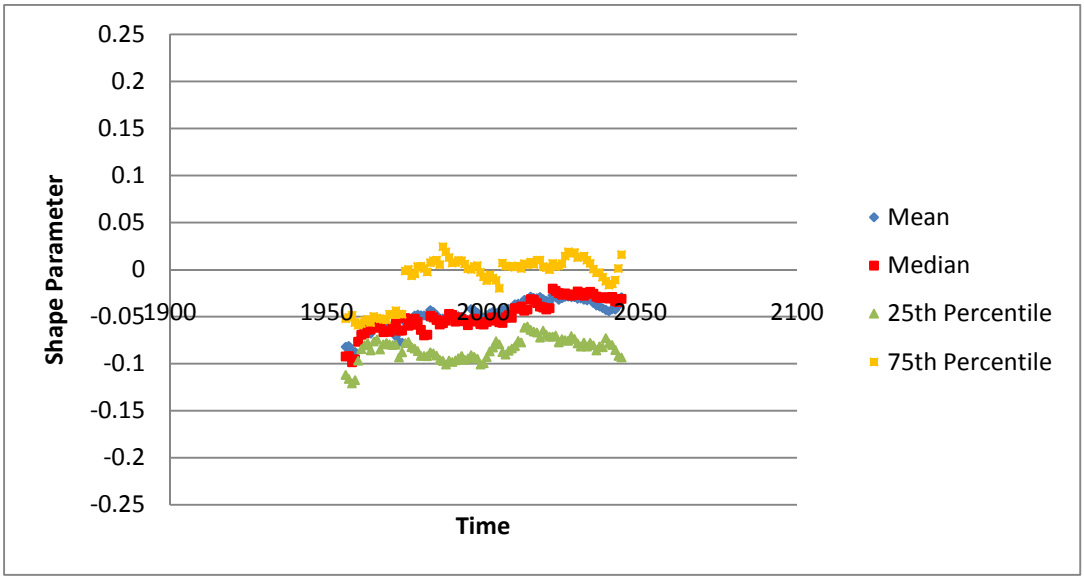

Figure 4-31. Shape Parameter as a Function of Time Calculated within 111-yr Windows.

The window length greatly influences the temporal trend of the shape parameter. Martins and Stedinger (2000) confirm that irrational values can result from estimating the shape parameter based on small samples. Likewise, they showed that the root-mean-square error of quantile estimates increases as the sample size decreases. Additionally, Koutsoyiannis (2004) proposed the regionalization of the shape parameter due to poor shape parameter estimates from short record lengths at individual stations. This suggests that the moving windows method for estimating the shape parameter may not provide rational estimates of the shape parameter due to the reduction in sample size. This is supported by the smoothing of the sinusoidal trend in the shape parameter as the window length is increased.

Based on these studies, shape parameter estimates calculated from sub-samples within the entire 200-yr record will most likely be poor estimates of the true parameter

values. Therefore, it was determined that the shape parameter should be held at a constant value, calculated from the entire time series. Kharin and Zwiers (2005) made similar assumptions based on their analysis of changes in the GEV parameters of the global precipitation distribution. They found that varying the shape parameter based on the trend identified in their analysis was not statistically different from a model in which the parameter was held constant. These results were true for the A2, IS92a, and B2 scenarios in the study.

The shape parameter was calculated for each CSIRO grid based on the respective 200-yr record. The results are shown in Table 4-9. The average shape parameter value equals -0.05. Martins and Stedinger (2000) claim that hydrologic extremes most likely follow a GEV Type II distribution with shape parameters ranging from 0 to 0.3 based on the notation used in this study; however, they state that a reasonable hydrologic distribution can result from a shape parameter ranging from -0.3 to 0.3. Therefore, while the negative shape parameter for the GCM data suggests a GEV Type III distribution, it is still a rational distribution for hydrologic data. Additionally, shape parameters with a magnitude less than 0.3 represent the Gumbel distribution (Stedinger et al. 1993), which suggests that within this range, the shape parameter does not have as great an influence on the distribution. Likewise, Kharin and Zwiers (2005) also found a fairly constant, near zero shape parameter for their global analyses, suggesting a Gumbel distribution rather than a GEV Type II or III distribution. Therefore, a constant shape parameter equal to -0.05 was selected to represent the CSIRO simulated precipitation data distribution within the 12 grids for the SRES A2.

Table 4-9. Shape Parameter for 12 Grids from CSIRO Precipitation Data Based on 200-yr Recordsfor SRES A2.

Grid	1	2	3	4	5	6	7	8	9	10	11	12
k	-0.05	-0.04	-0.09	-0.01	-0.07	-0.09	0.05	-0.08	-0.02	-0.01	-0.11	-0.04

The shape parameters for grids 1 through 12 and SRES A1B are shown in Table 4-10 for each entire time series. The average shape parameter equals -0.05 and will be used as a constant value to represent the data for the A1B scenario.

Table 4-10. Shape Parameter for 12 Grids from CSIRO Precipitation Data.

Grid	1	2	3	4	5	6	7	8	9	10	11	12
K	-0.08	-0.05	-0.02	-0.04	-0.16	-0.02	0.07	-0.06	-0.08	-0.02	-0.07	-0.05

As with the A2 and A1B scenarios, the shape parameter was held constant for the entire time series for the B1 scenario. The shape parameter was calculated for each grid and is shown in Table 4-11. The spatial mean for the B1 scenario shape parameter equals -0.02.

Table 4-11. Shape Parameter for 12 Grids from CSIRO Precipitation Data.

Grid	1	2	3	4	5	6	7	8	9	10	11	12
K	-0.02	-0.03	-0.02	-0.08	-0.04	-0.05	0.02	0.01	-0.03	-0.06	0.01	0.03

4.3.4.6 Comparison of SRES Statistical Models

The statistical models developed for the location and scale parameter for the SRES A2, A1B, and B1 are shown in Figures 4-32 and 4-33, based on the CSIRO annual maximum 24-hr precipitation. The models suggest that the A1B scenario results in the greatest change in precipitation extremes, followed by the A2 scenario and the B1 scenario. The B1 scenario represents the lowest emissions rate. Therefore, it is expected that the B1 GEV parameters experience the lowest rate of change over time. However,

the A2 scenario is defined as the highest emissions rate between the three scenarios. This suggests that the A2 GEV parameters should increase at the greatest rate rather than the A1B scenario. Therefore, further analysis was conducted to determine the cause of this shift in rank from emissions rate to GEV parameter magnitude for each scenario.

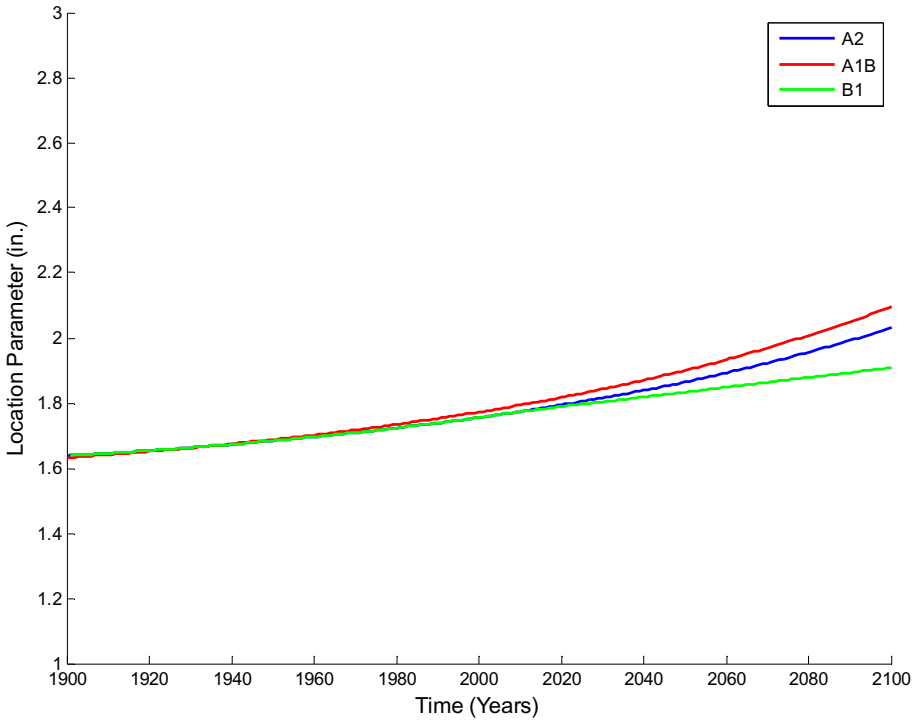

Figure 4-32. Statistical Models for GEV Location Parameter as a Function of Time based on CSIRO Annual Maximum 24-hr Precipitation.

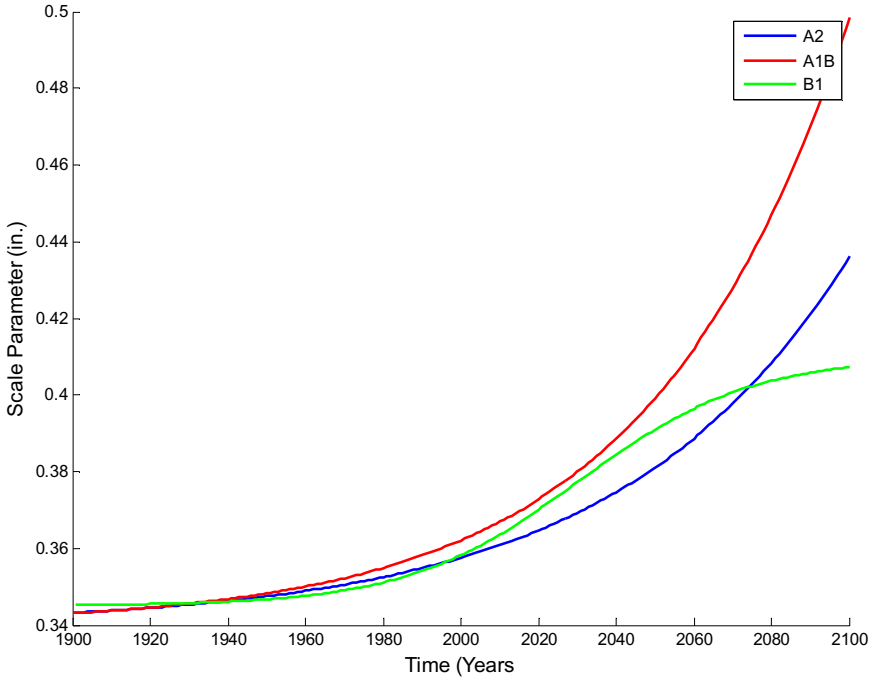

Figure 4-33. Statistical Models for GEV Scale Parameter as a Function of Time based on CSIRO Annual Maximum 24-hr Precipitation.

The annual maximum 24-hr precipitation time series for the A1B and A2 scenarios were compared to determine whether the disagreement in rank between the emissions scenarios and the resulting GEV parameter values existed within the simulated precipitation data or was an error in statistical modeling. Table 4-12 provides the mean and standard deviation of the annual maximum 24-hr precipitation from 1901-2100 for the A2 and A1B scenarios for grids 1 through 12. The mean annual maximum precipitation for scenario A1B is greater than or equal to the mean of A2 for 11 out of 12 grids. Likewise, the standard deviation of the A1B scenario precipitation data is greater than or equal to A2 for 8 out of the 12 grids. This suggests that the simulated

precipitation data for scenario A1B is heavier than for scenario A2, which supports the statistical models for the GEV parameters.

The precipitation data for scenario A1B may exceed scenario A2 because of the atmospheric concentration of greenhouse gases rather than the emission rates throughout the twenty-first century. Regardless of the emissions rates at the end of a given time period, the path of the emissions rate throughout the time period influences the overall atmospheric concentration of greenhouse gases (See Chapter 2 for more details). The atmospheric concentration of greenhouse gases for the A1B scenario may be greater than the A2 scenario at points throughout the twenty-first century, which may cause large precipitation events that influence the GEV distribution parameters. Therefore, the models developed should not be extrapolated beyond 2100, as the precipitation distribution for the A2 scenario may surpass the A1B scenario in magnitude.

Table 4-12. Characteristics of the A2 and A1B Simulated Annual Maximum 24-hr Precipitation Data from CSIRO.

A2	**1**	**2**	**3**	**4**	**5**	**6**	**7**	**8**	**9**	**10**	**11**	**12**
Mean	51.9	47.9	43.2	54.0	51.2	44.0	55.4	52.0	47.1	51.1	50.1	52.0
std. dev.	14.1	11.5	9.5	12.6	11.3	9.6	13.7	12.3	11.5	14.0	10.7	12.5
A1B	**1**	**2**	**3**	**4**	**5**	**6**	**7**	**8**	**9**	**10**	**11**	**12**
mean	52.3	48.3	43.3	54.3	50.8	44.7	55.9	52.5	47.1	51.2	50.5	52.5
std. dev.	13.6	11.5	10.2	12.6	10.7	10.4	13.9	13.1	10.8	13.7	11.6	12.8

4.3.4.7 Analysis of Regional GEV Parameters from Observed Data.

The final step to assess the model rationality of the GEV parameters for the three emissions scenarios was to ensure that the parameters were representative of observed precipitation in the study region. Precipitation records were retrieved from 32 rain gauge locations within the study region. The coordinates for each rain gauge location are shown in Table 4-13.

Table 4-13. Rain Gauge Locations and Coordinates for Region of Interest.

Location		Coordinates
Maryland	Baltimore	39°10'N / 76°41'W
	Brighton	39°11'N / 77°00'W
	Chestertown	39°13'N / 76°03'W
	Conowingo Dam	39°39'N / 76°11'W
	Cumberland	39°38'N / 78°50'W
	Dalecarlia Reservoir	38°56'N / 77°07'W
	Emmitsburg	39°41'N / 77°17'W
	Hancock	39°42'N / 78°11'W
	Oakland	39°25'N / 79°24'W
	Salisbury	38°22'N / 75°35'W
Virginia	Alta Vista	37°04'N / 79°10'W
	Appomattox	37°21'N / 78°50'W
	Ashland	37°45'N / 77°29'W
	Bremo Bluff	37°43'N / 78°17'W
	Hopewell	37°18'N / 77°17'W
	Martinsville	36°42'N / 79°52'W
	Mt. Weather	39°04'N / 77°53'W
	Norfolk	36°54'N / 76°12'W
	Washington, DC (Reagan)	38°51'N / 77°02'W
	Richmond	37°30'N / 77°19'W
	Roanoke	37°19'N / 79°58'W
	Somerset	38°15'N / 78°16'W
	Suffolk	36°44'N / 76°36'W
	West Point	37°34'N / 76°48'W
	Williamsburg	37°18'N / 76°42'W
Delaware	Dover	39°16'N / 75°31'W
	Georgetown	38°38'N / 75°27'W
	Lewes	38°47'N / 75°08'W
	Milford	38°54'N / 75°26'W
	Newark	39°40'N / 75°45'W
	Wilmington	39°40'N / 75°36'W

The GEV parameters for the annual maximum precipitation time series for each location were calculated and are shown in Table 4-14. Then, the KS-1 test was applied to each the precipitation data at each gauge location to determine whether the GEV

distribution with the calculated parameters is representative of the data. The calculated test statistic along with the critical values for each sample size and the 1% and 5% levels of significance are also shown in Table 4-14. Based on the KS-1 test results, the null hypothesis is accepted at each location, which implies that the annual maximum precipitation data at each of the 32 rain gauges follows the GEV distribution with the specified parameter values.

Table 4-14. GEV Parameters and KS-1 Test Results for the 32 Rain Gauges in the MD-VA-DE Region, with CV = Critical Value.

	GEV Parameters			KS1 Test			
Rain Gauge Location	**Location**	**Scale**	**Shape**	**Test Statistic**	**n**	**CV (5%)**	**CV (1%)**
Alta Vista	2.440	0.741	-0.072	0.083	55	0.183	0.220
Appomattox	2.419	0.708	0.258	0.076	64	0.170	0.204
Ashland	2.450	0.850	-0.061	0.092	62	0.173	0.207
Baltimore	2.414	0.713	0.156	0.093	61	0.174	0.209
Bremo Bluff	2.545	0.860	-0.079	0.100	63	0.171	0.205
Brighton	2.298	0.834	0.094	0.090	46	0.201	0.240
Chestertown	2.408	0.778	0.125	0.058	62	0.173	0.207
Conowingo Dam	2.408	0.778	0.125	0.075	61	0.174	0.209
Cumberland	1.777	0.478	0.124	0.146	37	0.224	0.268
Dalecarlia Reservoir	2.433	0.766	0.143	0.122	62	0.173	0.207
Dover	2.670	0.853	0.115	0.082	62	0.173	0.207
Emmitsburg	2.108	0.652	0.264	0.062	52	0.189	0.226
Georgetown	2.434	0.606	0.223	0.120	49	0.194	0.233
Hancock	1.988	0.567	0.166	0.163	49	0.194	0.233
Hopewell	2.335	0.714	0.256	0.052	75	0.157	0.188
Lewes	2.607	0.709	0.128	0.066	60	0.176	0.210
Martinsville	2.383	0.657	0.147	0.074	60	0.176	0.210
Milford	2.457	0.757	0.106	0.082	49	0.194	0.233
Mt. Weather	2.424	0.878	0.035	0.078	79	0.153	0.183
Newark	2.322	0.704	0.280	0.071	58	0.179	0.214
Norfolk	2.755	0.934	0.186	0.054	64	0.170	0.204
Oakland	1.859	0.530	0.088	0.070	62	0.173	0.207
Richmond	2.531	0.804	0.119	0.070	62	0.173	0.207
Roanoke	2.342	0.657	0.141	0.097	62	0.173	0.207

	GEV Parameters			KS1 Test			
Rain Gauge Location	**Location**	**Scale**	**Shape**	**Test Statistic**	**n**	**CV (5%)**	**CV (1%)**
Salisbury	2.628	0.890	0.133	0.086	62	0.173	0.207
Solomons	2.452	0.998	0.224	0.119	44	0.205	0.246
Somerset	2.161	0.697	0.330	0.119	43	0.207	0.249
Suffolk	2.645	0.825	0.231	0.067	65	0.169	0.202
Washington, DC (Reagan)	2.142	0.640	0.362	0.075	62	0.173	0.207
West Point	2.455	0.795	0.220	0.121	56	0.182	0.218
Williamsburg	2.575	1.005	0.354	0.084	62	0.173	0.207
Wilmington	2.402	0.611	0.267	0.117	62	0.173	0.207

Next, the spatial mean within the region was calculated for each of the GEV parameter values to develop regional location, scale, and shape parameters. In GIS, a shapefile was created that consisted of the location of each rain gauge based on the latitude and longitude coordinates. The spatial reference of the shapefile was set to Geographic Coordinate System, North American Datum 1983. Census tract data were retrieved from *www.esri.com* to outline the region of interest including the states of Maryland, Virginia, and Delaware. The spatial extent of the shapefile was then limited to the state boundaries and a longitude boundary equal to 80.23W. As mentioned previously, this additional boundary was implemented so as to not misrepresent the mountainous, western portion of Virginia from which precipitation data were not retrieved. The areas within these boundaries were then allocated to the nearest rain gauge based on a Euclidean distance calculation. The allocation results are shown in Figure 4-34.

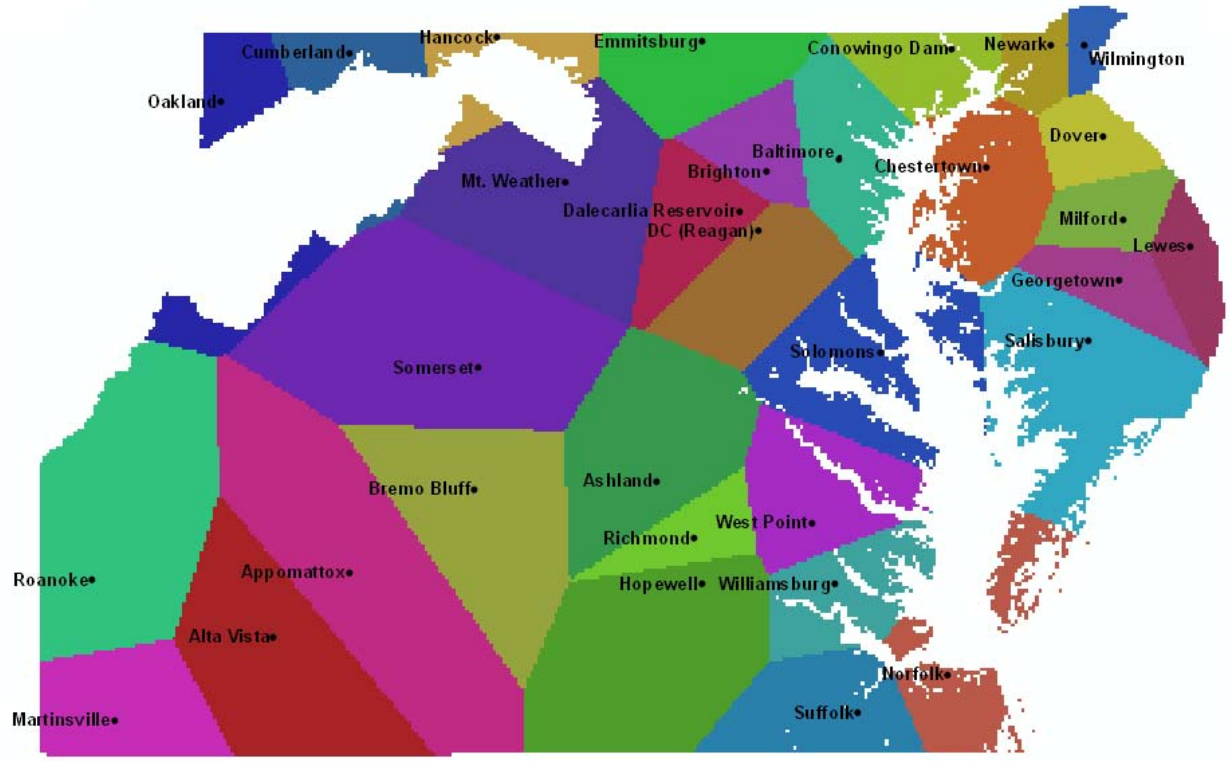

Figure 4-34. Area Allocation for Spatial Mean Calculation for the 32 Rain Gauge Locations.

The spatial mean was calculated based on the percentage of the total area allocated to each rain gauge based on the following equation:

$$\text{Spatial Mean} = \frac{\sum_{i=1}^{n} A_i * C_i}{\sum_{i=1}^{n} A_i} \qquad \text{Eq. 4-6}$$

where n = the total number of rain gauges in analysis; *i* = specifies the rain gauge; A_i = area allocated to rain gauge '*i*'; and C_i = mean coefficient value at rain gauge '*i*'. The final spatial mean parameter values were as follows: (1) location = 2.44 (in.); (2) scale = 0.772 (in.); and (3) shape = 0.155.

A sensitivity analysis was conducted to determine the uncertainty involved when using the spatial mean rather than the parameters calculated for the individual rain gauges. The 100-yr, 50-yr, 20-yr, 10-yr, 5-yr, and 2-yr storms were calculated based on the GEV parameter values for each individual rain gauge location and for the spatial mean parameters. Then, the relative bias was calculated for the location specific storm depths versus the spatial mean storm depths. The results are shown in Figure 4-35.

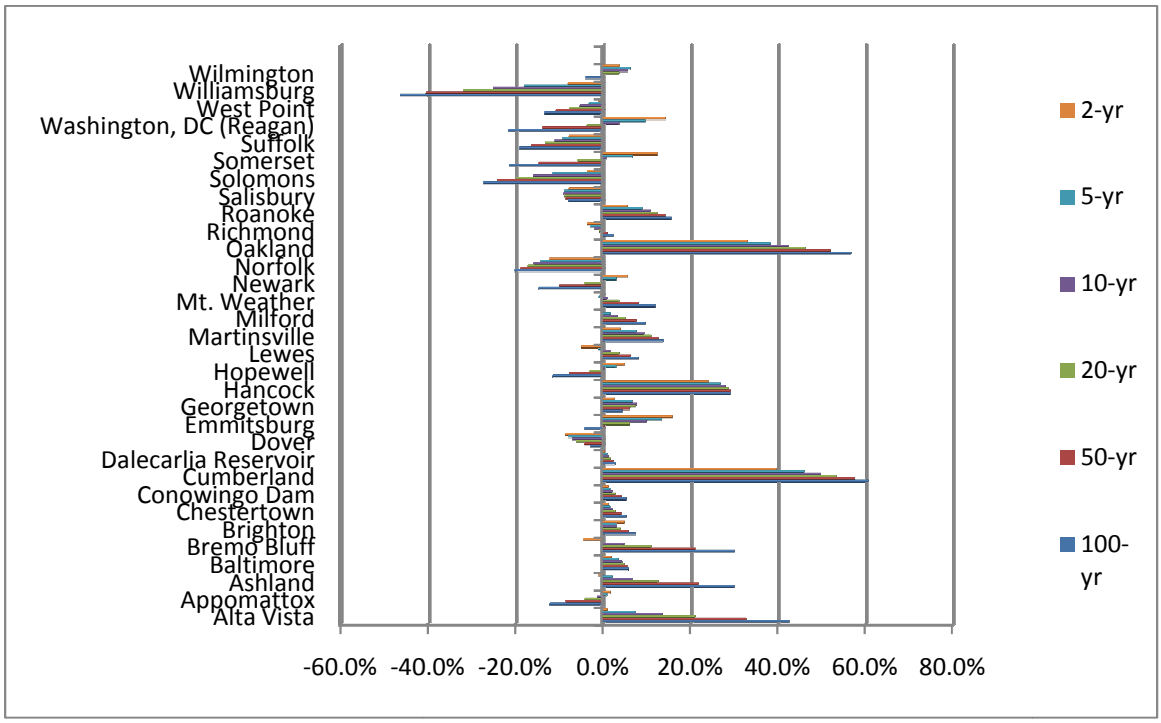

Figure 4-35. Relative Bias for Location Specific GEV Parameters vs. Spatial Mean GEV Parameters.

The sensitivity anlaysis results for each location, shown in Figure 4-35, provides the expected bias when storm depths for a particular return period are estimated based on the spatial mean GEV parameters rather than the location specific GEV parameters. The majority of the rain gauge locations show relative biases less than 20% for all return

periods. The analysis suggests that lower return periods are less sensitive to the spatial mean GEV parameters than higher return periods for all locations. Estimates based on the spatial mean GEV parameters tend to overestimate the north and western portion of the region and underestimate the south-eastern portion of the region.

Williambsurg, Hancock, Oakland, and Cumberland appear to be the most sensitive to the spatial mean GEV parameters. Hancock, Oakland, and Cumberland are located in the most north-west portion of Maryland, which suggests that the spatial mean should be used with caution in this region. This region is more mountainous than the remaining parts of the region. However, the rain gauges surrounding Williamsburg, such as Norfolk and West Point, do not show significant biases relative to Williamsburg. This suggests that the sensitivity is location specific for Williambsurg. The scale and shape parameter for Williambsurg are the greatest and second greatest in magnitude, respectively, compared to the values for the other rain gauge locations. Both of these parameters influence extreme values, which mathematically explains the large bias when the spatial mean parameter values are used for Williambsurg. However, the deviation of the parameter values from the mean can only be explained by the observed precipitation data. This could be the result of poor sampling at the Williamsburg rain gauge.

4.3.5 Comparison of Observed and GCM Simulated GEV Parameters.

The GEV parameters were calculated for the region based on both observed data from the 32 rain gauges and simulated data from the GCM selected. The parameters were then compared to determine whether the GCM values were representative of the observed data in the region. The coefficient, C1 (see Tables4-5 and 4-8), for location and scale parameter models was compared to the spatial mean values for each parameter.

The C1 coefficient represents the y-intercept of each parameter model. Because the location and scale parameters are relatively stationary in the twentieth century, the C1 coefficient is a reasonable estimate of each parameter for the twentieth century. Likewise, the constant shape parameter calculated for the GCM data was compared to the regional spatial mean value.

It is apparent that the location, scale, and shape parameters are greater for the spatial mean of the observed precipitation data within the MD-VA-DE region than those derived from the GCM simulations. The shape parameter for the observed data is positive, which suggest a Type II distribution, a popular representation of hydrologic data. Additionally, Koutsoyiannis (2004) found that a constant shape parameter value equal to 0.15 was representative of rainfall distributions throughout Europe and North America. Therefore, the spatial mean shape parameter value for the MD-VA-DE region is representative of many geographic locations as a regional shape parameter, and most likely a better estimate than the -0.05 shape parameter calculated based on the GCM data.

These results may lead to the intepretation that the GCM simulation of annual maximum 24-hr precipitation may underestimate realistic precipitation extremes. It is difficult for current GCMs to accurately simulate precipitation extremes for small spatial extents. Despite the availability of GCM projections for specified latitudinal and longitudinal grids, the confidence in the changes projected by global models decreases at smaller scales. In fact, for smaller scales, higher intensities and rainfall depths will occur. AOGCMs have coarse resolutions and large scale systematic errors, whereas extreme precipitation events generally occur on a smaller spatial scale. So while AOGCMs have proven to predict temperature extremes fairly well, the intensity, frequency, and

distribution of precipitation extremes has proven to be more difficult to simulate (Randall et al. 2007). This was confirmed in a study conducted by Sun et al. (2006) of daily precipitation simulated by 18 AOGCMs. The results showed that the models underestimated both the frequency and intensity of heavy precipitation events, defined as 10 mm/day. However, Iorio et al. (2004) found that simulations of daily precipitation events improved as the resolution of the AOGCM increased. Therefore, as the resolution of AOGCMs increase with advancements in modeling, projections of extreme precipitation are expected to improve as well (Randall et al. 2007).

This also is a common issue when precipitation is estimated at an ungauged site based on precipitation within the same region. For example, depth-area curves are often used in hydrology to adjust point rainfalls to represent mean rainfalls over larger areas. This method results in a reduction in a point 24-hr rainfall depth by 10% for an area of 400 mi^2. The grid size for the CSIRO GCM outputs is roughly 36,000 km^2, which would suggest that the estimate of precipitation over the entire area would be greatly reduced from the precipitation event at a specific location of interest.

Based on these observations, it is clear that the magnitudes of the parameters calculated based on the GCM data are less than those of the observed data; however, for this study it was assumed that the rate of change of the parameters is still applicable for climate change scenarios. Therefore, it was determined that parameter models would be based on the rate of change for the scale and location parameters developed based on the GCM simulated data and the magnitude of the observed GEV parameters. As GCMs become more sophisticated in the future and provide better estimates of extreme

precipitation data at a regional scale, this method can be adjusted to rely entirely on the parameter models developed based on the GCM simulations.

The fitted parameter models were scaled so that the 1950 parameter value was within 0.001 of the spatial mean for the observed parameter values. The assumption was made that while the magnitude of the parameter values differ, the rate of change determined from the CSIRO GCM data was representative of the expected changes in the regional spatial mean GEV parameters over the twentieth and twenty-first centuries. The final models are shown in Figures 4-36 and 4-37 and the coefficients are shown in Tables 4-15, 4-16, and 4-18 for the A2, A1B, and B1 scenarios, respectively.

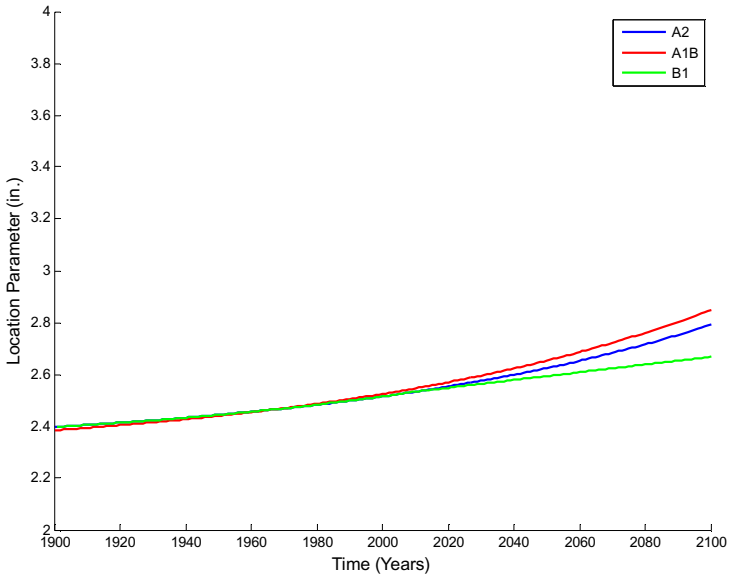

Figure 4-36. Final Location Parameter Model.

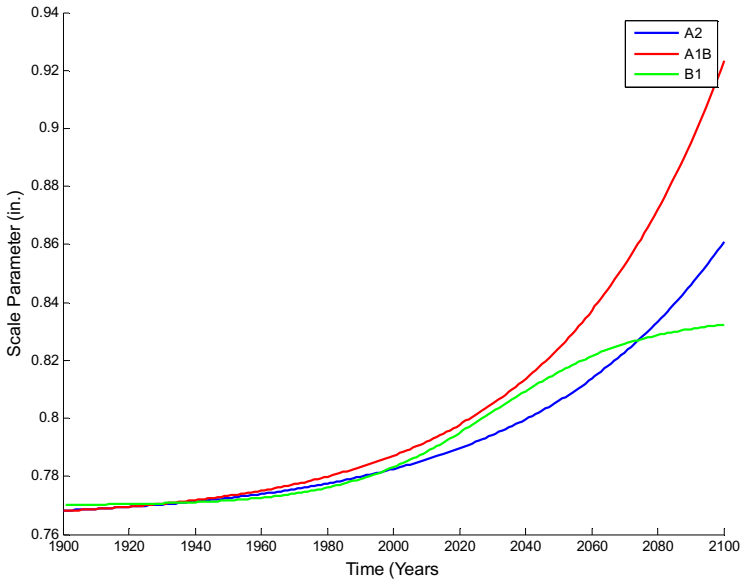

Figure 4-37. Final Scale Parameter Model.

Table 4-15. Final Location, Scale, and Shape Parameter Coefficients for the A2 Scenario.

Parameter	Coefficient Values	
Location	C1	2.31
	C2	0.1114995
	C3	0.0085
	C4	1928.1861
Scale	C1	0.765
	C2	0.006
	C3	0.017
	C4	1936.86
Shape		0.155

Table 4-16. Final Location, Scale, and Shape Parameter Coefficients for the A1B Scenario.

Parameter	Coefficient Values	
Location	C1	2.278
	C2	0.1315

Parameter	Coefficient Values	
	C3	1926.008
	C4	-1.388
Scale	C1	0.765
	C2	0.00637
	C3	0.0197
	C4	1936.84
Shape		0.155

Table 4-17. Final Location, Scale, and Shape Parameter Coefficients for the B1 Scenario.

Parameter	Coefficient Values	
Location	C1	2.31
	C2	0.1115
	C3	0.00852
	C4	2.186
	C5	1.227
	C6	1.2
	C7	1.7
	C8	0.005
	C9	13.4
Scale	C1	0.77
	C2	0.065
	C3	3
	C4	0.045
	C5	70
Shape		0.155

4.3.6 Sensitivity Analysis for Twentieth Century Models

The data base used to model the GEV parameters over time was simulated by the CSIRO Mark 3.5 GCM based on measured greenhouse gas emissions data from 1900 through 2000 and three projected scenarios of greenhouse gas emissions data for the year 2001 to 2100. The data for the latter period varied with the emissions scenario. Realistically, the GEV parameters should be the same throughout the twentieth century regardless of the emission scenario. However, the scale and location parameters for the three emissions scenarios differ slightly during the twentieth century time period due to the inclusion of the twenty-first century GCM data in fitting the functions.

A sensitivity analysis was conducted to determine whether or not the differences of the functions for the twentieth century caused a significant change in the precipitation event that would result from the twentieth century parameters. Because the 100-yr rainfall is often used in design and the greater return periods are more sensitive to the parameter values, the magnitude of the 100-yr rainfall based on the models developed for A2, A1B, and B1 were compared from 1901 to 2000, as the emissions scenarios diverge in the year 2000.

The 100-yr rainfall for each scenario is shown in Figure 4-38 for the twentieth and twenty-first centuries. The average value of the 100-yr rainfall for all three scenarios equals 7.64 in. for the twentieth century. The largest difference in the estimated 100-yr rainfall for a given year during the twentieth century for scenarios A1B and A2 occurred in the year 2000 and equaled 0.040 in. or 0.5% of the average 100-yr rainfall from 1901 to 2000. The largest difference in the estimated 100-yr rainfall for a given year for scenarios A1B and B1 equaled 0.036 in. or 0.5% of the average 100-yr rainfall for the

time period and occurred in 2003. The largest difference in the estimated 100-yr rainfall for a given year for scenarios B1 and A2 occurred in 1901 and equals 0.013 in. or 0.2% of the average 100-yr rainfall for the time period.

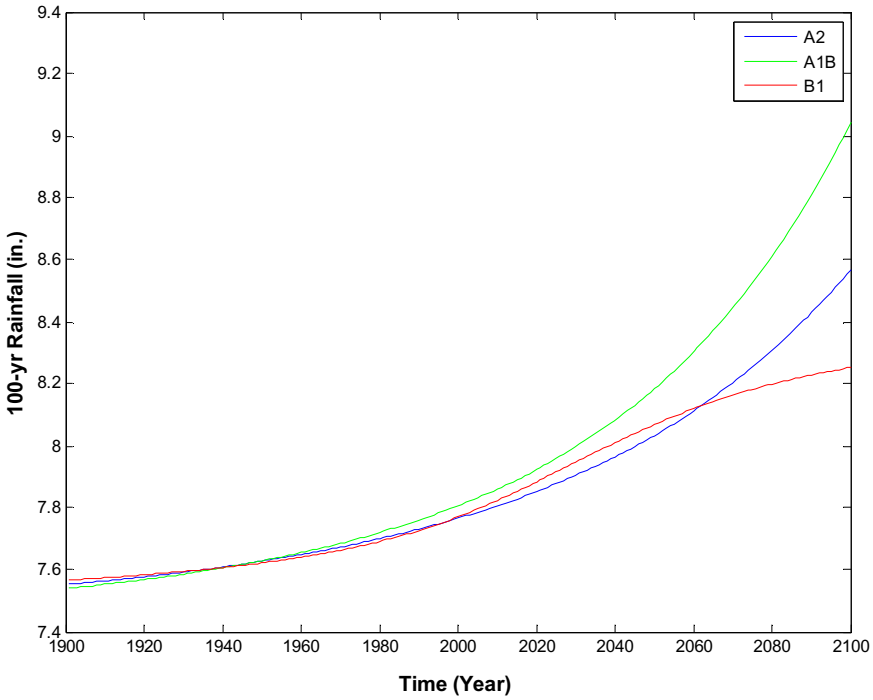

Figure 4-38. 100-yr Storm as a Function of Time and Emissions Scenario.

In the year 2100, the difference in the 100-yr rainfall for the three scenarios are much larger (see Figure 4-38), by as much as 0.78 in. or 10% of the average 100-yr rainfall in the twentieth century. The less than one-half percent errors for the 100-yr rainfall in the year 2000 is, therefore, not a meaningful contribution to errors in the twenty-first century.

4.3.7 Final Climate Change Adjustment Factor

The final climate change adjustment factor consists of the difference in the expected storm depth for a given return period from the observed year to the design year. The temporal changes in the storm depths for the 100-yr, 50-yr, 20-yr, 10-yr, and 2-yr

return periods are graphed in Figures 4-39, 4-40, and 4-41 for the A2, A1B, and B1 emissions scenarios, respectively. The figures are based on the cumulative distribution for each emissions scenario over time based on the statistical models for the GEV parameters. The change in additional return periods can be calculated based on the statistical models for each GEV parameter and emissions scenario previously defined.

To adjust an observed precipitation event, the return period of the event in the precipitation record must be calculated first. Then, the expected precipitation depth for the particular return period can be identified based on the emissions scenario and the year using the statistical models for the GEV parameters. Finally, the ratio of the expected precipitation depth in the design and the observation year will be multiplied by the observed precipitation depth to determine the adjusted value in the design year. This method would be applied to the entire precipitation record to develop a record with the same length under stationary conditions in the design year.

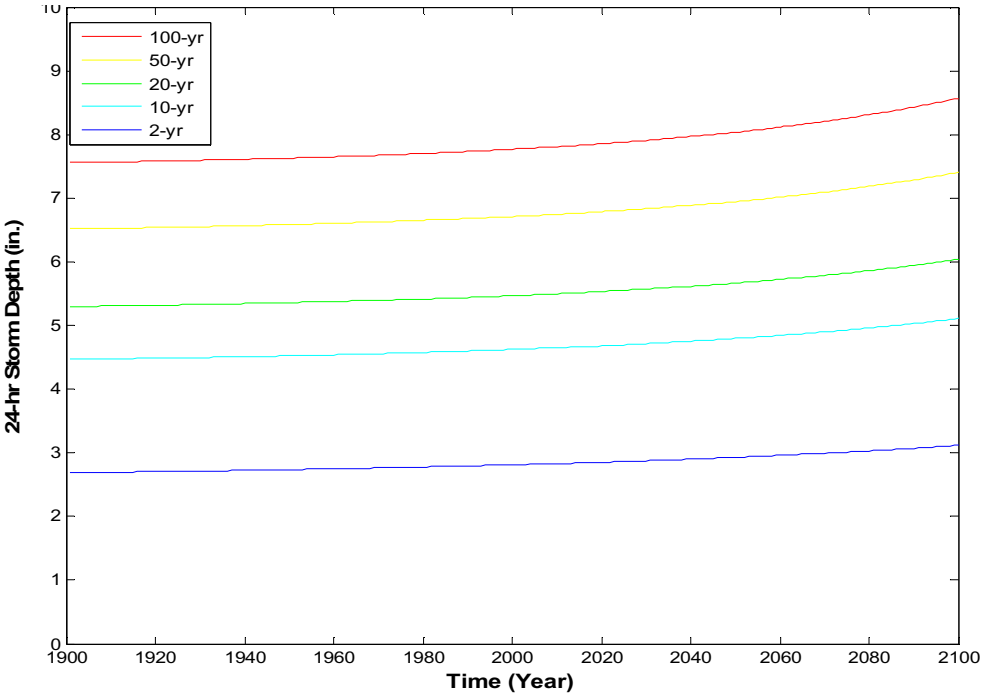

Figure 4-39. Final Climate Change Adjustment Factor Graph for SRES A2.

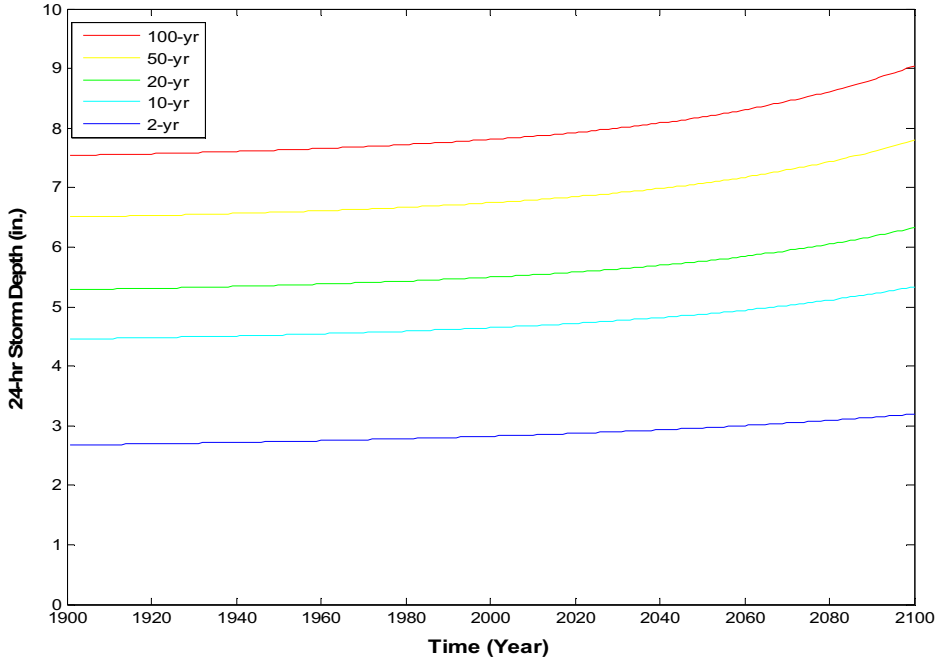

Figure 4-40. Final Climate Change Adjustment Factor Graph for SRES A1B.

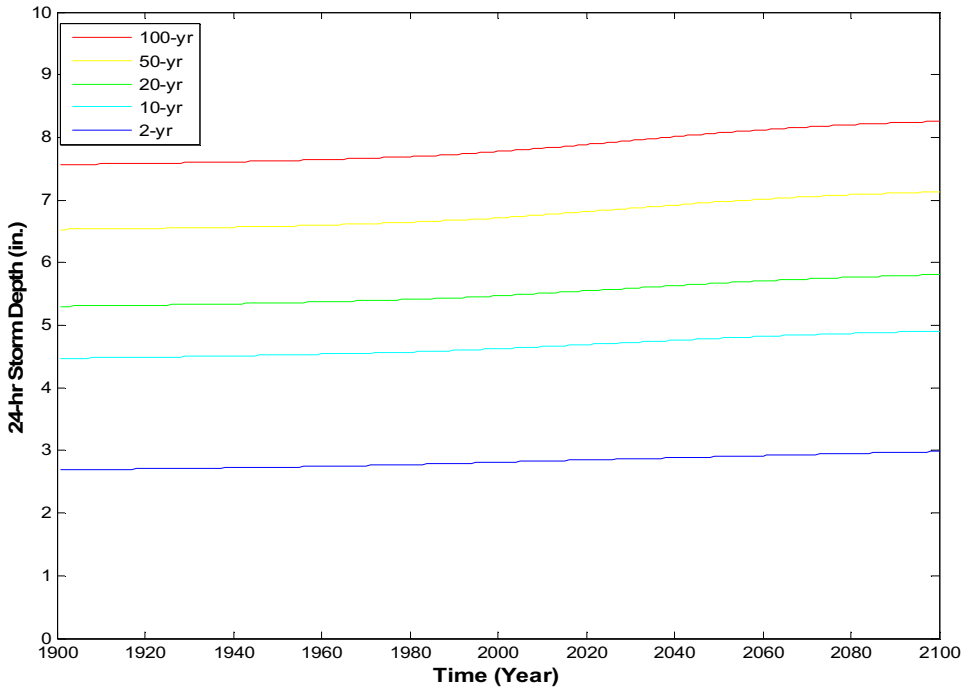

Figure 4-41. Final Climate Change Adjustment Factor Graph for SRES B1.

4.3.7.1 Verification

Kharin and Zwiers (2005) used the second version of the CCCma coupled global climate model (CGCM2) to provide future estimates of the 20-yr return period. Kharin et al. (2007) used the ensemble median of data from 14 CGCMs provided by the Program for Climate Model Diagnosis and Intercomparison to also estimate future 20-yr return periods. The results from these studies will be compared to the present study and discussed herein.

Table 4-18 shows the projected percent increase in the 20-yr storm from the current study for the MD-VA-DE region and by Kharin et al. (2007) for global land areas and the northern hemisphere for the time periods 2046-2065 and 2081-2100, relative to the time period 1981-2000. For the A2 scenario, the current study provides estimates

closest to the land values provided by Kharin et al. (2007); however, the current study is 1.2% and 2.3% below the range provided by Kharin et al. (2007) for land for the 2046-2065 and 2081-2100 time periods, respectively. The A1B scenario projections provided by the current study are within the range of the land estimates provided by Kharin et al. (2007) for both time periods. The B1 scenario projections for the current study equal the lower bound provided by Kharin et al. (2007) for land and is 0.5% lower than the range for 2081-2100. Therefore, while the magnitude of the projected increases is similar, the current study slightly underpredicts the projected global increases by Kharin et al. (2007) for land areas.

Table 4-18. Change in 20-yr Storm from Time Periods 2046-2065 and 2081-2100 Relative to 1981-2000.

	A2		A1B		B1	
	2046-2065	**2081-2100**	**2046-4065**	**2081-2100**	**2046-4065**	**2081-2100**
This Study	4.7%	9.3%	6.3%	13.3%	4.6%	6.4%
Kharin et al. 2007: Land	$10^{14.7}_{5.5}$	$19.5^{33.3}_{11.6}$	$10.3^{16}_{5.9}$	$16.2^{24.3}_{9.8}$	$7.3^{11.1}_{4.6}$	$10.3^{15.1}_{6.9}$
Kharin et al. 2007: NHE	$10.6^{12.2}_{7}$	$21.8^{24.1}_{16}$	$10.6^{13.8}_{8.7}$	$17.9^{22.0}_{13.2}$	$7.7^{10}_{5.8}$	$10.7^{14.3}_{8.1}$

While the global land and northern hemisphere projections provided by Kharin et al. (2007) suggest that the current study underestimates the increase in precipitation with climate change, regional estimates provided by Kharin et al. 2007 shown in Figure 4-42 suggest that the MD-VA-DE region falls within the lower range of the land and northern hemisphere estimates. For example, for the time period 2046-2065, Figure 4-42 suggests a 5-10% increase in the MD-VA-DE region for the A1B scenario while other land areas suggest a 15-20% increase relative to the time period 1981-2000. Likewise, from 2081-2100, Figure 4-43 suggests that the MD-VA-DE region will experience a 10-15%

increase in the 20-yr return period while other land areas will experience a 20-30% increase. Therefore, the lower projections from this study may be the result of regional versus larger scaled estimates relative to the time period 1981-2000.

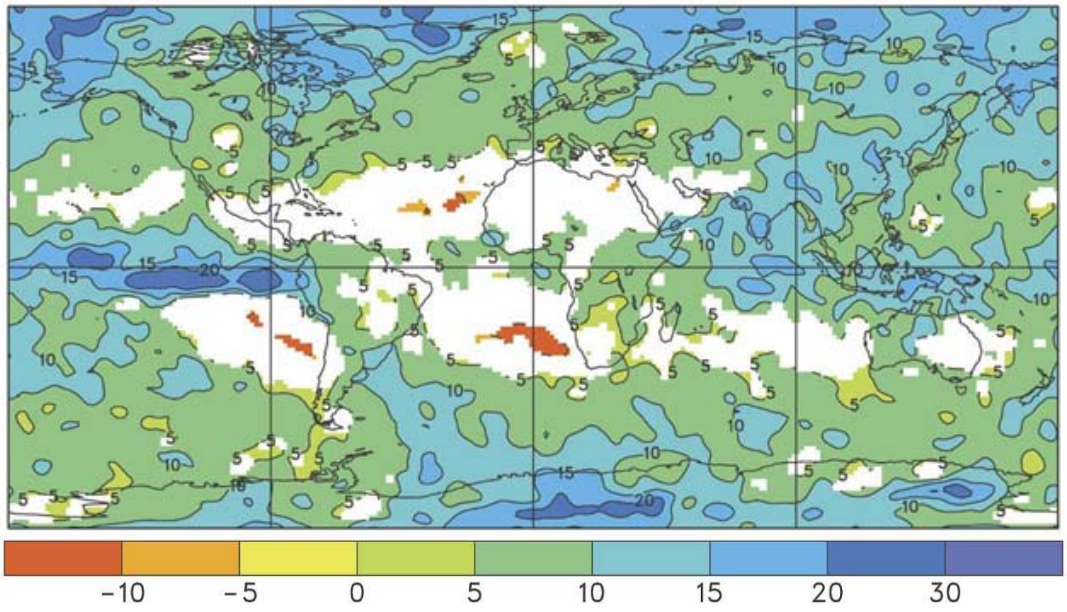

Figure 4-42. Projected Percent Increase in the 20-yr Return Period from 1981-2000 to 2046-2065 provided by Kharin et al. (2007).

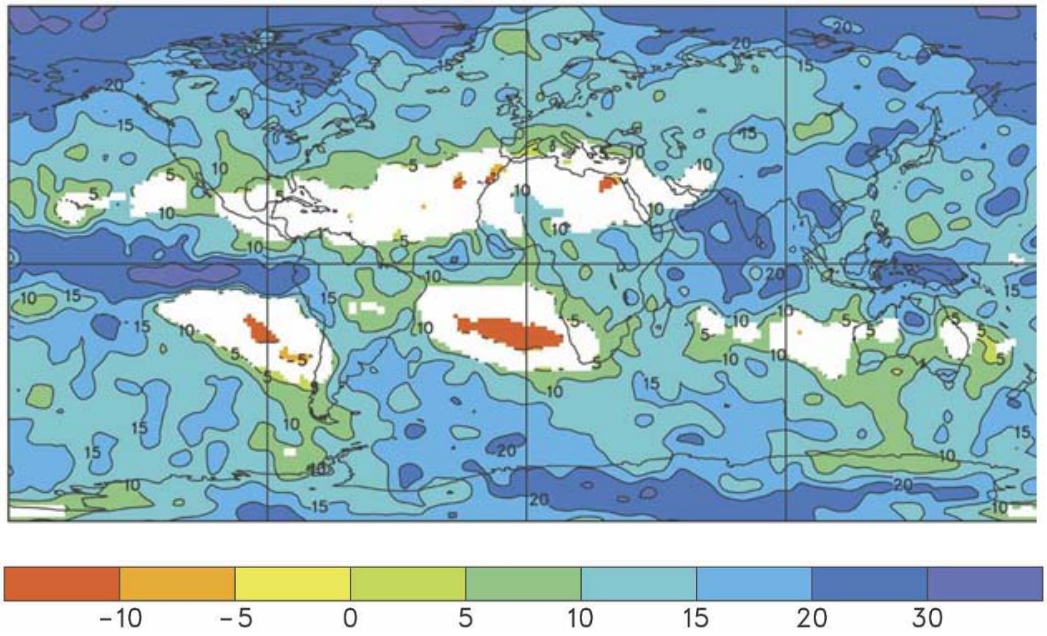

Figure 4-43. Projected Percent Increase in the 20-yr Return Period from 1981-2000 to 2081-2100 provided by Kharin et al. (2007).

The results from this study suggested that the A1B scenario would affect precipitation at a faster rate than the A2 scenario, which differs from the emissions rates for each scenario. Kharin et al. (2007) found that the A1B scenario affected precipitation at a faster rate as well for the 2046-2065. However, the A2 scenario had a greater effect on precipitation from 2081-2100. Therefore, as previously stated, the models developed for this study should not be extrapolated beyond 2100, as the effects of the A2 scenario will most likely eventually surpass those of the A1B scenario. This is the result of the variations inherent to the data used to calibrate the models.

Kharin and Zwiers (2005) estimated the changes in the scale and location parameter based on the same method used in this study, but with 51-yr windows for each parameter. Figures 4-44 and 4-45 show the regional percent change from the year 2000 to 2050 for the A2 scenario. Table 4-19 shows the percent change for the current study in

the scale and shape parameter from 2000 to 2050 for each scenario. Kharin and Zwiers (2005) suggest a 0 to 2% increase in both the scale and location parameter for the A2 scenario in the MD-VA-DE region based on Figures 4-44 and 4-45. The results for the current study suggest a 3% and 4.3% increase for the scale and location parameter, respectively. Therefore, while the magnitude of the increase is the same, the current study provided slightly greater estimated increases in the GEV parameters than Kharin and Zwiers (2005) for the study region. Therefore, while Kharin et al. (2007) provided estimates greater than those found in this study, Kharin and Zwiers (2005) projected slightly lower increases in the GEV parameters than found in this study.

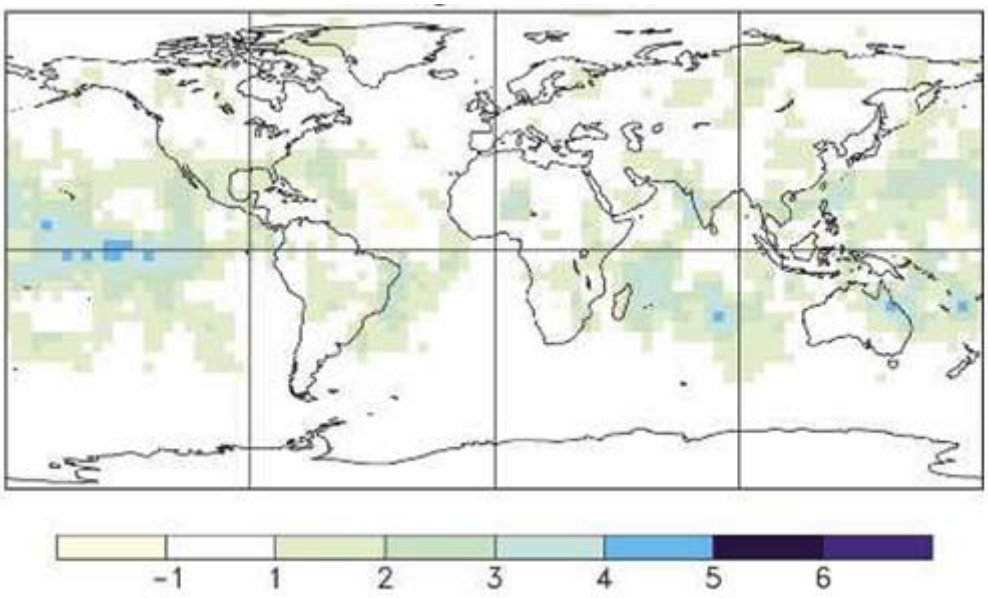

Figure 4-44. Percent Change in Scale Parameter from 2000 to 2050 provided by Kharin and Zwiers (2005).

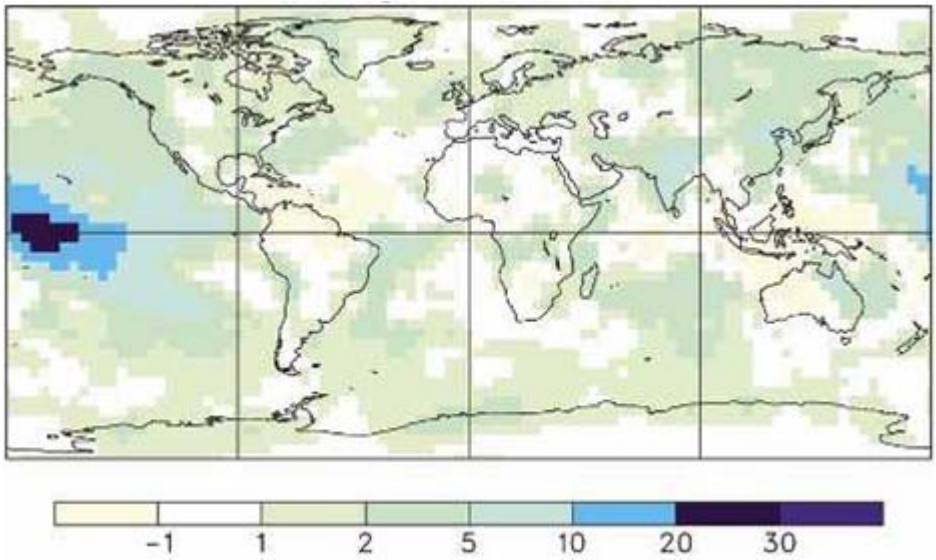

Figure 4-45. Percent Change in Location Parameter from 2000 to 2050 provided by Kharin and Zwiers (2005).

Table 4-19. Change in GEV Scale and Location Parameter from 2000 to 2050 for this Study.

SRES	Scale	Location
A2	3.0%	4.3%
A1B	4.7%	5.1%
B1	4.2%	3.1%

4.4 Rainfall-Runoff Model Selection

With the 24-hour rainfall event adjusted from observed climate conditions to design year climate conditions, the next step was to select a method to convert the rainfall to runoff. To develop a regional adjustment method, the rainfall-runoff model needed to be applicable to a variety of watersheds. The NRCS graphical-peak-discharge method was selected based on the availability of input data and its widely accepted use in hydrology. The NRCS model is a standard approach that uses the same inputs and model structure as currently used in design (Soil Conservation Services 1986).

The selection of appropriate curve numbers and watershed characteristics to be used in applying the NRCS graphical-peak-discharge method was also necessary. The initial approach was to base these factors on the urbanization condition of the watershed during the observation year and the design year; however, after finalizing the urbanization adjustment component which will be explained in Section 4.5, it was determined that rural characteristics would be assigned to the NRCS method variables to maintain consistency in the application regardless of the watershed being analyzed. Then the rural peak discharge estimates will be converted to urbanized values, as explained in Section 4.5.

The curve number selected for rural conditions and soil groups A, B, C, and D equaled 39, 61, 74, and 80, respectively. The land use description selected for rural conditions was good conditions with grass cover on 75% or more of the area (McCuen 2005). Specification of the curve number values enables the simplification of the NRCS graphical-peak-discharge method.

4.4.1 NRCS Graphical Peak- Discharge Method.

The NRCS graphical-peak-discharge method is represented by the following equation provided by McCuen (2005):

$$q_p = q_u * A * Q \qquad \text{Eq. 4-7}$$

where q_p =peak discharge (cfs); q_u = peak unit discharge (cfs/mi^2/in.); A = watershed area (mi^2); and Q = runoff depth (in.).

The unit peak discharge is calculated based on the following equation fit to the NRCS graphical method:

$$\text{Log}(q_u) = C_0 + C_1\log(T_C) + C_2(\log(T_C))^2 \quad \text{Eq. 4-8}$$

where C_0, C_1, and C_2 are coefficients based on the variables I_a/P and shown in Table 4-20 and T_C is the time of concentration (hr).

Table 4-20. TR-55 Coefficients for Unit Peak Discharge Equation for Type II Storm.

P	Ia/P	c0	c1	c2
10.76923	0.1	2.55323	-0.61512	-0.16403
3.589744	0.3	2.46532	-0.62257	-0.11657
3.076923	0.35	2.41896	-0.61594	-0.0882
2.692308	0.4	2.36409	-0.59857	-0.05621
2.393162	0.45	2.29238	-0.57005	-0.02281
2.153846	0.5	2.20282	-0.51599	-0.01259

The method used to calculate the time of concentration (t_c) was dependant on the drainage area of the watershed. For watersheds of 2,000 acres or less, the time of concentration was calculated based on the lag equation:

$$t_c = 0.00526 * L^{0.8} * \left(\frac{1000}{CN} - 9\right)^{0.7} * S^{-0.5} \quad \text{Eq. 4-9}$$

where tc = time of concentration in minutes, L = length of the watershed (ft), CN = the curve number, and S = slope (ft/ft) (McCuen 2005). The length of the watershed for the lag equation is calculated based on the following equation:

$$L = 209*A^{0.60} \quad \text{Eq. 4-10}$$

where L = length (ft) and A = area (acres).

For watersheds with an area greater than 2,000 acres, a method based on hydraulic geometry relationships was developed. The method assumes that the time of concentration refers to all channel flow (i.e., ignores sheetflow). First, the watershed was

divided into subwatersheds and the drainage area and channel length within each subwatershed is calculated. Then, the bankfull discharge (cfs) was estimated based on the following equation derived from Dunne and Leopold (1978):

$$Q = 52*A^{0.829} \quad \text{Eq. 4-11}$$

where Q = bankfull discharges (cfs) and A = area (square miles). Next, the travel velocity is calculated based on the bankfull discharge for each subwatershed and the following equation derived from Dunne and Leopold (1978):

$$V = 0.39 * A^{-0.1634}*Q^{0.44} \quad \text{Eq. 4-12}$$

where V = velocity (ft/s) and A = area (square miles). The travel velocity for the channel within each subwatershed is then divided by the length of the channel segment within the subwatershed. This results in the travel time through each subwatershed. The time of concentration equals the sum of the travel times for each subwatershed.

Finally, the depth of runoff in inches is calculated based on the NRCS rainfall-runoff depth relationship as follows:

$$Q = \frac{(P - 0.2S)^2}{(P + 0.8S)} \quad \text{Eq. 4-13}$$

where $S = I_a / 0.2$ (McCuen 2005).

4.4.2 Simplification of the Peak Unit Discharge Equation

First, the TR-55 coefficient values for the peak unit discharge were graphed and a function was fit to each coefficient based on the Ia/P variable, show in Figures 4-46, 4-47, and 4-48. The curve number values were then substituted into each of the equations to produce four simplified equations, one for each soil group, as a function of only precipitation. The resulting functions for each TR-55 coefficient value are shown in

Table 4-21. It is important to note that these equations must not be extrapolated beyond the Ia/P less than 0.1 or greater than 0.5.

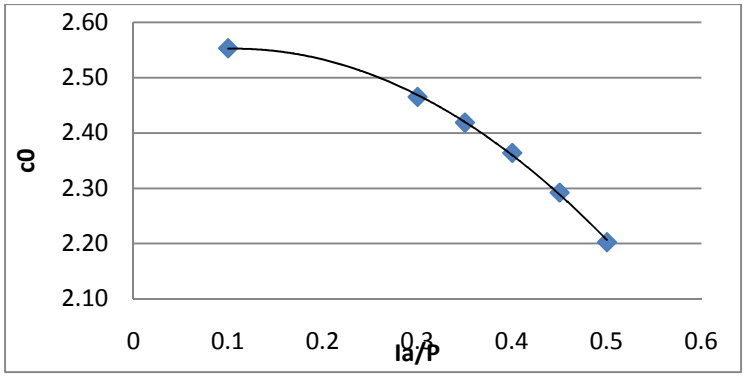

Figure 4-46. C0 as a function of Ia/P.

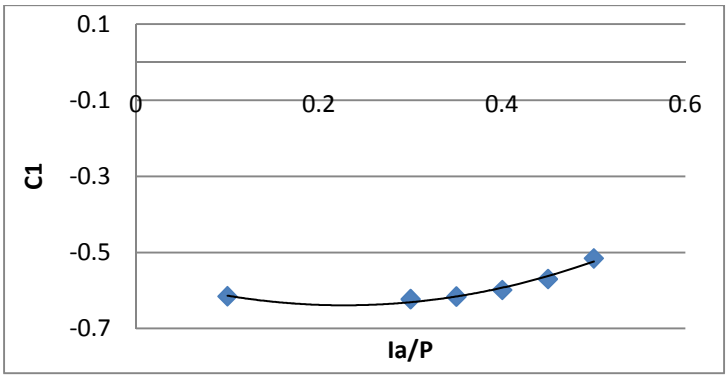

Figure 4-47. C1 as a Function of Ia/P.

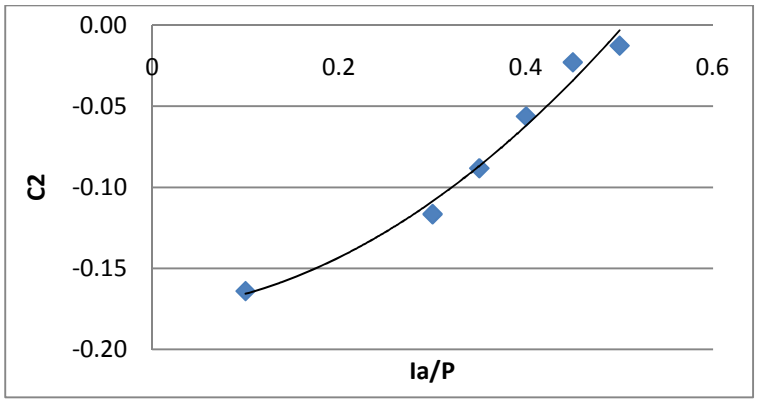

Figure 4-48. C2 as a Function of Ia/P.

Table 4-21. Equations for TR-55 Coefficients for Unit Peak Discharge Equation.

Soil Group	C0	C1	C2
A	-21.861/(P^2) + 1.486/P + 2.527	15.217/(P^2) - 2.215/P -0.558	5.911/(P^2) + 0.135/P - 0.176
B	-3.653/(P^2) + 0.607/P + 2.527	2.542/(P^2) - 0.905/P -0.558	0.988/(P^2) + 0.055/P - 0.176
C	-1.103/(P^2) + 0.334/P + 2.527	0.768/(P^2) - 0.498/P -0.558	0.298/(P^2) + 0.03/P - 0.176
D	-0.559/(P^2) + 0.238/P + 2.527	0.389/(P^2) - 0.354/P -0.558	0.151/(P^2) + 0.022/P - 0.176

The peak unit discharge equation must be solved for the peak unit discharge as follows:

$$q_u = 10^{C0 + C1\log(TC) + C2(\log(TC))2} \quad \text{Eq. 4-14}$$

where C_0, C_1, and C_2 are defined in Table 4-20 and T_C = the time of concentration (hrs).

4.4.3 Simplification of Time of Concentration

For the use in small watersheds, **t**he time of concentration calculation based on the lag equation was converted to hours and then simplified for each soil group through the substitution of the equation for watershed length and the curve number as follows:

$$T_c = C_4 * A^{0.48} * S^{-0.5} \quad \text{Eq. 4-15}$$

where T_C = time of concentration (hrs), A = watershed area (mi^2), S = slope (ft/ft), and C_4 is dependent on soil group and defined in Table 4-22. The simplifications and conversions of the time of concentration equation are shown in Appendix B.

Table 4-22. Soil Group Specific Values for C4 in Time of Concentration Calculations.

Soil Group	C4
A	7.9199
B	4.4884
C	3.1773
D	2.6592

4.4.4 Simplification of the Total Runoff Equation.

The total runoff (Q) can be simplified through the substitution of the curve number for the variable S as follows:

$$Q = \frac{(P - C_5)^2}{P + C_6} \qquad \text{Eq. 4-16}$$

where P equals the 24-hr precipitation depth (in.) and C_5 and C_6 are shown in Table 4-23.

Table 4-23. Coefficient Values for Total Runoff Simplification.

Soil Group	C5	C6
A	3.13	12.51
B	1.28	5.11
C	0.70	2.81
D	0.50	2.00

4.4.5 Final Peak Discharge Equation

Therefore, the final equation for the peak discharge is as follows:

$$q_p = 10^{C0 + C1\log(TC) + C2(\log(TC))2} * A * \frac{(P-C_5)^2}{P+C_6} \qquad \text{Eq. 4-17}$$

with $T_c = C_4 * A^{0.48} * S^{-0.5}$ for small watersheds and based on hydraulic geometry relationships defined by Eqs. 4-11 and 4-12; A = area (mi^2), S = slope (ft/ft), P = 24-hr precipitation (in.), and the coefficients are previously provided. The equation inputs now include only the 24-hr precipitation depth (which is solved for through the climate change adjustment), the watershed area, the watershed slope, and the soil group of the study location.

4.5 Urbanization Adjustment Factor Development

The final component in the adjustment process was to develop a method for the urbanization adjustment of both peak discharge events output by the NRCS method. The peak discharge adjustment method provided by Moglen and Shivers (2006) and discussed in Chapter 2 was selected. Moglen and Shivers (2006) provided seven models varying in both complexity and the input variables. For this study, the Population Density Distribution and Impervious Distribution Models were selected, as they both outperformed the other five models in regards to prediction accuracy and consisted of rational parameter trends. Both models require the input of a rural peak discharge, an urbanization indicator (i.e., percent impervious area or population density), and a measure of the difference between the 10th and 90th percentiles of this indicator within the watershed. Therefore, the final model selection will be determined by the user based on the ease of data collection for the study region.

The model form for each distribution model is as follows:

$$Q_U = \left(\frac{1}{C_{1,T}}\right)^{\frac{1}{C_{2,T}}} * Q_R^{\frac{1}{C_{2,T}}} * (U + 0.001)^{\frac{C_{3,T}}{C_{2,T}}} * (\Delta U + 0.001)^{\frac{-C_{4,T}}{C_{2,T}}} \qquad \text{Eq. 4-18}$$

where Q_u = urban peak discharge (cfs), Q_R = rural peak discharge (cfs), U = urbanization indicator, either impervious area (%) or population density (thousands of people per square mile), and ΔU = the difference between the 10^{th} and 90^{th} percentiles of the urbanization indicator within the watershed.

The coefficients provided by Moglen and Shivers (2006) for each model are based on the return period of each event. Therefore, the model coefficients will differ for each peak discharge record, as each record corresponds to a different return period. Therefore, 'n' sets of USGS coefficients must be calculated based on each of the 'n' return periods. Moglen and Shivers (2006) provide coefficient values for the 2-yr, 5-yr, 10-yr, 25-yr, 50-yr, 100-yr, and 500-yr return periods. Therefore, it was necessary to fit a model to the coefficients as a function of return period in order to make the approach applicable to every return period and, therefore, every peak discharge record in a time series. The coefficients for the urbanization adjustment component for the impervious and the population density distribution models based on Moglen and Shivers (2006) as a function of return period are shown in Table 4-24 and 4-25, respectively, along with the coefficient of determination.

Table 4-24. Urban Peak Discharge Equation Coefficient Values for the Impervious Distribution Model as a Function of Return Period (T).

Coefficient	Value	R^2
C1	y = 0.437T^-0.0649	0.9967
C2	1.1	NA
C3	y = 0.3036x^T-0.4415	0.8614
C4	y = 0.0259T^0.1994	0.9702

Table 4-25. Urban Peak Discharge Equation Coefficient Values for the Population Density Distribution Model as a Function of Return Period (T).

Coefficient	Value	R^2
C1	$0.2831*T^{0.0307}$	0.9993
C2	1.1	NA
C3	$0.1670*T^{-0.0079}$	0.9985
C4	$0.0628*T^{0.0961}$	0.9935

4.6 Summary of Adjustment Factor Development

This new adjustment method is a combination of both theoretical and empirical analyses. It is based on a climate indicator (i.e., precipitation and the driving force, GHG emissions), a hydrologic indicator (i.e., peak discharge), and an urbanization indicator (i.e., percent impervious area or population density) as inputs. The method is as accurate as the GCM outputs, NRCS method, and USGS method can be. Also, the input requirements are minimal and available through USGS, NOAA, and census data or GIS maps. The new adjustment factor method reflects the change in peak discharge based on both urbanization and climate change.

4.7 Application of Adjustment Factor

With the adjustment method for nonstationarity developed, the next step was to apply the method and adjust a peak discharge series to design year climate change and urbanization conditions. The application of the adjustment factor, which includes the location selection, input data retrieval, scenario development, and adjustment of peak discharge records, will be discussed herein.

4.7.1 Selection of Location

The first step in the application of the adjustment method was to select a study location within the MD-VA-DE region for which the adjustment method was developed.

The most important criteria for the study location were that the rain and discharge gauges within the location were no more than a reasonable distance apart and the precipitation and discharge records provided 50 or more overlapping years of data. Additionally, daily precipitation was required in order to extract each 24-hr precipitation event that coincided with the recorded peak discharge event.

Based on these criteria, the watershed outlet located at Guilford, Maryland, was selected along with the rain gauge in Laurel, Maryland. The rain gauge is identified by NOAA as COOPID 185111 and located at the coordinates 39°05'N and 76°54'W. The watershed outlet is identified as USGS gauge 01593500 Little Patuxent River at Guilford, Maryland, and located at the coordinates 39°10'03.9"N and 76°51'04.5"W. The distance between the rain and discharge gauge is 6.4 miles. The records consisted of 64 years in which both daily rainfall and peak discharge data were available.

The Guilford, Maryland, discharge gauge is located in Howard County, Maryland, on the Little Patuxent River, which is a tributary to the Patuxent River and, therefore, the Chesapeake Bay. Figure 4-49 shows the delineated watershed as well as the stream network within Howard County and the watershed. The drainage area equals 38 square miles. The Guilford watershed is a subwatershed within the Little Patuxent River Watershed, which is 51 square miles and is made up of a variety of land uses including residential, parks, open space, institutional, commercial, industrial, and agricultural (Morales and Saltzman 2002).

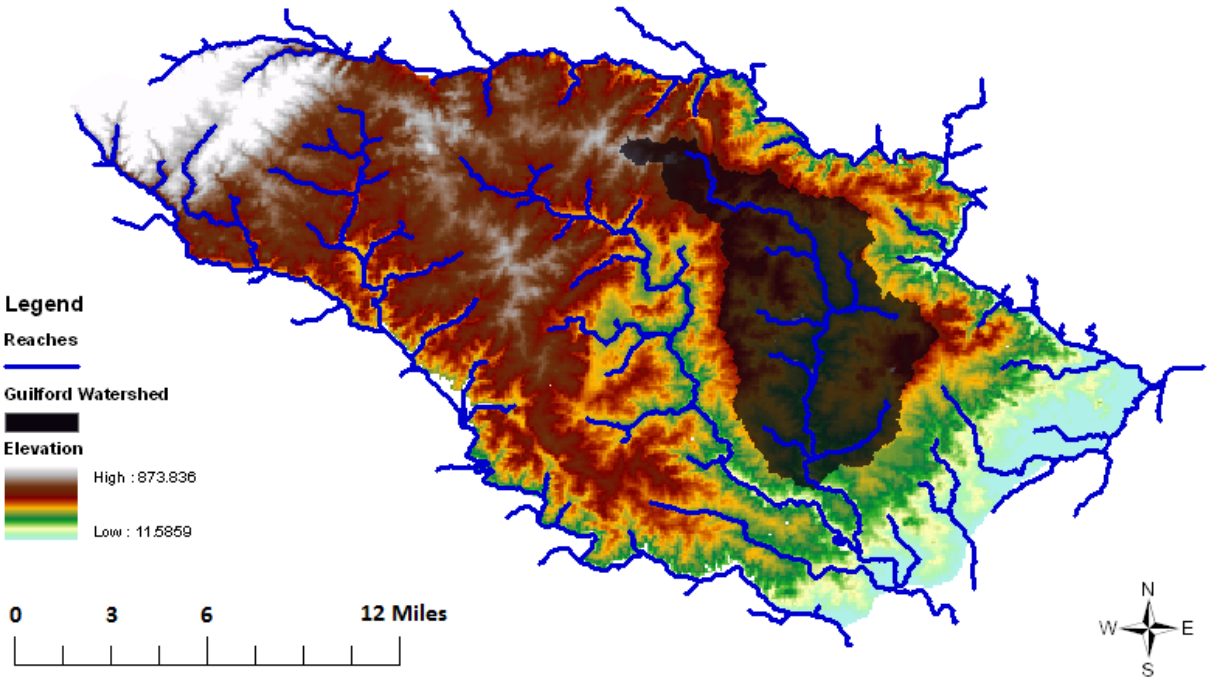

Figure 4-49. Stream Networks within Howard County and Guilford Watershed.

4.7.2 Adjustment Method Inputs

Application of the adjustment factor requires retrieval of the following data for the selected study location:

- Time series of annual peak discharge(cfs) over time period, Qp
- Vector of return periods associated with peak discharge events based on the Log Pearson III distribution (T);
- Time series of 24-hour rainfall depth (in.) associated with each annual peak discharge, P;

- Urbanization indicator over time period (i.e., impervious area or population density), U;
- Area (A) (mi^2) of the watershed.

The annual peak discharge data for stream gauges are available online through USGS. Likewise, the area of the watershed is available through USGS. The rainfall data for gauges are available through NOAA. The population density can be retrieved through GeoLytics (2003) or 2000 census data is provided by www.esri.com. Data can also be retrieved through state planning websites and census reports. The urbanization and climate change indicators would ideally span the length of the discharge and rainfall data. Missing values should be interpolated in a manner that best fits the data.

4.7.2.1 Retrieval of Precipitation and Discharge Data.

The precipitation and discharge data were retrieved first to ensure that despite the distance between the gauges, the data records were correlated. The annual peak discharge was retrieved from the USGS gauge01593500 Little Patuxent River at Guilford, Maryland. Daily precipitation data were retrieved from the NOAA rain gauge COOPID 185111 in Laurel, Maryland. Next, the date on which each annual peak discharge occurred was stored and the corresponding 24-hr precipitation event was retrieved. The peak discharge and corresponding precipitation records are shown in Figure 4-50.

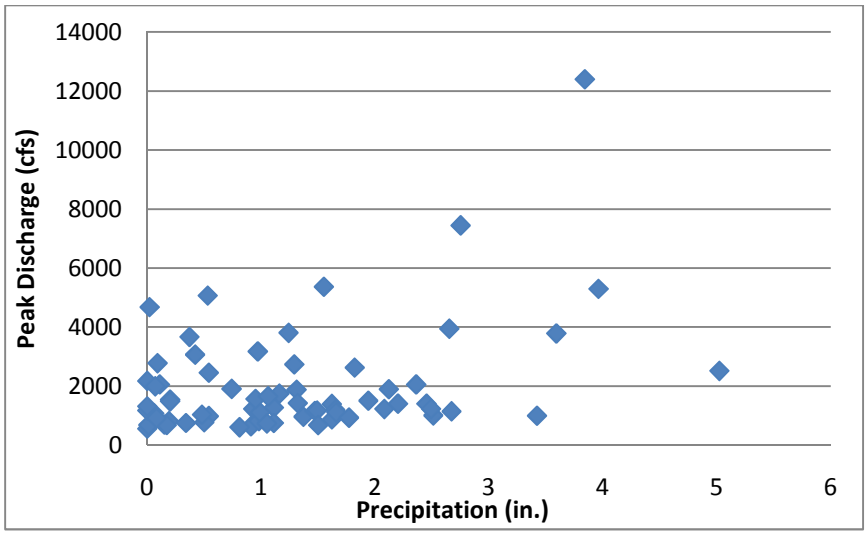

Figure 4-50. Annual Max Peak Discharge and Precipitation based on Precipitation Occurring on Day of Peak for Guilford, Maryland.

The coefficient of determination equaled 0.14, which suggests that 14percent of the variation in the peak discharge data is explained by the precipitation data. However, it is apparent that a few peak discharge events correspond to zero precipitation. This suggested that precipitation from preceding days may have caused the peak discharge event. Therefore, the 24-hr precipitation was retrieved both on the day of each peak discharge event and the day before each peak discharge event. The maximum precipitation depth between these two days was then stored and plotted versus the peak discharge event. An additional analysis was conducted to include the precipitation depth two days before the peak discharge event as well. The results for both analyses are shown in Figures 4-51 and 4-52. It is apparent from the graphs that include preceding day in the analysis eliminates the issue in which peak discharge events correspond to zero precipitation events. The coefficient of determination for the analysis that consisted of the day of the peak and the day before the peak equaled 0.19, which suggests that 19 percent of the variation in the peak discharge data is explained by the corresponding

precipitation data. The coefficient of determination for the analysis that added precipitation from two days before the peak equaled 0.20which suggests that 20 percent of the variation in the peak discharge data is explained by the corresponding precipitation data. The two-day analysis provides the greatest coefficient of determination. Therefore, the precipitation data based on two-day analysis was selected for the analysis. All of these have statistical rejection probabilities smaller than 0.0005, which indicate they are statistically significant.

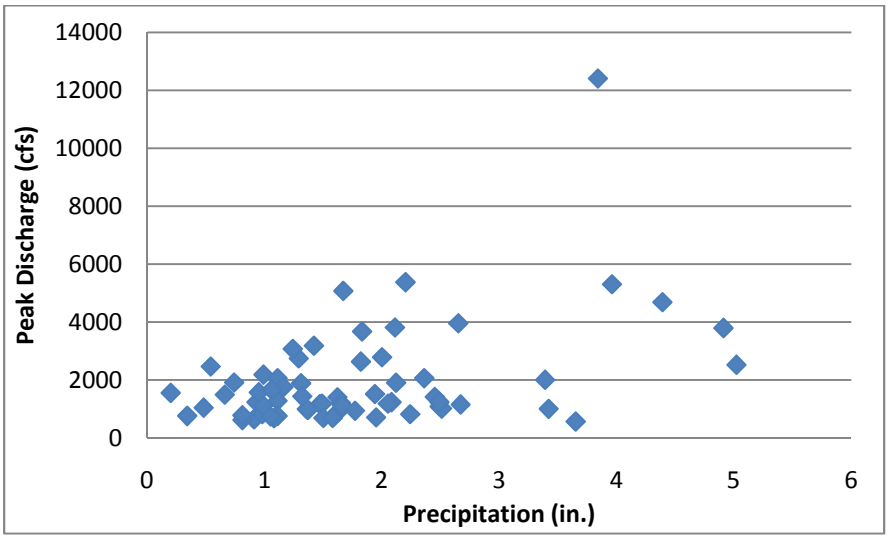

Figure 4-51. Annual Max Peak Discharge and Precipitation based on Maximum Precipitation Occurring within One Day Before or Day of Peak for Guilford, Maryland.

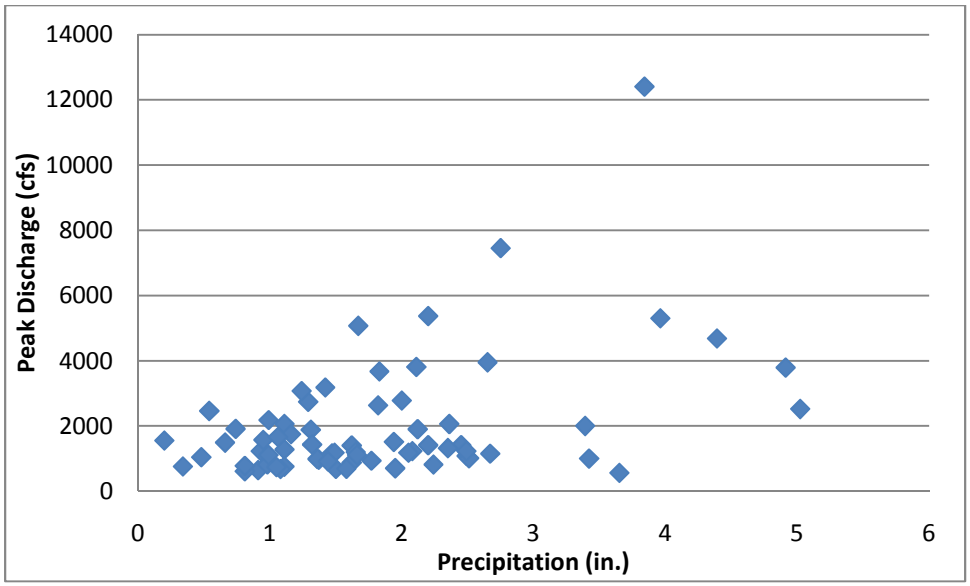

Figure 4-52. Annual Max Peak Discharge and Precipitation based on Maximum Precipitation Occurring within Two Days Before or Day of Peak for Guilford, Maryland.

4.7.2.2 Inputs for Urbanization Adjustment Component.

As previously explained in Section 4.5, the USGS equations developed to adjust rural peak discharge values to urbanized peak discharge values require either a measurement of urbanization or population density within the watershed. For this study, the population density input was selected based on data availability. The necessary input values include the average population density for the watershed as well as the difference in the population density between the 10th and 90th percentiles of the distribution of population density in the watershed. These input values were calculated for the year 2000 in GIS and based on census data retrieved from www.esri.com.

4.7.2.2.1 Calculation of Population Density Variable

To calculate population density within the watershed, the census tracts and census data from the 2000 census for Howard County, Maryland, were retrieved from www.esri.com. Then, the delineated watershed at Guilford, Maryland, and the Howard

County Census tracts are shown in Figure 4-53. The census tracts within the watershed were extracted as shown in Figure 4-54. This provided the necessary information to calculate the mean population density and difference between the 10th and 90th percentiles within the study watershed.

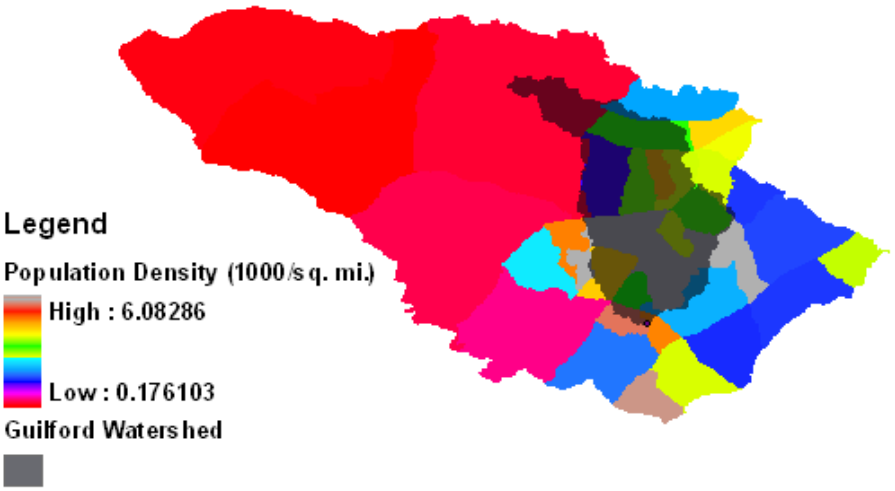

Figure 4-53. Guilford Watershed Overlaying Howard County Population Density Map (1000 people/square mile).

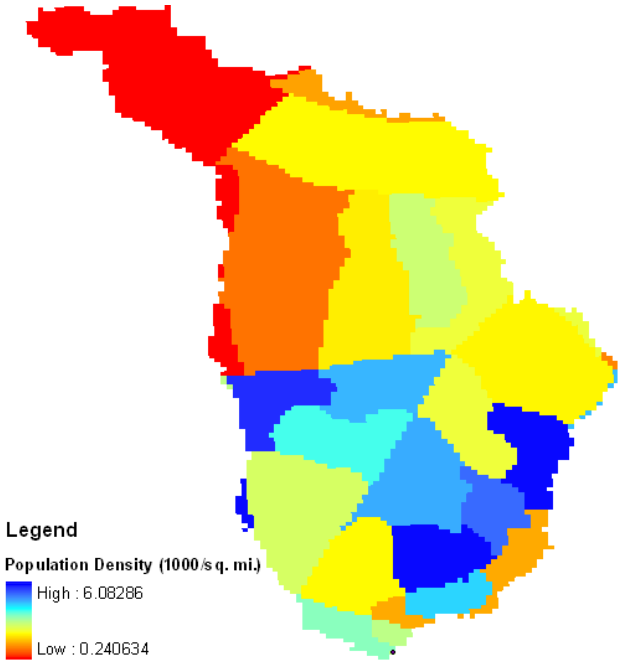

Figure 4-54. Population Density (1000 people/ mi2) within Guilford Watershed in Howard County.

The mean population density was calculated through the spatial mean equation as follows:

$$\text{Spatial Mean} = \frac{\sum_{i=1}^{n} A_i * PD_i}{\sum_{i=1}^{n} A_i} \qquad \text{Eq. 4-19}$$

where n = the total number of census tracts in the watershed; i = specifies the census tract; A_i = area allocated to census tract '*i*'; and PD_i = population density within census tract '*i*'. The average population density within the Guilford watershed equaled 2.33 (1000 people/sq. mi).

Next, the difference between the 10th and 90th percentiles of the distribution of population density within the watershed was calculated. The population density for each census tract was plotted against fraction of the total area within the watershed, shown in Figure 4-55. The 10th and 90th percentiles from this graph were calculated. The final

inputs into the urbanization adjustment component for the conditions in the year 2000 are shown in Table 4-26.

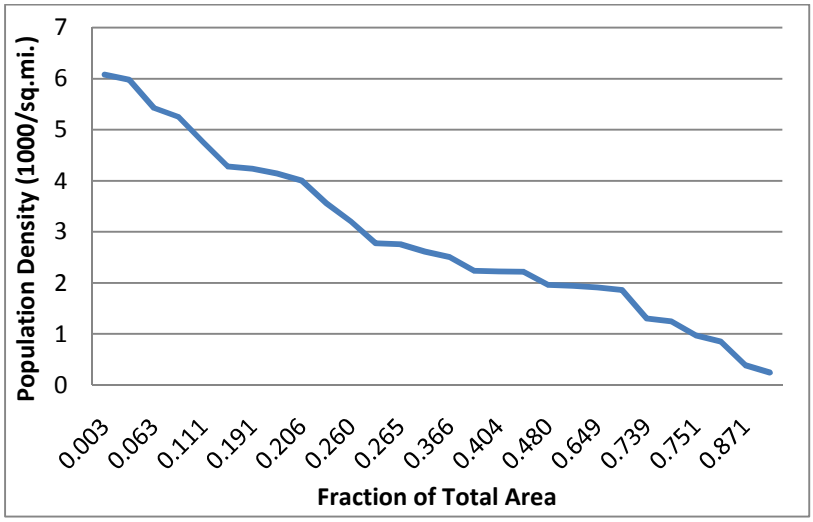

Figure 4-55. Distribution of population density as a fraction of the total watershed area for U.S. Geological Survey Streamgage1593500, Patuxent River at Guilford, Maryland.

Table 4-26. Population Density Statistics for USGS Equations for 2000 Census Data for Guilford Watershed in Howard County.

90th Percentile	**0.27**
10th Percentile	**4.98**
Average Pop. Dens	**2.33**

The inputs were developed for the year 2000; however, to conduct a complete analysis, urbanization criteria must be developed from the start year of the peak discharge record to the final design year of interest. For this study, the year 2100 was selected as the final design year. Census data are not available through www.esri.com for years other than 1990 and 2000; however, the Maryland Department of Planning provides total population values for Howard County from 1970 to 2000 and projections of the total

population from 2005 to 2040 (Maryland 2009). Additionally, the total population for Howard County in 1950 and 1960 were retrieved from the 1960 Census (US Department 1961) and 1930 and 1940 from the 1940 Census (Treusdell 1942).

The assumption was made that the ratio of population density to total population in 2000 would be consistent throughout the 20th and 21st century. Therefore, this ratio was multiplied by the total population recorded or projected within each decade from 1930 to 2040 to estimate the population density during the respective decade. The results are shown in Figure 4-56. The same method was repeated to estimate the 10th and 90th percentiles of the distribution of population density as a fraction of the total watershed area. The results are shown in Table 4-27.

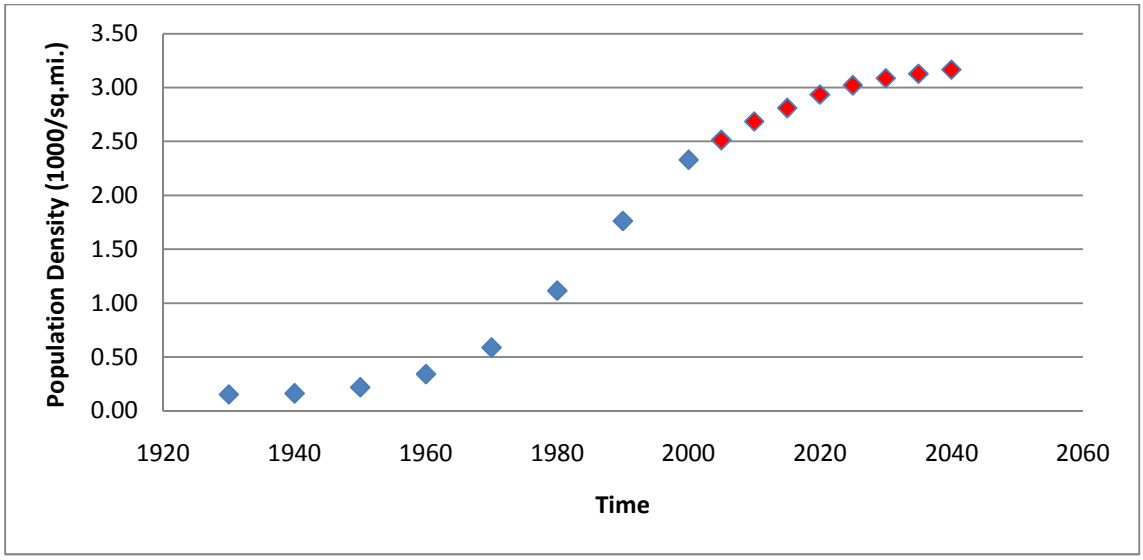

Figure 4-56. Population Density Based on the Total Population Observed from 1930 to 2000 (Shown in Blue) and Projected from 2005 to 2040 (Shown in Red).

Table 4-27. Total Population and Estimated Population Density, 10th, and 90th Percentile based on the Observed 2000 Values for Howard County.

Year	Howard County	Average Pop. Dens	10th Percentile	90th Percentile

Year	Howard County	Average Pop. Dens	10th Percentile	90th Percentile
1930	16,169	0.15	0.33	0.02
1940	17,175	0.16	0.35	0.02
1950	23,174	0.22	0.47	0.03
1960	36,152	0.34	0.73	0.04
1970	62,394	0.59	1.25	0.07
1980	118,572	1.11	2.38	0.13
1990	187,328	1.76	3.77	0.21
2000	**247,842**	**2.33**	**4.98**	**0.27**
2005	267,200	2.51	5.37	0.29
2010	285,600	2.68	5.74	0.32
2015	298,800	2.81	6.01	0.33
2020	312,200	2.94	6.28	0.34
2025	321,200	3.02	6.46	0.35
2030	328,200	3.09	6.60	0.36
2035	332,800	3.13	6.69	0.37
2040	336,800	3.17	6.77	0.37

4.7.2.2.2 Statistical Models for Population Density

Functions were then fitted to the population density and the difference between the 10th and 90th percentile data sets in order retrieve values for any year within the time series. The functions were then extrapolated to the year 2100. A composite model based on the following functional form was fitted to the population density data set:

$$PD = C_1 + C_2*x + C_3*x^2 \quad \text{for } x<=X_C \quad \text{Eq. 4-20}$$

$$PD = C_5 + C_6*(1-e^{-C4x}) \quad \text{for } x>X_C \quad \text{Eq. 4-21}$$

where PD = population density (1000 people/square mile); x = year – 1920; X_c equals 82; C_1, C_2,C_3, and C_4 are defined in Table 4-28; and C_6 and C_5 are defined based on the following equations:

$$C_6 = \frac{C2 + 2*C3*Xc)}{C4*e^{-C4*Xc}} \quad \text{Eq. 4-22}$$

$$C_5 = C_1 + C_2*X_c + C_3*X_c^2 - C_6*(1- e^{-C4*Xc}) \quad \text{Eq. 4-23.}$$

The coefficients C_5 and C_6 are used to provide continuity of magnitude and slope of the two functions (Eq. 4-20 and 4-21) at the intersection time X_C. A composite model was selected with the intention to develop a second urbanization scenario for comparison. This would require identical models in the twentieth century for both models to ensure an accurate comparison of the changes in the twenty-first century relative to the urbanization in the twentieth century.

Table 4-28. Calibrated Coefficient Values for the Population Density Scenario 1 Function.

C_1	0.1
C_2	-0.00695
C_3	0.000425
C_4	0.075
X_c	82

The fitted population density function for Scenario 1 is shown in Figure 4-57. The goodness-of-fit statistics are shown in Table 4-29. The ratio of the standard error to the standard deviation equaled 0.087, which suggests that the model is a significant improvement over the mean for data predictions. The coefficient of determination equaled 0.995, which suggests that 99.5% of the variation in the data is explained by the model. The relative bias is positive and near zero. The slightly positive bias is the result of the high level of curvature in the data set.

To demonstrate the effect of nonstationarity due to urbanization, two projected scenarios were going to be used. However, both sequences would use the same

twentieth-century data, as this data were known. Therefore, the composite model was used to represent the data. The composite model ensured that both scenarios would have an identical data for the twentieth century. In order to satisfy the constraints required for the composite model and provide the level of curvature in the data set, calibration of additional coefficients would be required. This would increase the degrees of freedom and, therefore, lower the goodness-of-fit of the model given the small sample size of population density data. The slight bias in the model was acceptable for a composite model that would ensure an accurate comparison between Scenario 1 and an additional population density scenario.

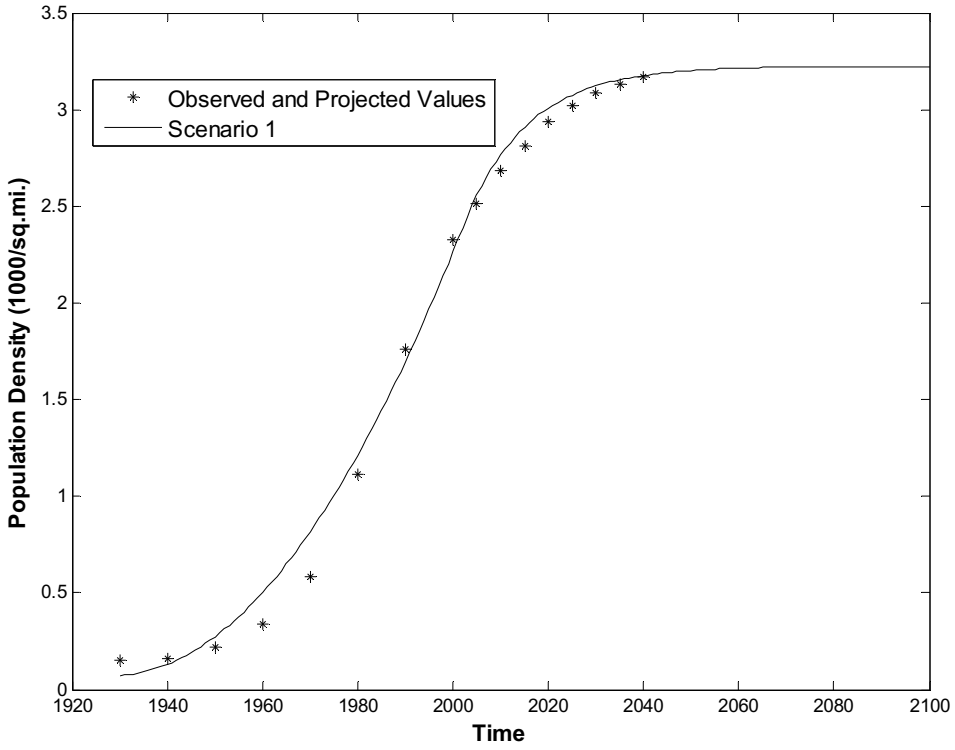

Figure 4-57. Population Density within the Watershed over Time for Scenario 1.

Table 4-29. Goodness-of-Fit Statistics for Population Density Models for Scenario 1 where Se = Standard Error of Estimate; Se/Sy = Standard Error Ratio; e = Mean Bias; e/y = Relative Bias; R2 = Coefficient of Determination.

Data Set	S_e	S_e/S_y	e	e/y	R^2
Population Density: Scenario 1	0.106	0.087	0.046	0.024	0.995

A second population density scenario was then developed based on the model fitted to the Maryland State Planning projections. The extrapolated value at the year 2100 was calculated and then increased by 50%. The same model form was then fitted so that the population density was 50% greater in the year 2100. The calibrated values for coefficients C_1, C_2, C_3, and C_4 for Scenario 2 are defined in Table 4-30. The final composite models for population density Scenarios 1 and 2 are shown in Figure 4-58.

Table 4-30. Calibrated Coefficient Values for the Population Density Scenario 2 Function.

C_1	0.1
C_2	-0.00695
C_3	0.000425
C_4	0.025
X_c	82

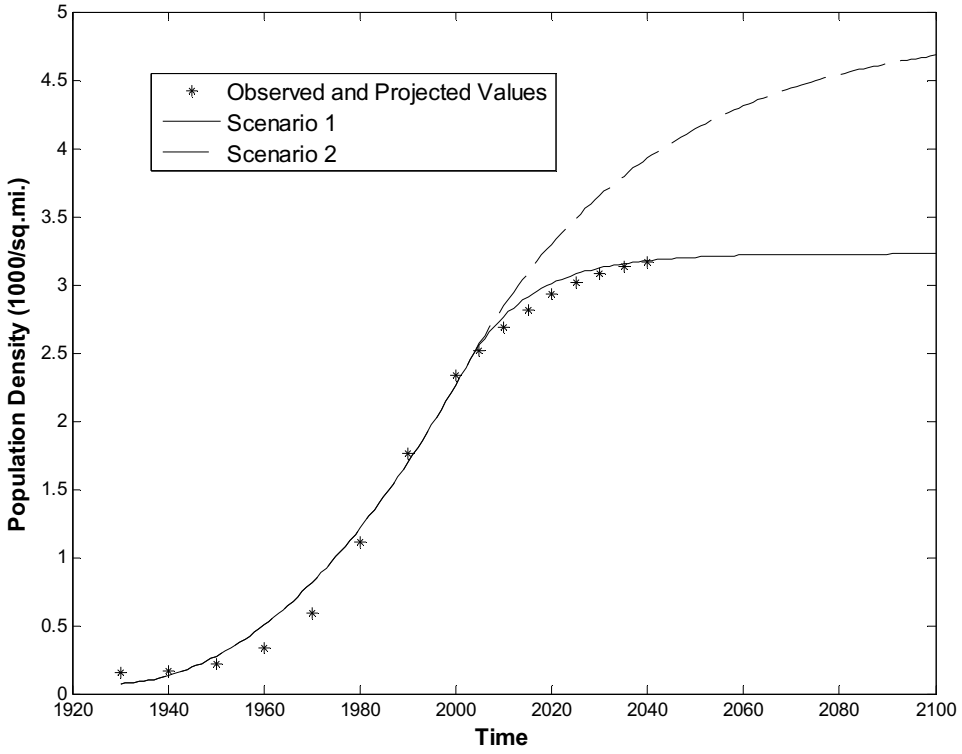

Figure 4-58. Population Density within Watershed over Time for Scenarios 1 and 2.

Statistical models were fitted to the 10th and 90th percentiles of the population density within the watershed. For Scenario 1, this data set was derived based on the ratio of the value in the year 2000 to the total population for each decade from 1930 to 2040, as shown in Table 4-27. For Scenario 2, the difference between the 10th and 90th percentiles of the population density within the watershed is equivalent to Scenario 1 for the twentieth century. The projections from 2000 to 2040 for Scenario 2 were determined based on the ratio between the difference in the percentiles in the year 2000 and the population density in the year 2000. This ratio was multiplied by the population density projected for Scenario 2 from the year 2000 to 2040 to project the respective

difference between the 10^{th} and 90^{th} percentiles of the population density within the watershed for these years.

The data sets were fitted to the same composite model used for the population density models and provided in Eqs. 4-20 and 4-21. The fitted coefficients, C_1, C_2, C3, and C_4, for Scenarios 1 and 2 are shown in Table 4-31. The final models are shown in Figure 4-59 for Scenarios 1 and 2 and the goodness-of-fit statistics are shown in Table 4-32. The ratio between the standard error of estimate and standard deviation equaled 0.115 and 0.089 for the Scenarios 1 and 2 models, respectively. This suggests that the models provide very accurate representation of the actual data. Likewise, the coefficient of determination equaled 0.959 and 0.921 for the models for Scenarios 1 and 2, respectively. This suggests that 95.9% and 92.1% of the variation in the data were explained by the models for Scenarios 1 and 2, respectively.

The relative bias for both models is positive but essentially zero. The positive bias is apparent in Figure 4-59 as the model overestimates the data in the middle of the twentieth century and the beginning of the twenty-first century for the first scenario. As with the population density models, this positive bias is due to the high degree of curvature within the data set. In order to satisfy the constraints required for the composite model and provide the level of curvature in the data set, calibration of additional coefficients would be necessary for a model. This would decrease the degrees of freedom and lower the goodness-of-fit of the model. Therefore, it was determined that the small bias in the models was acceptable in order to provide a composite model that would ensure an accurate comparison between the results of the two scenarios.

Table 4-31. Calibrated Coefficient Values for Models of the Difference between the 10th and 90th Percentiles of Population Density within the Watershed for Scenarios 1 and 2.

Coefficient	Scenario 1	Scenario 2
C_1	0.25	0.25
C_2	-0.009	-0.009
C_3	0.0008	0.0008
C_4	0.0745	0.025
X_c	82	82

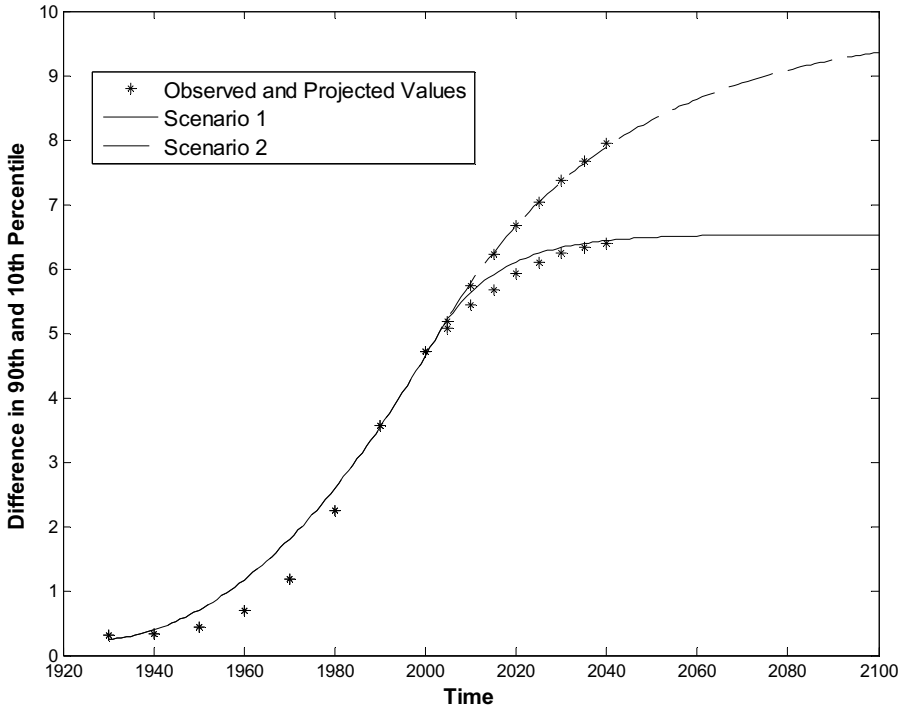

Figure 4-59. Difference between the 10th and 90th Percentiles of Population Density within the Watershed over Timefor Scenarios 1 and 2.

Table 4-32. Goodness-of-Fit for Models of Difference between the 10th and 90th Percentiles of Population Density for Scenarios 1 and 2 where Se = Standard Error of Estimate; Se/Sy = Standard Error Ratio; e = Mean Bias; e/y = Relative Bias; R2 = Coefficient of Determination

Data Set	S_e	S_e/S_y	e	e/y	R^2
Difference in Percentiles: Scenario 1	0.284	0.115	0.167	0.044	0.959
Difference in Percentiles: Scenario 2	0.259	0.089	0.099	0.024	0.921

4.7.2.2.3 Calculating Time of Concentration.

Two methods for the calculation of the time of concentration were proposed in Section 4.4.1. The NRCS method was proposed for watersheds with a drainage area less than 2,000 acres. The Guilford watershed has a drainage area equal to 39 square miles or roughly 25,000 acres. Therefore, the method based on hydraulic geometry relationships was selected for the application to the Guilford watershed.

First, the watershed was divided into five sections based on the length of the main channel within the watershed. The subwatersheds are shown in Figure 4-60. Then, the length of the channel in each subwatershed as well as the drainage area of each subwatershed were calculated. The bankfull discharge at the downstream point of each subwatershed was calculated based on Eq. 4-11. Then, the travel velocity within the channel for each subwatershed was calculated based on Eq. 4-12. Finally, the length was divided by the velocity of the channel within each subwatershed to calculate the travel time through each subwatershed. The calculations are shown in Table 4-33. The individual travel times were summed to determine the time of concentration of the watershed. The time of concentration was estimated to be 26,777 seconds or 7.44 hours.

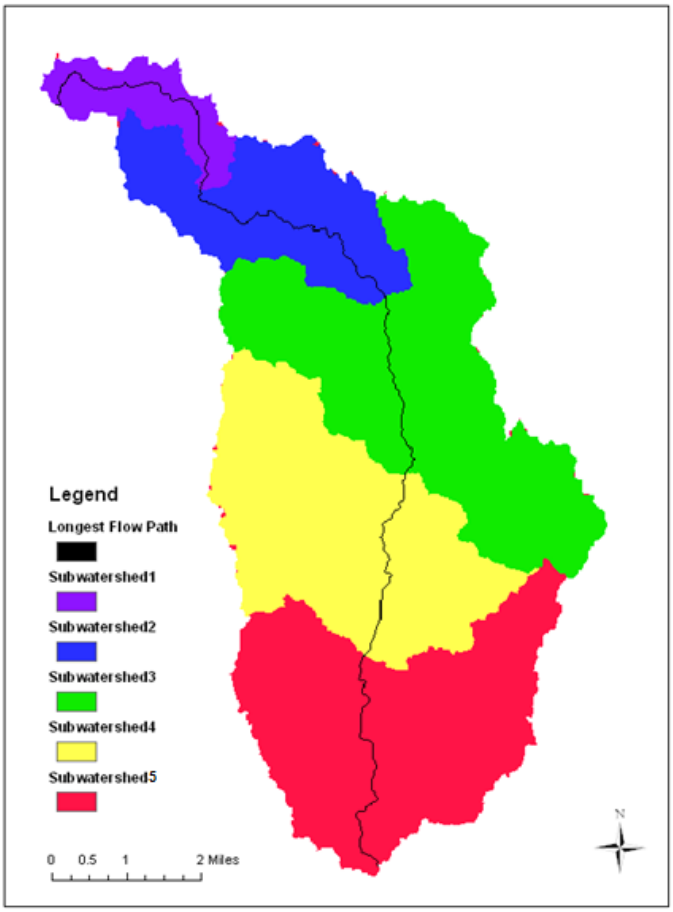

Figure 4-60. Subwatersheds for Time of Concentration Calculation for Flowpath.

Table 4-33. Time of Concentration Calculations.

Channel Section	Contributing Area (mi^2)	Individual Flow Path Length (ft)	Bankfull Discharge (cfs)	Velocity (ft/sec)	Travel Time (s)
1	1.976	21972.57	91.46	2.54	8634.06
2	7.083	21175.00	263.53	3.29	6434.54
3	18.048	15085.76	572.25	3.97	3797.23
4	27.616	15865.12	814.19	4.33	3665.60
5	37.894	19584.06	1058.37	4.61	4245.57

4.7.3 Summary of Final Adjustment Scenarios

Based on the available emissions scenarios and population density data, six scenarios were developed for adjustments of peak discharge records. Three climate change scenarios have already been explained based on emissions scenarios and identified as SRES A2, A1B, and B1 (See Chapter 2 for more details). Two urbanization scenarios were developed based on the rate of increase of population density within the watershed. Table 4-34 shows the six combinations of the three climate change and two urbanization scenarios and the notation that will be used to refer to each scenario.

Table 4-34. Analysis Scenarios.

	Urbanization Scenario	
Climate Change Scenario	**1**	**2**
A2	A2:1	A2:2
A1B	A1B:1	A1B:2
B1	B1:1	B2:2

4.7.4 Application of Climate Change Adjustment Method.

Given the calculated input variables, the adjustment process of the observed peak discharge record can be applied. The process requires the individual adjustment of each observed peak discharge. The adjustment procedure can be conducted as two parts: (1) climate change and (2) urbanization. Within the explanation of the adjustment method, the term observation year refers to the year in which the peak discharge event to be adjusted occurred and the term design year refers to the year to which the event is being adjusted. The adjustment method can be applied for any design year from the present to the year 2100. The design year is constrained only by the time period for which the adjustment method was developed, particularly for the climate change component.

As shown in the method development, the adjustment methods for climate change and urbanization are dependent on return period. Therefore, the return period must be calculated for the observed peak discharge record based on the Weibull plotting position formula distribution. The assumption was made that the return periods for the peak discharge record and the associated 24-hr rainfall record are the same. Then, the adjustments based on climate change conditions are conducted.

For the climate change component, the effect of climate change is modeled using the change in precipitation that would result due to an increase in the climate change indicator, the greenhouse gas emissions scenario. Therefore, the each 24-hour rainfall record is adjusted based on the projected change in rainfall for the design year selected. The precipitation GEV distribution parameters based on the observation year emissions rates and the design year emissions rates are determined (See Section 4.3.5for further clarification). Then, based on the return period of the record, the expected 24-hour rainfall event can be determined for the observation year as well as the design year. The ratio of the expected 24-hr rainfall depth for the observation year and the design year is then multiplied by the actual observed rainfall depth (P_1) to calculate the adjusted 24-hour rainfall event for the design year (P_2). Therefore, two different 24-hour rainfall depths associated with the return period of interest exist: (1) the actual (P_1) and (2) the projected based on climate change in the design year (P_2). This step is repeated for each 24-hr precipitation record based on the respective return period.

Next, each 24- hour rainfall depth, $P_1$and P_2, is converted to a peak discharge (cfs) based on natural conditions. Each rainfall depth is individually input into the SCS method to calculate the resulting peak discharge, Q_p (cfs):

$$Q_p = 10^{C0 + C1\log(TC) + C2(\log(TC))2} * A * \frac{(P-C_5)^2}{(P+C_6)} \quad \text{Eq. 4-24}$$

where T_c = time of concentration (hours), A = area (mi^2), P = 24-hr precipitation (in.), and the coefficients are provided in Section 4.4.1. Therefore, two natural condition peak discharge rates for the return period of interest are calculated: (1) the current climate condition (Q_{P1}) and (2) the future climate condition (Q_{P2}). It is important to note that both peak discharge rates are for natural watershed conditions, not the actual or projected urbanized conditions of the watershed. This ensures that the peak discharge rates for both climate conditions are applicable as input into the USGS urbanization adjustment component.

The USGS urbanization equations convert a peak discharge from a rural watershed to a peak discharge from the same watershed under urbanized conditions. Therefore, Q_{P1} is adjusted to the observation year urbanization conditions and Q_{P2} is adjusted to projected urbanization conditions for the design year based on the following equation (Moglen and Shivers 2006):

$$Q_U = \left(\frac{1}{C_{1,T}}\right)^{\frac{1}{C_{2,T}}} * Q_{Pi}^{\frac{1}{C_{2,T}}} * (PD + 0.001)^{\frac{C_{3,T}}{C_{2,T}}} * (\Delta PD + 0.001)^{\frac{-C_{4,T}}{C_{2,T}}} \quad \text{Eq. 4-25}$$

where '*i*' corresponds to either the observation year or design year, C_1, C_2, C_3,, and C_4,are the USGS coefficients previously calculated for each return period, T corresponds to the return period, 'PD' is the population density for the watershed, and 'PD' represents the difference in the population density between the 10th and 90th percentiles of the distribution of population density in the watershed. The final adjustment factor is the quotient of the urbanized design year peak discharge, Q_{P1}, and the urbanized observed

year peak discharge, Q_{P2}. This final adjustment factor is multiplied by the observed peak discharge value to determine the peak discharge adjusted for future climate change and urbanization conditions. These steps are repeated for each recorded peak discharge value.

4.8 Adjustment Results

The observed peak discharge time series is shown in Figure 4-61 for the Guilford, Maryland, gauge. The data range from 1940 to 2009. Each observed peak discharge was adjusted to urbanization and climate change conditions for design years 2025, 2050, 2075, and 2100 based on the six different scenarios developed: (1) Emissions Scenario A2 and Urbanization Scenario 1; (2) Emissions Scenario A2 and Urbanization Scenario 2; (3) Emissions Scenario A1B and Urbanization Scenario 1; (4) Emissions Scenario A1B and Urbanization Scenario 2; (5) Emissions Scenario B1 and Urbanization Scenario 1; (6) Emissions Scenario B1 and Urbanization Scenario 2. The results of these adjustments will be discussed herein.

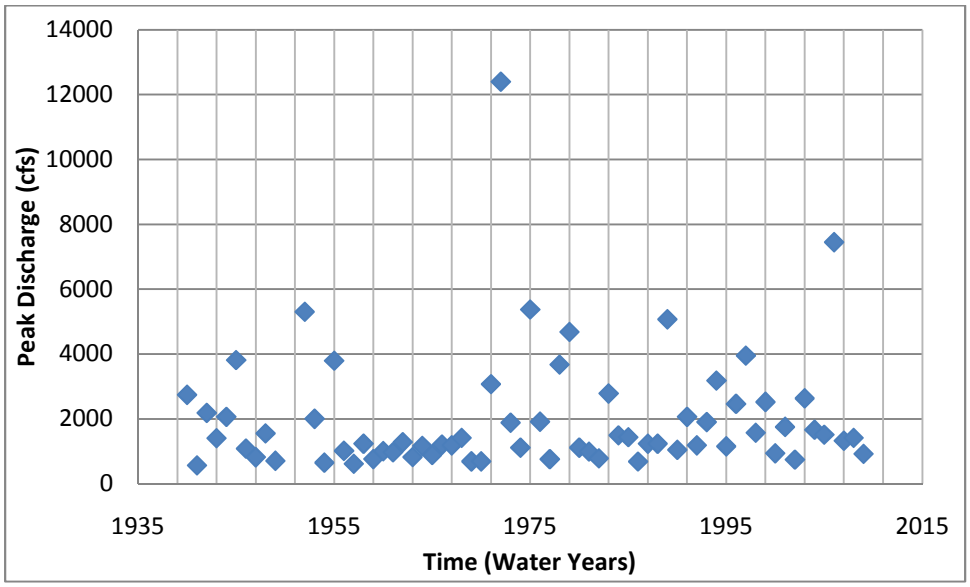

Figure 4-61. Peak Discharge Time Series for Guilford, Maryland.

The adjusted peak discharge data sets for the design year 2100 and Emissions Scenarios A2, A1B, and B1 are shown in Figures 4-62, 4-63, and 4-64, respectively. Each figure displays the corresponding observed values as well as the adjusted values for the respective climate change scenario and the urbanization scenarios 1 and 2. The adjusted peak discharge data sets for design years 2025, 2050, and 2075 for each climate change scenario are shown in Figures 8-1 through8-9 in Appendix B.

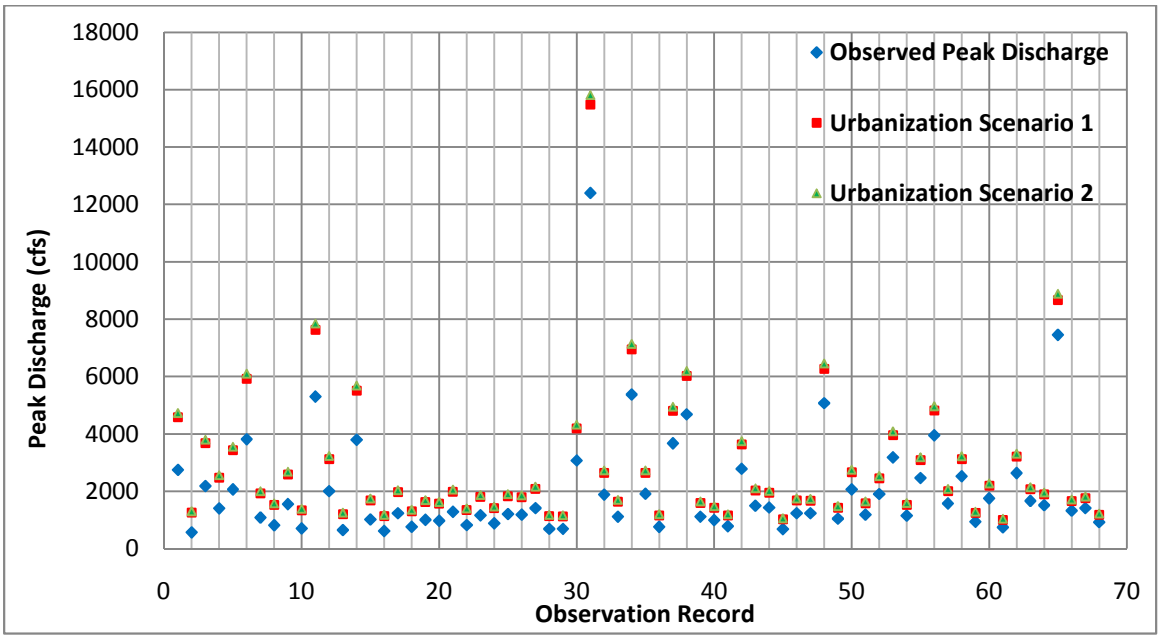

Figure 4-62. Observed and Adjusted Peak Discharge Records (cfs) for the A2 Emissions Scenario, Urbanization Scenarios 1 and 2, and Design Year 2100.

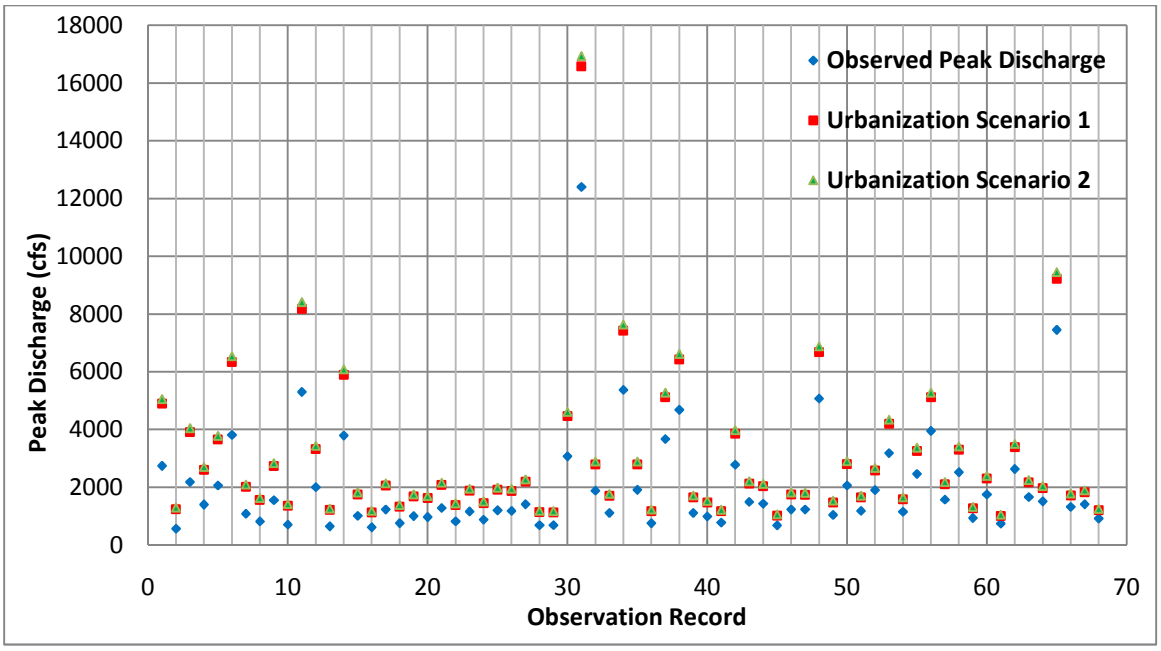

Figure 4-63. Observed and Adjusted Peak Discharge Records (cfs) for the A1B Emissions Scenario, Urbanization Scenarios 1 and 2, and Design Year 2100.

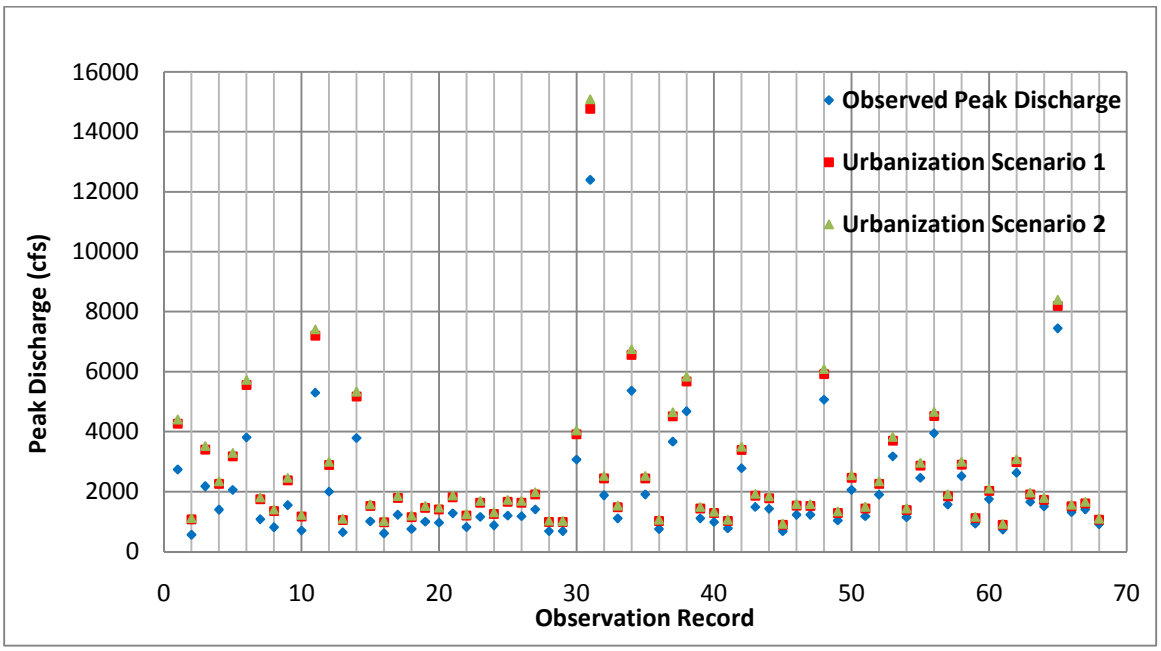

Figure 4-64. Observed and Adjusted Peak Discharge Records (cfs) for the B1 Emissions Scenario, Urbanization Scenarios 1 and 2, and Design Year 2100.

It is apparent from Figures 4-62, 4-63, and 4-64 that the difference in the effect of each urbanization scenario is small compared to the overall adjustment for each climate change and urbanization scenario. A greater difference in the adjusted peak discharge

rates is apparent between the three emissions scenario. As expected, the A1B emissions scenario results in the greatest adjustment in the peak discharge records followed by the A2 and B1 emissions scenarios. This corresponds to the ranking of the moments calculated for the precipitation GEV parameters for each emissions scenario in Section 4.3.7. The GEV parameters for the A1B scenario resulted in the greatest rainfall depth regardless of the return period for the design years analyzed (See Figure 4-38), followed by the A2 and B1 scenarios. Therefore, it is physically rational that the A1B scenario results in the greatest adjustments to the peak discharges, followed by the A2 and B1 scenarios.

The percent increase between each observed peak discharge record and the corresponding adjusted peak discharge record for each emissions scenario and urbanization scenario was calculated. The results for the design year 2100 are shown in Figures 4-65, 4-66, and 4-67. The figures suggest that two factors influence the percent increase, the time at which the observed record occurred and the magnitude of the observed record. The percentage of increase of the adjusted peak discharge values decreases as the data set progresses, or as the discharge records observed later in the time series are adjusted. This is because the difference between the climate change and urbanization scenario is less between the observation year 2000 and design year 2100 than the observation year 1940 and the design year 2100. Therefore, peak discharge events that occurred earlier in the twentieth century will require greater adjustments, as expected.

The second factor is the magnitude of the observed peak discharge event. It is apparent from Figures 4-65, 4-66, and 4-67 that the greatest percent increase occurs for

the second value in the data record, or the year 1942. The second data record value in the observed time series shown in Figure 4-61 is the minimum peak discharge value of the entire time series. Likewise, the lowest percent increase is applied to the 31st data record or year 1972, which is corresponds to the largest observed peak discharge in the entire time series in Figure 4-61.While the magnitude of increase will be greater for the larger events, the percent increase relative to the observed value will be smaller. Therefore, the level of adjustment is dependent on both the time at which the observed peak discharge occurred and the magnitude of the event.

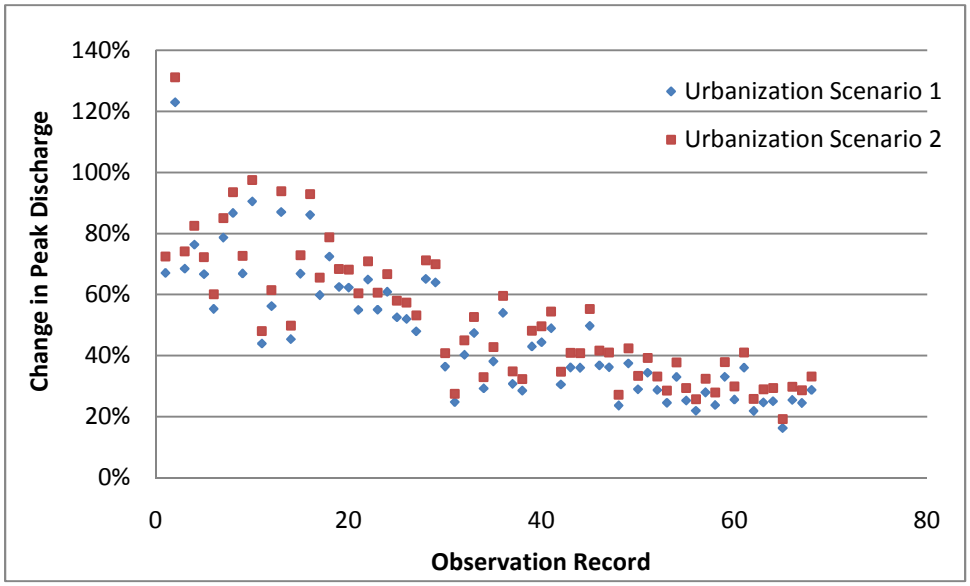

Figure 4-65. Percent Increase of the Observed Peak Discharge Records to the Year 2100 for Emissions Scenario A2 and Urbanization Scenarios 1 and 2.

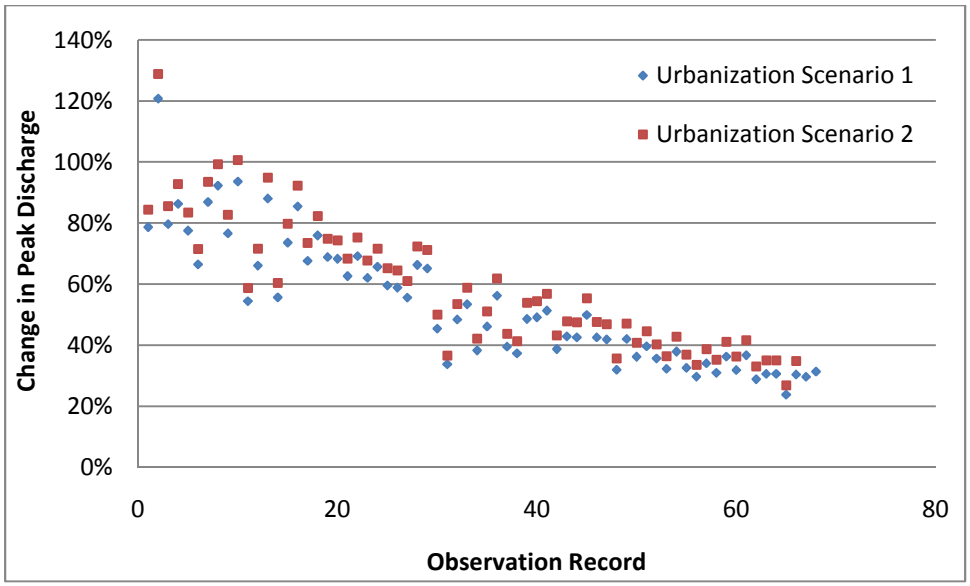

Figure 4-66. Percent Increase of the Observed Peak Discharge Records to the Year 2100 for Emissions Scenario A1B and Urbanization Scenarios 1 and 2.

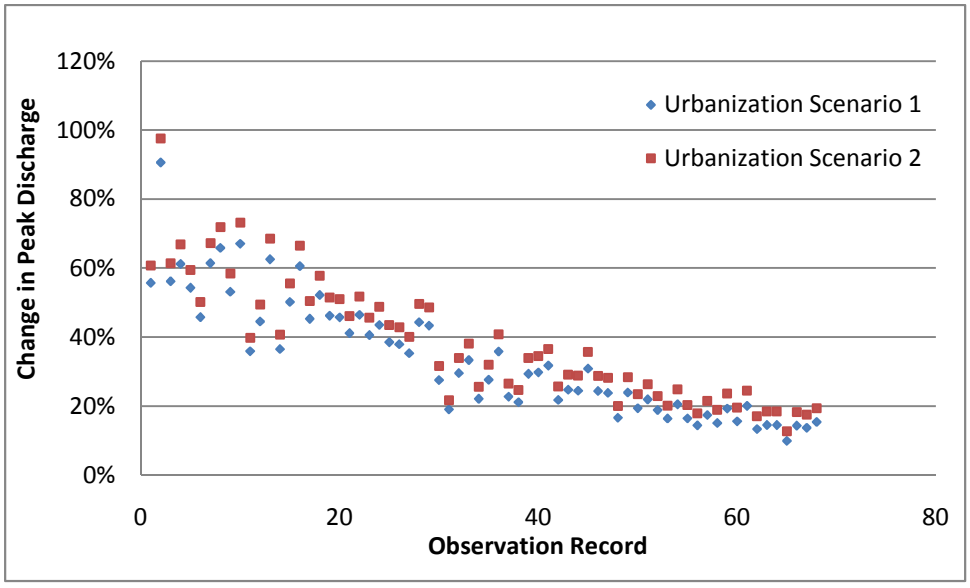

Figure 4-67. Percent Increase of the Observed Peak Discharge Records to the Year 2100 for Emissions Scenario B1 and Urbanization Scenarios 1 and 2.

The statistics of the percent increase of each peak discharge record for each emissions scenario, urbanization scenario, and design year are shown in Table 4-35. As expected, the average percent increase is the greatest for the A1B emissions scenario

followed by the A2 and B1 scenario regardless of the design year. Likewise, urbanization scenario 2 results in a greater percent increase than the urbanization scenario 1 regardless of the climate change scenario or design year. The average percent increase ranges from 33.7% to 58.5% for the design year 2100 and 21.4% to 25.3% for the design year 2025 for the six scenarios. The level of adjustment increases as the design year increases, which coincides with the expected increase in greenhouse gases and increased impervious area over time with the climate change and urbanization scenarios.

Table 4-35. Statistics for Percent Change in Peak Discharge Values for Design Years 2025, 2050, 2075, and 2100.

Percent Change		A2		A1B		B1	
Design Year	Statistic	1	2	1	2	1	2
2100	Average	47.1%	52.1%	53.3%	58.5%	33.7%	38.3%
	Standard Deviation	21.3%	22.2%	20.6%	21.5%	17.1%	17.9%
	Maximum	123.0%	131.2%	120.7%	128.8%	90.6%	97.6%
	Minimum	16.3%	19.2%	23.7%	26.9%	9.9%	12.7%
2075	Average	37.0%	41.2%	41.4%	45.7%	29.8%	33.7%
	Standard Deviation	18.9%	19.7%	19.4%	20.2%	15.9%	16.5%
	Maximum	103.4%	110.1%	107.2%	114.0%	79.8%	85.7%
	Minimum	10.3%	12.8%	14.2%	16.8%	8.5%	11.0%
2050	Average	29.0%	32.0%	31.9%	35.0%	25.8%	28.7%
	Standard Deviation	16.8%	17.3%	17.7%	18.2%	15.0%	15.4%
	Maximum	85.9%	90.6%	91.3%	96.2%	71.5%	75.8%
	Minimum	6.1%	7.9%	7.9%	9.8%	6.3%	8.2%
2025	Average	22.2%	23.6%	23.9%	25.3%	21.4%	22.8%
	Standard Deviation	15.0%	15.2%	15.9%	16.1%	14.4%	14.6%
	Maximum	70.4%	72.5%	75.3%	77.5%	65.1%	67.1%
	Minimum	2.8%	3.7%	3.4%	4.3%	3.2%	4.0%

4.9 Analysis of the Flood Distribution Parameters over Time

With the peak discharge record adjusted to urbanization and climate change conditions from design years 2010 to 2100, the next step was to calculate the Log Pearson 3 (LP3) parameters of each adjusted data record in each design year. With the parameters calculated, a flood frequency analysis can be conducted for each design year and the peak discharge corresponding to a given return period can be determined for a selected design year. To calculate the LP3 parameters, the logarithms of each discharge within each of the 92 adjusted design year data sets were calculated. The LP3 parameters equaled the mean, standard deviation, and skew of each of the logarithm peak discharge data sets. The LP3 parameters for each design year were then stored in a time series. Figures 4-68, 4-69, and 4-70 show the time series for the mean, standard deviation, and skew of the adjusted data records for each design year.

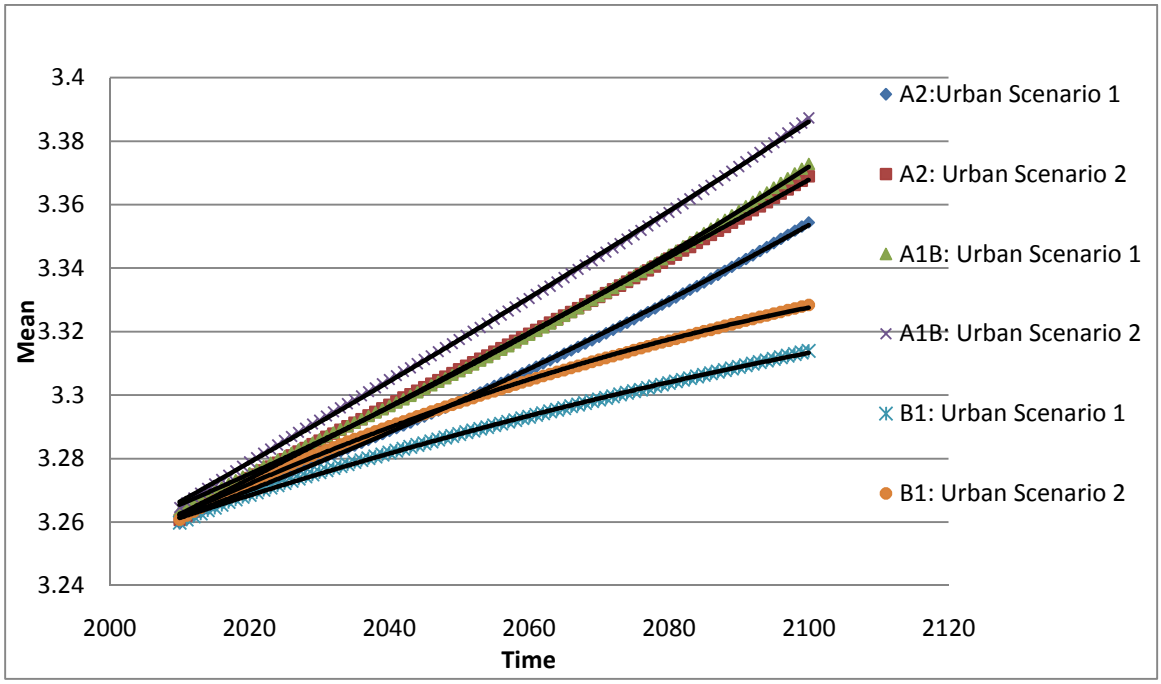

Figure 4-68. The Temporal Change in Log Mean of Peak Discharge Rates over Time.

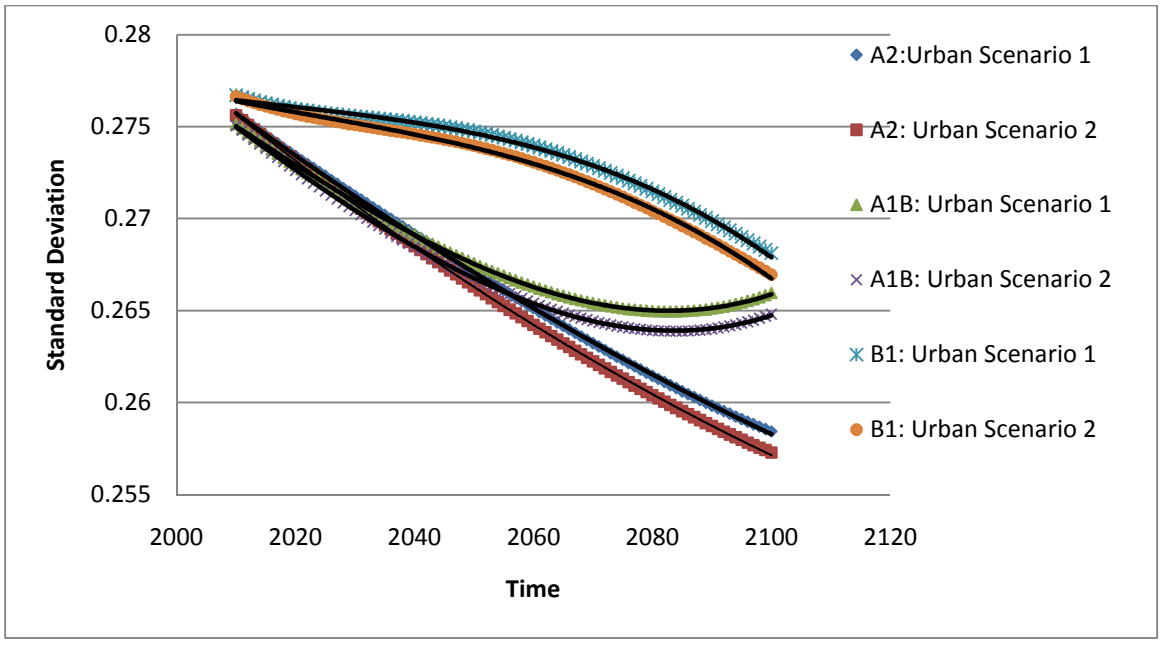

Figure 4-69. The Temporal Change in Log Standard Deviation of Peak Discharge Rates over Time.

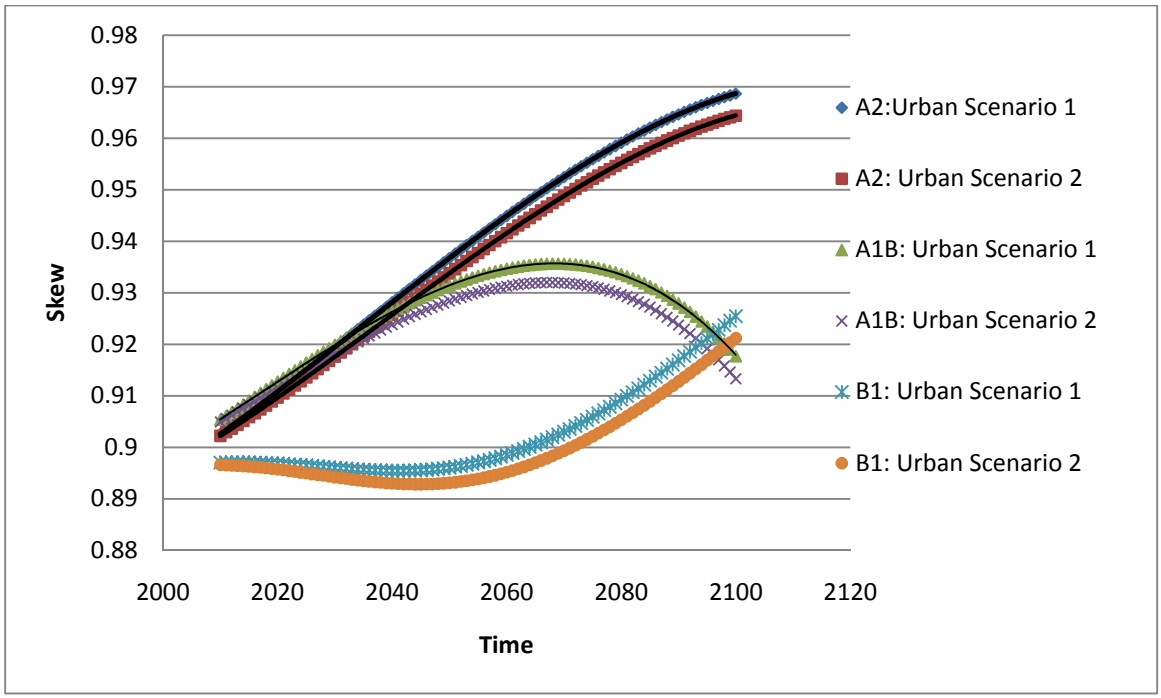

Figure 4-70. The Temporal Change in Log Skew of Peak Discharge Rates over Time.

4.9.1 Analysis of the Parameter Functions

It is apparent from the figures that the mean of the logarithms of the peak discharge values increases over time regardless of the scenario. This is expected based on the increases in the peak discharge records previously discussed. However, the standard deviation of the logarithms slightly decreases with time. The data sets for the design years 2025 and 2100 for the A2 emissions scenario and urbanization scenario 2 were analyzed to study the cause of the decrease in the standard deviation. The adjusted peak discharge for each design year in the normal space is shown in Figure 4-71 while the values in the log-space are shown in Figure 4-72. In the normal space, the standard deviation equals 2097 and 2373 for the years 2025 and 2100, respectively. However, in the log-space, the standard deviation equals 0.272 and 0.278 for the years 2025 and 2100, respectively. It is apparent from Figures 4-71 and 4-72 that the standard deviation of the peak discharge values in normal space is increasing in the twenty-first century; however, in log-space, the spread between the larger values is compressed whereas the spread between the smaller values is not as greatly influenced. Therefore, the standard deviation of the log space decreases over time. This very slight decrease in the log-space standard deviation, however, is counteracted by the increase in the log-space mean of the data.

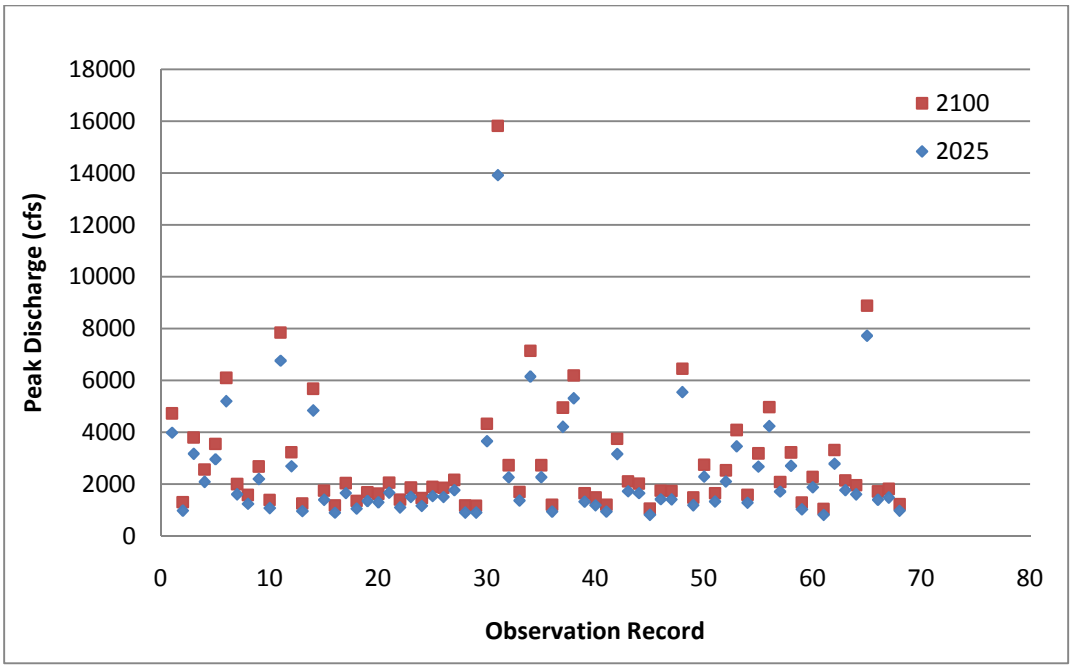

Figure 4-71. Adjusted Peak Discharge Records in Normal Space for Emissions Scenario A2 and Urbanization Scenario 2 for Design Years 2025 and 2100.

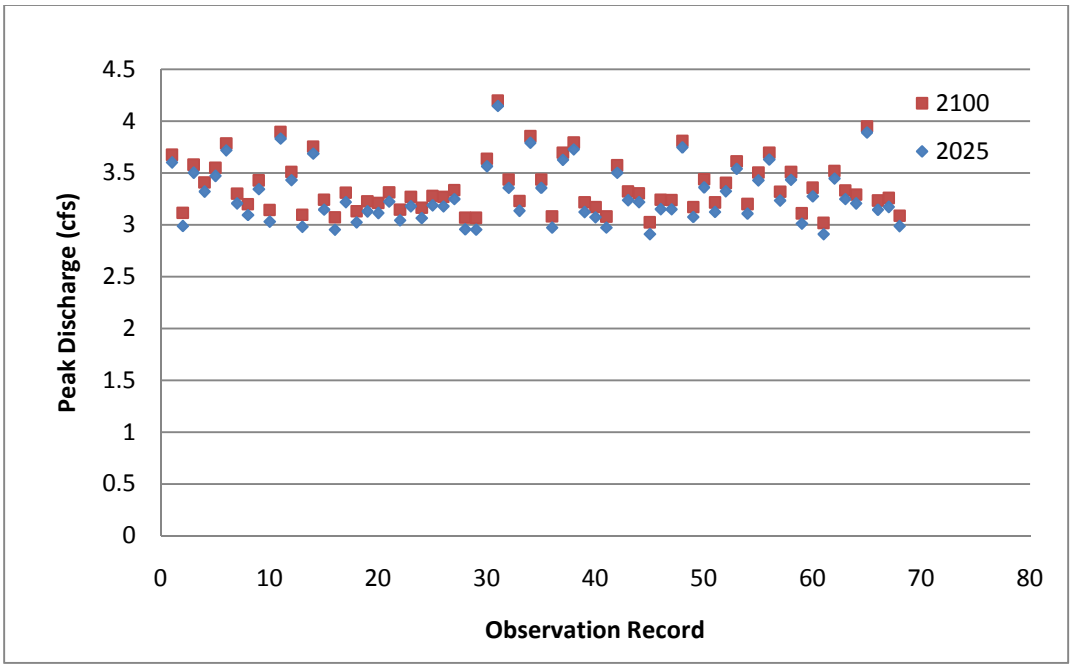

Figure 4-72. Adjusted Peak Discharge Records in Log-Space for Emissions Scenario A2 and Urbanization Scenario 2 for Design Years 2025 and 2100.

In addition to the overall decreasing trend in the standard deviation of the logarithms in the twenty-first century, the A1B scenarios show a slight increase at the end of the twenty-first century. Likewise, if the function fitted for the A2 scenario were extrapolated, an increase would occur as well. The data was analyzed further in an attempt to explain this shift in the data trend. The standard deviation of the peak discharge data in normal space was calculated for each scenario and plotted in Figure 4-73 to analyze this trend. It is apparent from Figure 4-73 that the normal space standard deviation is increasing for each scenario; however, the B1 scenario appears to be stabilizing around the year 2080 while the rate of increase of the standard deviation for the A1B and A2 scenarios appears to increase. These trends coincide with the trends in the standard deviations of logarithms shown in Figure 4-69 in that the B1 scenarios are the only scenarios that appear to continue to decrease into the twenty-second century. This suggests that when the rate of increase of the standard deviation in the normal space reaches a certain threshold, the standard deviation of the logarithms begin to increase as well.

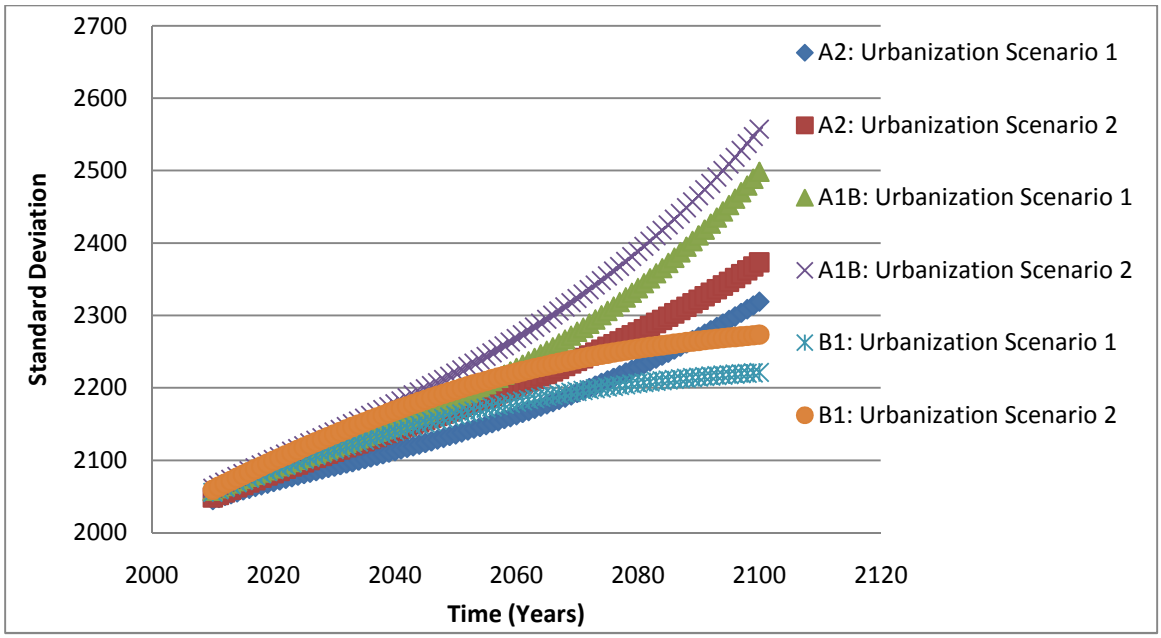

Figure 4-73. Standard Deviation of the Adjusted Peak Discharge Records in Normal Space over Time.

In addition to the standard deviation, the skew parameter was analyzed further. The estimated skew value as function of time suggests a polynomial swing throughout the 21st century. However, this is likely to be due to sampling variation. As was determined in the development of the adjustment factor for precipitation data, estimation of the skew is difficult for small samples. Likewise, for use in the LP3 distribution, the skew is rounded to the nearest tenth. Therefore, the minor difference in skew that results from the adjusted data is not meaningful. However, it is important that the models are not extrapolated beyond the time period specified for this study.

4.9.2 Fitting Statistical Models to the LP3 Parameters

To estimate the LP3 parameters at a give design year, statistical models were fitted to each data set for each scenario. Polynomial functions were used:

$$Y = C_0 + C_1*x + C_2*x^2 + C_3*x^3 \qquad \text{Eq. 4-26}$$

where the coefficient values for each moment equation and each climate change and urbanization scenario are given in Table 4-36. The coefficient of determination for each model exceeded 0.99, which suggests that more than 99% of the variation in the LP3 parameters is explained by the fitted models.

Table 4-36. Coefficient Values and Coefficient of Determination for Statistical Models of Mean, Standard Deviation, and Skew of the Log of the Peak Discharge Values over Time.

	Scenario		Coefficient Value				
Moment	Climate Change	Urbanization	C0	C1	C2	C3	R^2
Mean	A2	1	10.549	-0.008	0.0000022	0	1.00
	A2	2	3.721	-0.002	0.0000007	0	1.00
	A1B	1	12.057	-0.010	0.0000026	0	1.00
	A1B	2	5.253	-0.003	0.0000011	0	1.00
	B1	1	-4.869	0.007	-0.0000017	0	0.99
	B1	2	-11.631	0.014	-0.0000032	0	0.99
Standard Deviation	A2	1	2.564	-0.002	0.0000005	0	1.00
	A2	2	3.102	-0.003	0.0000006	0	1.00
	A1B	1	-95.796	0.144	-0.0000720	0.000000012	1.00
	A1B	2	-92.408	0.139	-0.0000698	0.000000012	1.00
	B1	1	77.202	-0.114	0.0000566	-0.000000009	0.99
	B1	2	80.852	-0.119	0.0000590	-0.00000001	0.99
Skew	A2	1	368.640	-0.543	0.0002667	-0.000000044	1.00
	A2	2	356.509	-0.526	0.0002590	-0.000000042	1.00
	A1B	1	805.872	-1.197	0.0005928	-0.000000098	1.00
	A1B	2	793.232	-1.179	0.0005847	-0.000000097	1.00
	B1	1	-272.439	0.414	-0.0002093	0.000000035	0.99
	B1	2	-283.628	0.430	-0.0002163	0.000000036	0.99

4.9.3 Multinonstationary Flood Frequency Analysis

Based on the LP3 parameter models, flood frequency analyses were then conducted for each emissions scenario and urbanization scenario for the years 2010, 2050, 2075, and 2100. Figure 4-74 shows the results for the A1B emissions scenario and

urbanization scenario 2. Figure 9-10 in Appendix C show the results for emissions scenario A1B and urbanization scenario 1; Figures 9-11 and 9-12 in Appendix C show results for emissions scenario A2 and urbanization scenarios 1 and 2, respectively; and Figures 9-13 and 9-14 in Appendix C show results for emissions scenario B1 and urbanization scenarios 1 and 2, respectively. As expected, the flood frequency analysis shifts upwards over time under each scenario as a result of the effects of multinonstationarity.

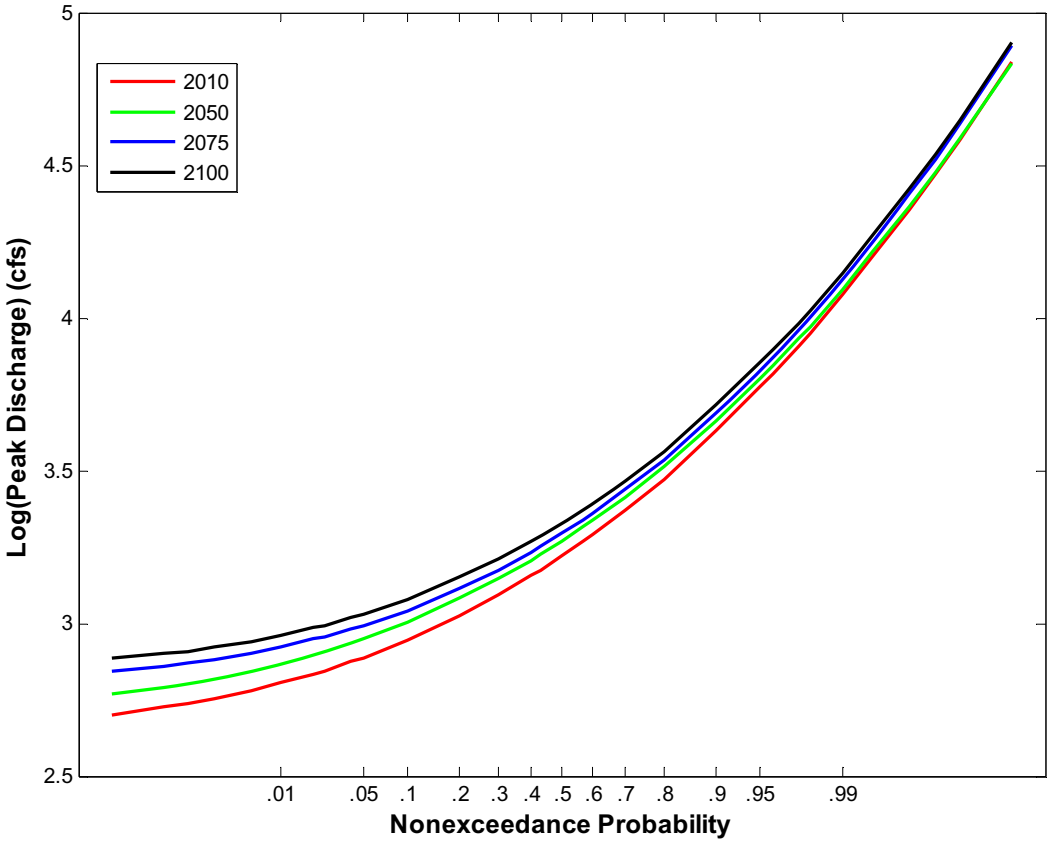

Figure 4-74. Flood Frequency Analysis for Emissions Scenario A2 and Urbanization Scenario 2

The multinonstationary flood frequency analyses for each scenario were compared based on the 100-yr and 500-yr flood for design years 2050, 2075, and 2100. The values are given in Tables 4-37 and 4-38 for the three emissions scenarios and two urbanization scenarios for the 100-yr and 500-yr floods, respectively. Figures 4-75 and 4-76 show the 100-yr flood peak discharge rates for the urbanization scenario 1 and 2, respectively, as well as the 100-yr flood peak discharge based on the observed peak discharge. Likewise, Figures 4-77 and 4-78 show the 500-yr flood peak discharge rates for urbanization scenarios 1 and 2, respectively, as well as the 500-yr flood peak discharge based on the observed peak discharge.

The results show that regardless of the emissions or urbanization scenario, a flood frequency analysis based on the observed peak discharge records will underestimate the 100-yr and 500-yr floods. For each emissions scenario and design year, the urbanization scenario 2 results in a greater peak discharge than that from urbanization scenario 1. For the design year 2100, the emissions scenario A1B results in the greatest 100-yr and 500-yr flood, followed by the A2 and B1 emissions scenarios. These trends coincide with the adjustment results as well as the general trends of the GEV parameters for the three emissions scenarios and the fact that greater impervious areas will result in greater runoff.

Exceptions to these trends exist, however, for the design years 2050 and 2075. The results suggest that the B1 emissions scenario will result in the greatest peak discharge for both the 100-yr and 500-yr flood in the year 2050. Analysis of the moments shows that the standard deviation of the logarithms for the B1 emissions scenario is greater than the A1B and A2 emissions scenario for this design year. As previously discussed, the standard deviation decreases over time in the log-space despite

an increase in the normal space for most scenarios and design years. Therefore, despite the greater standard deviation in the normal space for the A1B and A2 scenario, the standard deviation in log-space is less than that of the B1 scenario. If the individual scenarios are analyzed over time, the decrease in the standard deviation of the logarithms is counteracted by the greater increase in the mean logarithms. However, when the A1B, A2, and B1 scenarios are compared in the same design year, the difference in the standard deviation in the logarithms may overpower that of the mean. This results in a greater projected flood for the B1 scenario despite the greater moments in the normal space for the A1B and A2 scenarios. However, for the year 2100, the 100-yr and 500-yr floods are greater for the A1B and A2 scenario than the B1 scenario. This suggests that the difference in the means begins to counteract that of the standard deviation in the year 2100 as the scenarios continue to diverge.

Another exception occurs in the year 2075. The A2 scenario results in a 500-yr flood that exceeds the A1B scenario. Analysis of the moments shows that the magnitude of the skew for the A2 scenario is greater than that of the A1B scenario by roughly 0.003 for the year 2075. However, the LP3 distribution requires the skew to be rounded to the nearest tenth, which results in a difference in of 0.1, with the skew values of 1.0 and 0.9 for the A1B and A2 scenarios, respectively. Therefore, as the skew coefficient influences the tail of the extremes, this difference results in a greater 500-yr flood for the A2 scenario. It is important to note that both of these exceptions are the result of limitations of the application of the LP3 distribution for a flood frequency analysis and should be considered when conclusions are made based on these results.

Table 4-37. 100-yr Flood Peak Discharge (cfs) for each Emissions Scenario and Urbanization Scenario for the Years 2025, 2050, 2075, and 2100.

		2100		2075		2050	
	Urbanization Scenario	1	2	1	2	1	2
	Observed	10587	10587	10587	10587	10587	10587
Emissions Scenario	A2	13663	14014	13086	13387	12244	12465
	A1B	14432	14806	13234	13538	12554	12778
	B1	13314	13655	12771	13067	12596	12892

Table 4-38. 500-yr Flood Peak Discharge (cfs) for each Emissions Scenario and Urbanization Scenario for the Years 2025, 2050, 2075, and 2100.

		2100		2075		2050	
	Urbanization Scenario	1	2	1	2	1	2
	Observed	20012	20012	20012	20012	20012	20012
Emissions Scenario	A2	25758	26346	24906	25416	22816	23185
	A1B	26821	27442	24546	25052	23419	23792
	B1	25703	26287	24082	24581	23893	24290

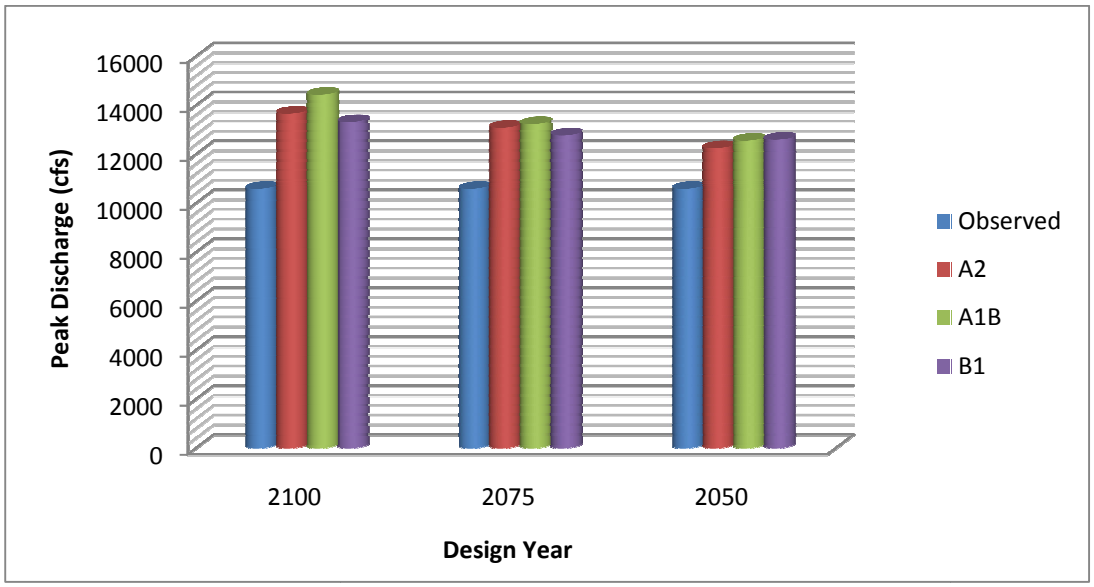

Figure 4-75. 100-yr Flood Based on Observed Data and Adjusted Data for Urbanization Scenario 1 and Climate Change Scenarios A2, A1B, and B1.

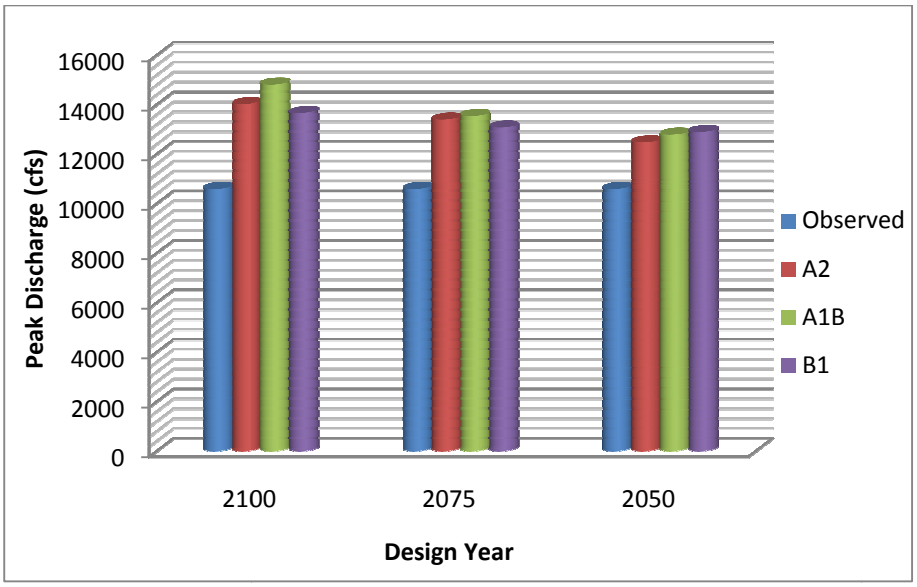

Figure 4-76. 100-yr Flood Based on Observed Data and Adjusted Data for Urbanization Scenario 2 and Climate Change Scenarios A2, A1B, and B1.

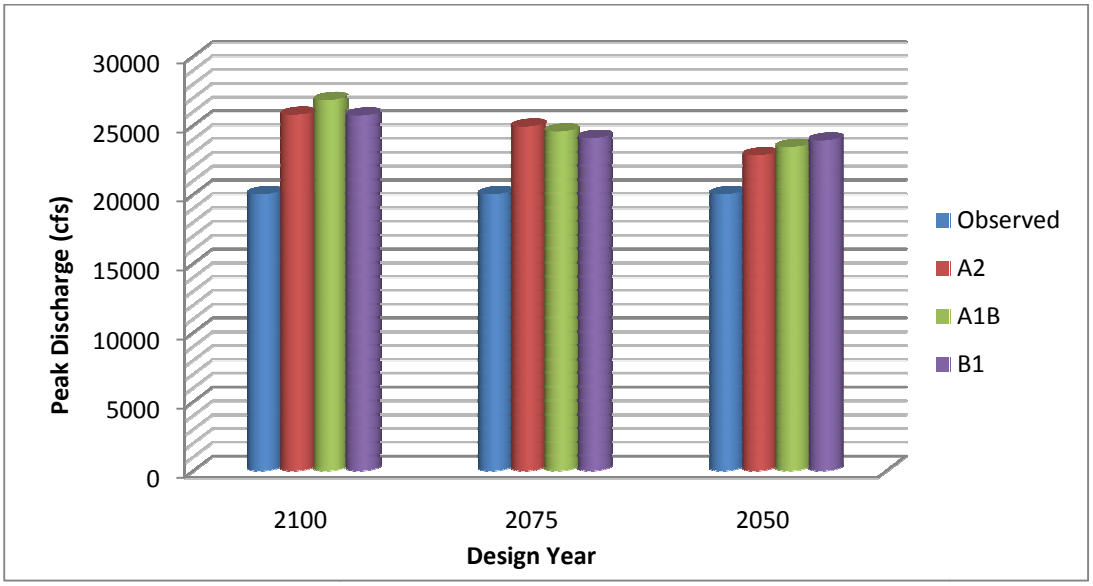

Figure 4-77. 500-yr Flood Based on Observed Data and Adjusted Data for Urbanization Scenario 1 and Climate Change Scenarios A2, A1B, and B1.

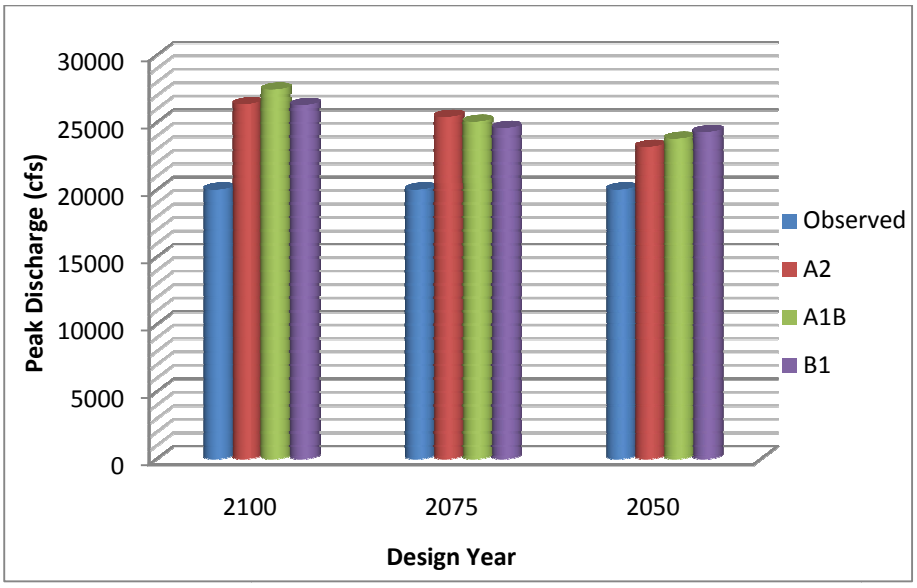

Figure 4-78. 500-yr Flood Based on Observed Data and Adjusted Data for Urbanization Scenario 2 and Climate Change Scenarios A2, A1B, and B1..

Tables 4-39 and 4-40 show the percent increase from the 100-yr and 500-yr floods, respectively, based on the observed data to the 100-yr and 500-yr floods based on the adjusted data for each design year and climate change and urbanization scenario. For the design year 2100, the A1B scenario results in a 39.9% increase in the 100-yr flood and a 37.1% increase in the 500-yr flood for the urbanization scenario 2. The lowest projected increase equals 25.8% for the B1 emissions scenario and the urbanization scenario 1 for the 100-yr. The lowest projected increase for the 500-yr flood equaled 28.4% for the B1 scenario. Therefore, if stormwater management structures are designed based on the observed data, the structures would be under designed for both the 100-yr and 500-yr floods.

Table 4-39. Increase (%) from Observed to Adjusted 100-yr Flood Peak Discharge (cfs) for each Emissions Scenario and Urbanization Scenario for the Years 2050, 2075, and 2100.

		2100		2075		2050	
	Urbanization Scenario	1	2	1	2	1	2
Emissions Scenario	A2	29.1	32.4	23.6	26.4	15.7	17.7
	A1B	36.3	39.9	25.0	27.9	18.6	20.7
	B1	25.8	29.0	20.6	23.4	19.0	21.8

Table 4-40. Increase (%) from Observed to Adjusted 500-yr Flood Peak Discharge (cfs) for each Emissions Scenario and Urbanization Scenario for the Years 2050, 2075, and 2100.

Skew based on Moment Equations		2100		2075		2050	
	Urbanization Scenario	1	2	1	2	1	2
Emissions Scenario	A2	28.7	31.7	24.5	27.0	14.0	15.9
	A1B	34.0	37.1	22.7	25.2	17.0	18.9
	B1	28.4	31.4	20.3	22.8	19.4	21.4

5 Risk Assessment

5.1 Introduction

While the term risk has many definitions, for the purpose of this study risk will be defined as a combination of the probability of occurrence and the consequences associated with an event (See Chapter 2). A risk assessment was conducted based on the projected changes in the flood frequency analysis under nonstationary conditions. The risk assessment approach followed the method used by the Interagency Performance Evaluation Task Force, established by the United States Army Corps of Engineers, in the analysis of the New Orleans and Southern Louisiana Hurricane Protection System following Hurricane Katrina (USACE 2009). The FEMA HAZUS Flood Model for riverine flooding was used to define the hazard based on the developed flood frequency distributions and estimate the consequences of each event analyzed. The program has three levels of complexity that vary based on the user inputs and the level of sophistication of the program outputs. For this study, the simplest level was selected based on the availability of user inputs and the requirement of a means for comparison between risk under nonstationary conditions rather than an accurate estimate of the damage.

5.2 Risk Assessment Methodology

In the IPET risk assessment, risk is defined as the product of the vulnerability to the hazard and the consequences that would result. The vulnerability to a hazard consists of three parts: (1) the probability of occurrence; (2) the identification of the hazard; and (3) the system performance. The probability of occurrence is based on a frequency analysis. Identification of the hazard can have multiple components. For example, the hazards assessed for a hurricane include surge levels and wave levels (USACE 2009).

For floods, the HAZUS program defines the hazard components as flood depth and velocity. The third component, system performance, refers to reliability of any hazard mitigation methods implemented under the conditions identified for the hazard. A combination of these three components defines the vulnerability to a specific hazard (USACE 2009).

5.2.1 Vulnerability to the Hazard

For this study, the hazard was identified as the flood depth. The inclusion of a velocity analysis in the hazard identification was not available for the HAZUS program for a Level 1 analysis. Flood events with 1% and 0.2% probability of occurrence, i.e., 100-yr and 500-yr return periods were analyzed for the Guilford watershed study.

The 100-yr and 500-yr floods were analyzed based on three scenarios: (1) stationary conditions; (2) worst case scenario for the design year 2100 under nonstationary conditions; (3) best case scenario for the design year 2100 under nonstationary conditions. The hazard for the stationary scenario was based on the flood frequency analysis derived from the observed peak discharge data. The hazard for the worst case scenario was based on the frequency analysis for the A1B emissions scenario and the urbanization scenario 2, which resulted in the greatest 100-yr and 500-yr flood in the year 2100. The best case scenario was based on the frequency analysis for the B1 emissions scenario and the urbanization scenario 1. While the A2 scenario resulted in the minimum peak discharge for the 500-yr flood, the B1 scenario resulted in the minimum peak discharge for the 100-yr flood for the year 2100. The 100-yr flood for the A2 emissions scenario is 2.4% greater than that of the B1 emissions scenario for the year 2100, while the 500-yr flood for the B1 emissions scenario is only 0.2% greater than that

of the A2 emissions scenario. Therefore, the emission scenario B1 and urbanization scenario 1 were selected as the best case scenario which will result in the least increase in the hazard for the design year 2100.

The vulnerability of the study region to the hazard was analyzed for two conditions: (1) without the implementation of a mitigation system and (2) with the implementation of a mitigation system implemented. The mitigation selected consisted of zoning laws to limit development in vulnerable areas. Federal policies have attempted to decrease the vulnerability of areas through structural mitigation methods, such as levees, as well as safe building standards. Likewise, the have attempted to minimize the losses that result from the residual risk through the National Flood Insurance Policy as well as disaster relief. As a result, development has increased in at risk areas. Therefore, Burby (2006) argues that the most efficient way to mitigate losses is through the restriction of development in vulnerable areas by local governments.

The mitigation system analyzed consisted of zoning laws that limited development within the 100-yr floodplain based on stationary conditions. The conserved area will be referred to as the Special Protection Area (SPA). Therefore, when the mitigation system is implemented, damage that occurs within the SPA due to flooding will be assessed based on the 2010 inventory, because the assumption is made that development does not increase following the implementation of the zoning laws. However, the damage that occurs outside of the SPA due to flooding was assessed based on the projected development for the scenario analyzed. The performance of the system in the mitigation of risks was then compared to the risks associated without the implementation of a mitigation system.

5.2.2 Consequences

The second part of the risk assessment is the evaluation of the consequences that result from the hazard. This includes the potential loss of life and property damage (USACE 2009). For Level 1, the HAZUS program estimates the consequences based on default data within the HAZUS program. This includes the general building stock within the United States as well as national data for essential facilities such as police stations, high potential loss facilities such as stormwater management structures, transportation and lifeline systems, agriculture, vehicles, and demographics (FEMA 2009). This information is available at the census block level for the flood model.

HAZUS assesses both direct and indirect losses. Direct losses included physical damage to the general building stock, essential and high potential loss facilities, lifelines such as transportation and utilities, vehicles, and agricultural. The level of damage is estimated based on default data curves within the HAZUS program. For example, for the assessment of damage to buildings within the study area, the damage curve provides estimates of the level of damage based on the different water depths. The loss estimate is then calculated based on the expected replacement cost. Other direct losses include induced damages from debris or the release of hazardous materials and direct social losses such as casualties and displaced households. Indirect losses are defined as additional disruption to economic activity as a result of the direct damage incurred by the hazard.

The consequences provided by HAZUS are based on the default inventory data for the year 2006 and census data for the year 2000. Therefore, for the stationary scenario assessed, the HAZUS estimates for the consequences were assumed to be

representative of the 2010 conditions. However, for the nonstationarity scenarios based on the design year 2100, the consequences estimated by HAZUS based on the new flood frequency analyses were adjusted based on the projected development conditions for the year 2100. The application of the HAZUS program for each scenario as well as the adjustments of the estimated consequences for 2100 development conditions will be discussed herein.

5.3 Application of Risk Assessment Methodology to the Guilford Watershed

The risk assessment methodology was applied to the Guilford Watershed stationarity and nonstationarity scenarios using FEMA's HAZUS model. For level 1, the HAZUS program required the user to define the study region based on the state, county, census tract, or census block. For this study, Howard County was selected for the study region, as the Guilford watershed of the Little Patuxent River is within Howard County. The program then retrieves inventory to be used in the damage assessment based on census data, building stock data, and agricultural products. Then, the user must input a digital elevation model for the study region, available through USGS. Prompted by the user, the program will delineate the stream networks within the study region based on the elevations. Figure 5-1 shows the study area of Howard County, the elevation map, delineated stream networks, and Guilford Watershed.

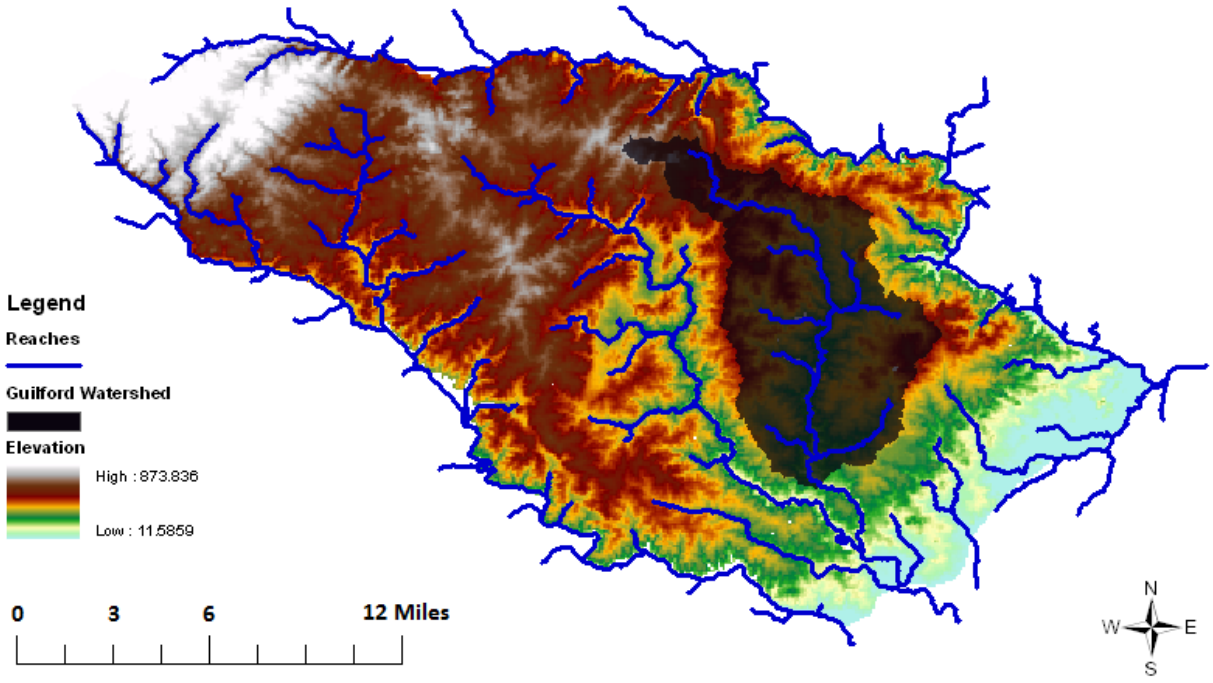

Figure 5-1. Study Region of Howard County, Digital Elevation Map, Stream Networks within Study Region, and Guilford Watershed.

5.3.1 Delineation of the Floodplain

Next, the user must select the stream or channel to be studied. The Little Patuxent River was selected from the headwaters to the Guilford discharge gauge monitored by USGS. Then, the user must choose to analyze return periods stored in the program that correspond to peak discharge rates based on USGS equations for each return period or input peak discharge values manually. The program then delineates the floodplains that would result from the selected flood event and provides estimates of the expected damage. For this study, the peak discharge rates were input manually based on the flood frequency analysis and return period for each scenario. This approach requires that peak discharge rates be input for each segment within the selected channel or stream for the analysis. The segments are defined by the HAZUS program and are typically based on

locations where additional streams flow into the channel, which would suggest an abrupt change in the peak discharge from upstream values. The analyses preceding this point are only conducted based on one study gauge from which discharge data was retrieved from USGS. Therefore, it was necessary to adjust the estimated peak discharge for the study gauge for upstream points defined by the HAZUS program.

A method was developed to estimate the upstream peak discharge rates as a function of the peak discharge both observed and adjusted at the Guilford gauge. First, the subwatersheds were delineated for the downstream point of each segment of the channel. The delineated watersheds are shown in Figure 5-2. The area of each subwatershed was calculated and is shown in Table 5-1 as well as the coordinates of each subwatershed outlet.

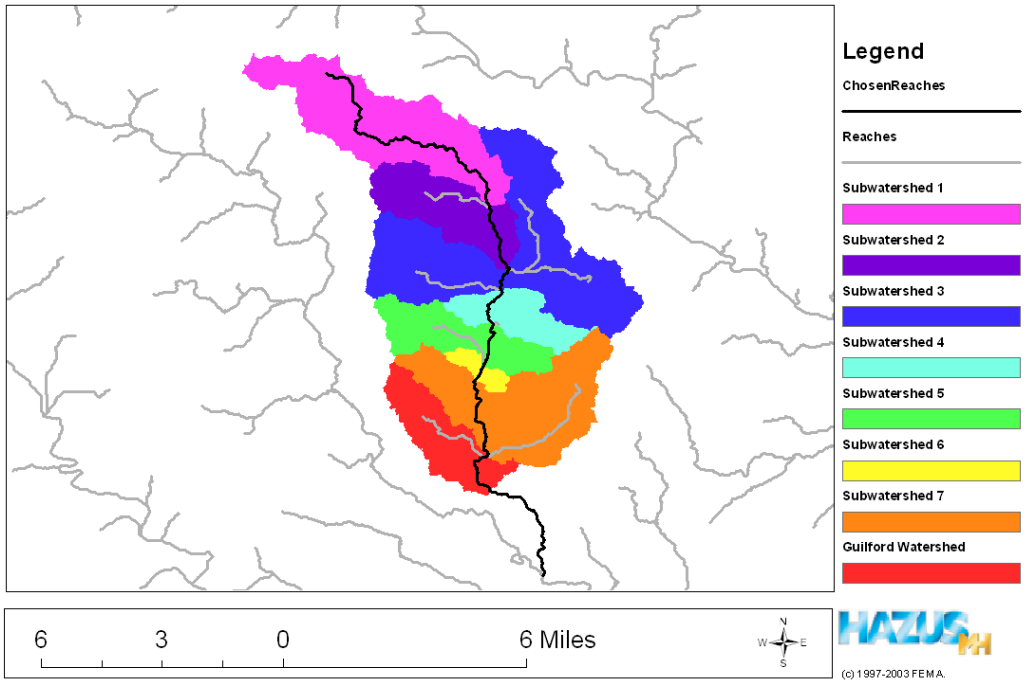

Figure 5-2. Subwatersheds based on HAZUS Defined Segments of the Little Patuxent River in the Guilford Watershed.

Table 5-1. Latitude and Longitude (Degrees) Coordinates of Outlet and Area of each Subwatershed within the Guilford Watershed.

Subwatershed	Longitude	Latitude	Area (sq. mi.)
1	76.851	39.269	7.711
2	76.844	39.247	11.674
3	76.847	39.240	22.625
4	76.850	39.227	24.956
5	76.853	39.212	28.255
6	76.857	39.206	28.866
7	76.852	39.180	35.959
Guilford Watershed			39.246

To estimate the peak discharge for the subwatersheds, regression equations developed by Dillow (1996) for ungauged watersheds in the state of Maryland were used. Dillow (1996) provided the following equation to estimate the 100-yr peak discharge for the Piedmont region based on drainage area and forest cover:

$$q = 3{,}060 * A^{0.557}(F+10)^{-0.241} \quad \text{Eq. 5-1}$$

where q = peak discharge (cfs), A = area (square miles), and F = forest cover (%). The ratio of this equation for the peak discharge at the Guilford outlet and the subwatershed outlet of interest was solved for the peak discharge at the subwatershed outlet of interest, which resulted in the following equation:

$$q_{Subwatershed} = \frac{(3{,}060 * A_{GuilfordWatershed}^{0.557} * (F_{GuilfordWatershed}+10)^{-0.241}) * q_{GuilfordOutlet}}{3{,}060 * A_{Subwatershed}^{0.557} * (F_{Subwatershed}+10)^{-0.241}} \quad \text{Eq. 5-2}$$

Since actual forest cover areas were not available for each subarea over the period of record, the assumption was made that the percentage of forest cover within the subwatershed would be the same as the entire watershed. This assumption seems reasonable since the coefficient in the forest cover terms is significantly less than that for

the area; therefore, forest cover is the input variable of lesser importance. Therefore, the equation can be simplified as follows:

$$q_{Subwatershed} = \frac{A_{GuilfordWatershed}^{0.557} * q_{GuilfordOutlet}}{A_{Subwatershed}^{0.557}} \quad \text{Eq. 5-3}$$

The peak discharge at each HAZUS defined segment within the Little Patuxent River can be estimated based on the area of the subwatershed, the area of the Guilford watershed, and the peak discharge at the Guilford streamgauge site. Note that this equation is specific to the 100-yr return period. Dillow (1996) provides additional equations with the same functional form for return periods that range from the 2-yr to the 500-yr. In addition, this equation is specific to the Piedmont region of Maryland; however, Dillow (1996) provides equations for the for the Appalachian Plateaus and Alleghany Ridges Region, the Blue Ridge and Great Valley Region, the Western Coastal Plain Region, and the Eastern Coastal Plain Region. The user can apply these equations with their own discretion if used outside of the Maryland region based on regional characteristics.

This method was applied to each subwatershed for both the 100-yr and 500-yr floods in the Guilford Watershed. The results are shown in Tables 5-2 and 5-3 for the 100-yr and 500-yr floods, respectively. These peak discharge values were manually input into the HAZUS program and the floodplains were delineated for each scenario and return periods analyzed. The floodplain delineation defined the flood depth, or the hazard, at each location within the study region. Then, a final analysis was conducted in which the HAZUS program assessed the consequences that would result from the defined hazard for each scenario. The program then provided a global summary of the

consequences that would result from each hazard analyzed for this study based on the 2010 default inventory provided by the program.

Table 5-2. Estimated 100-yr Peak Discharge (cfs) for HAZARD Program Defined Subwatersheds within the Guilford Watershed.

Watershed/ Subwatershed	Nonstationarity: Worst Case	Nonstationarity: Best Case	Stationary Conditions
Guilford Watershed	14806	13314	10587
1	5982	5379	4277
2	7536	6777	5389
3	10894	9796	7790
4	11506	10346	8227
5	12330	11087	8816
6	12478	11220	8922
7	14102	12681	10084

Table 5-3. Estimated 500-yr Peak Discharge (cfs) for HAZARD Program Defined Subwatersheds within the Guilford Watershed.

Watershed/ Subwatershed	Nonstationarity: Worst Case	Nonstationarity: Best Case	Stationary Conditions
Guilford Watershed	27442	25703	20012
1	11342	10623	8271
2	14206	13306	10360
3	20348	19059	14839
4	21461	20101	15650
5	22958	21503	16742
6	23226	21754	16938
7	26169	24511	19084

5.3.2 Resulting Floodplains for Stationarity and Nonstationarity Scenarios

Figure 5-3, 5-4, and 5-5 show the floodplain that would result from a 500-yr return period calculated based on the assumption of stationarity, the best case nonstationarity scenario, and the worst case nonstationarity scenario, respectively. Figures 10-1, 10-2, and 10-3 in Appendix D show the 100-yr return periods for the three

scenarios. The floodplains and flood depths represent the hazard upon which the consequences are assessed.

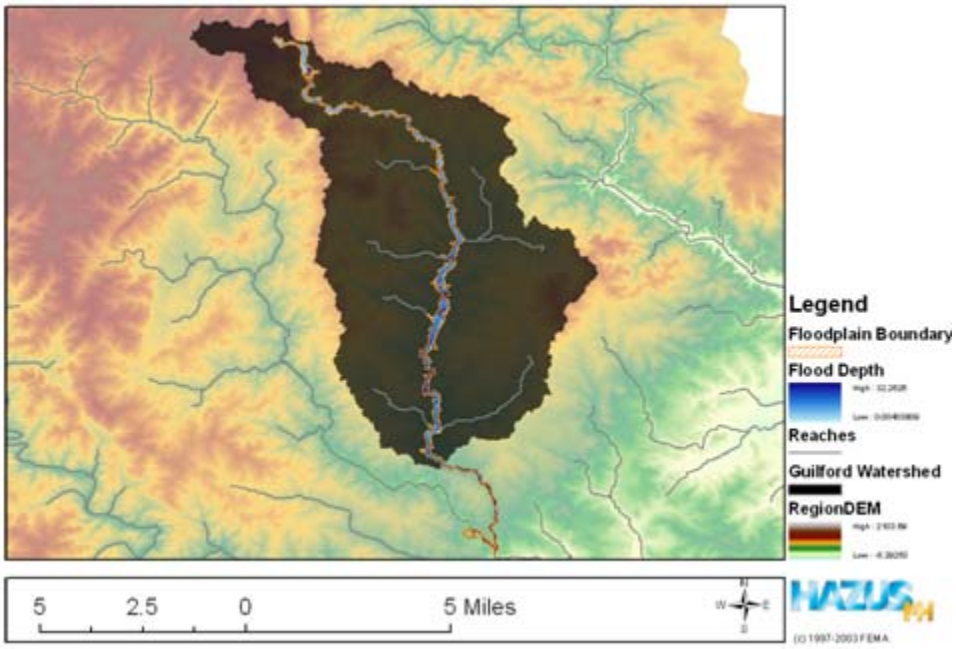

Figure 5-3. 500-yr Return Period Floodplain for Stationary Scenario.

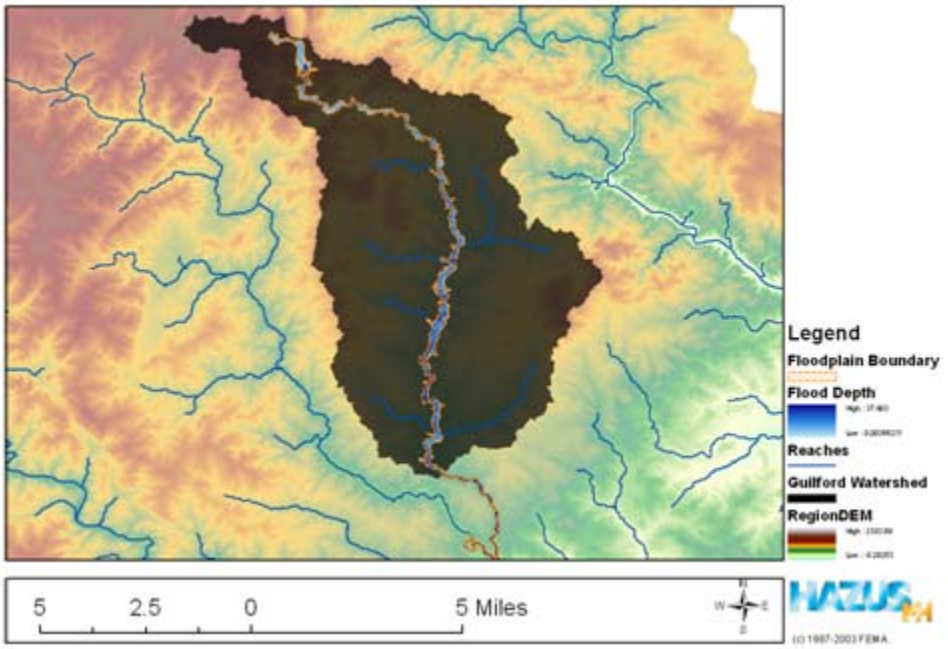

Figure 5-4. 500-yr Return Period Floodplain for Best Case Scenario in 2100.

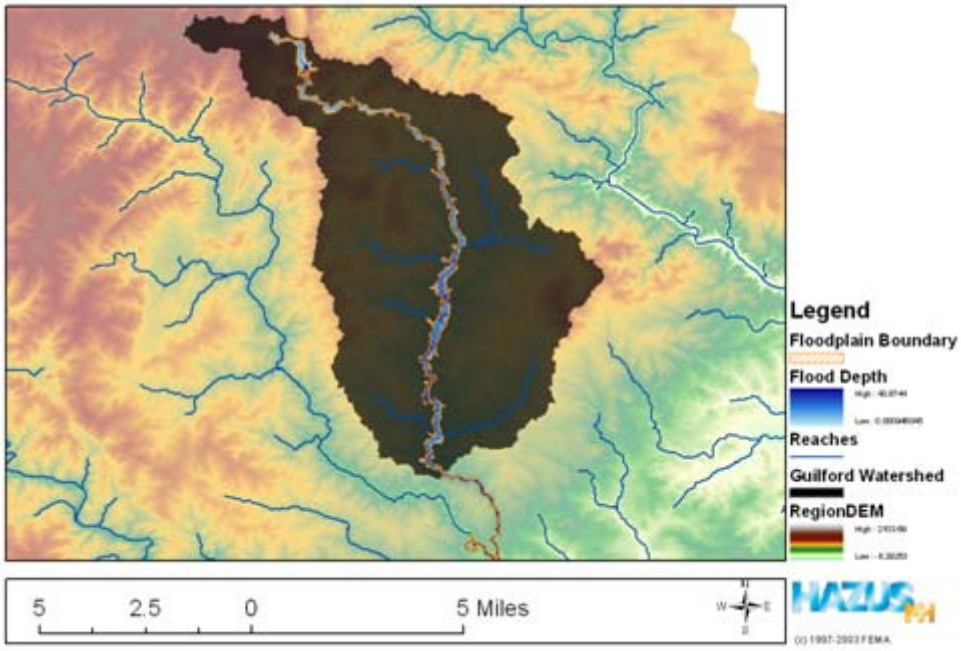

Figure 5-5. 500-yr Return Period Floodplain for Worst Case Scenario in 2100.

5.3.3 Adjustments of Consequences for the Design Year 2100

The consequences defined by the HAZUS program represent census data and general building stock data for the year 2006. Therefore, it was necessary to adjust the consequences assessed for expected development for the year 2100. As the watershed is further developed, the potential consequences will increase because more people and property will be located within the floodplains. Therefore, estimates of the change in consequences from the present day estimates to the 2100 design year were needed. Characteristics of existing development within the watershed were analyzed as well as the projected changes in the population density for each scenario to determine realistic assumptions for future development.

5.3.3.1 USACE National Economic Development Principles and Guidelines

The projections of consequences for the year 2100 were conducted based on the USACE National Economic Development Principles and Guidelines (USACE 2009b). The guidelines provide a systematic approach to estimate the benefits of urban flood damage projects. The guidelines can be summarized into ten steps, in which steps 3 and 5 aim to forecast the increased economic activity within the floodplain in order to demonstrate future benefits and costs of the proposed project. For the use in this study, these steps will be followed to project the increase in consequences within the floodplain and the benefit of implementing a zoning system to mitigate risk.

5.3.3.2 Demographic Projections for Study Region

Step 3 within the guidelines requires that the activities in the affected area be projected as follows:

> "Base economic and demographic projections on the most recent available studies and include the following: population, personal income, recreation demand, and manufacturing employment and output" (USACE 2009b).

For this study, the projected demographic increases are developed based on total population projections provided by Maryland State Planning and were discussed in Chapter 4. Therefore, the demographic projections will be based on the projected increase in population density within Howard County, which is assumed to apply within the watershed.

5.3.3.3 Conversion of Demographic Projections to Land Development

Step 4 within the guidelines requires that the potential land use within the affected area be estimated based on the demographic projections as follow:

> "Estimate potential land use within the affected area by converting demographic projections to acres. The conversion factors can normally be derived from published secondary sources, from agency studies of similar areas or from empirical and secondary data available in the affected area. The categories of potential land use need be only as detailed as necessary to reflect the incidence of the flood hazard and to establish the benefits derived from a plan" (USACE 2009b).

For this study, the conversion was based on the following model between population density and urbanization developed by Moglen and Shivers (2006) for the central region of Maryland to determine the change in impervious area:

$$IA = 12.1935*(PD)^{0.5195} \qquad \text{Eq. 5-4}$$

where IA = impervious area (%) and PD = population density (1000 people). The increase in population density projected in Section 4.7.2.2.1 from 2010 to 2100 was calculated for both urbanization scenarios included in this study and the change in impervious area was estimated based on equation 5-4. The expected increase in the percentage of urbanized area is 7% and 22% for the best case and worst case scenarios, respectively.

These values represent the percent increase in impervious area within the watershed. The guidelines specify the conversion of demographic data to landuse type. Therefore, the assumption was made that impervious area would correspond to either residential or commercial and industrial landuse types.

5.3.3.4 Distribution of Land Development within Study Region

Step 5 in the guidelines requires that the changes in land use are allocated to the floodplain and non-floodplain areas. The basic factors considered in this allocation are as follows:

> "Base the allocation on a comparison of the floodplain characteristics, the characteristics sought by potential occupants and the availability of sought-after characteristics in the nonfloodplain portions of the affected area" (USACE 2009b).

To approach this step, the land cover within the watershed was retrieved from USGS. Figure 5-6 shows the different land cover classifications provided by the NLCD 2001 data set as well as the 100-yr floodplain based on stationary conditions. The map suggests that urbanized and forested land covers are spatially distributed throughout the watershed and floodplain. This suggests that development within and outside of the

floodplain is desired by the community. It is important to note that the agricultural land use, however, is located mainly in the northern and western portion of the watershed, with little interaction with the floodplain. Based on these observations, it was assumed that development within the watershed can be assumed to occur evenly distributed between the available areas within and outside of the floodplain. Agricultural areas were not considered in the analysis, as it does not appear that they will be affected by flooding issues based on the scenarios in this study.

The second component considered in Step 5 was the availability of land for development. The NLCD data set defines the developed land based on four classifications: (1) open space; (2) low intensity; (3) moderate intensity; and (4) high intensity. These classifications are based on the percent impervious area as follows: (1) open space corresponds to less than 20% impervious area; (2) low intensity corresponds to between 20-49% impervious area; (3) moderate intensity corresponds to 50-79% impervious area; and (4) high intensity corresponds to between 80-100% impervious area. The developed open space classification refers to golf courses and other recreational sites while the moderate and high density development areas were assumed to be completely developed. Therefore, it was assumed that increased impervious area and, therefore, development will occur only in the Low Intensity land cover classifications and result in a shift from low intensity to moderate intensity.

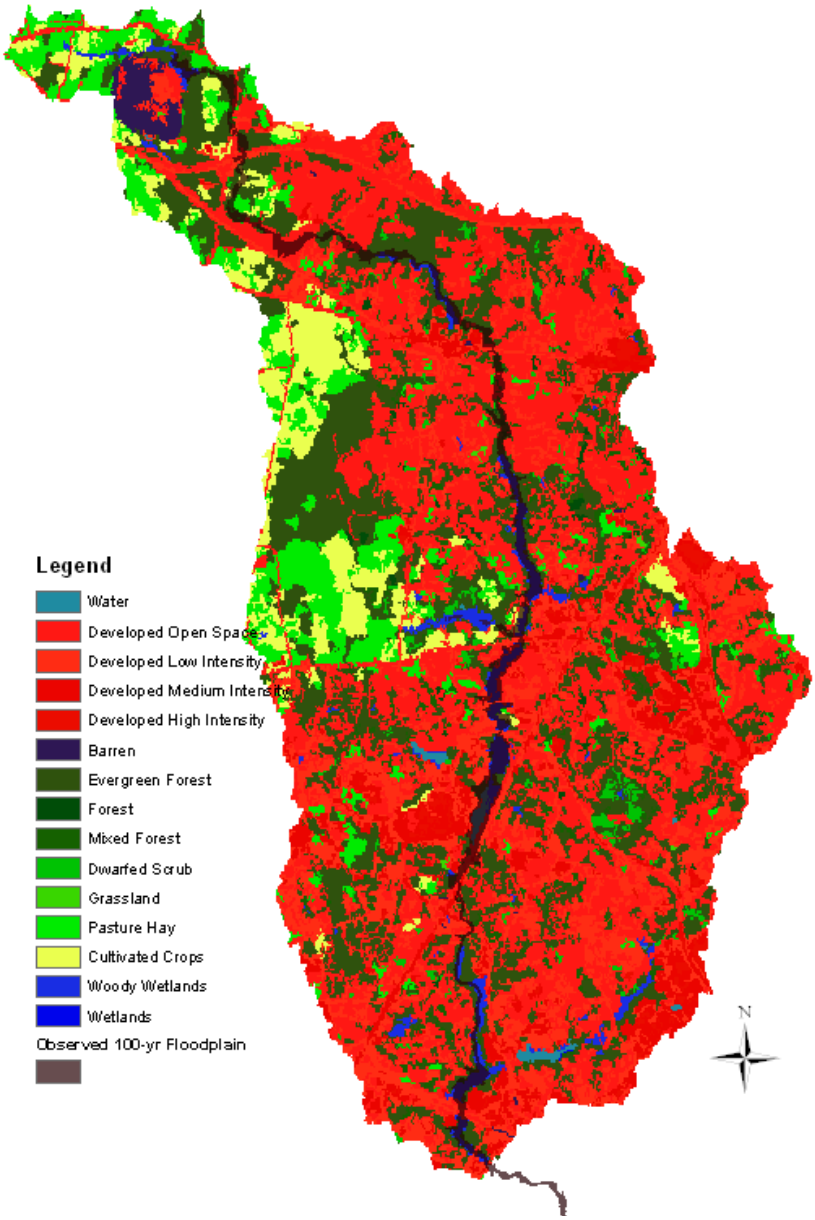

Figure 5-6. Landuse Types for the year 2001 within the Watershed and the 100-yr Floodplain based on Stationarity Conditions.

To determine the total area of impervious land that will increase based on the projected percent increases, the total impervious area within the watershed was estimated. As the land use data is provided in the form of a grid, the area will be referred to in terms of the number of cells or pixels. Each cell represents an equal area of land. First, the

total area associated with each of the four developed classifications was calculated. Then the average impervious area was assumed to represent each classification. For example, the total area classified as open space was assumed to consist of 10% impervious area; low intensity consisted of 35% impervious area; moderate intensity was assumed to consist of 65% impervious area; and high intensity was assumed to consist of 90% impervious area. Therefore, the total impervious area was estimated to be 15,576 cells out of 100,009 cells total within the watershed. Therefore, the watershed is 14.2% impervious area. The results of these calculations are shown in Table 5-4.

Table 5-4. Total Impervious Area within Watershed in Terms of Cell Count and Based on Description of Land cover Classification in Regards to Percent Impervious Area.

Classification	Area in 2010 (Cell Count)	Impervious Area in 2010 (Cell Count)
Open	36227	3623
Low	19005	6652
Moderate	6812	4428
High	971	874
Total for 4 Classifications	63015	15576

The next step was to determine the relationship between the calculated increase in impervious area and the conversion of low intensity developed land cover area to moderate intensity land cover area. The total percent impervious area is projected to increase by 7% and 22% for the best and worst case scenarios, respectively. Therefore, in the best case scenario, the watershed will consist of 15.2% and 17.3% impervious area. For ease of calculation, it was assumed that each cell equals 1 m^2. Therefore, the total area of the watershed equaled 110009 m^2. For the best case scenario, the percent impervious area within the watershed increases by 7% to a total 15.2%. This equals

16721.4 m^2 within the watershed. Therefore, for the best case scenario, an additional 1145.4 m^2 will be added to the watershed for the best case scenario. For the worst case scenario, the percent impervious area will increase by 22% within the watershed, which equals 17.3% impervious area within the watershed or 19031.6 m^2. Therefore, 3455.6 m^2 of impervious area will be added to the watershed for the worst case scenario.

As previously stated, increases in impervious area will only be added to low intensity land cover classifications and will result in a conversion of existing low intensity land cover cells to moderate intensity land cover cells. The average percent impervious area for low and moderate intensity land cover equals 35% and 65%, respectively. If each cell is 1 m^2, it can be assumed that converting from 0.35 m^2, which would be the impervious area within one low intensity land cover cell, to 0.65 m^2, which would be the impervious area within one moderate intensity land cover cell, results in the addition of 0.3 m^2 to the watershed. Based on this value, it was assumed that for the worst case scenario, the addition of 3455.6 m^2 of impervious area would result in the conversion of 11,519 low intensity cells to moderate intensity cells. This represents 61% of the low intensity cells within the watershed. Likewise, for the best case scenario, the addition of 1145.4 m^2 of impervious area would result in the conversion 3818 low intensity cells to moderate intensity cells. This represents 20% of the low intensity cells within the watershed.

The assumption was made that the conversion of low intensity to moderate intensity development would be distributed evenly throughout the watershed. Therefore, within every census block, the 20% and 61% of the area defined as low intensity development will be converted to moderate intensity development by 2100 for the best

case and worst case scenarios, respectively. Additionally, a small portion of the floodplain exists outside of the watershed. It was assumed that the same percentage of low intensity development within these census tracts would be converted to moderate intensity as well.

To conduct this conversion, the census tracts reported by HAZUS as being affected by the largest flood in the analysis were analyzed. The area of developed open space, low intensity, moderate intensity, and high intensity land cover were recorded. Then, for each census block, the 20% and 61% of the low intensity area was converted to moderate intensity area for the best and worst case nonstationarity scenarios, respectively. The results for each census block are shown in Tables 10-1 and 10-2 in Appendix D for the best and worst case nonstationarity scenarios, respectively.

5.3.3.5 Conversion of Projected Change in Developed Land to Projected Increase in Consequences

The final step was to adjust the consequences based on the increased development within each census block. The total economic loss and total number of people displaced was recorded for each individual census block. For the total economic loss, the property associated with each land cover type was assumed to be related to the average percent impervious area for the land cover classification (i.e. open equals 10%, low equals 35%, moderate equals 65%, and high equals 90%). Therefore, the increase in consequences was determined based on the assignment of weights to each land cover type. Open space was assigned a weight of 1, low intensity was assigned a weight of 3.5, moderate intensity was assigned a weight of 6.5, and high intensity was assigned a weight of 9. Then, for each census block, the consequences were assumed to increase based on the following equation:

$$\Delta Consequences = \frac{\sum_{i=1}^{4} W_i * A_i}{\sum_{j=1}^{4} W_j * A_j} \quad \text{Eq. 5-5}$$

where ‘i' refers to the land cover classification in the year 2100; ‘j’ refers to the land cover classification in the year 2010; W = weight assigned to the specified land cover classification; A = area of the census bloc. Therefore, as the area of the moderate intensity area increases and the area of the low intensity area increases, the greater weight of the moderate intensity development will be multiplied by a greater area. The result is an increase in consequences that corresponds to the increase in development.

For the best case nonstationarity scenario, the population density within the study region is expected to increase by 11.8%. For the worst case nonstationarity scenario, the population density is expected to increase by 67.5%. It was assumed that the increase in population density would be evenly distributed throughout the study region. Therefore, for the best and worst case nonstationarity scenarios, the estimated number of displaced people for the stationary 2010 scenario would increase by 11.8% and 67.5%, respectively.

Tables 10-3 and 10-4 in Appendix D show the adjustments of the total building loss ($ millions) for each census block for the best case nonstationarity scenario and the 100-yr and 500-yr floods, respectively. Tables 10-5 and 10-6 in Appendix D show the adjustments of the total building loss ($ millions) for each census block for the worst case nonstationarity scenario and the 100-yr and 500-yr floods, respectively. Tables 10-7 and 10-8 in Appendix D show the adjustments of the total people displaced for each census block for the best case nonstationarity scenario and the 100-yr and 500-yr floods, respectively. Tables 10-9 and 10-10in Appendix D show the adjustments of the total

people displaced for each census block for the worst case nonstationarity scenario and the 100-yr and 500-yr floods, respectively.

5.3.4 Results for Risk Assessment without Mitigation System

Figure 5-7 and 5-8 show the total economic loss ($ millions) and total number of people displaced, respectively, for each of the three scenarios analyzed and the 100-yr and 500-yr return periods. Table 5-5 shows the total economic loss ($ millions) and total number of people displaced for each scenario and return period analyzed. For the best case scenario, the total economic loss is projected to increase by 26.6% and 19.8% for the 100-yr and 500-yr floods, respectively. Likewise, the number of displaced people is projected to increase by 17.1% and 21.0% for the 100-yr and 500-yr floods, respectively. For the worst case scenario, the total economic loss is expected to increase by 55.2% and 39.5% for the 100-yr and 500-yr, return periods. The number of displaced people is expected to increase by 41.5% for both return periods. Therefore, if nonstationary factors are not incorporated into a risk assessment, the potential consequences are underestimated considerably for both the best case and worst case nonstationary scenarios.

Comparison of the increase in consequences as a result of nonstationarity provides insight into the sensitivity of the system to the nonstationary climate and urbanization factors. For example, a 25.8% increase in the peak discharge was projected for the best case scenario 100-yr flood, which resulted in a 26.6% increase in the total economic loss. Likewise, a 39.9% increase in the peak discharge projected for the worst case scenario resulted in a 55.2% increase in the total economic losses estimated. For the 500-yr flood, a 28.4% and 37.1% increase in the peak discharge was projected for the

best and worst case scenarios, respectively, which resulted in a 21.0% and 39.5% increase in the estimated economic loss. With the exception of the best case 500-yr flood, the estimated percent increase in the building loss was greater than the corresponding percent increase in the peak discharge. These results suggest that the study region is highly sensitive to the nonstationary factors analyzed. Therefore, it is important to consider nonstationary factors in risk assessment to ensure that the sensitivity of the potential consequences are understood and appropriate action for flood mitigation can be considered.

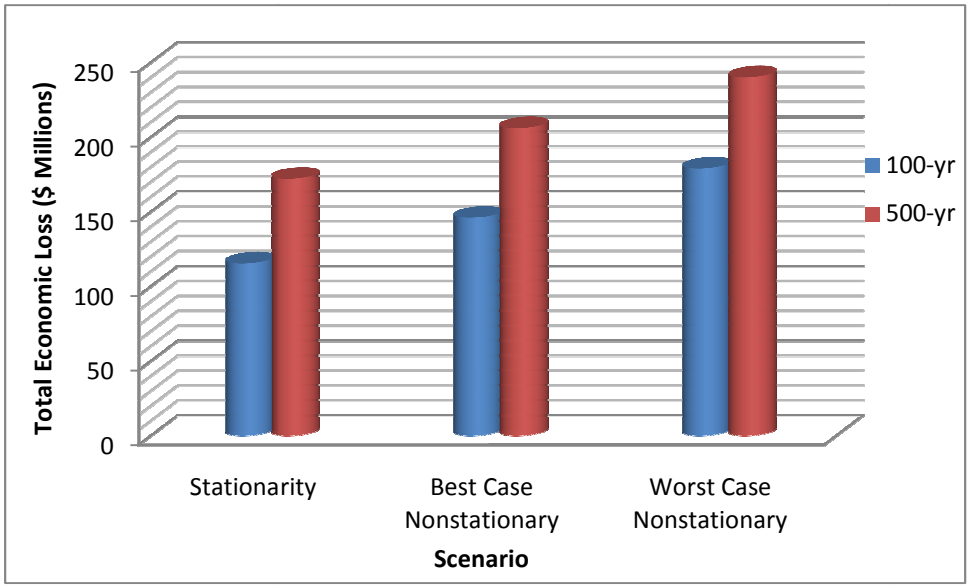

Figure 5-7. Total Loss ($ millions) for Stationarity, Best Case Nonstationarity, and Worst Case Nonstationarity Scenarios for the Year 2100 and the 100-yr and 500-yr Floods.

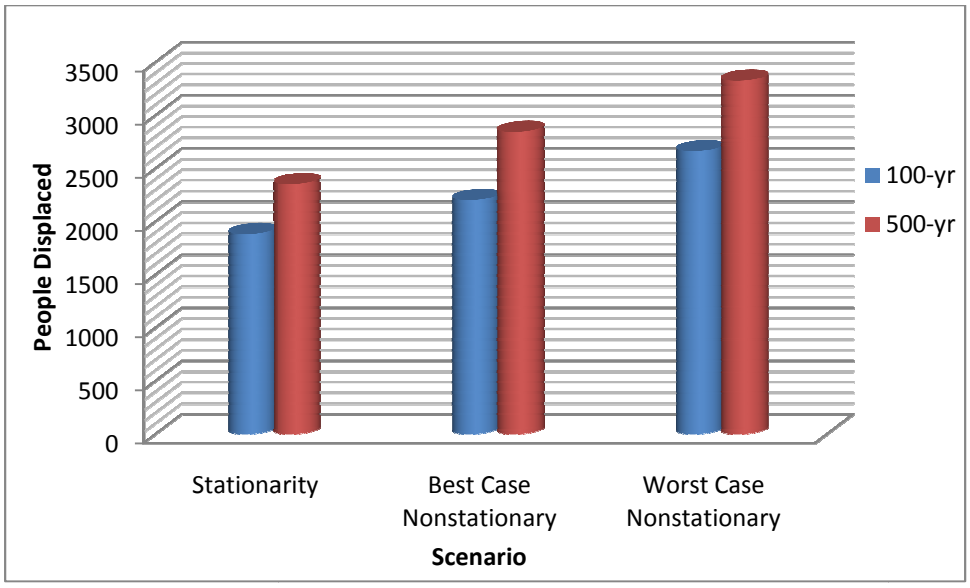

Figure 5-8. People Displaced for Stationarity, Best Case Nonstationarity, and Worst Case Nonstationarity Scenarios for the Year 2100 and the 100-yr and 500-yr Floods.

Table 5-5. Total Loss and People Displaced for Stationarity, Best Case Nonstationarity, and Worst Case Nonstationarity Scenarios for the Year 2100 and the 100-yr and 500-yr Floods.

	100-yr Flood		500-yr Flood	
Scenario	**Total Economic Loss ($ Millions)**	**Total People Displaced**	**Total Economic Loss ($ Millions)**	**Total People Displaced**
Stationarity	115	1881	172	2351
Best Case Nonstationary	146	2202	206	2844
Worst Case Nonstationary	179	2662	240	3326

5.3.5 Implementation of Mitigation System

With the consequences and associated risks calculated for each scenario, the next step in the risk assessment was to implement the mitigation system. The mitigation system consists of zoning laws that would prohibit further development within the 100-yr

floodplain. This area will be referred to as the Special Protection Area (SPA), but is equivalent to the 100-yr floodplain based on the assumption of stationarity. If this mitigation system were implemented, then the consequences within the Special Protection Area would remain the same as those estimated with the default HAZUS data for the year 2006 for the stationarity scenario. However, for scenarios that resulted in a floodplain with area outside the SPA, the consequences outside the SPA would be assessed based on the adjusted consequences for 2100 development conditions and inside the SPA would be assessed based on the 2010 development conditions.

5.3.5.1 Development of Depth-Damage Relationship

The expected damage within a floodplain is dependent on the depth of flooding that occurs. The United States Army Corps of Engineers New Orleans District provides tabled values for the percent damage associated with specific depths of flooding for different types of residential and commercial buildings (GEC 2006). HAZUS reported that in the study region, 92% of the building stock consisted of residential buildings. Therefore, the residential depth-damage was used to estimate the percentage of damage inside and outside the special protection area. The two story residential building constructed on slab rather than piers was selected to represent the housing type in Howard County. The depth-damage values are shown in Table 5-6 and Figure 5-9.

The percent damage values were provided for both short and long term flooding. The percent damage values varied by less than 2% for each depth between these two categories; therefore, depth-damage curve for short term flooding was selected for the purpose of this study, as long term flooding is not common in Maryland. The following function was fit to the depth-damage data:

$$D = 5.5 + 22*d^{0.3} \quad \text{Eq. 5.6}$$

where d = depth of flooding (ft) and D equals the percent damage. The model provides a near zero relative bias equal to 0.01. The coefficient of determination equals 0.95, which implies that 95% of the variation is explained by the model. The standard error ratio equals 0.32, which shows that the model provides a better prediction than the mean damage value.

Table 5-6. Depth-Damage (%) Values from GEC (2006) for 2 Story Residential Building on Slab.

Depth (ft)	Short	Long
0	5.5	5.6
0.5	18.1	18.5
1	23.1	24.4
1.5	23.8	25.2
2	26.8	28.4
3	29.0	30.7
4	36.8	38.6
5	39.4	40.8
6	40.0	41.4
7	40.3	41.7
8	43.3	44.5
9	52.5	54.2
10	54.6	56.1
11	55.4	57.1
12	57.2	58.8
13	59.2	60.7
14	59.2	60.7
15	59.3	60.8

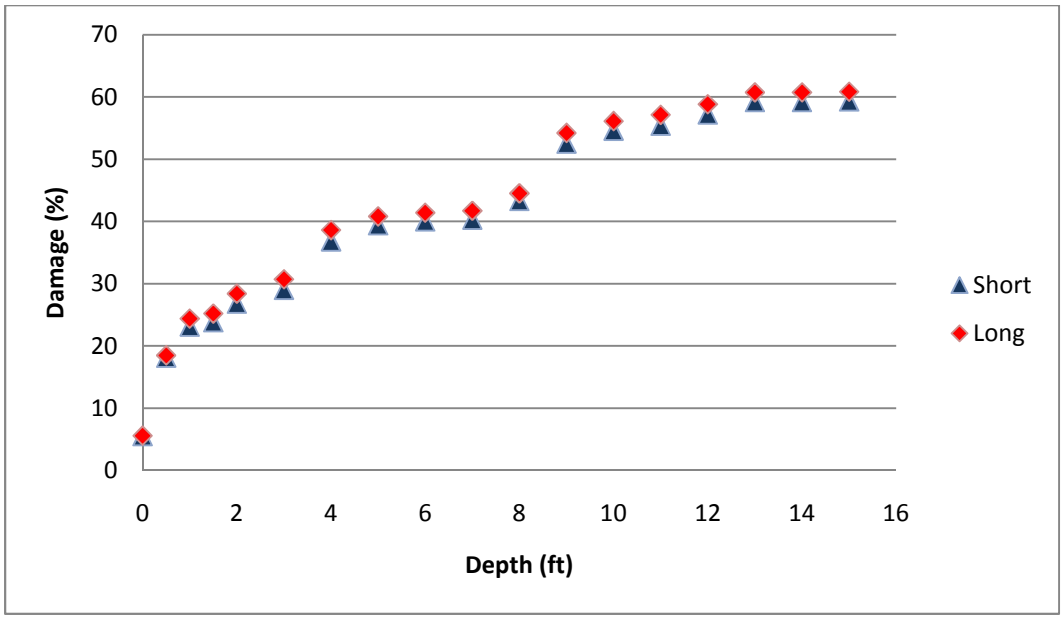

Figure 5-9. Depth (ft) - Damage (%) Curve from GEC (2006) for Two Story Residential Building on Slab.

5.3.5.2 Analysis of Flood Depths within Floodplain Areas Inside and Outside SPA

Because the depth-damage model is nonlinear and the flood depths are not uniformly distributed throughout the floodplain, it was necessary to analyze the flood depths both inside and outside the SPA for each floodplain and scenario. For each scenario, the floodplain areas located within the SPA and outside the SPA were extracted from the entire floodplain and analyzed individually. Figure 5-10 shows an example for the worst case scenario 500-yr flood in which the area within the SPA and outside the SPA has been differentiated. Figures 10-4 through 10-7 in Appendix D provide figures for the additional scenarios and return periods. Then, for each census block, the area of the floodplain within the SPA and the area of the floodplain outside of the SPA were retrieved.

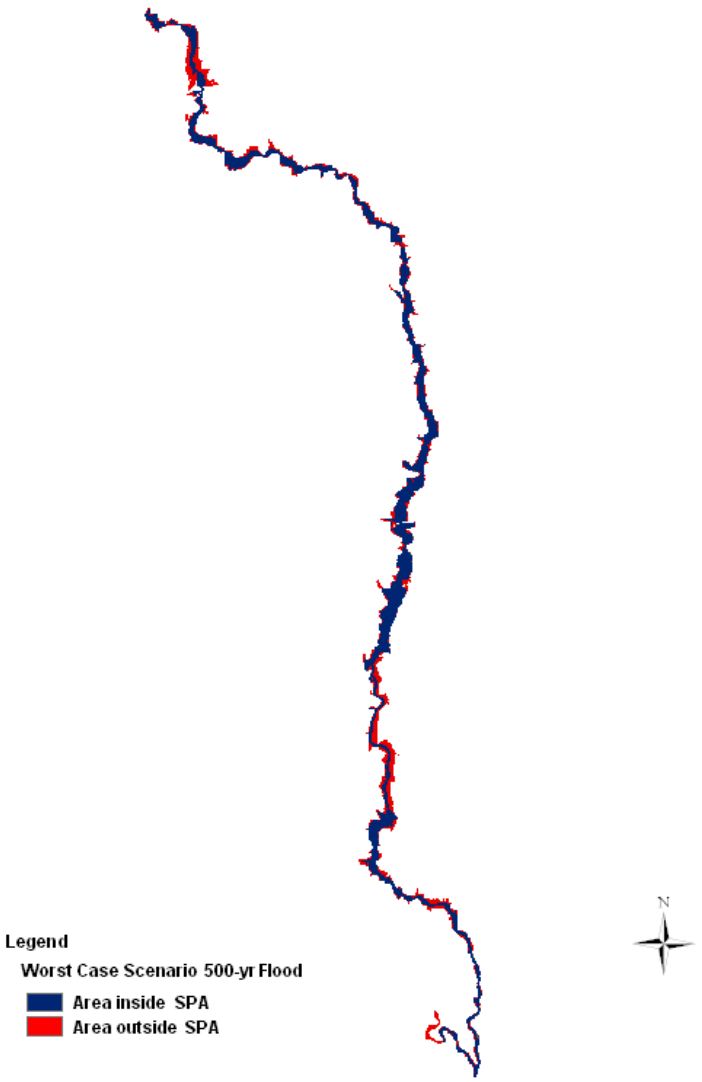

Figure 5-10. Area Inside and Outside of SPA for Worst Case Scenario 500-yr Flood

The flood depths within each portion of the total floodplain for each scenario were analyzed. The mean and standard deviation of the flood depths within each floodplain are shown in Table 5-7. The flood depths were retrieved for each scenario and the depth-damage model was used to estimate the proportion of the damage within each census block that occurred within the SPA and outside the SPA for each scenario. The results are shown in Table 5-8**.** As would be expected, the worst case scenario results in the greatest expected damage, followed by the best case.

Table 5-7. Statistical Characteristics of Flood Depths for each Scenario.

Scenario	Area Analyzed	Mean Flood Depth	Std. Dev.
Best Case 100	Entire Floodplain	7.24	4.47
	Within SPA	7.61	4.33
	Outside SPA	5.3	4.67
Best Case 500	Entire Floodplain	9.24	5.69
	Within SPA	10.86	5.1
	Outside SPA	5.53	5.2
Worst Case 100	Entire Floodplain	7.53	4.74
	Within SPA	8.14	4.53
	Outside SPA	4.97	4.71
Worst Case 500	Entire Floodplain	9.74	5.85
	Within SPA	11.31	5.18
	Outside SPA	6.09	5.74
Observed 500	Entire Floodplain	8.51	5.25
	Within SPA	9.47	4.8
	Outside SPA	1.33	3.5
Observed 100 (SPA)	Entire Floodplain	6.91	4.76

Table 5-8. Expected Percent Damage based on Simulated Flood Depths and Depth-Damage Model for each Scenario and Return Period.

		Expected Damage (%)
Best Case 100	**Inside SPA**	44.7
	Outside SPA	38.4
Best Case 500	**Inside SPA**	49.6
	Outside SPA	39
Worst Case 100	**Inside SPA**	45.6
	Outside SPA	37.8
Worst Case 500	**Inside SPA**	50.2
	Outside SPA	39.9

5.3.5.3 Method of Adjustment for Mitigation System

The developed depth-damage model and simulated flood depth distributions for each scenario were then used to determine the expected change in consequences with the implementation of the mitigation system or the Special Protection Area. For each scenario and return period analyzed, the expected percent damages were calculated for the floodplain area within the SPA and the floodplain area outside the SPA based on Equation 5-7. Then, the proportion of the consequences within each census block that would be estimated based on 2010 inventory and 2100 development conditions was determined based on the following equation:

$$Fraction\ of\ Consequences = \frac{\overline{D_1} * A_1}{\overline{D_1} * A_1 + \overline{D_2} * A_2} \qquad \text{Eq. 5-7}$$

where the indices 1 and 2 refer to either the floodplain area inside or outside the SPA, depending on which calculation is being conducted; $\overline{D}$ is the expected percent damage based on the flood depth distribution for the designated index; and A is the area for the designated index.To determine the proportion of the consequences that will be estimated based on the 2010 inventory, index 1 would equal the area of the floodplain within the SPA. Likewise, to determine the proportion of the consequences that will be estimated based on the 2100 projected increase in inventory, index 1 would equal the area of the floodplain outside of the SPA. This equation was applied to each census block, using the areas of each portion of the floodplain inside the census block. The results are shown in Table 10-11 and 10-12 in Appendix D for the best case nonstationarity scenario and the 100-yr and 500-yr flood, respectively, and Tables 10-13 and 10-14 the Appendix D for the worst case scenario and the 100-yr and 500-yr flood, respectively.

The final step was to calculate the combined consequences that would occur both inside and outside of the SPA for each census block and for each scenario. The calculated proportions shown in Tables 10-13 and 10-14in Appendix D were applied to the consequences provided by HAZUS for each scenario based on the building inventory and census data used for the 2010 conditions and the adjusted consequences for the 2100 conditions for each census block based on the following equation:

$$\text{Total Consequences for Census Block} = C_1 * F_{1+} C_2 * F_2 \qquad \text{Eq. 5-8}$$

where C_1 = the consequences estimated for the census block based on the 2010 conditions; F_1 = the proportion of the consequences estimated to occur within the SPA; C_2= the consequences adjusted for the census block based on the 2100 conditions; and F_2 = the proportion of the consequences estimated to occur outside the SPA. The total consequences for each scenario with the mitigation system implemented equaled the sum of the total consequences for each census block.

5.3.6 Results for Risk Assessment with Mitigation System

The estimated consequences with the implementation of the development zoning mitigation system are shown in Table 5-9. It is apparent that the implementation of the special protection error reduces the consequences for both nonstationarity scenarios and return periods analyzed. For the best case scenario, the total loss was reduced by 5.5% and 4.4% for the 100-yr and 500-yr flood, respectively. Likewise, the number of people displaced was reduced by 6.0% and 5.1% for the 100-yr and 500-yr floods, respectively. For the worst case scenario, the total loss was reduced by 14.0% and 12.1% for the 100-yr and 500-yr return periods. The number of people displaced for the worst case scenario was reduced by 15.6% and 13.1%, respectively, for the 100-yr and 500-yr floods.

While the consequences were reduced, it is clear that the consequences assessed for the stationary scenario continue to noticeably under predict the nonstationary scenarios. The total loss for the best case scenario is still 16.4% and 12.7% greater than the stationary scenario for the 100-yr and 500-yr floods, respectively. For the worst case scenario, the total loss is under estimated by 25.1% and 18.5% for the 100-yr and 500-yr floods, respectively. The total number of people displaced is underestimated by 9.1% and 12.9% for the 100-yr and 500-yr floods, respectively, for the best case scenario, and 16.3% and 18.6% for the 100-yr and 500-yr floods, respectively for the worst case scenario. This is because the 100-yr floodplains for the nonstationary scenarios extend beyond the Special Protection Area determined based on stationary conditions for the 100-yr flood. Therefore, while the mitigation system reduces the consequences for the 2100 design scenario, the implementation of a system that takes into account the changing 100-yr floodplain under nonstationary conditions would be more effective.

Table 5-9. Estimated Consequences for each Scenario and Return Period With and Without a Mitigation System.

		Stationary Scenario	Best Case Scenario		Worst Case Scenario	
T	**Category**		**Without System**	**With System**	**Without System**	**With System**
100-yr	**Total Economic Loss ($ Millions)**	115	146	138	179	154
	Total People Displaced	1881	2202	2070	2662	2248
500-yr	**Total Economic Loss ($ Millions)**	172	206	197	240	211
	Total People Displaced	2351	2844	2700	3326	2889

5.4 Discussion of Risk Assessment

The method conducted in this study provides a multinonstationary approach to risk assessment. While the results showed noticeable changes in the consequences associated with the design floods, it is apparent that the study region selected for this research consisted of a small watershed for such a detailed risk assessment. The HAZUS program works on a census block basis. Therefore, consequences are estimated based on the percentage of the hazard within the census block. However, the approach used in this study can be replicated for larger watersheds where the risks may be greater and climate change and urbanization will have a more significant hydrologic effect. In a larger watershed, the consequences will show a more significant change from the stationarity to the nonstationarity scenarios.

Additionally, the topography within the region of study is fairly steep. Therefore, the floodplain did not experience much change between the different scenarios, despite an increase in the peak discharges. The result was an increase in flood depth rather than the floodplain area. While this resulted in greater consequences based on the depth-damage curve method applied within the HAZUS program, the mitigation system was not as effective as expected between nonstationarity and stationarity conditions. However, in flatter areas and a larger watershed, the scenarios would most likely show a greater difference in floodplains and the zoning for the 100-yr floodplain would show a greater reduction in risk.

6 Conclusions and Recommendations

6.1 Introduction

Recent events and existing research suggest that nonstationary factors are influencing the characteristics of hydrologic data. Studies have shown the effects of greenhouse gases on climate and, therefore, the hydrologic cycle. Characteristics of precipitation data are expected to change throughout the 21st century, with the effects varying spatially. Likewise, urbanization continues to influence the runoff characteristics within watersheds. As land development occurs, infiltration capabilities within the watershed decreases, which results in more runoff. As runoff is dependent on precipitation as well as land cover characteristics, future climate change and urbanization are expected to contribute to nonstationary characteristics of flood data.

Current policies and design methods for flood management are based on the 100-yr flood derived from a flood frequency analysis. The current method of conducting a flood frequency analysis, however, assumes stationarity. Therefore, as climate change and urbanization continue to influence characteristics of hydrologic data, the effectiveness of existing methods will most likely diminish. For example, a levee designed for a 100-yr storm based on observed data will most likely not perform as expected as the magnitude of the flood associated with the design return period increases with nonstationarity.

The goal of this study was to enhance the current state of knowledge related to the detection and modeling of nonstationarity in hydrologic processes. This goal was achieved through the development of a statistical test to detect change points within a time series, the development and application of a method to adjust a flood frequency

series for future nonstationary conditions, and a procedure for the assessment of risks associated with nonstationary flood frequency series.

6.2 Discussion of Uncertainties

It is important to note that the analyses conducted within this study contain uncertainties. Uncertainties exist in each of the future urbanization and climate change scenarios developed for this study. The IPCC states that the emissions scenarios adopted for use in research, designated as A2, A1B, and B1, are not assigned any probability of occurrence. They were developed to provide a foundation upon which climate change studies could be compared and represent three potential ranges of future emission rates. Likewise, the projected changes in population density and, therefore, urbanization are based on projections by Maryland State Planning; however, a variety of other potential changes in urbanization could occur during the twenty-first century. Therefore, the accuracy of any of these scenarios existing in the future would be difficult to assess.

In addition to uncertainties within the urbanization and climate change scenarios, uncertainties exist within the models used in this study. GCMs are assessed based on their ability to reproduce observed twentieth century climate conditions; however, much uncertainty still exists in regards to the representation of physical processes within the models and, therefore, the accuracy of predicted future climate responses to greenhouse gas emissions and aerosols. The approach developed within this study consisted of an adjustment method to reduce these uncertainties by incorporating the change in the simulated and projected data over time rather than the actual data values; however, uncertainties still exist in the magnitude of change predicted by the model. Uncertainties also exist within the conversion from precipitation to runoff. While the NRCS method is

a widely accepted hydrologic model, the method greatly simplifies the physical processes involved. Finally, uncertainties are introduced in the risk assessment through the many assumptions included in the HAZUS model methodology. Therefore, uncertainties exist within both the developed climate change and urbanization scenarios and the model components in this study.

The uncertainties associated with the developed model can be reduced through further research. As science advances, the ability of GCMs to predict precipitation events will improve. Additionally, a comparison of existing GCMs will provide a greater insight into the variation of the precipitation projections between models and the optimal precipitation estimates to incorporate in the development of the climate change adjustment method. The implementation of a more sophisticated rainfall-runoff model into the method will reduce the uncertainty introduced by both the NRCS method and Moglen and Shiver's (2006) model. The adjustment for different urbanization scenarios can be analyzed directly with the rainfall-runoff model. The risk analysis can be conducted based on a higher level of risk assessment within the HAZUS model to provide additional information in regards to the consequences and the floodplain within the watershed analyzed; however, this requires additional inputs that may themselves be uncertain. Each of these components will minimize the uncertainties within the developed model, however, the future climate change and urbanization scenarios will still remain unknown.

The results from this study were not meant to be absolute predictions of future hydrologic or economic changes and, therefore, the associated risks. Emphasis should be placed on the procedures developed to relate GCM model outputs to flood risk estimates.

The many uncertainties that exist within components in this developed method are apparent. However, application of the developed approach will provide a better understanding of the sensitivity of a watershed to potential future climate change and urbanization conditions. The findings from this study are meant to begin a discussion among engineers, scientists, and policy makers about the potential changes and the associated risks that nonstationarity may bring, and to provide a method that considers recent scientific observations to promote well-informed risk management decisions.

6.3 Change Point Test

The first objective was to develop a statistical test to aid in the detection of nonstationarity. Many factors influence hydrologic data. As these factors begin to affect the data at a given period in time, the statistical characteristics of the data may be altered and the time series will become nonstationary. This will influence the frequency distribution and parameter values selected to represent the data. It is important that scientists and engineers have a thorough understanding of the time at which these outside factors begin to significantly affect the measured data in order to provide statistical models of the data.

Existing methods to detect a change point depend on the assumption that no more than one change point exists within the data (Reeves et al. 2007). As previously discussed, the future will likely consist of multiple nonstationary factors that will influence hydrologic data. Likewise, an individual factor, such as urbanization, may not continue to influence the time series for the entire duration following the initial effect. Therefore, to accurately assess the individual effects of these multiple factors and,

therefore, model hydrologic data based on potential future conditions, a method to detect multiple change points within a time series is needed.

The breakpoint test developed in this study will aid in the detection of change points within a time series. The theory behind the developed test is that change points within a time series will result in a change in the slope of sub-samples within the data. The slope of the data is directly related to the correlation coefficient between the flood magnitudes and time. Therefore, if the correlation coefficients for different sub-samples within the entire time series are calculated and converted to Z-values through the Fisher's 'Z' transformation, the variance between the Z-values can be calculated. The null hypothesis of equal slopes and, therefore, no significant change is most likely rejected at the times when the test statistic is maximum. If the sub-samples are divided at the true but unknown change point locations, then the variance of the Z-values for the sub-samples will be at a maximum value.

New critical values were needed for the test statistic as the independent variable of the time series is not a random variable, i.e., time is an integer, uniformly distributed variable. Critical values were developed and verified for the test statistic. The test statistic was then verified using simulated data. Analysis of the response surface of the calculated Z-values for varying sub-samples within a time series proved that the theory behind the test statistic holds for multiple change points. These findings improve upon the existing change point tests that fail to identify more than one change point within a time series. The developed statistical test will aid scientists and engineers in the identification of change points within hydrologic data in order to provide optimal modeling accuracy.

6.4 Nonstationarity Adjustment Method

A method was developed to account for nonstationary conditions in a flood frequency series. The method combines traditional statistical methods used in hydrology with both theoretical and empirical projections of future conditions. The future conditions were based on two nonstationary factors: (1) climate change and (2) urbanization.

The method required the development of three components: (1) the adjustment of a precipitation record for a selected climate change scenario; (2) the conversion of the precipitation data to a peak discharge value for the selected watershed; and (3) the adjustment of the resulting peak discharge value for future urbanization scenarios. The climate change adjustment component was developed based on the expected change in the precipitation distribution. The expected change was modeled on daily precipitation projections from a GCM for the twentieth and twenty-first century provided through the CMIP3 multi-model data set for three emissions scenarios. The conversion from a precipitation depth to a peak discharge for a selected watershed was conducted based on the NRCS method. The adjustment for urbanization scenarios was developed based on the USGS urbanization equations provided by Moglen and Shivers (2006).

The method was then applied to the Guilford Watershed in Howard County, Maryland. Three climate change emission rate scenarios were analyzed as well as two potential urbanization scenarios for the twenty-first century. The observed peak discharge record for the Little Patuxent River in Guilford, Maryland, was adjusted to design years ranging from 2010 to 2100. Stationary flood frequency analyses were then developed for the design years 2050, 2075, and 2100 to compare peak discharges

associated with selected return periods to those under the nonstationary conditions that would reflect a measured record.

The results for the Guilford, Maryland analysis showed that for the 100-yr flood, failure to account for multinonstationarity will result in a noticeable underprediction of peak discharge rates. Depending on the climate change and urbanization scenario, the 100-yr flood was underestimated from 25.8% to 39.9% for the design year 2100 when the assumption of stationarity was incorrectly made. Likewise, the 500-yr flood was underestimated from 28.4% to 37.1%, depending on the climate change and emissions scenario, for the 2100 design year when nonstationarity was not taken into account. These noticeable differences in peak discharge estimates prove the importance of accurately modeling nonstationarity for future flood mitigation. The performance of flood structures designed based on assumed stationary conditions is likely to decline as nonstationarity increases the magnitude of the flood associated with a selected return period.

6.5 Risk Assessment

The final component of the study consisted of a risk assessment using FEMA's HAZUS program. This risk assessment approach was based on the method used by the IPET in the analysis of the New Orleans and Southern Louisiana Hurricane Protection System following Hurricane Katrina (USACE 2009a). The 100-yr and 500-yr floods were analyzed based on three scenarios: (1) stationarity; (2) best case nonstationarity; and (3) worst case nonstationarity. The HAZUS program was used to define the hazard for each event, or the flood depth, and estimate the consequences that would results. The

consequences associated with the 100-yr and 500-yr return period were then calculated and compared for the three scenarios.

In addition to the comparison of consequences associated with stationary and nonstationary conditions, the effectiveness of a mitigation system incorrectly designed with the assumption of stationarity was assessed. The mitigation system consisted of zoning laws to prohibit further development within the 100-yr floodplain designed based on stationary conditions, referred to as the Special Protection Area. The stationary 100-yr flood was selected as the design criteria because it is the most common return period upon which flood mitigation systems and policies are based. The reduction in consequences with the implementation of the mitigation system was then assessed.

The risk assessment was conducted for the design year 2100. The results showed that, if nonstationarity is not accounted for, the consequences for the 100-yr and 500-yr flood will be noticeably underestimated. For the 100-yr flood, the total building loss would be underestimated by 26.6% and 55.2% for the best case and worst case nonstationary scenarios, respectively, when nonstationarity was ignored. For the 500-yr flood, the total building loss was underestimated by 19.8% and 39.5% for the best case and worst case nonstationary scenarios, respectively. Likewise, the number of people displaced was underestimated by 17.1% and 21.0% for the 100-yr and 500-yr floods, respectively, for the best case scenario and41.5% for both the 100-yr and 500-yr floods for the worst case scenario when nonstationarity was ignored. Therefore, if nonstationary factors are not incorporated into a risk assessment, the potential consequences will be very significant from the standpoint of public welfare and safety.

The implementation of the mitigation system, in which development is prohibited within the Special Protection Area, proved to mitigate the consequences for each scenario. However, the resulting consequences were still greater for the nonstationary scenario than for the stationary scenario because the floodplain extends beyond the Special Protection Area. The results showed that the mitigation system reduced the total losses by 5.4% and 4.4% for the 100-yr and 500-yr flood, respectively, for the best case scenario and 14.0% and 12.1%, respectively, for the 100-yr and 500-yr return periods for the worst case scenario. Likewise, the number of people displaced was reduced by 6.0% and 5.1% for the 100-yr and 500-yr floods, respectively, for the best case scenario and 15.6% and 13.1%, respectively, for the 100-yr and 500-yr floods for the worst case scenario.

While the system reduced the consequences, estimates made based on stationary conditions still greatly underestimated the consequences associated with each of the nonstationary conditions regardless of the implemented system. The total loss for the best case scenario is still 16.4% and 12.7% greater than the stationary scenario for the 100-yr and 500-yr floods, respectively. For the worst case scenario, the total loss is underestimated by 25.1% and 18.5% for the 100-yr and 500-yr floods, respectively. The total number of people displaced is underestimated by 9.1% and 12.9% for the 100-yr and 500-yr floods, respectively, for the best case scenario, and 16.3% and 18.6% for the 100-yr and 500-yr floods, respectively for the worst case scenario. Therefore, unless nonstationarity is accounted for in the design of mitigation systems, the reduction in consequences will be greatly underestimated for future conditions.

While risk assessment is practiced by many agencies, the application to compare multinonstationarity conditions has not been conducted. The nonstationary application of a risk assessment shown in this study can be used to test the sensitivities of a community to a range of potential future climate change and urbanization scenarios. As a result, stakeholders can make better informed decisions in regards to flood mitigation for an uncertain future.

6.6 Conclusion

Through this research, methods to detect and model multinonstationarity in hydrologic data as well as to assess risks for a nonstationary future were developed. A statistical method to detect change points was developed to improve the modeling of a multinonstationary time series. A method to adjust measured flood series for the changing influences of urbanization and climate change to a state that reflects conditions over the design life of a project was both developed and applied. Finally, a multinonstationary risk assessment method was demonstrated to show the effect of failing to account for nonstationarity. These advancements in the state of the art will aid both engineers and policy makers in understanding and planning for nonstationary conditions in the future.

Flood management designs and policies can be adapted based on the analysis of the sensitivities of a particular watershed to climate change and urbanization. If estimates show that urbanization will cause a certain increase in risk, zoning laws can be implemented today rather than tomorrow to mitigate this risk. If the sensitivity of flooding based on established emission rates can be determined, policy makers can attempt to control emissions to meet the set rates by the year 2100. If the sensitivities of

the system are understood, the factors could potentially be controlled to mitigate the consequences. While it may be difficult to predict the future, through methods such as those proposed in this study, the range of possibilities will be better understood to ensure that well informed decisions are being made to mitigate risks in a nonstationary environment.

6.7 Future Research

While the results of this research greatly improve the current methods for the detection and modeling of nonstationarity as well as the assessment of the associated risks, future research is needed. The proposed further research in regards to the developed change point test, adjustment method for nonstationarity, and nonstationary risk assessment will be discussed herein.

6.7.1 Change Point Test

In addition to a nonparametric test, the test developed within this study can be improved through the development of additional critical values. This will improve the power of the statistical test in detecting change points within time series with high random variation. The critical values of the test were sensitive to the correlation coefficients of the individual sub-samples created by potential change point locations. Likewise, the test can identify multiple locations for change points that provided statistically significant test statistics. Therefore, determination of the distribution of the critical values would enable the rejection probabilities associated with each potential change point location rather than the critical values to be compared in order to best identify the change point locations.

Assessment of the constraints of the developed test would also be beneficial to ensure that the test is used appropriately. As was discussed by Reeves et al. (2007), the power of statistical tests can decrease when applied to data that does not meet the criteria for the test. It would be beneficial to understand the power of the developed change point test under specific data characteristics, such as the sample size and random variation, in order to better understand the likelihood of a type 2 error when applying the test to hydrologic data.

In addition to further research in regards to the test statistic developed for this test, a nonparametric multi-change point test would be beneficial as well. The change point detection test developed for this study assumes independent and normally distributed errors. However, for extreme hydrologic data, this assumption does not apply. Therefore, development of a nonparametric change point detection to detect multiple change points would be a beneficial addition to the statistical detection of changes in hydrologic data due to nonstationarity.

6.7.2 Adjustment Method for Nonstationarity

Much future research can be conducted to improve both the method developed for nonstationarity and the application of the method. For the climate change adjustment component, daily precipitation projections were analyzed from the CSIRO model for the twentieth and twenty-first centuries. The CMIP3 provides projections for additional models as well; however, not all models provide daily projections. As the field of climate science advances and daily precipitation projections become more available and reliable, it would be beneficial to apply this method to outputs from other climate models in order to provide a more complete analysis of the projected changes in precipitation.

Likewise, as advancements in GCMs continue, the ability of models to provide projections of extreme hydrologic data will improve and, therefore, increase the accuracy of the adjustments made with this method.

Based on existing studies and methods, the GEV distribution was selected to represent precipitation and the LP3 distribution was selected to conduct the flood frequency analysis. However, it would be beneficial to conduct a sensitivity analysis and determine the effect of the probability distribution on the adjustments in the peak discharge as well as the assessed risk. Identification of the appropriate distribution to represent hydrologic data is important to ensure the most optimal projections for future conditions.

The method developed in this study used the NRCS method to compute a peak discharge value from the adjusted rainfall. However, more advanced rainfall-runoff models could be applied. To increase the accuracy of the adjustments, a watershed specific rainfall-runoff model could be calibrated and applied. This would improve the estimates of the peak discharge series from the adjusted precipitation depths.

In addition to using a more complex rainfall-runoff model, consideration of factors such as antecedent moisture conditions when the rainfall is converted to runoff would greatly improve the model. The developed method selects the 24-hr precipitation depth associated with the day of the annual maximum peak discharge event. The assumption was made that the return periods of the computed peak discharge rate and the 24-hr precipitation depth would be the same. However, it is feasible that the 24-hr event does not represent the magnitude of the peak discharge event, but rather the antecedent moisture conditions due to previous wet days contributed to the increased runoff depth

and peak discharge. If only the 24-hr precipitation depth is adjusted, it is likely that the adjustment of the observed peak discharge event will be underestimated. Therefore, incorporating antecedent moisture conditions into the proposed method would improve the physical rationality of the calculated adjustment factors and, therefore, the resulting nonstationary flood frequency analyses and risk assessments.

While the method developed in this study was based on data from the Maryland, Delaware, and Virginia region, the method could be calibrated for additional regions. The method can be developed for different climatic regions through the retrieval of projected precipitation data for the region of interest. A region-specific adjustment factor can then be developed and applied based on the statistical characteristics of the precipitation distribution within that region. For areas in the southwest, low flows could be analyzed rather than peak discharge records by assessing the changes in precipitation and adjusting existing low flow records. Coastal flooding could also be analyzed and adjusted through a similar process. The method is adaptable for other regions and hazards, as it is based on data available to the public and models that are widely accepted in hydrology.

The projections provided through this method are subject to the uncertainties associated with the data inputs and the models developed and applied. While it is not possible to accurately assess the uncertainties of future climate projections, assessment of the uncertainties of the statistical and hydrologic models applied would provide additional information in regards to the potential range of future flood frequency scenarios. Uncertainties associated with the estimation of the GEV parameters for the precipitation distributions would provide greater insight into the range of potential

changes in precipitation based on each emissions scenario. For this study, the maximum likelihood method was used; however, additional methods are available and should be compared to determine the optimal method of estimating the GEV parameters. Likewise, a moving window method was applied to calculate the change in the parameters over time. This method could be improved through a more detailed sensitivity analysis to determine the optimal sample size or window length to calculate each GEV parameter.

6.7.3 Application of Method

In this study, method developed was applied to a small watershed in Howard County using basic input data. However, the accuracy of predictions could be improved if more accurate input data were available. Urbanization data can be retrieved from satellite images to replace the use of population density as an urbanization indicator for the USGS equations. Likewise, additional climate change and urbanization scenarios can be applied in order to provide a greater range of results and analyze the sensitivity of the system more thoroughly. The nonstationary factors can also be analyzed individually to compare the sensitivity of a watershed to climate change compared to urbanization. Each of these components would provide a more detailed analysis of the sensitivity of a watershed to multinonstationarity.

6.7.4 Risk Assessment

Risk assessment is an important component in the decision making for flood risk management. While the risk assessment was meant to provide a preliminary assessment of the sensitivities of the community to nonstationarity, a more sophisticated approach would be beneficial of future research. First, the HAZUS program can be applied at a more sophisticated level in order to assess the velocity hazard associated with flooding.

This would provide a more accurate assessment of the expected damage for a particular flood. Additionally, the study area only consisted of the Little Patuxent River; however, the Guilford watershed consists of additional first-order streams that drain into the Little Patuxent. Analysis of the consequences of nonstationarity in these additional streams would provide a more accurate assessment of the associated risks.

Projections for the future economic development within the watershed were made based on existing land use data and projected increases in population density following the guidelines provided by USACE (2009b). Then, the consequences based on the default inventory were adjusted accordingly for the nonstationary conditions in the design year 2010. However, it is possible to manipulate the inventory within the HAZUS, which would provide a more objective assessment of the consequences based on the projections developed.

Likewise, the application of this method to a larger watershed would provide the opportunity to analyze a more complicated mitigation system. For this study, zoning laws were implemented in order to assess the effectiveness of mitigation systems designed based on the assumption of stationarity. Additional systems, such as levees, can be analyzed within HAZUS to provide additional sensitivity analyses of communities and existing flood risk management methods to nonstationarity.

The assessment of the consequences for additional design years and return periods would provide a more thorough understanding of the potential risks over the twenty-first century for a selected community. The annualized risk can be calculated to provide policy makers with a cumulative risk estimate for a variety of potential floods. Likewise, the assessment of risks for additional design years would provide a time series of the

change in risk for different climate change and urbanization scenarios. It is important that risk be presented in a time span that will promote the optimal course of action in flood mitigation. The design life of many flood management structures does not extend to the year 2100. Therefore, providing an estimate of the change in risk over time will enable stakeholders to better understand how nonstationarity will affect communities in the near future.

7 Appendix A

The Kendall Tau test was adjusted in an attempt to develop a statistical test to detect multinonstationarity. Two different approaches were attempted: (1) Systematically apply the Kendall Tau test to sub-samples within the data and determine the largest sum of the resulting Z-statistics and (2) Systematically apply the Kendall Tau test to sub-samples within the data and determine the greatest difference between the resulting Z-statistics. The results will be discussed herein.

Approach 1

The first approach applied the Kendall Tau test over different parts of the entire time series. A matlab program was written to alter the location and duration within the actual data series to be analyzed. The program simulated 10,000 data samples with the following characteristics: (1) mean = 1,000; (2) standard error = 150; (3) length = 100; and (4) trend magnitude = 2. Then, the Kendall Tau test was systematically applied to each sample. First, the entire sample was analyzed (i.e., start time = 1 and duration = 100). Then the duration was decreased by increments of 10 until the sample size is decreased to 30. Next, the start time was increased by increments of 10 and the durations at this start time were decreased by increments of 10 accordingly. The Kendall Tau test was conducted for each sub-sample constructed from the original sample. At the end of the analyses, the program identified the greatest Z value calculated from each Kendall Tau analysis. The start time and duration associated with this Z value was stored in a vector. At the end of the 10,000 simulations, the mean of the start time and duration were analyzed. The results for various combinations of start times and durations are shown in Table 7.1.

Table 7-1. Estimated Start and Duration Results of Partial Duration Trend for Systematically Applying the Kendal Tau Test.

Partial Trend Characteristics		Estimated Start	Estimated Duration
Start	Duration	Mean	Mean
1	100	5.66	89.45
	75	6.50	82.98
	50	9.32	66.42
	25	19.60	48.30
25	75	11.34	83.53
	50	12.00	76.87
	25	16.60	59.33
50	50	25.04	66.36
	25	24.83	59.54
75	25	32.75	48.12

The results show that the duration was underestimated for the full duration sample; however, the duration of the remaining samples was consistently overestimated based on the maximum Z-value within the different sub-samples. The smaller the partial trend duration, the greater the duration is overestimated. The start times are overestimated for an actual start time of zero and underestimated for all other start times. Comparison of the three scenarios with an actual duration of 50 shows that when the trend of length 50 is centered in the data (i.e., starts at position 25 and ends at position 75) rather than occuring towards the beginning or end of the data series (i.e., starts at position 0 and ends at position 50 or starts at position 50 and ends at position 100), the estimate of the start time and duration are more accurate. This coincides with the results from the power analysis for partial duration trends in which the trends in the middle of the data resulted in greater power, implying a greater Z-value. These results suggest that the Z-value alone may not be an accurate representation of a partial trend within a time

series. It is apparent that inclusion of additional data values within a sample increases the Z-value resulting in a false trend.

Approach 2

The second approach was to again systematically create sub-samples within the data; however, this approach splits the entire sample into two sub-samples, applies the Kendal Tau test to each sub-sample, and calculates the difference between the two Z-values, Z1 and Z2. The hypothesis is that the span of the partial duration trend will have a greater difference in Z value from the span of the data that does not contain a trend. A potential breakpoint, or potential location of the transition between the trend and no-trend portion of the data, is first located at position 20 in the time series. This breakpoint divides the entire time series into two samples, S1 and S2. The Kendall Tau test is then applied to both S1 and S2 and the test statistics, Z1 and Z2, respectively, were stored in a vector. The absolute value of the difference between Z2 and Z1 was also stored in a vector. The potential breakpoint was then systemically shifted by an increment of 1 and the previous steps were repeated. The time series position (n-20) in the time series was the final breakpoint tested. This decision was made to ensure that each of the sub-samples consisted of at least 20 values.

After Z1 and Z2 are evaluated at each breakpoint, the greatest difference between the two is identified. For portions of the data in which a trend does not exist, the random variation is assumed to be evenly distributed and the resulting Z value will be zero. The portion of the data that contains the entire partial trend duration would then have the highest Z-value, and not contain any portion of the no-trend data. This would result in

the greatest difference between the Z-values and enable the actual breakpoint to be identified.

This procedure was applied to 1,000 simulations and the average Z1-value, Z2-value, and differences between at each breakpoint were calculated and compared. The characteristics of the data for each analysis are as follows: (1) mean = 1,000; (2) standard error = 25; (3) sample size= 100; (4) slope = 2; and (5) breakpoint at 50. The standard error was kept to a minimum to first explore how the Kendall Tau test would react to the partial duration trend without adding the complication of random variation.

Figures 7-1 and 7-2 show the values of Z1, Z2, and the Z1-Z2 difference for a sample with a partial duration trend beginning at position 0 and ending at position 50 and beginning at position 50 and ending at position 100, respectively. For both scenarios, the greatest difference between Z1 and Z2 would in theory occur at the 50^{th} position in the time series. However, Figure 7-1 suggests that the greatest difference in Z-values does not appear at the actual breakpoint. Instead, it appears (see Figure A-1) that the difference increases as the breakpoint increases. As the breakpoint increases, the length of S1 increases. S1 represents the trend portion of the data up to location 50 and any portion of the no-trend data after location 50. This implies that even if the increase in the length of S1 includes no-trend values, the additional values still increase the value of Z1. However, Z2, the no-trend portion of the data, converges to 0 at a breakpoint location of 50. This is expected and suggests that the Kendall Tau test is able to accurately identify a no-trend location. Since Z2 converges to zero while Z1 continues to increase, the greatest difference, Z1-Z2, occurs at the latest possible breakpoint. This implies that the method will inaccurately identify the breakpoint for a partial duration trend.

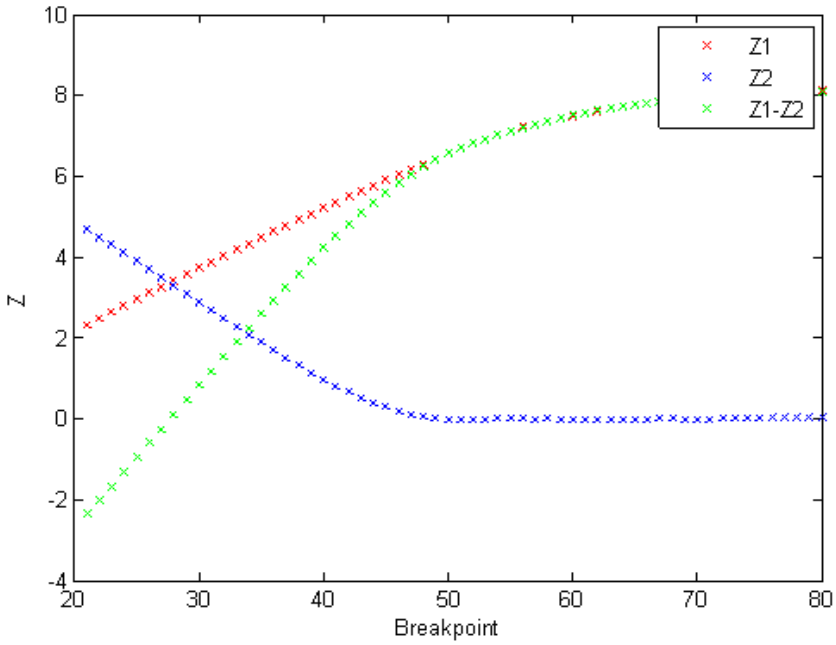

Figure 7-1. Z1, Z2, and Difference between for Sample with Partial Duration Trend from position 0 to 50.

Figure 7-2 shows similar results for the sample consisting of a partial duration trend beginning at position 50 and ending at position 100; however, the difference in Z-values now increases as the breakpoint decreases rather than as the breakpoint increases. For this analysis, S2 is the portion that contains the trend and decreasing the breakpoint lengthens S2. Z1 converges to 0 from the locations 0 to 50 within the entire sample, again implying that the method results in an accurate assessment of the no-trend portion of the data. Therefore, the findings are consistent with Figure A-1. The Z-value associated with the trend portion of the data increases as the sample increases and includes no-trend portions of the data. This results in an inaccurate estimate of the breakpoint based on the differences in Z-values at each potential breakpoint.

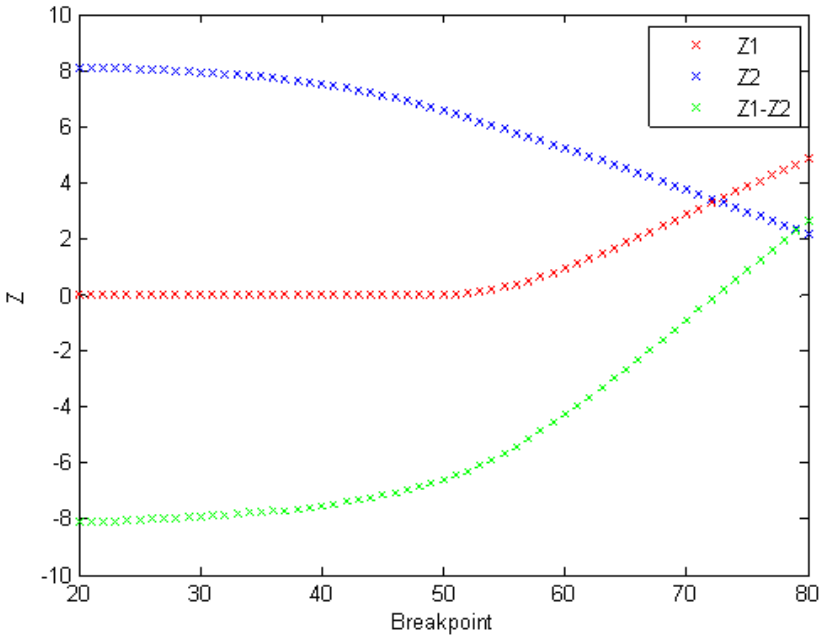

Figure 7-2. Z1, Z2, and Difference between for Sample with Partial Duration Trend from position 50 to 100.

Analysis of Kendal Tau Test Statistic under Partial Trend Duration Conditions

Further analyses were conducted to determine the factors that cause the Kendall Tau test statistic to increase in magnitude when no-trend portions of the data sample are included. The test statistic consists of two parts: (1) the S-value in the numerator and (2) the standard deviation of S in the denominator. The S-value represents the sum of concordances ('pluses') and discordances ('minuses') as each value in the sample is systematically compared to each other. To analyze the behavior of this test statistic under partial trends, a sample of length 100 was created with a partial trend from 0 to 50 and a trend magnitude equal to 20%. For this analysis, the standard error was set equal to zero to explore the test statistic under perfect trend and no- trend conditions. The sample was again systematically divided into sub-samples; however, the beginning of the sub-sample remained at the first position in the time series and the end of the sub-sample began at the

20th position and was increased by increments of 1. The end point is referred to as the breakpoint, as it would potentially be the end of the trend and beginning of the no-trend portion of the data. For each sub-sample, the Kendall Tau test was applied and the Z-value, S-value, and standard deviation were stored in vectors.

Figure 7-3 shows the Z-value for each sub-sample, identified by the breakpoint location. It is apparent that the Z-value is increasing beyond that of the trend, as was discovered in previous analyses. However, it is noted that the rate of increase in the Z-value is changing as the breakpoint shifts. The S-values and Standard Deviations of S are shown in Figures 7-4 and 7-5, respectively, to explain the changes in the Z-value.

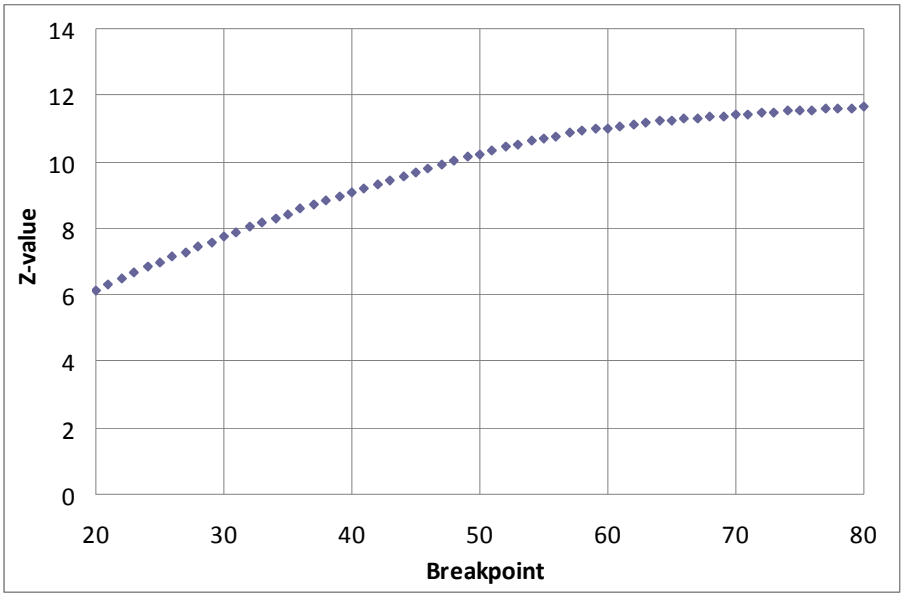

Figure 7-3. Z-value for Sub-samples defined by the Breakpoint.

It is apparent from the figures that the S-values are also increasing as the breakpoint increases. However, the rate of increase is non-linear from breakpoints 20 to 50 and linear from breakpoints 50 and greater. The standard deviation is increasing as

well; however, it is increasing at a slower rate than the S-value . This explains the increase in the Z-value as the breakpoint increases. With the S-value in the numerator and the standard deviation in the denominator of test statistic, the numerator is increasing at a faster rate and thus the Z-value is increasing.

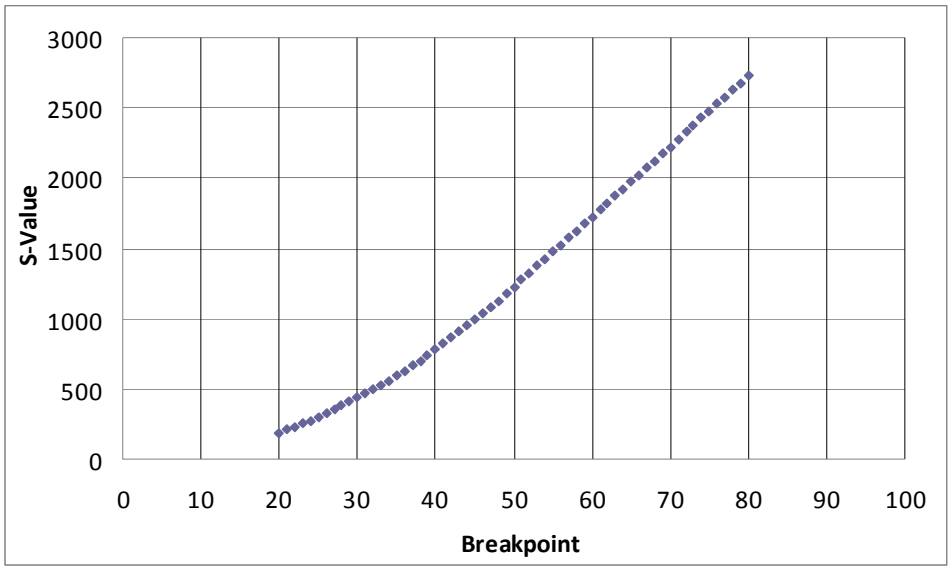

Figure 7-4. S-Value for Sub-samples defined by the Breakpoint.

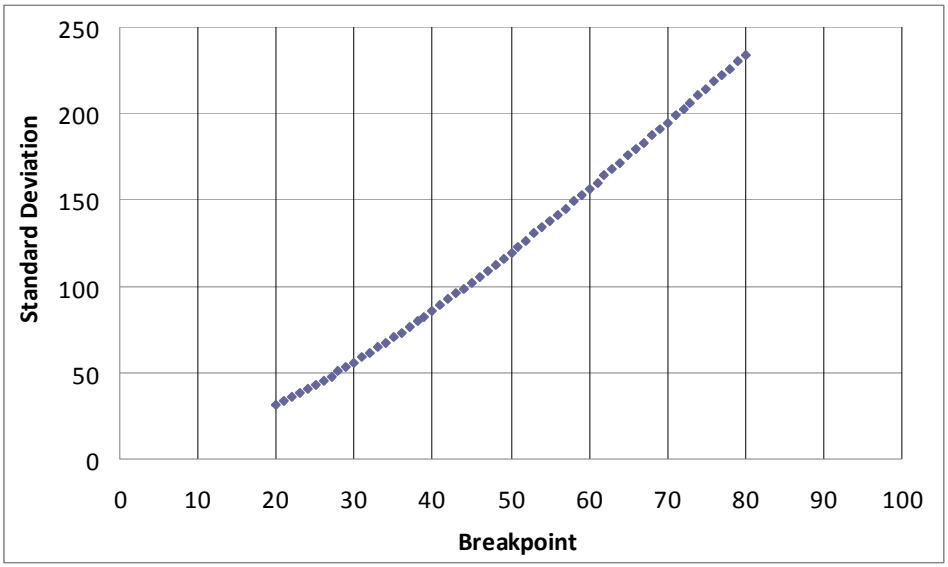

Figure 7-5. Standard Deviation of S-Values for Sub-sample defined by the Breakpoint.

The first derivative of the S-values was calculated to explore the rate of change of the S-value as the breakpoint changes. The results are shown in Figure 7-6. The first derivative, Delta S, increases at a linear rate from position 0 to 50; however, beyond the 50th breakpoint, Delta S stabilizes at 50. Further analyses of Delta S shows that where the trend occurs, the function of delta S versus sample size (which is defined by the breakpoint) is that Delta S equals one less than the sample size. This is rational because adding one value to the sample will create (n-1) additional comparisons between sample values. In a perfect trend, each of these comparisons will be a concordance or plus, resulting in an increase of (n-1) to the total S-value. Likewise, as the sample size or potential breakpoint extends beyond the actual breakpoint, 50, the increase in S stabilizes at a value of 50. This is also rational, because with each new value, 50 previous values will be of lesser value, adding a 'plus' value to the calculation of S.

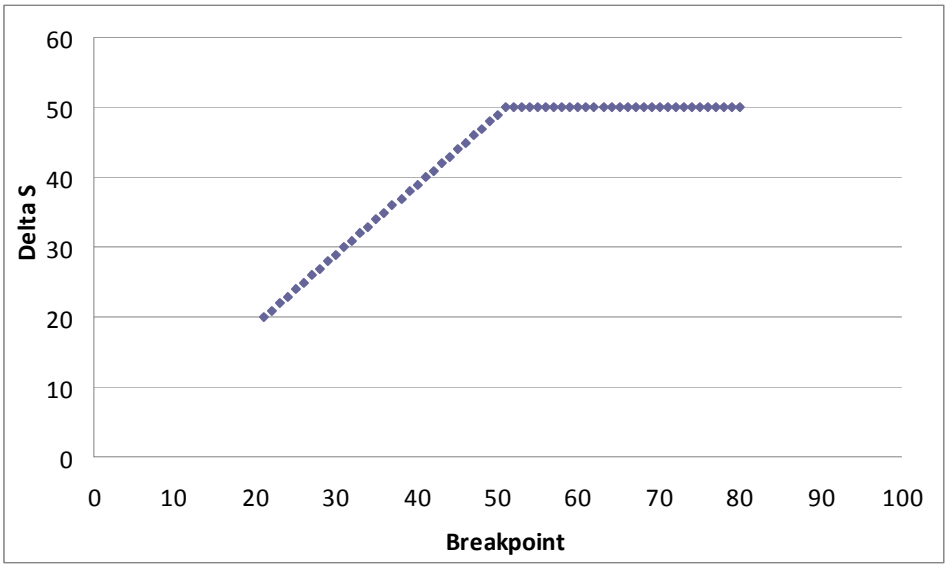

Figure 7-6. First Derivative of S (Delta S) for Sub-Sample defined by the Breakpoint.

Based on this information, it is apparent that the Z-value increases as 'no trend' data values are included in the sub-sample because a significant amount of values remain less than the values being added to the sub-sample. Therefore, while the Kendall Tau test is very powerful in detecting gradual trends, it is not capable of detecting partial duration trends within a time series.

8 Appendix B

Simplifications for NRCS Graphical Peak Discharge Method

Simplifications of the Time of Concentration

The time of concentration (tc) is calculated based on the lag equation:

$$t_c = 0.00526 * L^{0.8} * \left(\frac{1000}{CN} - 9\right)^{0.7} * S^{-0.5} \qquad \text{Eq. 8-1}$$

where tc = time of concentration (minutes), L = length of the watershed (ft), CN = the curve number, and S = slope (ft/ft) (McCuen 2005). The length of the watershed for the lag equation is calculated based on the following equation:

$$L = 209*A^{0.60} \qquad \text{Eq. 8-2}$$

where L = length (ft) and A = area (acres). The time of concentration equation must be converted to hourly units and the area must be converted to square miles to be consistent with the units in the NRCS Graphical Peak Discharge equation. Additionally, the curve number for each soil group can be substituted into the equation to further simplify the inputs. The following steps were taken to simplify the time of concentration equation. The steps are conducted for each soil group.

1) $L = 209*A^{0.60}$
    a. The area units for the rest of the peak discharge equation are square miles; therefore, a conversion was necessary:
        i. $L = 209*A^{0.60}$
        ii. $L = 209*(640A)^{0.6} = 133{,}760*A^{0.6}$
2) Substitute L into the T_c equation

a. $t_c = 0.00526 * (133{,}760 * A^{0.6})^{0.8} * \left(\frac{1000}{CN} - 9\right)^{0.7} * S^{-0.5}$

b. Distribute the exponent and simplify the numeric values in the expression in 2a

   i. $t_c = 66.381 * A^{0.48} * \left(\frac{1000}{CN} - 9\right)^{0.7} * S^{-0.5}$

c. Convert from minutes to hours by dividing by 60 minutes per hour

   i. $t_c = 1.106 * A^{0.48} * \left(\frac{1000}{CN} - 9\right)^{0.7} * S^{-0.5}$

d. For each soil group, solve the expression: $\left(\frac{1000}{CN} - 9\right)^{0.7}$

   i. Soil Group A: 7.158566

   ii. Soil Group B: 4.056885

   iii. Soil Group C: 2.871841

   iv. Soil Group D: 2.403519

e. Substitute the above values in for the CN expression and multiply by 0.002478 to simplify the equation as follows

   i. $T_c = C_4 * A^{0.48} * S^{-0.5}$

   ii. With A = area (mi^2), S = slope (ft/ft), and C_4 defined as the product of the CN expression and 0.002478 for each soil group as follows

      1. Soil Group A: 7.9199
      2. Soil Group B: 4.4884
      3. Soil Group C: 3.1773
      4. Soil Group D: 2.6592

Simplifications for the TR-55 Equation Coefficients

The coefficients, C0, C1, and C2, were graphed versus Ia/P based on the values provided in TR-55. Polynomial functions were then fit to the coefficients as a function of Ia/P as shown in Figures 4.46, 4.47, and 4.48. The coefficient values and the fitted polynomial coefficient values are shown in Table 8-1.

Table 8-1. Coefficients for Polynomial Functions fit to the TR-55 Coefficients where x = Ia/P.

Equation	b0 + b1x + b2x^2		
Coefficient	**b0**	**b1**	**b2**
c0	2.527	0.475	-2.234
c1	-0.558	-0.708	1.555
c2	-0.176	0.043	0.604

Then, for each soil group, I_a corresponding to the appropriate curve number was substituted into the polynomial equations and the functions were simplified. The resulting coefficients are shown in Table 8-2.

Table 8-2. Coefficient Values for Polynomial Functions fit to the TR-55 Coefficients as a function of P (in.).

Soil Group	Equation	b0 + b1/P + b2/(P^2)		
	Coefficient	**b0**	**b1**	**b2**
A	**c0**	2.527	1.486	-21.861
	c1	-0.558	-2.215	15.217
	c2	-0.176	0.135	5.911
B	**c0**	2.527	0.607	-3.653
	c1	-0.558	-0.905	2.542
	c2	-0.176	0.055	0.988
C	**c0**	2.527	0.334	-1.103
	c1	-0.558	-0.498	0.768
	c2	-0.176	0.030	0.298
D	**c0**	2.527	0.238	-0.559
	c1	-0.558	-0.354	0.389
	c2	-0.176	0.022	0.151

9 Appendix C

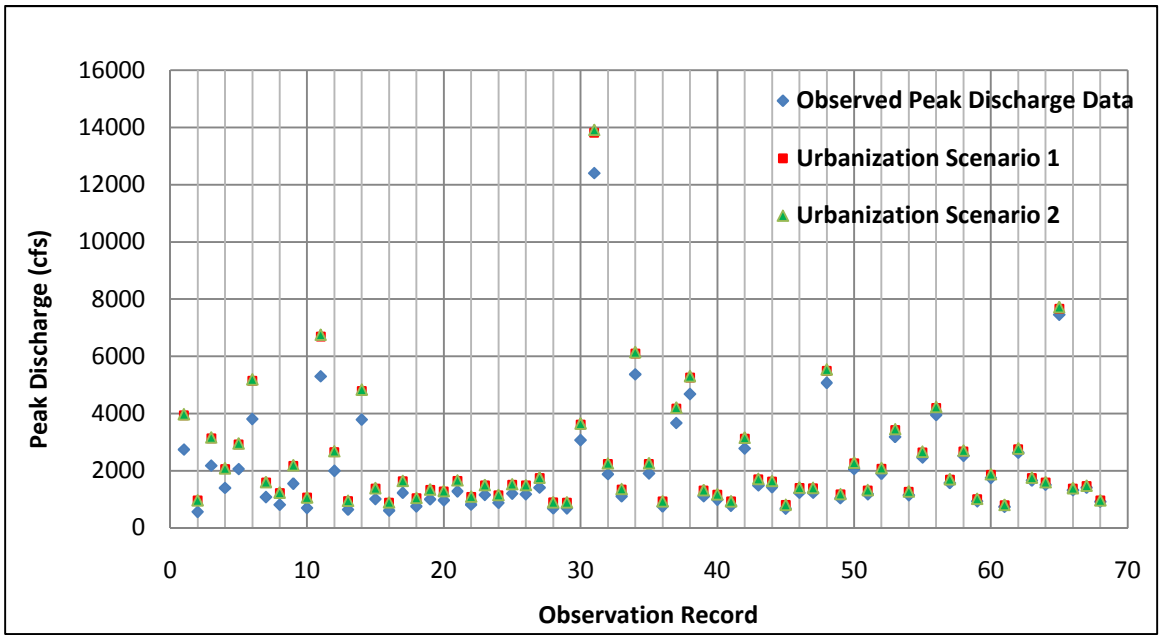

Figure 9-1. Observed and Adjusted Peak Discharge Records (cfs) for the A2 Emissions Scenario, Urbanization Scenarios 1 and 2, and Design Year 2025.

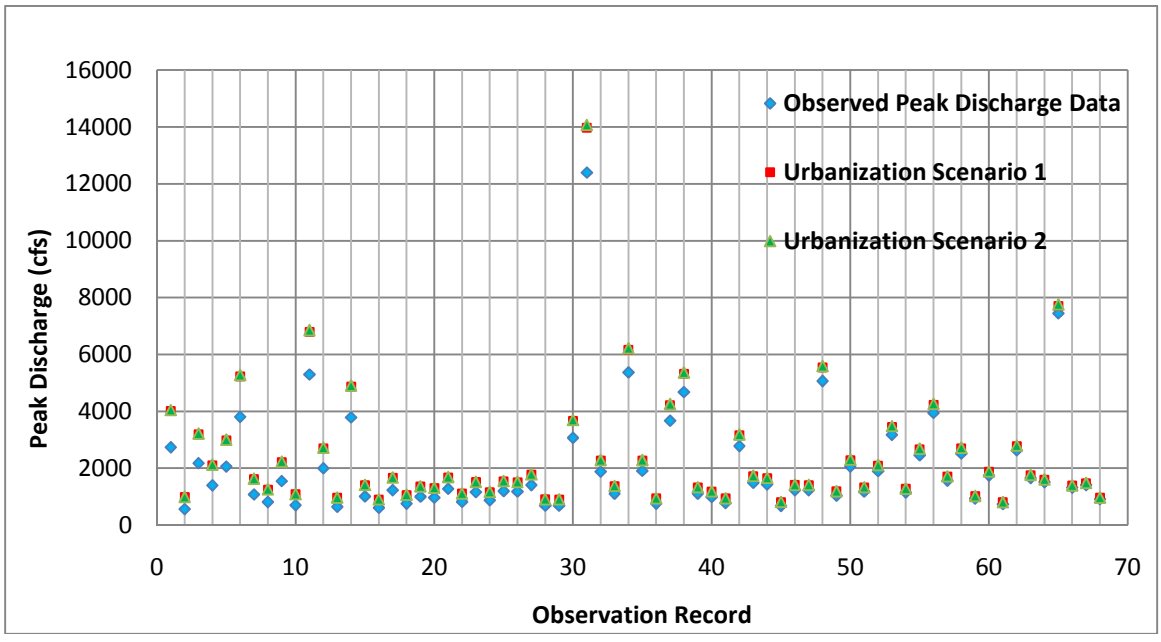

Figure 9-2. Observed and Adjusted Peak Discharge Records (cfs) for the A1B Emissions Scenario, Urbanization Scenarios 1 and 2, and Design Year 2025.

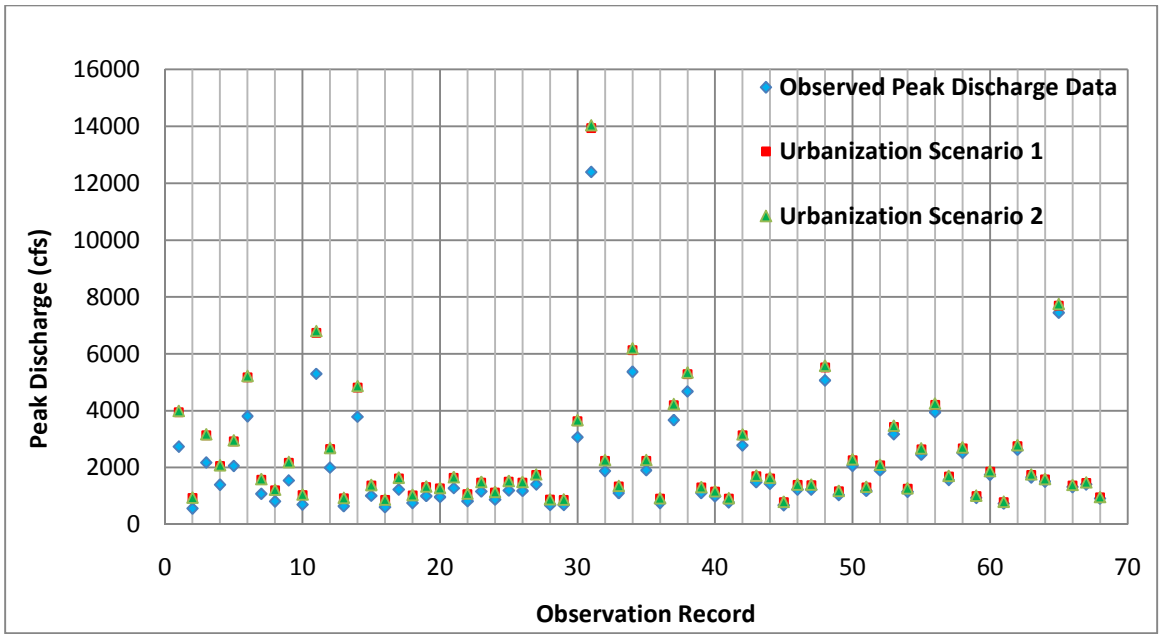

Figure 9-3. Observed and Adjusted Peak Discharge Records (cfs) for the B1 Emissions Scenario, Urbanization Scenarios 1 and 2, and Design Year 2025.

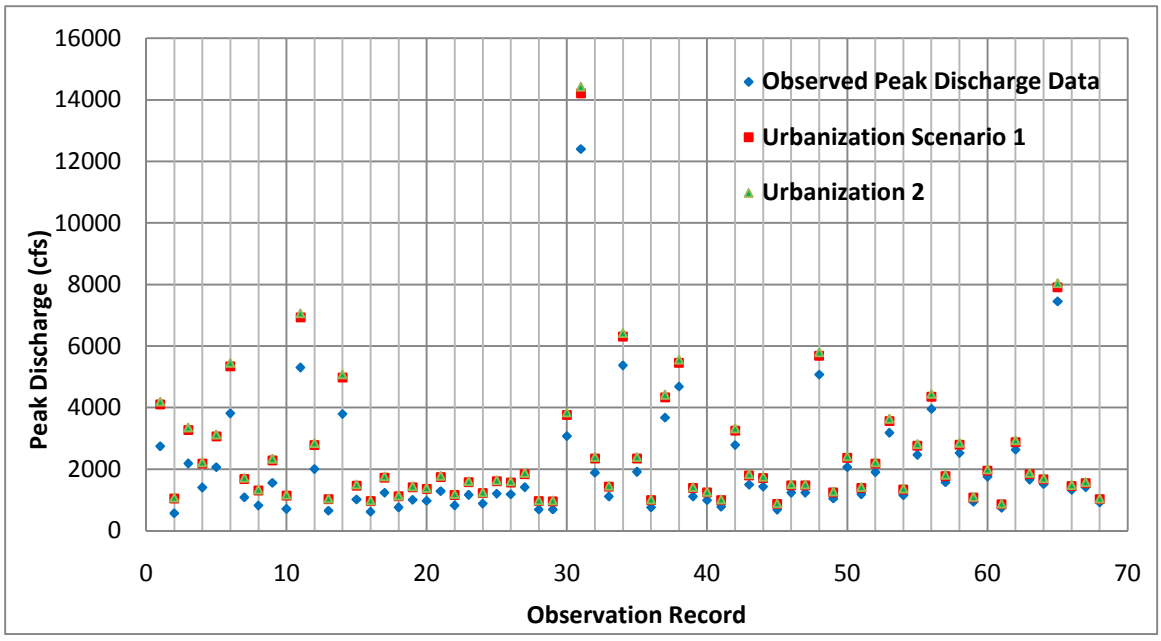

Figure 9-4. Observed and Adjusted Peak Discharge Records (cfs) for the A2 Emissions Scenario, Urbanization Scenarios 1 and 2, and Design Year 2050.

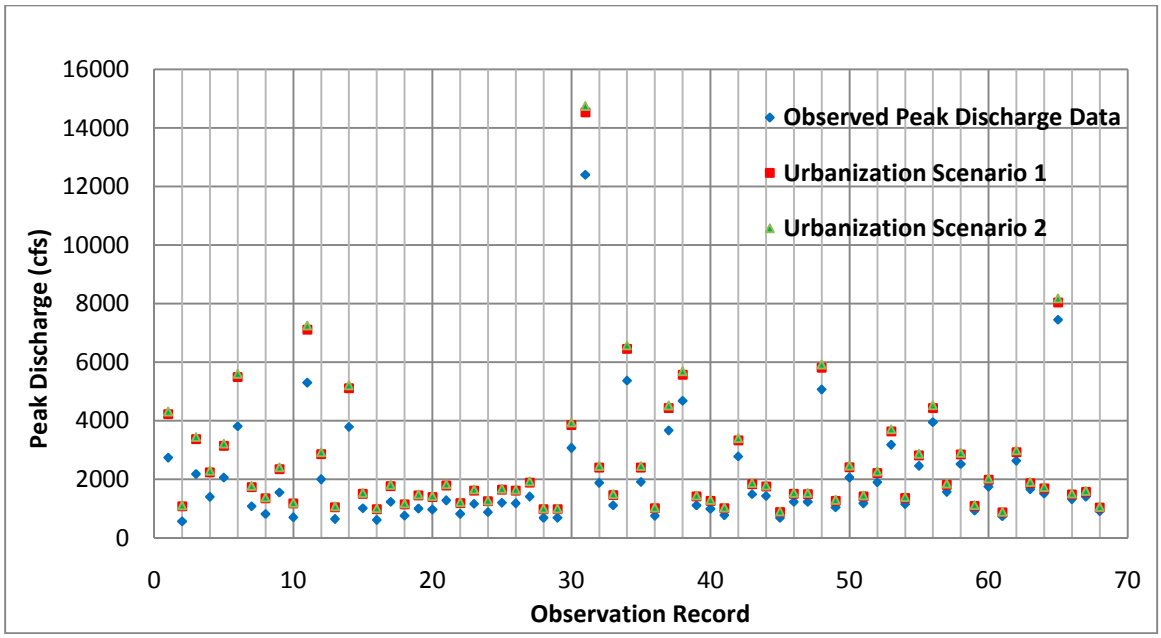

Figure 9-5. Observed and Adjusted Peak Discharge Records (cfs) for the A1B Emissions Scenario, Urbanization Scenarios 1 and 2, and Design Year 2050.

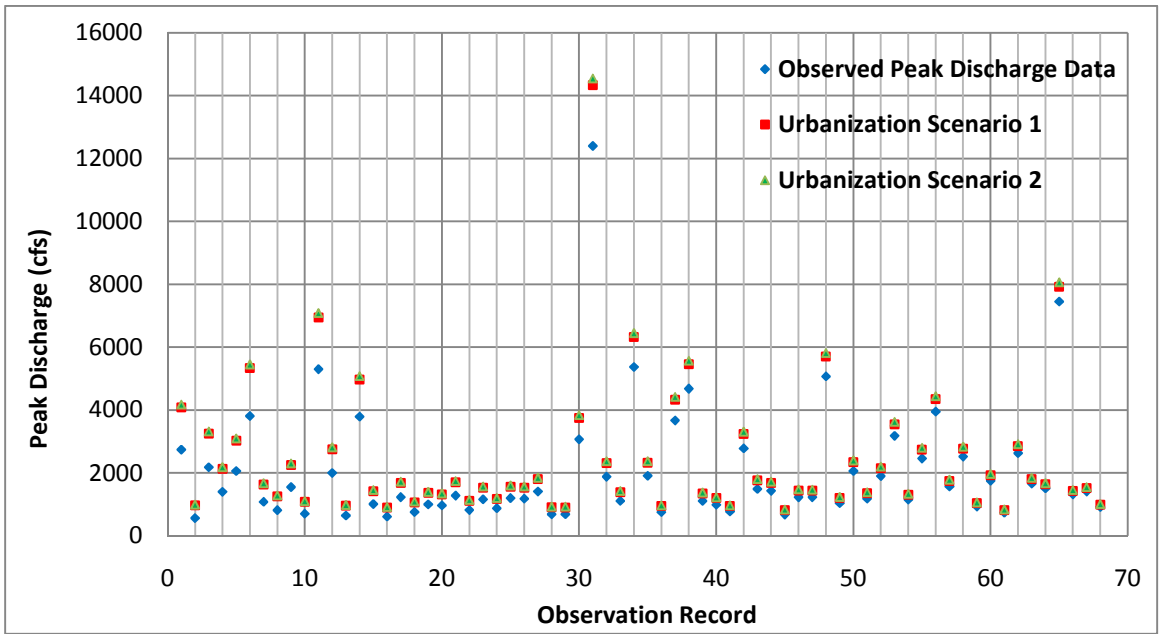

Figure 9-6. Observed and Adjusted Peak Discharge Records (cfs) for the B1 Emissions Scenario, Urbanization Scenarios 1 and 2, and Design Year 2050.

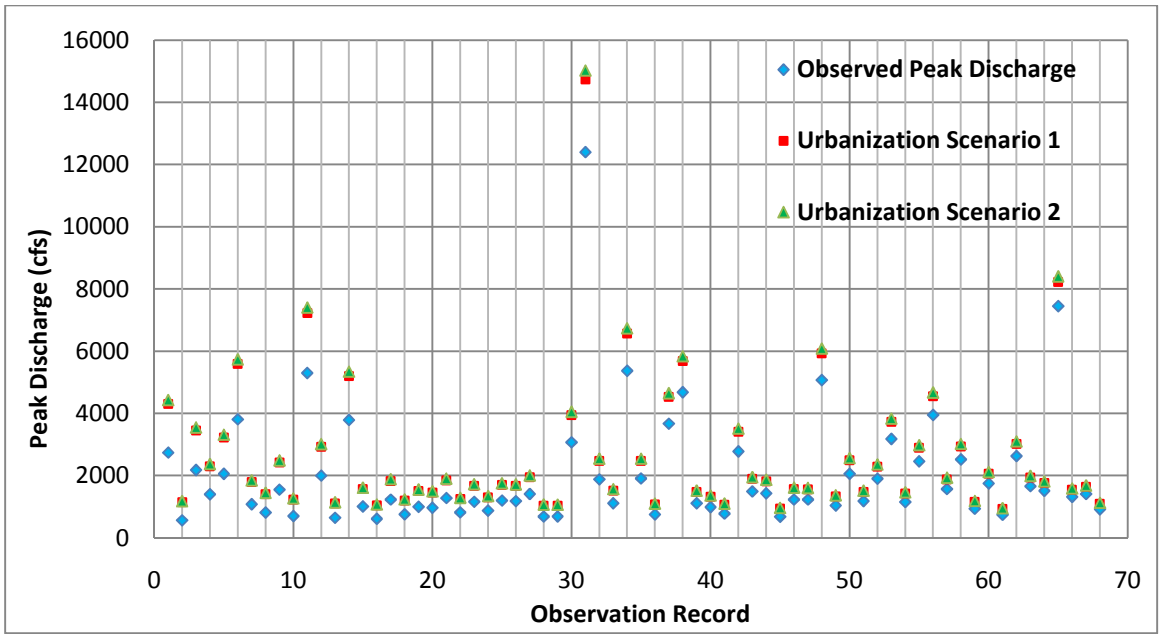

Figure 9-7. Observed and Adjusted Peak Discharge Records (cfs) for the A2 Emissions Scenario, Urbanization Scenarios 1 and 2, and Design Year 2075.

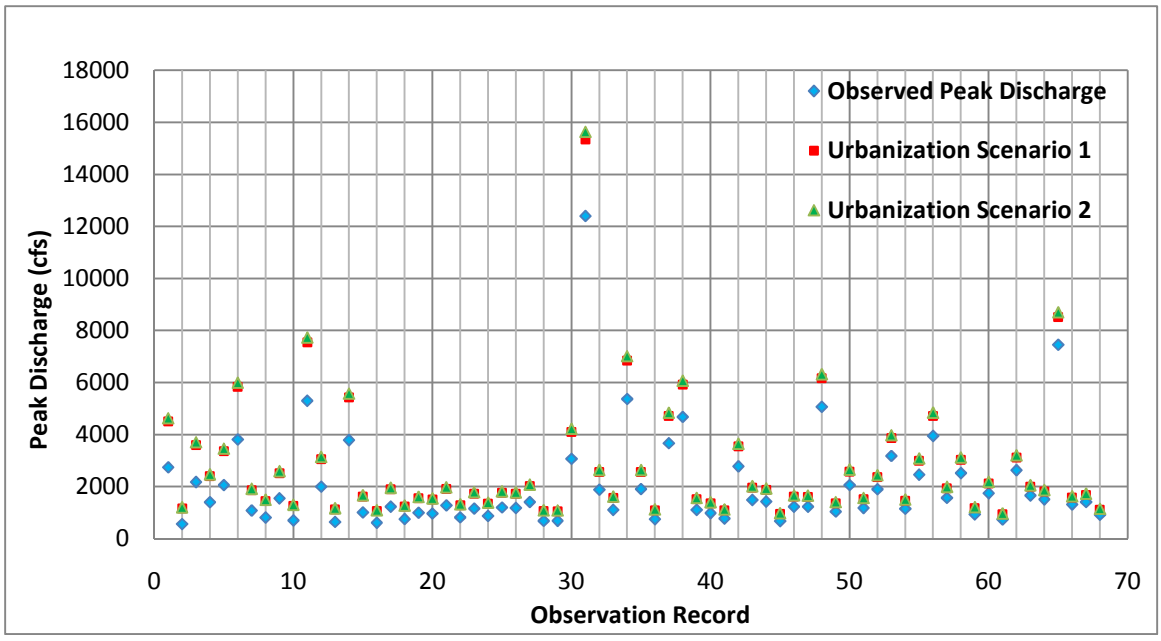

Figure 9-8. Observed and Adjusted Peak Discharge Records (cfs) for the A1B Emissions Scenario, Urbanization Scenarios 1 and 2, and Design Year 2075.

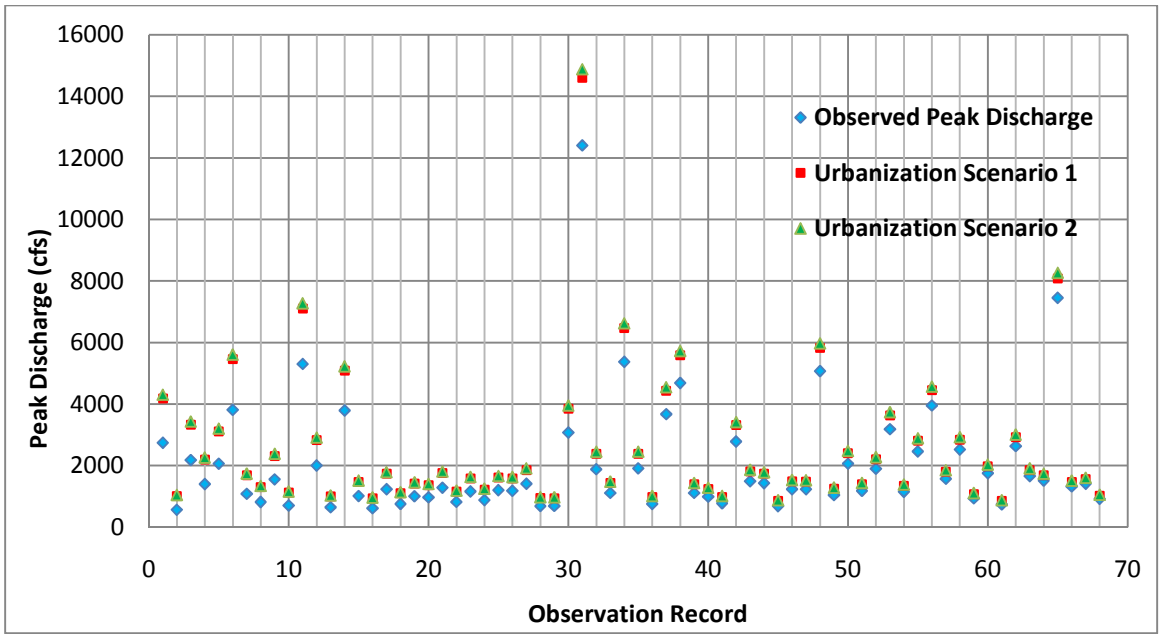

Figure 9-9. Observed and Adjusted Peak Discharge Records (cfs) for the B1 Emissions Scenario, Urbanization Scenarios 1 and 2, and Design Year 2075.

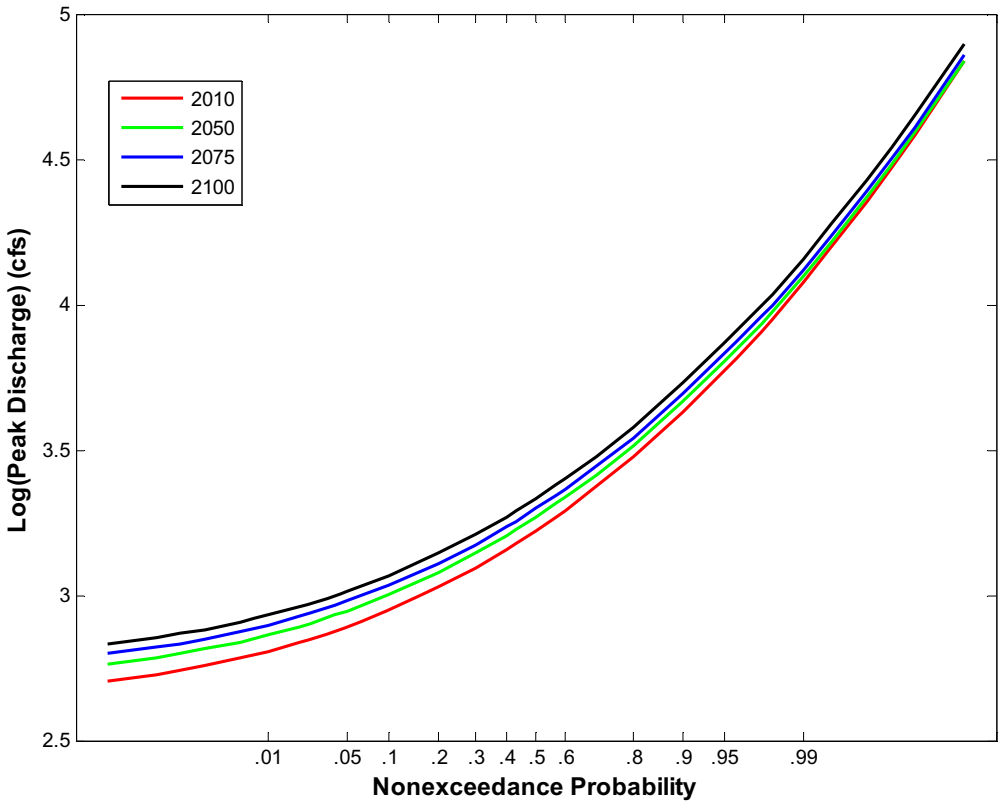

Figure 9-10. Flood Frequency Analysis for Emissions Scenario A1B and Urbanization Scenario 1

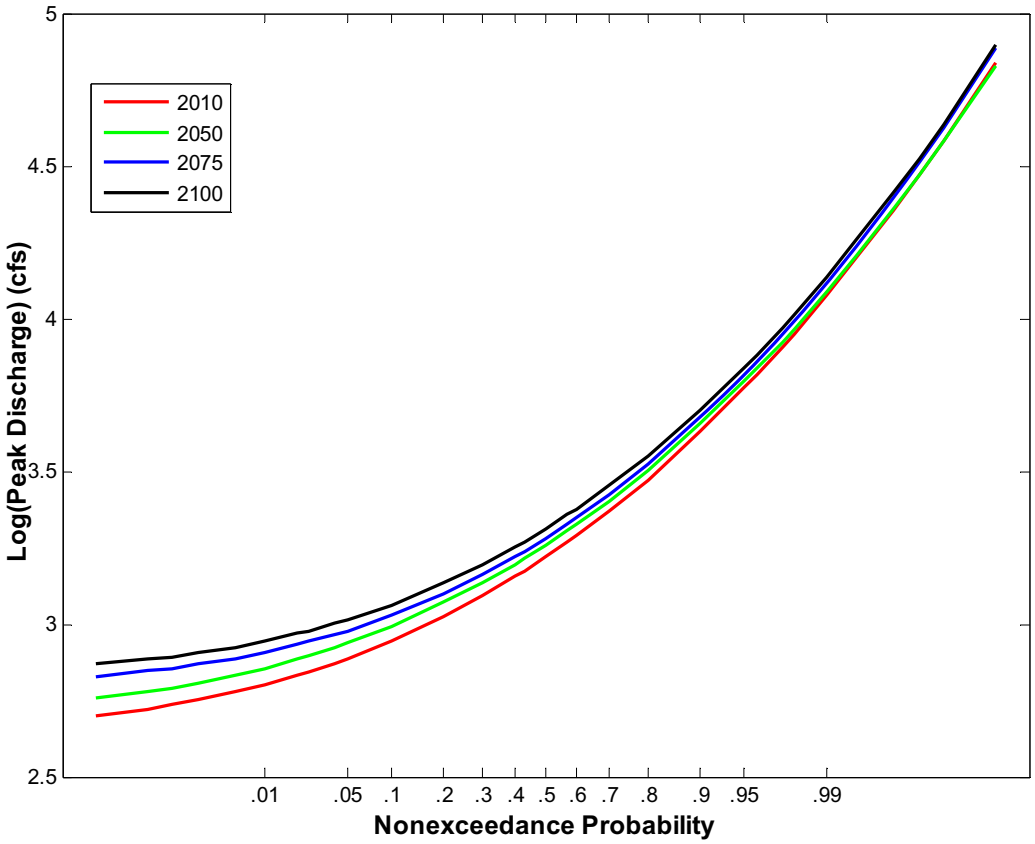

Figure 9-11. Flood Frequency Analysis for Emissions Scenario A2 and Urbanization Scenario 1

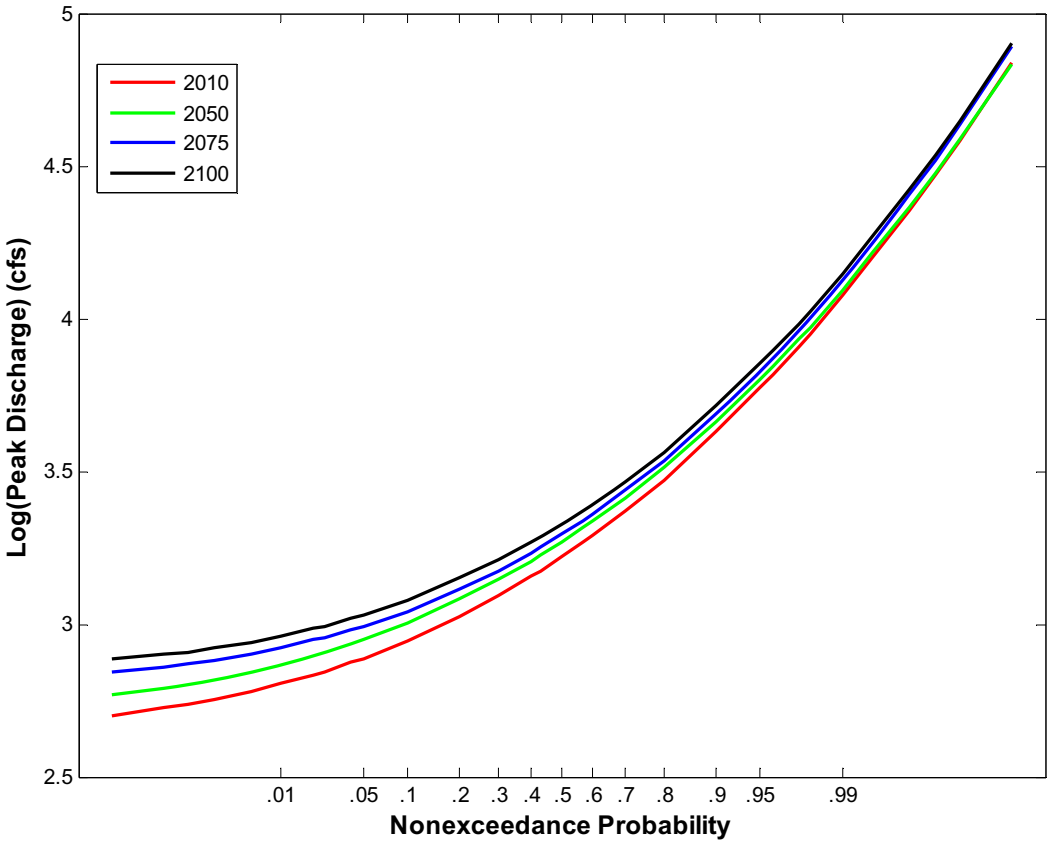

Figure 9-12. Flood Frequency Analysis for Emissions Scenario A2 and Urbanization Scenario 2

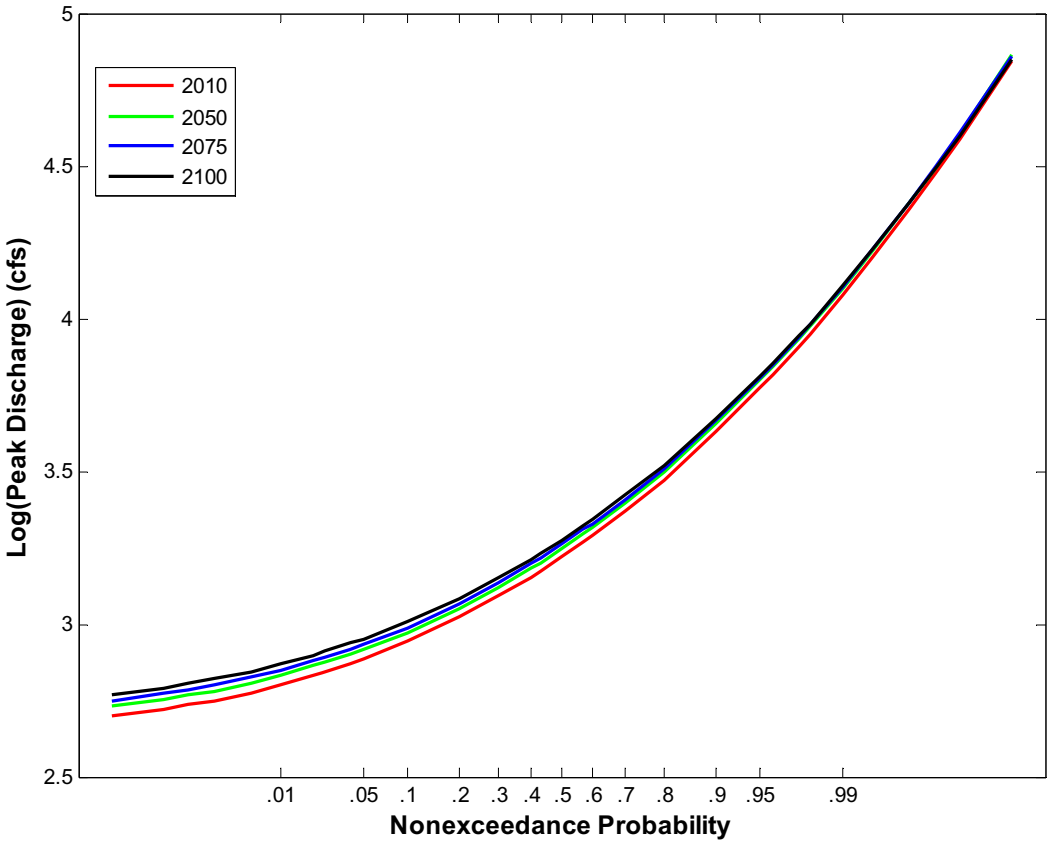

Figure 9-13. Flood Frequency Analysis for Emissions Scenario B1 and Urbanization Scenario 1

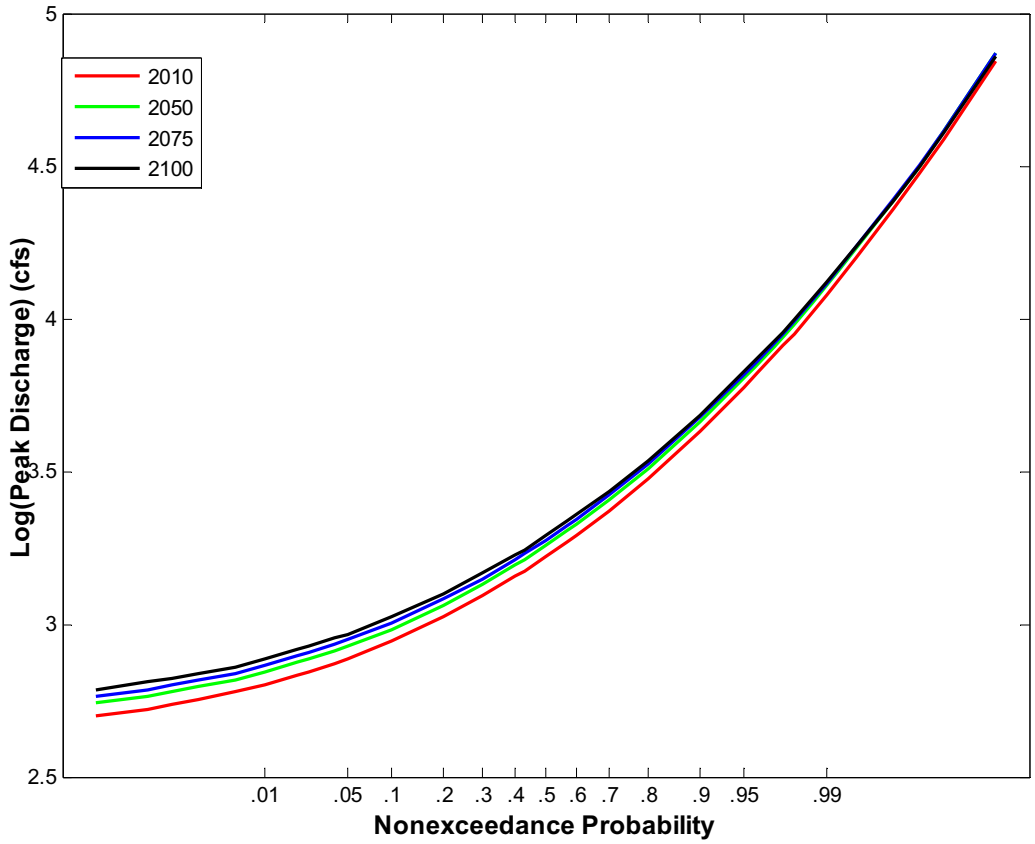

Figure 9-14. Flood Frequency Analysis for Emissions Scenario B1 and Urbanization Scenario 2

10 Appendix D

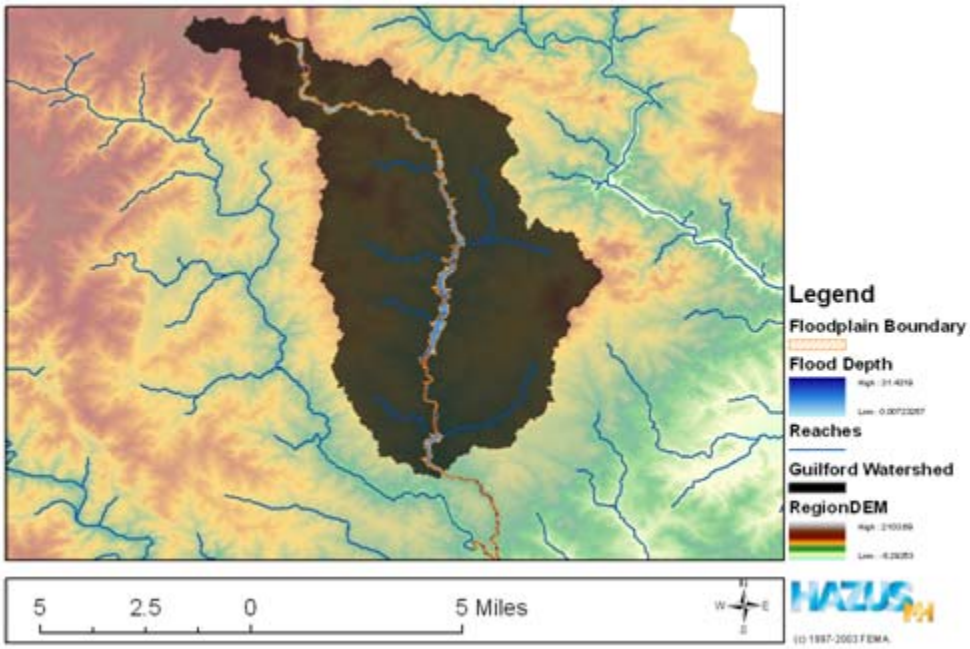

Figure 10-1. 100-yr Return Period Floodplain for the Stationarity Scenario.

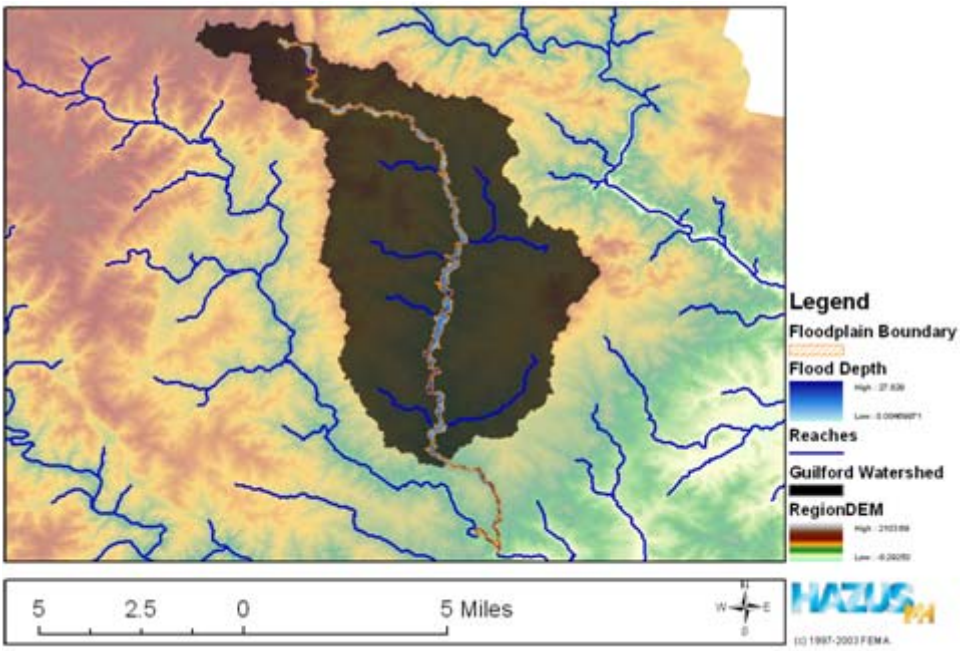

Figure 10-2. 100-yr Return Period Floodplain for the Best Case Scenario.

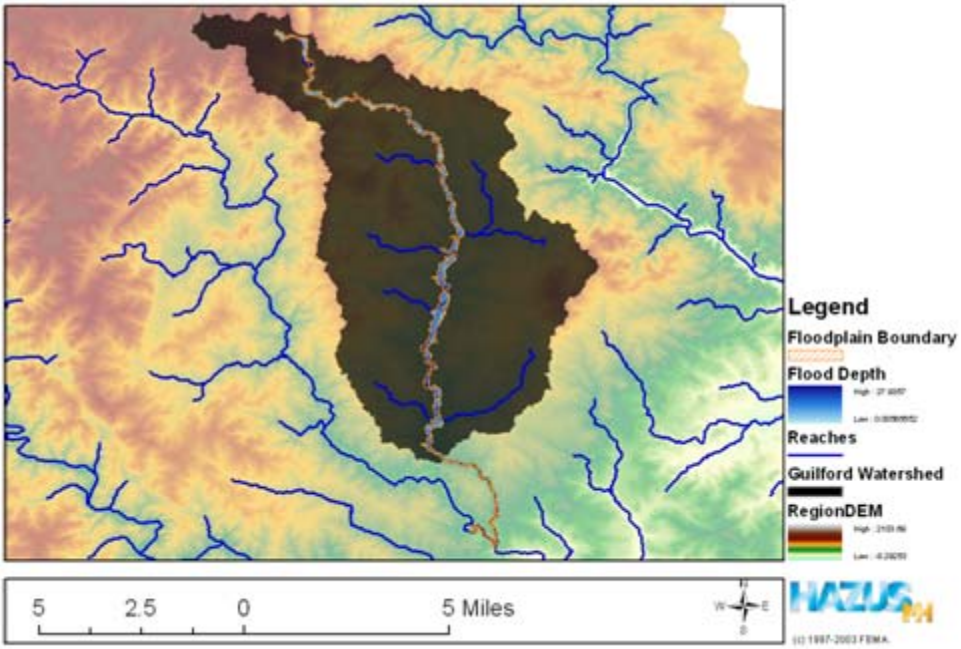

Figure 10-3. 100-yr Return Period Floodplain for the Best Case Scenario.

Table 10-1. Conversion of Land cover from 2010 to 2100 Conditions for Best Case Scenario.

	2010 Conditions				2100 Conditions			
Census Block	High	Mod	Low	Open	High	Mod	Low	Open
240276030002000	0	4	13	109	0	7	11	109
240276030002001	0	0	3	1	0	1	2	1
240276030002002	0	0	4	7	0	1	3	7
240276030002003	0	1	7	11	0	2	5	11
240276023041012	0	0	5	26	0	1	4	26
240276023041019	0	0	1	28	0	0	1	28
240276023041020	0	0	0	2	0	0	0	2
240276023041021	0	0	0	0	0	0	0	0
240276030001005	0	0	3	19	0	1	3	19
240276030001006	0	2	31	57	0	8	25	57
240276030001007	0	0	1	2	0	0	1	2
240276030001008	0	2	15	88	0	5	12	88
240276054011003	0	1	5	12	0	2	4	12
240276054011004	0	4	5	15	0	5	4	15
240276054011005	0	0	1	1	0	0	1	1
240276054011006	0	0	0	1	0	0	0	1
240276054011007	0	4	9	13	0	6	7	13

	2010 Conditions				2100 Conditions			
Census Block	High	Mod	Low	Open	High	Mod	Low	Open
240276054011008	0	1	3	0	0	2	2	0
240276054011009	0	0	1	0	0	0	1	0
240276054011010	0	0	10	4	0	2	8	4
240276054012000	0	1	10	24	0	3	8	24
240276056023017	0	2	4	8	0	3	3	8
240276056023019	0	2	1	1	0	2	1	1
240276056023020	0	0	0	2	0	0	0	2
240276054023019	0	1	1	2	0	1	1	2
240276054023020	0	0	1	2	0	0	1	2
240276066031003	0	3	18	16	0	7	14	16
240276066032001	0	2	6	21	0	3	5	21
240276066032003	0	2	2	2	0	3	2	2
240276066032004	0	4	5	2	0	5	4	2
240276022003004	0	1	5	40	0	2	4	40
240276022003008	0	0	11	23	0	2	9	23
240276022003010	1	6	5	1	1	7	4	1
240276022004000	0	1	15	150	0	4	12	150
240276022004001	0	12	26	56	0	17	21	56
240276022004002	0	0	14	22	0	3	11	22
240276023041000	0	5	4	8	0	5	3	8
240276023041005	0	0	0	5	0	0	0	5
240276023041006	0	0	0	7	0	0	0	7
240276023042010	0	0	5	12	0	1	4	12
240276023042011	0	0	3	7	0	1	2	7
240276023042015	0	0	7	11	0	1	5	11
240276023042016	0	0	0	0	0	0	0	0
240276023042017	0	0	0	2	0	0	0	2
240276023051000	0	0	22	92	0	5	18	92
240276023052001	0	0	3	14	0	1	2	14
240276023062015	0	1	2	0	0	1	2	0
240276023062016	0	0	2	1	0	1	2	1
240276030002016	0	0	0	33	0	0	0	33
240276068032000	1	14	8	18	1	16	7	18
240276068032004	0	3	0	1	0	3	0	1
240276068033000	0	0	1	1	0	0	1	1
240276068033001	0	4	19	10	0	8	15	10
240276068033003	0	0	4	0	0	1	3	0
240276068033004	0	1	2	1	0	2	1	1

	2010 Conditions				2100 Conditions			
Census Block	High	Mod	Low	Open	High	Mod	Low	Open
240276068041000	0	1	0	7	0	1	0	7
240276068041001	0	6	0	2	0	6	0	2
240276054012002	0	0	3	18	0	1	2	18
240276054012003	0	0	2	2	0	0	1	2
240276054023000	0	1	5	17	0	2	4	17
240276054023001	0	1	10	2	0	3	8	2
240276054023003	0	2	5	1	0	3	4	1
240276054023006	0	0	3	1	0	1	3	1
240276054023007	0	14	11	2	0	16	9	2
240276054023009	0	1	3	0	0	2	2	0
240276067011004	0	0	0	0	0	0	0	0
240276067011005	0	0	2	1	0	1	2	1
240276067011006	1	8	3	0	1	9	2	0
240276067011007	0	0	5	11	0	1	4	11
240276067011023	0	0	3	4	0	1	3	4
240276067011000	0	1	2	2	0	1	2	2
240276067011001	0	6	7	5	0	8	6	5
240276067011002	0	0	0	1	0	0	0	1
240276067011003	0	5	7	1	0	6	5	1
240276067012008	0	0	1	2	0	0	1	2
240276067012010	0	0	2	4	0	1	2	4
240276067031003	1	20	9	1	1	21	7	1
240276067042000	1	14	34	36	1	20	27	36
240276068041005	0	1	1	1	0	1	1	1
240276068041006	0	1	7	4	0	2	6	4
240276068041007	0	5	11	1	0	7	9	1
240276068041008	0	0	1	1	0	0	1	1
240276068041009	0	0	0	1	0	0	0	1
240276068041010	0	5	0	22	0	5	0	22
240276069023001	0	8	0	19	0	8	0	19
240276069023002	0	3	0	1	0	3	0	1
240276069024002	0	1	0	6	0	1	0	6
240276069024003	0	1	0	20	0	1	0	20
240276069024005	0	4	0	9	0	4	0	9
240276069024006	0	0	0	9	0	0	0	9
240276069024007	0	3	0	12	0	3	0	12
240276023062014	0	1	8	3	0	3	6	3
240276067041008	0	1	61	56	0	13	49	56

	2010 Conditions				2100 Conditions			
Census Block	High	Mod	Low	Open	High	Mod	Low	Open
240276067041018	0	5	38	55	0	13	30	55
240276069024000	0	9	9	23	0	11	7	23
240276067011020	0	0	12	58	0	2	10	58
240276054011000	0	75	230	195	0	121	184	195
240276054013000	0	9	65	86	0	22	52	86
240276054011011	0	12	1	9	0	12	1	9
240276022003006	0	0	19	118	0	4	15	118
240276023052002	0	0	4	49	0	1	3	49
240276066031000	0	51	188	330	0	89	150	330
240276068021000	7	35	81	84	7	51	65	84
240276068042001	0	0	104	203	0	21	83	203

Table 10-2. Conversion of Land cover from 2010 to 2100 Worst Case Scenario Conditions.

	2010 Conditions				2100 Conditions			
Census Block	High	Mod	Low	Open	High	Mod	Low	Open
240276030002000	0	4	13	109	0	12	5	109
240276030002001	0	0	3	1	0	2	1	1
240276030002002	0	0	4	7	0	2	1	7
240276030002003	0	1	7	11	0	5	3	11
240276023041012	0	0	5	26	0	3	2	26
240276023041019	0	0	1	28	0	1	0	28
240276023041020	0	0	0	2	0	0	0	2
240276023041021	0	0	0	0	0	0	0	0
240276030001005	0	0	3	19	0	2	1	19
240276030001006	0	2	31	57	0	21	12	57
240276030001007	0	0	1	2	0	1	1	2
240276030001008	0	2	15	88	0	11	6	88
240276054011003	0	1	5	12	0	4	2	12
240276054011004	0	4	5	15	0	7	2	15
240276054011005	0	0	1	1	0	1	0	1
240276054011006	0	0	0	1	0	0	0	1
240276054011007	0	4	9	13	0	10	3	13
240276054011008	0	1	3	0	0	3	1	0
240276054011009	0	0	1	0	0	1	0	0
240276054011010	0	0	10	4	0	6	4	4
240276054012000	0	1	10	24	0	7	4	24

	2010 Conditions				2100 Conditions			
Census Block	High	Mod	Low	Open	High	Mod	Low	Open
240276056023017	0	2	4	8	0	5	1	8
240276056023019	0	2	1	1	0	2	0	1
240276056023020	0	0	0	2	0	0	0	2
240276054023019	0	1	1	2	0	1	0	2
240276054023020	0	0	1	2	0	1	0	2
240276066031003	0	3	18	16	0	14	7	16
240276066032001	0	2	6	21	0	5	2	21
240276066032003	0	2	2	2	0	3	1	2
240276066032004	0	4	5	2	0	7	2	2
240276022003004	0	1	5	40	0	4	2	40
240276022003008	0	0	11	23	0	7	4	23
240276022003010	1	6	5	1	1	9	2	1
240276022004000	0	1	15	150	0	10	6	150
240276022004001	0	12	26	56	0	28	10	56
240276022004002	0	0	14	22	0	8	5	22
240276023041000	0	5	4	8	0	7	2	8
240276023041005	0	0	0	5	0	0	0	5
240276023041006	0	0	0	7	0	0	0	7
240276023042010	0	0	5	12	0	3	2	12
240276023042011	0	0	3	7	0	2	1	7
240276023042015	0	0	7	11	0	4	3	11
240276023042016	0	0	0	0	0	0	0	0
240276023042017	0	0	0	2	0	0	0	2
240276023051000	0	0	22	92	0	14	9	92
240276023052001	0	0	3	14	0	2	1	14
240276023062015	0	1	2	0	0	2	1	0
240276023062016	0	0	2	1	0	2	1	1
240276030002016	0	0	0	33	0	0	0	33
240276068032000	1	14	8	18	1	19	3	18
240276068032004	0	3	0	1	0	3	0	1
240276068033000	0	0	1	1	0	1	0	1
240276068033001	0	4	19	10	0	15	7	10
240276068033003	0	0	4	0	0	3	2	0
240276068033004	0	1	2	1	0	2	1	1
240276068041000	0	1	0	7	0	1	0	7
240276068041001	0	6	0	2	0	6	0	2
240276054012002	0	0	3	18	0	2	1	18
240276054012003	0	0	2	2	0	1	1	2

	2010 Conditions				2100 Conditions			
Census Block	High	Mod	Low	Open	High	Mod	Low	Open
240276054023000	0	1	5	17	0	4	2	17
240276054023001	0	1	10	2	0	7	4	2
240276054023003	0	2	5	1	0	6	2	1
240276054023006	0	0	3	1	0	2	1	1
240276054023007	0	14	11	2	0	21	4	2
240276054023009	0	1	3	0	0	3	1	0
240276067011004	0	0	0	0	0	0	0	0
240276067011005	0	0	2	1	0	2	1	1
240276067011006	1	8	3	0	1	10	1	0
240276067011007	0	0	5	11	0	3	2	11
240276067011023	0	0	3	4	0	2	1	4
240276067011000	0	1	2	2	0	2	1	2
240276067011001	0	6	7	5	0	10	3	5
240276067011002	0	0	0	1	0	0	0	1
240276067011003	0	5	7	1	0	9	3	1
240276067012008	0	0	1	2	0	0	0	2
240276067012010	0	0	2	4	0	2	1	4
240276067031003	1	20	9	1	1	25	4	1
240276067042000	1	14	34	36	1	34	13	36
240276068041005	0	1	1	1	0	1	0	1
240276068041006	0	1	7	4	0	5	3	4
240276068041007	0	5	11	1	0	12	4	1
240276068041008	0	0	1	1	0	1	0	1
240276068041009	0	0	0	1	0	0	0	1
240276068041010	0	5	0	22	0	5	0	22
240276069023001	0	8	0	19	0	8	0	19
240276069023002	0	3	0	1	0	3	0	1
240276069024002	0	1	0	6	0	1	0	6
240276069024003	0	1	0	20	0	1	0	20
240276069024005	0	4	0	9	0	4	0	9
240276069024006	0	0	0	9	0	0	0	9
240276069024007	0	3	0	12	0	3	0	12
240276023062014	0	1	8	3	0	6	3	3
240276067041008	0	1	61	56	0	38	24	56
240276067041018	0	5	38	55	0	28	15	55
240276069024000	0	9	9	23	0	14	4	23
240276067011020	0	0	12	58	0	7	5	58
240276054011000	0	75	230	195	0	215	90	195

	2010 Conditions				2100 Conditions			
Census Block	High	Mod	Low	Open	High	Mod	Low	Open
240276054013000	0	9	65	86	0	49	25	86
240276054011011	0	12	1	9	0	13	0	9
240276022003006	0	0	19	118	0	12	7	118
240276023052002	0	0	4	49	0	2	2	49
240276066031000	0	51	188	330	0	166	73	330
240276068021000	7	35	81	84	7	84	32	84
240276068042001	0	0	104	203	0	63	41	203

Table 10-3. Adjustments of Total Building Loss for Best Case Scenario and 100-yr Flood.

Census Block	2010 Total Economic Loss ($ Thousands)	Increase in Consequences for Census Block	2100 Total Economic Loss ($ Thousands)
240276022003004	495	4.4%	517
240276022003008	450	10.8%	499
240276022003010	5448	4.3%	5685
240276022004000	1296	4.4%	1353
240276022004001	11586	6.9%	12390
240276023041000	894	4.7%	936
240276023041005	726	3.0%	748
240276023041006	410	1.7%	417
240276023041012	6442	7.1%	6897
240276023041019	2212	2.3%	2263
240276023041020	6	0.0%	6
240276023041021	595	17.1%	697
240276023042010	232	9.7%	255
240276023042015	30	11.6%	33
240276023042016	0	0.0%	0
240276023042017	106	0.0%	106
240276023051000	6385	7.8%	6881
240276023052001	1026	6.8%	1095
240276023062015	1007	9.9%	1107
240276023062016	524	12.7%	591
240276030001005	259	6.6%	276
240276030001006	21	10.5%	23
240276030001007	0	12.5%	0
240276030001008	570	6.0%	604
240276030002000	159	4.3%	166

Census Block	2010 Total Economic Loss ($ Thousands)	Increase in Consequences for Census Block	2100 Total Economic Loss ($ Thousands)
240276030002001	0	15.1%	0
240276030002016	77	0.4%	77
240276054011003	4160	7.8%	4484
240276054011004	2706	4.8%	2836
240276054011005	63	13.7%	72
240276054011007	3370	7.5%	3622
240276054011009	0	16.0%	0
240276054011010	3893	15.2%	4486
240276054012000	2834	9.0%	3090
240276054012002	171	6.1%	181
240276054023000	0	8.0%	0
240276054023001	2853	12.9%	3220
240276054023006	0	15.9%	0
240276054023007	11754	4.9%	12335
240276054023019	278	4.6%	291
240276054023020	0	9.5%	0
240276056023017	39	6.2%	41
240276056023019	0	2.9%	0
240276056023020	0	8.3%	0
240276066031003	2958	10.6%	3272
240276066032001	2610	6.7%	2784
240276066032003	0	5.6%	0
240276066032004	0	6.2%	0
240276067011000	882	9.0%	962
240276067011001	47	6.0%	50
240276067011002	524	6.3%	557
240276067011003	6720	7.3%	7208
240276067011004	0	2.9%	0
240276067011005	0	14.6%	0
240276067011006	0	2.2%	0
240276067011007	5261	10.7%	5822
240276067011023	14	12.9%	16
240276067012010	1202	9.9%	1321
240276067031003	7211	3.3%	7450
240276068033000	0	14.0%	0
240276068033001	7479	11.0%	8302
240276068033003	1025	15.4%	1183

Census Block	2010 Total Economic Loss ($ Thousands)	Increase in Consequences for Census Block	2100 Total Economic Loss ($ Thousands)
240276068033004	5890	6.0%	6245
240276068041000	0	0.0%	0
240276068041001	6	0.0%	6
240276068041005	0	3.3%	0
240276068041006	0	12.6%	0
240276068041007	71	8.9%	77
240276068041008	1760	13.7%	2001
240276068041009	0	5.7%	0
240276068041010	15371	0.0%	15371
240276069023001	1994	0.0%	1994
240276069024002	579	0.0%	579
240276069024003	6	0.0%	6
240276069024005	764	0.0%	764
240276069024006	1165	0.0%	1165
240276069024007	345	0.0%	345
Total	**136961**		**145757**

Table 10-4. Adjustments of Total Building Loss for Best Case Scenario and 500-yr Flood.

Census Block	2010 Total Economic Loss ($ Thousands)	Increase in Consequences for Census Block	2100 Total Economic Loss ($ Thousands)
240276022003004	591	4.4%	617
240276022003008	753	10.8%	835
240276022003010	6513	4.3%	6796
240276022004000	1804	4.4%	1883
240276022004001	16585	6.9%	17736
240276022004002	19	11.8%	21
240276023041000	1147	4.7%	1201
240276023041005	1001	3.0%	1031
240276023041006	512	1.7%	521
240276023041012	8602	7.1%	9209
240276023041019	2864	2.3%	2930
240276023041020	22	0.0%	22
240276023041021	758	17.1%	888

Census Block	2010 Total Economic Loss ($ Thousands)	Increase in Consequences for Census Block	2100 Total Economic Loss ($ Thousands)
240276023042010	340	9.7%	373
240276023042011	1	10.4%	1
240276023042015	46	11.6%	51
240276023042016	0	0.0%	0
240276023042017	126	0.0%	126
240276023051000	8690	7.8%	9366
240276023052001	1217	6.8%	1299
240276023062015	1332	9.9%	1464
240276023062016	663	12.7%	747
240276030001005	373	6.6%	398
240276030001006	42	10.5%	46
240276030001007	0	12.5%	0
240276030001008	888	6.0%	941
240276030002000	223	4.3%	233
240276030002001	0	15.1%	0
240276030002002	54	11.2%	60
240276030002003	0	10.1%	0
240276030002016	108	0.4%	108
240276054011003	5201	7.8%	5606
240276054011004	3267	4.8%	3424
240276054011005	193	13.7%	219
240276054011006	0	6.3%	0
240276054011007	3692	7.5%	3968
240276054011008	137	9.9%	151
240276054011009	0	16.0%	0
240276054011010	5273	15.2%	6076
240276054012000	3775	9.0%	4117
240276054012002	485	6.1%	515
240276054012003	90	12.4%	101
240276054013000	34	10.5%	38
240276054023000	0	8.0%	0
240276054023001	4406	12.9%	4973
240276054023003	1046	9.2%	1142
240276054023006	0	15.9%	0
240276054023007	15901	4.9%	16686
240276054023009	1032	8.1%	1116

Census Block	2010 Total Economic Loss ($ Thousands)	Increase in Consequences for Census Block	2100 Total Economic Loss ($ Thousands)
240276054023019	415	4.6%	434
240276054023020	0	9.5%	0
240276056023017	53	6.2%	56
240276056023019	0	2.9%	0
240276056023020	0	8.3%	0
240276066031000	47	8.5%	51
240276066031003	5856	10.6%	6478
240276066032001	3463	6.7%	3694
240276066032003	0	5.6%	0
240276066032004	0	6.2%	0
240276067011000	1263	9.0%	1377
240276067011001	50	6.0%	53
240276067011002	954	6.3%	1014
240276067011003	8824	7.3%	9464
240276067011004	0	2.9%	0
240276067011005	0	14.6%	0
240276067011006	0	2.2%	0
240276067011007	6458	10.7%	7147
240276067011023	79	12.9%	89
240276067012008	123	9.9%	135
240276067012010	1581	9.9%	1737
240276067031003	9743	3.3%	10066
240276067042000	5	8.0%	5
240276068032000	2	3.4%	2
240276068032004	15	0.0%	15
240276068033000	0	14.0%	0
240276068033001	10224	11.0%	11348
240276068033003	1598	15.4%	1845
240276068033004	7788	6.0%	8257
240276068041000	0	0.0%	0
240276068041001	18	0.0%	18
240276068041005	0	3.3%	0
240276068041006	0	12.6%	0
240276068041007	1802	8.9%	1963
240276068041008	4073	13.7%	4630
240276068041009	0	5.7%	0

Census Block	2010 Total Economic Loss ($ Thousands)	Increase in Consequences for Census Block	2100 Total Economic Loss ($ Thousands)
240276068041010	20916	0.0%	20916
240276069023001	2711	0.0%	2711
240276069023002	0	0.0%	0
240276069024002	717	0.0%	717
240276069024003	985	0.0%	985
240276069024005	1315	0.0%	1315
240276069024006	1937	0.0%	1937
240276069024007	702	0.0%	702
Total	**193523**		**206196**

Table 10-5. Adjustments of Total People Displaced for Best Case Scenario and 100-yr Flood.

Census Block	2010 Population Displaced	Increase in Consequences for Census Block	2100 Population Displaced
240276022003004	12	4.4%	13
240276022003008	19	10.8%	21
240276022003010	0	4.3%	0
240276022004000	30	4.4%	31
240276022004001	149	6.9%	159
240276022004002	1	11.8%	1
240276023041000	6	4.7%	6
240276023041005	22	3.0%	23
240276023041006	7	1.7%	7
240276023041012	138	7.1%	148
240276023041019	49	2.3%	50
240276023041020	0	0.0%	0
240276023041021	17	17.1%	20
240276023042010	8	9.7%	9
240276023042011	0	10.4%	0
240276023042015	0	11.6%	0
240276023042016	0	0.0%	0
240276023042017	3	0.0%	3
240276023051000	166	7.8%	179
240276023052001	29	6.8%	31

Census Block	2010 Population Displaced	Increase in Consequences for Census Block	2100 Population Displaced
240276023062014	4	12.8%	5
240276023062015	27	9.9%	30
240276023062016	12	12.7%	14
240276030001005	11	6.6%	12
240276030001006	0	10.5%	0
240276030001007	0	12.5%	0
240276030001008	4	6.0%	4
240276030002000	3	4.3%	3
240276030002001	0	15.1%	0
240276030002016	1	0.4%	1
240276054011003	111	7.8%	120
240276054011004	79	4.8%	83
240276054011005	2	13.7%	2
240276054011006	0	6.3%	0
240276054011007	70	7.5%	75
240276054011008	1	9.9%	1
240276054011009	0	16.0%	0
240276054011010	135	15.2%	156
240276054012000	44	9.0%	48
240276054012002	5	6.1%	5
240276054023000	0	8.0%	0
240276054023001	67	12.9%	76
240276054023006	0	15.9%	0
240276054023007	0	4.9%	0
240276054023019	0	4.6%	0
240276054023020	0	9.5%	0
240276056023017	0	6.2%	0
240276056023019	0	2.9%	0
240276056023020	0	8.3%	0
240276066031003	159	10.6%	176
240276066032001	53	6.7%	57
240276066032003	0	5.6%	0
240276066032004	0	6.2%	0
240276067011000	0	9.0%	0
240276067011001	1	6.0%	1
240276067011002	7	6.3%	7
240276067011003	0	7.3%	0
240276067011004	0	2.9%	0

Census Block	2010 Population Displaced	Increase in Consequences for Census Block	2100 Population Displaced
240276067011005	0	14.6%	0
240276067011006	0	2.2%	0
240276067011007	90	10.7%	100
240276067011023	0	12.9%	0
240276067012010	18	9.9%	20
240276067031003	0	3.3%	0
240276067041008	0	13.3%	0
240276067041018	0	10.3%	0
240276067042000	0	8.0%	0
240276068032000	0	3.4%	0
240276068033000	0	14.0%	0
240276068033001	106	11.0%	118
240276068033003	20	15.4%	23
240276068033004	0	6.0%	0
240276068041000	0	0.0%	0
240276068041001	0	0.0%	0
240276068041005	0	3.3%	0
240276068041006	0	12.6%	0
240276068041007	0	8.9%	0
240276068041008	0	13.7%	0
240276068041009	0	5.7%	0
240276068041010	299	0.0%	299
240276069023001	11	0.0%	11
240276069024002	12	0.0%	12
240276069024003	7	0.0%	7
240276069024005	9	0.0%	9
240276069024006	22	0.0%	22
240276069024007	7	0.0%	7
Total	**2053**		**2202**

Table 10-6. Adjustments of Total People Displaced for Best Case Scenario and 500-yr Flood.

Census Block	2010 Population Displaced	Increase in Consequences for Census Block	2100 Population Displaced
240276022003004	13	4.4%	14
240276022003008	27	10.8%	30

Census Block	2010 Population Displaced	Increase in Consequences for Census Block	2100 Population Displaced
240276022003010	0	4.3%	0
240276022004000	33	4.4%	34
240276022004001	186	6.9%	199
240276022004002	3	11.8%	3
240276023041000	8	4.7%	8
240276023041005	25	3.0%	26
240276023041006	8	1.7%	8
240276023041012	160	7.1%	171
240276023041019	55	2.3%	56
240276023041020	1	0.0%	1
240276023041021	30	17.1%	35
240276023042010	8	9.7%	9
240276023042011	0	10.4%	0
240276023042015	0	11.6%	0
240276023042016	0	0.0%	0
240276023042017	3	0.0%	3
240276023051000	191	7.8%	206
240276023052001	32	6.8%	34
240276023062014	6	12.8%	7
240276023062015	37	9.9%	41
240276023062016	13	12.7%	15
240276030001005	11	6.6%	12
240276030001006	1	10.5%	1
240276030001007	0	12.5%	0
240276030001008	10	6.0%	11
240276030002000	4	4.3%	4
240276030002001	0	15.1%	0
240276030002002	1	11.2%	1
240276030002003	0	10.1%	0
240276030002016	1	0.4%	1
240276054011000	0	9.3%	0
240276054011003	121	7.8%	130
240276054011004	85	4.8%	89
240276054011005	4	13.7%	5
240276054011006	0	6.3%	0
240276054011007	76	7.5%	82

Census Block	2010 Population Displaced	Increase in Consequences for Census Block	2100 Population Displaced
240276054011008	7	9.9%	8
240276054011009	0	16.0%	0
240276054011010	202	15.2%	233
240276054011011	0	0.7%	0
240276054012000	50	9.0%	55
240276054012002	13	6.1%	14
240276054012003	2	12.4%	2
240276054013000	3	10.5%	3
240276054023000	0	8.0%	0
240276054023001	95	12.9%	107
240276054023003	28	9.2%	31
240276054023006	0	15.9%	0
240276054023007	0	4.9%	0
240276054023009	0	8.1%	0
240276054023019	0	4.6%	0
240276054023020	0	9.5%	0
240276056023017	0	6.2%	0
240276056023019	0	2.9%	0
240276056023020	0	8.3%	0
240276066031000	4	8.5%	4
240276066031003	233	10.6%	258
240276066032001	68	6.7%	73
240276066032003	0	5.6%	0
240276066032004	0	6.2%	0
240276067011000	0	9.0%	0
240276067011001	1	6.0%	1
240276067011002	16	6.3%	17
240276067011003	0	7.3%	0
240276067011004	0	2.9%	0
240276067011005	0	14.6%	0
240276067011006	0	2.2%	0
240276067011007	104	10.7%	115
240276067011020	0	7.2%	0
240276067011023	2	12.9%	2
240276067012008	4	9.9%	4
240276067012010	22	9.9%	24

Census Block	2010 Population Displaced	Increase in Consequences for Census Block	2100 Population Displaced
240276067031003	0	3.3%	0
240276067041008	0	13.3%	0
240276067041018	0	10.3%	0
240276067042000	13	8.0%	14
240276068032000	0	3.4%	0
240276068032004	0	0.0%	0
240276068033000	0	14.0%	0
240276068033001	130	11.0%	144
240276068033003	26	15.4%	30
240276068033004	0	6.0%	0
240276068041000	0	0.0%	0
240276068041001	0	0.0%	0
240276068041005	0	3.3%	0
240276068041006	0	12.6%	0
240276068041007	0	8.9%	0
240276068041008	0	13.7%	0
240276068041009	0	5.7%	0
240276068041010	353	0.0%	353
240276069023001	13	0.0%	13
240276069023002	0	0.0%	0
240276069024000	0	4.8%	0
240276069024002	13	0.0%	13
240276069024003	29	0.0%	29
240276069024005	13	0.0%	13
240276069024006	35	0.0%	35
240276069024007	13	0.0%	13
Total	**2645**		**2844**

Table 10-7. Total Building Loss for Worst Case Nonstationarity Scenario and 100-yr Flood.

Census Block	2010 Total Economic Loss ($ Thousands)	Increase in Consequences for Census Block	2100 Total Economic Loss ($ Thousands)
240276022003004	516	13.3%	585

Census Block	2010 Total Economic Loss ($ Thousands)	Increase in Consequences for Census Block	2100 Total Economic Loss ($ Thousands)
240276022003008	544	33.1%	724
240276022003010	5931	13.2%	6717
240276022004000	1340	13.3%	1518
240276022004001	11976	21.2%	14510
240276023041000	1334	14.3%	1525
240276023041005	781	9.2%	853
240276023041006	480	5.2%	505
240276023041012	6908	21.5%	8395
240276023041019	2236	7.0%	2393
240276023041020	6	0.0%	6
240276023041021	543	52.3%	827
240276023042010	282	29.7%	366
240276023042015	30	35.3%	41
240276023042016	0	0.0%	0
240276023042017	110	0.0%	110
240276023051000	7033	23.7%	8701
240276023052001	1281	20.6%	1545
240276023062015	837	30.2%	1090
240276023062016	538	38.8%	747
240276030001005	261	20.1%	313
240276030001006	26	31.9%	34
240276030001007	0	38.1%	0
240276030001008	576	18.3%	681
240276030002000	163	13.2%	185
240276030002001	0	46.0%	0
240276030002016	66	1.2%	67
240276054011003	4048	23.7%	5009
240276054011004	2793	14.6%	3201
240276054011005	168	41.8%	238
240276054011006	0	19.3%	0
240276054011007	3302	22.8%	4056
240276054011008	76	30.1%	99
240276054011009	0	48.8%	0
240276054011010	3864	46.5%	5659
240276054012000	2746	27.6%	3504
240276054012002	197	18.6%	234
240276054023000	0	24.3%	0

Census Block	2010 Total Economic Loss ($ Thousands)	Increase in Consequences for Census Block	2100 Total Economic Loss ($ Thousands)
240276054023001	3206	39.2%	4464
240276054023003	2	28.1%	3
240276054023006	0	48.6%	0
240276054023007	12679	15.1%	14589
240276054023019	331	14.1%	378
240276054023020	0	29.0%	0
240276056023017	40	18.9%	48
240276056023019	0	8.7%	0
240276056023020	0	25.2%	0
240276066031003	3732	32.4%	4941
240276066032001	3235	20.4%	3893
240276066032003	0	17.0%	0
240276066032004	0	19.0%	0
240276067011000	1197	27.6%	1527
240276067011001	52	18.2%	61
240276067011002	509	19.3%	607
240276067011003	6875	22.1%	8396
240276067011004	0	8.9%	0
240276067011005	0	44.5%	0
240276067011006	0	6.7%	0
240276067011007	5395	32.5%	7149
240276067011023	27	39.5%	38
240276067012010	1248	30.1%	1624
240276067031003	8001	10.1%	8809
240276068033000	0	42.6%	0
240276068033001	7907	33.5%	10559
240276068033003	1184	47.1%	1742
240276068033004	6753	18.4%	7993
240276068041000	0	0.0%	0
240276068041001	10	0.0%	10
240276068041005	0	10.0%	0
240276068041006	0	38.3%	0
240276068041007	372	27.2%	473
240276068041008	2758	41.7%	3908
240276068041009	0	17.4%	0
240276068041010	16485	0.0%	16485
240276069023001	2123	0.0%	2123

Census Block	2010 Total Economic Loss ($ Thousands)	Increase in Consequences for Census Block	2100 Total Economic Loss ($ Thousands)
240276069024002	679	0.0%	679
240276069024003	657	0.0%	657
240276069024005	1101	0.0%	1101
240276069024006	1313	0.0%	1313
240276069024007	555	0.0%	555
Total	**149418**		**178563**

Table 10-8. Total Building Loss for Worst Case Nonstationarity Scenario and 500-yr Flood.

CensusBlock	2010 Total Economic Loss ($ Thousands)	Increase in Consequences for Census Block	2100 Total Economic Loss ($ Thousands)
240276030002000	240	13.2%	272
240276030002001	0	46.0%	0
240276030002002	80	34.2%	107
240276030002003	0	30.8%	0
240276023041012	8711	21.5%	10586
240276023041019	2952	7.0%	3159
240276023041020	30	0.0%	30
240276023041021	817	52.3%	1244
240276030001005	382	20.1%	459
240276030001006	33	31.9%	44
240276030001007	0	38.1%	0
240276030001008	914	18.3%	1081
240276054011003	5234	23.7%	6476
240276054011004	3317	14.6%	3802
240276054011005	193	41.8%	274
240276054011006	0	19.3%	0
240276054011007	3841	22.8%	4718
240276054011008	134	30.1%	174
240276054011009	0	48.8%	0
240276054011010	5655	46.5%	8282
240276054011011	0	2.0%	0
240276054012000	3860	27.6%	4925
240276056023017	51	18.9%	61

CensusBlock	2010 Total Economic Loss ($ Thousands)	Increase in Consequences for Census Block	2100 Total Economic Loss ($ Thousands)
240276056023019	0	8.7%	0
240276056023020	0	25.2%	0
240276054023019	463	14.1%	528
240276054023020	0	29.0%	0
240276066031003	6188	32.4%	8193
240276066032001	4169	20.4%	5018
240276066032003	0	17.0%	0
240276066032004	0	19.0%	0
240276022003004	567	13.3%	643
240276022003006	54	18.8%	64
240276022003008	987	33.1%	1314
240276022003010	6883	13.2%	7795
240276022004000	1620	13.3%	1836
240276022004001	17092	21.2%	20709
240276022004002	19	36.0%	26
240276023041000	1721	14.3%	1967
240276023041005	1113	9.2%	1216
240276023041006	504	5.2%	530
240276023042010	357	29.7%	463
240276023042011	10	31.8%	13
240276023042015	50	35.3%	68
240276023042016	0	0.0%	0
240276023042017	127	0.0%	127
240276023051000	8914	23.7%	11028
240276023052001	1630	20.6%	1966
240276023052002	0	11.6%	0
240276023062015	1403	30.2%	1827
240276023062016	685	38.8%	951
240276030002015	0	0.0%	0
240276030002016	118	1.2%	119
240276068032000	21	10.5%	23
240276068032004	44	0.0%	44
240276068033000	0	42.6%	0
240276068033001	9333	33.5%	12464
240276068033003	1486	47.1%	2186
240276068033004	8010	18.4%	9481

CensusBlock	2010 Total Economic Loss ($ Thousands)	Increase in Consequences for Census Block	2100 Total Economic Loss ($ Thousands)
240276068041000	0	0.0%	0
240276068041001	21	0.0%	21
240276054012002	544	18.6%	645
240276054012003	94	37.9%	130
240276054013000	53	32.0%	70
240276054023000	0	24.3%	0
240276054023001	4574	39.2%	6369
240276054023003	1144	28.1%	1466
240276054023006	0	48.6%	0
240276054023007	17417	15.1%	20041
240276054023009	1074	24.7%	1339
240276067011004	0	8.9%	0
240276067011005	0	44.5%	0
240276067011006	0	6.7%	0
240276067011007	6701	32.5%	8880
240276067011023	106	39.5%	148
240276067011000	1275	27.6%	1627
240276067011001	72	18.2%	85
240276067011002	996	19.3%	1188
240276067011003	9087	22.1%	11098
240276067012008	114	30.1%	148
240276067012010	1648	30.1%	2144
240276067031003	9526	10.1%	10488
240276067042000	20	24.3%	25
240276068021000	1	22.5%	1
240276068041005	0	10.0%	0
240276068041006	0	38.3%	0
240276068041007	1969	27.2%	2505
240276068041008	4552	41.7%	6450
240276068041009	0	17.4%	0
240276068041010	20467	0.0%	20467
240276068042001	57	33.6%	76
240276069023001	2115	0.0%	2115
240276069023002	0	0.0%	0
240276069024002	763	0.0%	763
240276069024003	1075	0.0%	1075

CensusBlock	2010 Total Economic Loss ($ Thousands)	Increase in Consequences for Census Block	2100 Total Economic Loss ($ Thousands)
240276069024005	1171	0.0%	1171
240276069024006	2179	0.0%	2179
240276069024007	793	0.0%	793
Total	**199620**		**239798**

Table 10-9. Total People Displaced Best Case Nonstationarity Scenario and 100-yr Flood.

Census Block	2010 Population Displaced	Increase in Consequences for Census Block	2100 Population Displaced
240276022003004	12	0.13	14
240276022003008	23	0.33	31
240276022003010	0	0.13	0
240276022004000	30	0.13	34
240276022004001	153	0.21	185
240276022004002	1	0.36	1
240276023041000	8	0.14	9
240276023041005	22	0.09	24
240276023041006	8	0.05	8
240276023041012	143	0.22	174
240276023041019	50	0.07	54
240276023041020	0	0.00	0
240276023041021	17	0.52	26
240276023042010	8	0.30	10
240276023042011	0	0.32	0
240276023042015	0	0.35	0
240276023042016	0	0.00	0
240276023042017	3	0.00	3
240276023051000	176	0.24	218
240276023052001	34	0.21	41
240276023062014	4	0.39	6
240276023062015	26	0.30	34
240276023062016	12	0.39	17
240276030001005	11	0.20	13
240276030001006	1	0.32	1
240276030001007	0	0.38	0

Census Block	2010 Population Displaced	Increase in Consequences for Census Block	2100 Population Displaced
240276030001008	4	0.18	5
240276030002000	3	0.13	3
240276030002001	0	0.46	0
240276030002016	1	0.01	1
240276054011000	0	0.28	0
240276054011003	110	0.24	136
240276054011004	79	0.15	91
240276054011005	4	0.42	6
240276054011006	0	0.19	0
240276054011007	72	0.23	88
240276054011008	7	0.30	9
240276054011009	0	0.49	0
240276054011010	147	0.46	215
240276054012000	43	0.28	55
240276054012002	5	0.19	6
240276054023000	0	0.24	0
240276054023001	75	0.39	104
240276054023003	2	0.28	3
240276054023006	0	0.49	0
240276054023007	0	0.15	0
240276054023019	0	0.14	0
240276054023020	0	0.29	0
240276056023017	0	0.19	0
240276056023019	0	0.09	0
240276056023020	0	0.25	0
240276066031003	170	0.32	225
240276066032001	65	0.20	78
240276066032003	0	0.17	0
240276066032004	0	0.19	0
240276067011000	0	0.28	0
240276067011001	1	0.18	1
240276067011002	7	0.19	8
240276067011003	0	0.22	0
240276067011004	0	0.09	0
240276067011005	0	0.44	0
240276067011006	0	0.07	0
240276067011007	92	0.33	122

Census Block	2010 Population Displaced	Increase in Consequences for Census Block	2100 Population Displaced
240276067011023	0	0.39	0
240276067012010	20	0.30	26
240276067031003	0	0.10	0
240276067041008	0	0.40	0
240276067041018	0	0.32	0
240276067042000	0	0.24	0
240276068032000	0	0.10	0
240276068033000	0	0.43	0
240276068033001	108	0.34	144
240276068033003	23	0.47	34
240276068033004	0	0.18	0
240276068041000	0	0.00	0
240276068041001	0	0.00	0
240276068041005	0	0.10	0
240276068041006	0	0.38	0
240276068041007	0	0.27	0
240276068041008	0	0.42	0
240276068041009	0	0.17	0
240276068041010	305	0.00	305
240276069023001	11	0.00	11
240276069024000	0	0.15	0
240276069024002	13	0.00	13
240276069024003	23	0.00	23
240276069024005	12	0.00	12
240276069024006	24	0.00	24
240276069024007	11	0.00	11
Total	**2179**		**2662**

Table 10-10. Total People Displace for Worst Case Nonstationarity Scenario and 500-yr Flood.

Census Block	2010 Population Displaced	Increase in Consequences for Census Block	2100 Population Displaced
240276022003004	17	13.3%	19
240276022003006	9	18.8%	11
240276022003008	33	33.1%	44

Census Block	2010 Population Displaced	Increase in Consequences for Census Block	2100 Population Displaced
240276022003010	0	13.2%	0
240276022004000	30	13.3%	34
240276022004001	188	21.2%	228
240276022004002	3	36.0%	4
240276023041000	10	14.3%	11
240276023041005	25	9.2%	27
240276023041006	8	5.2%	8
240276023041012	161	21.5%	196
240276023041019	57	7.0%	61
240276023041020	1	0.0%	1
240276023041021	30	52.3%	46
240276023042010	9	29.7%	12
240276023042011	1	31.8%	1
240276023042015	0	35.3%	0
240276023042016	0	0.0%	0
240276023042017	3	0.0%	3
240276023051000	190	23.7%	235
240276023052001	44	20.6%	53
240276023052002	1	11.6%	1
240276023062014	6	39.0%	8
240276023062015	37	30.2%	48
240276023062016	13	38.8%	18
240276030001005	11	20.1%	13
240276030001006	1	31.9%	1
240276030001007	0	38.1%	0
240276030001008	10	18.3%	12
240276030002000	4	13.2%	5
240276030002001	0	46.0%	0
240276030002002	1	34.2%	1
240276030002003	0	30.8%	0
240276030002015	0	0.0%	0
240276030002016	1	1.2%	1
240276054011000	0	28.3%	0
240276054011003	121	23.7%	150
240276054011004	86	14.6%	99
240276054011005	4	41.8%	6

Census Block	2010 Population Displaced	Increase in Consequences for Census Block	2100 Population Displaced
240276054011006	0	19.3%	0
240276054011007	76	22.8%	93
240276054011008	7	30.1%	9
240276054011009	0	48.8%	0
240276054011010	213	46.5%	312
240276054011011	5	2.0%	5
240276054012000	51	27.6%	65
240276054012002	15	18.6%	18
240276054012003	3	37.9%	4
240276054013000	3	32.0%	4
240276054023000	0	24.3%	0
240276054023001	95	39.2%	132
240276054023003	28	28.1%	36
240276054023006	0	48.6%	0
240276054023007	0	15.1%	0
240276054023009	0	24.7%	0
240276054023019	0	14.1%	0
240276054023020	0	29.0%	0
240276056023017	0	18.9%	0
240276056023019	0	8.7%	0
240276056023020	0	25.2%	0
240276066031003	238	32.4%	315
240276066032001	78	20.4%	94
240276066032003	0	17.0%	0
240276066032004	0	19.0%	0
240276067011000	0	27.6%	0
240276067011001	2	18.2%	2
240276067011002	18	19.3%	21
240276067011003	0	22.1%	0
240276067011004	0	8.9%	0
240276067011005	0	44.5%	0
240276067011006	0	6.7%	0
240276067011007	106	32.5%	140
240276067011020	0	22.0%	0
240276067011023	2	39.5%	3
240276067012008	3	30.1%	4

Census Block	2010 Population Displaced	Increase in Consequences for Census Block	2100 Population Displaced
240276067012010	23	30.1%	30
240276067031003	0	10.1%	0
240276067041008	0	40.4%	0
240276067041018	0	31.5%	0
240276067042000	15	24.3%	19
240276068021000	0	22.5%	0
240276068032000	0	10.5%	0
240276068032004	0	0.0%	0
240276068033000	0	42.6%	0
240276068033001	120	33.5%	160
240276068033003	25	47.1%	37
240276068033004	0	18.4%	0
240276068041000	0	0.0%	0
240276068041001	0	0.0%	0
240276068041005	0	10.0%	0
240276068041006	0	38.3%	0
240276068041007	0	27.2%	0
240276068041008	0	41.7%	0
240276068041009	0	17.4%	0
240276068041010	347	0.0%	347
240276068042001	1	33.6%	1
240276069023001	10	0.0%	10
240276069023002	0	0.0%	0
240276069024000	0	14.6%	0
240276069024002	15	0.0%	15
240276069024003	28	0.0%	28
240276069024005	11	0.0%	11
240276069024006	39	0.0%	39
240276069024007	13	0.0%	13
Total	**2705**		**3326**

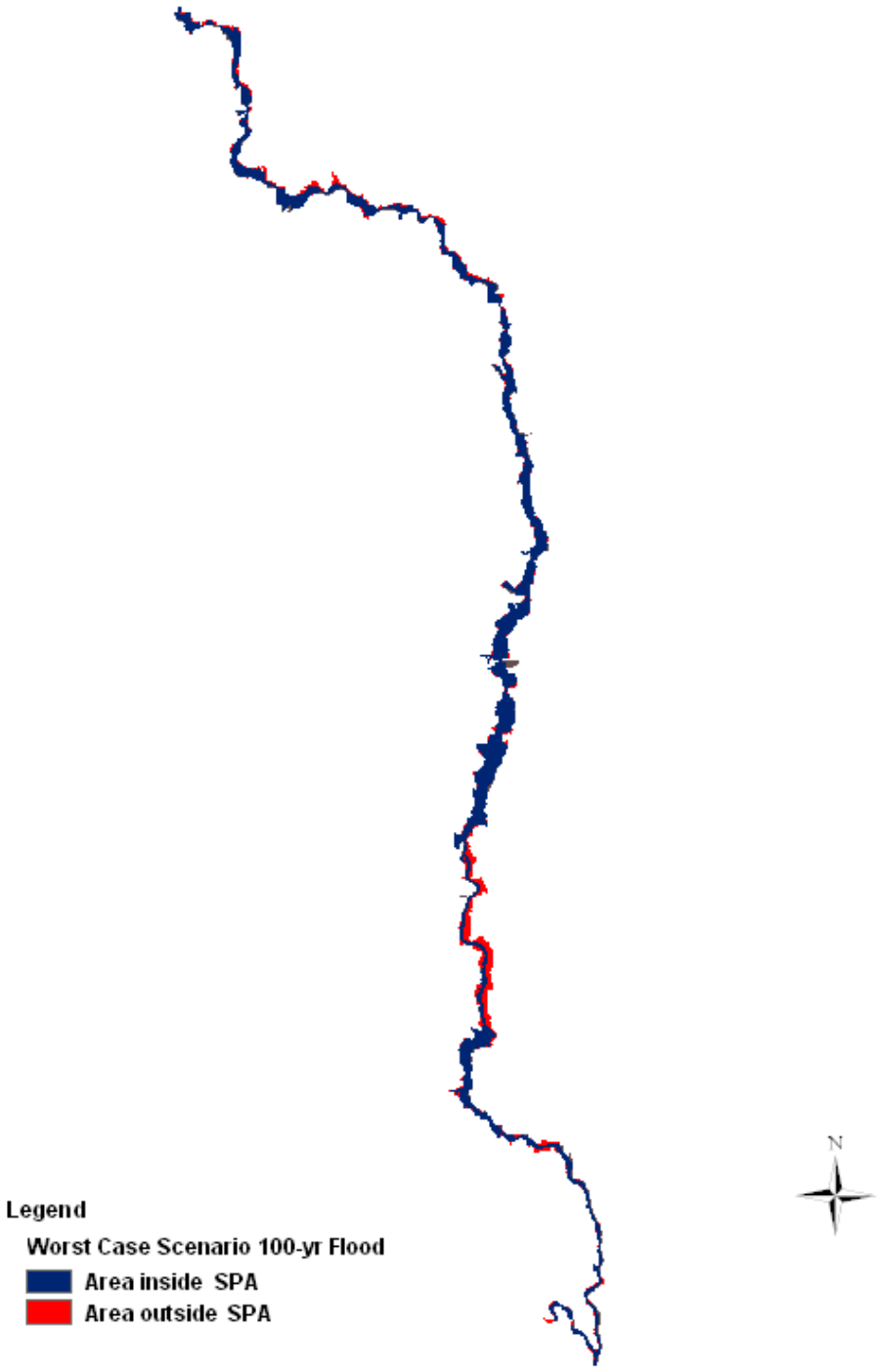

Figure 10-4. Area Within and Outside of SPA for Worst Case Scenario 100-yr Flood.

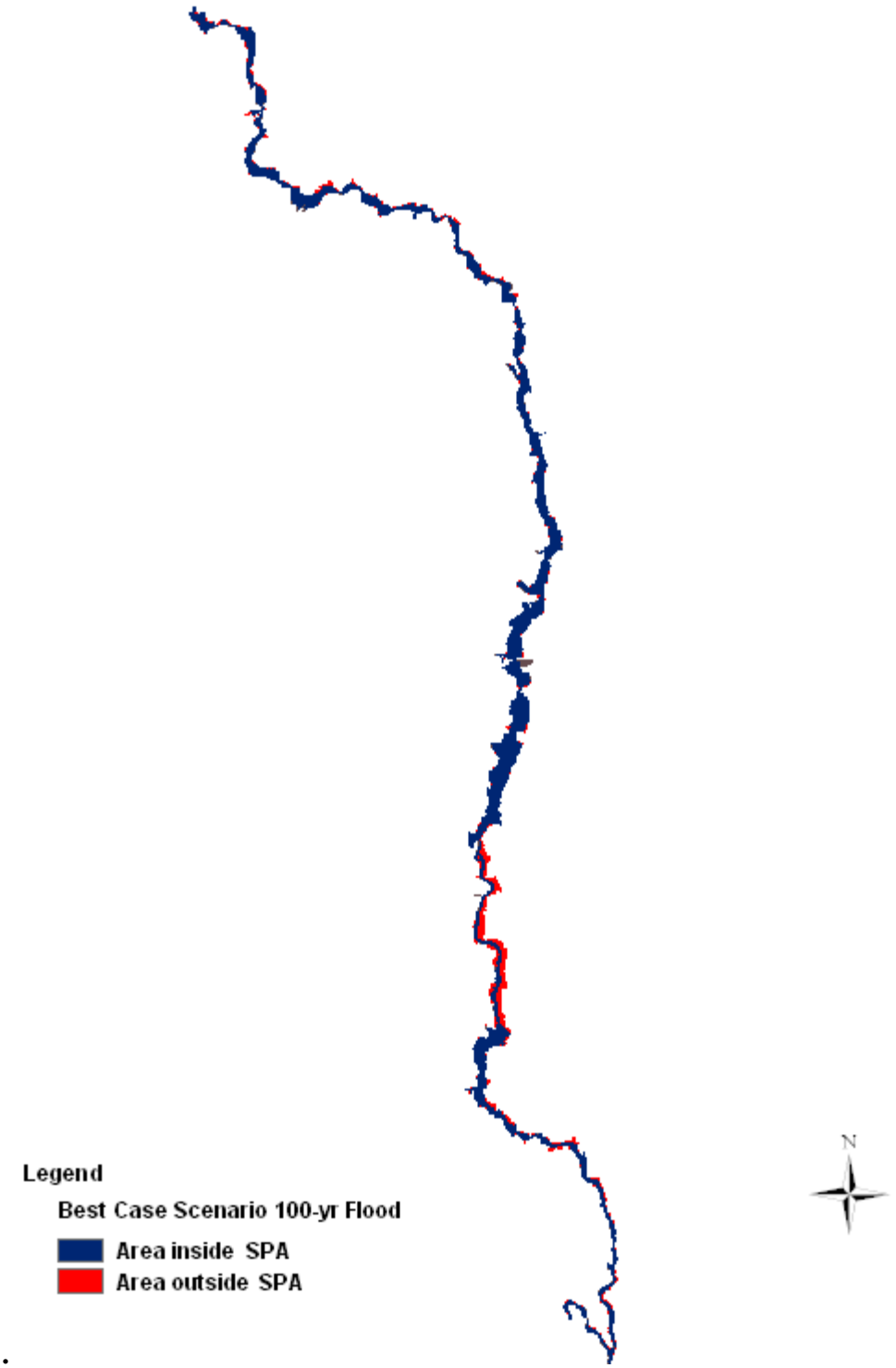

Figure 10-5. Area Within and Outside of SPA for Best Case Scenario 100-yr Flood.

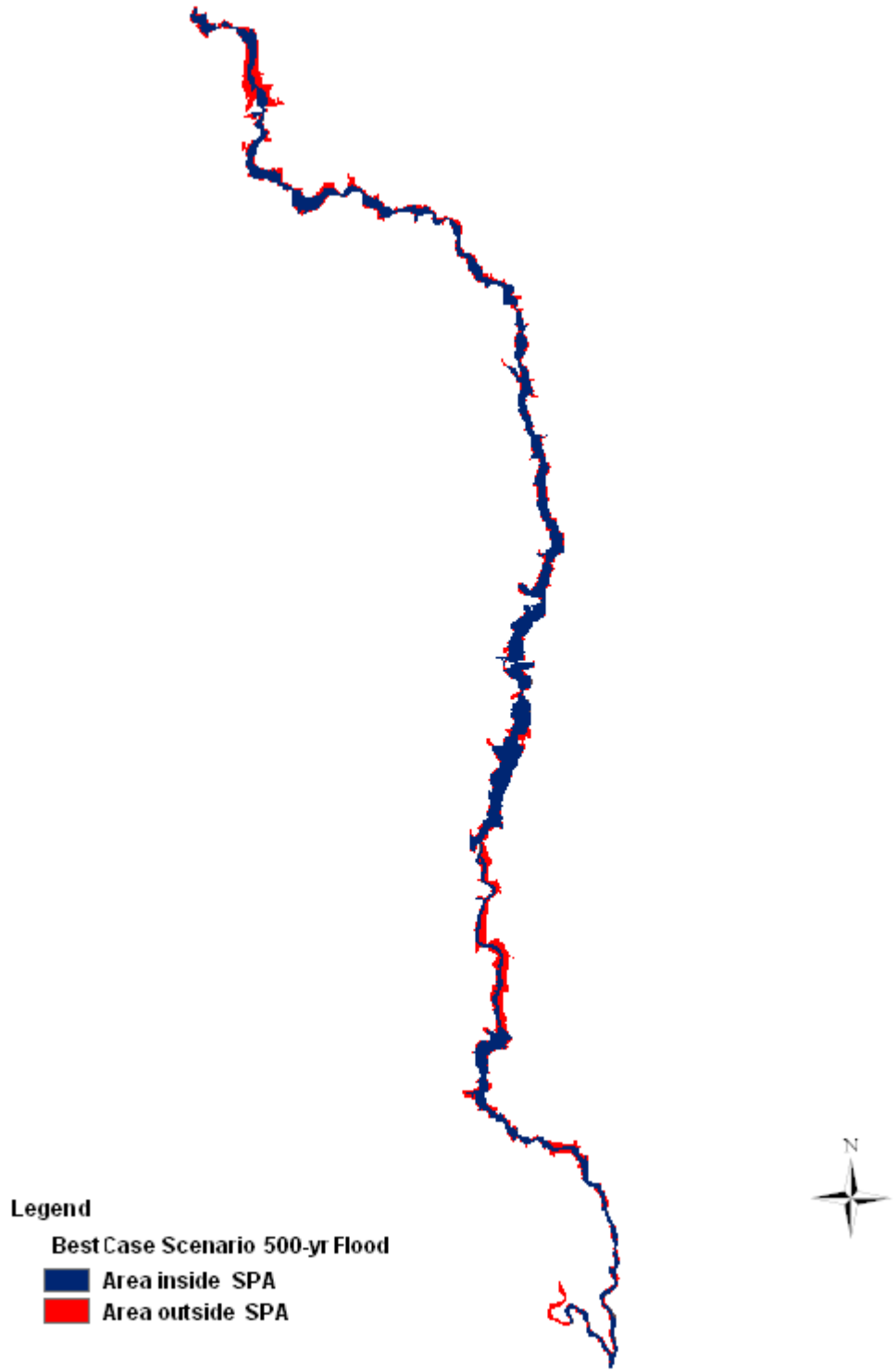

Figure 10-6. Area Within and Outside of SPA for Best Case Scenario 500-yr Flood.

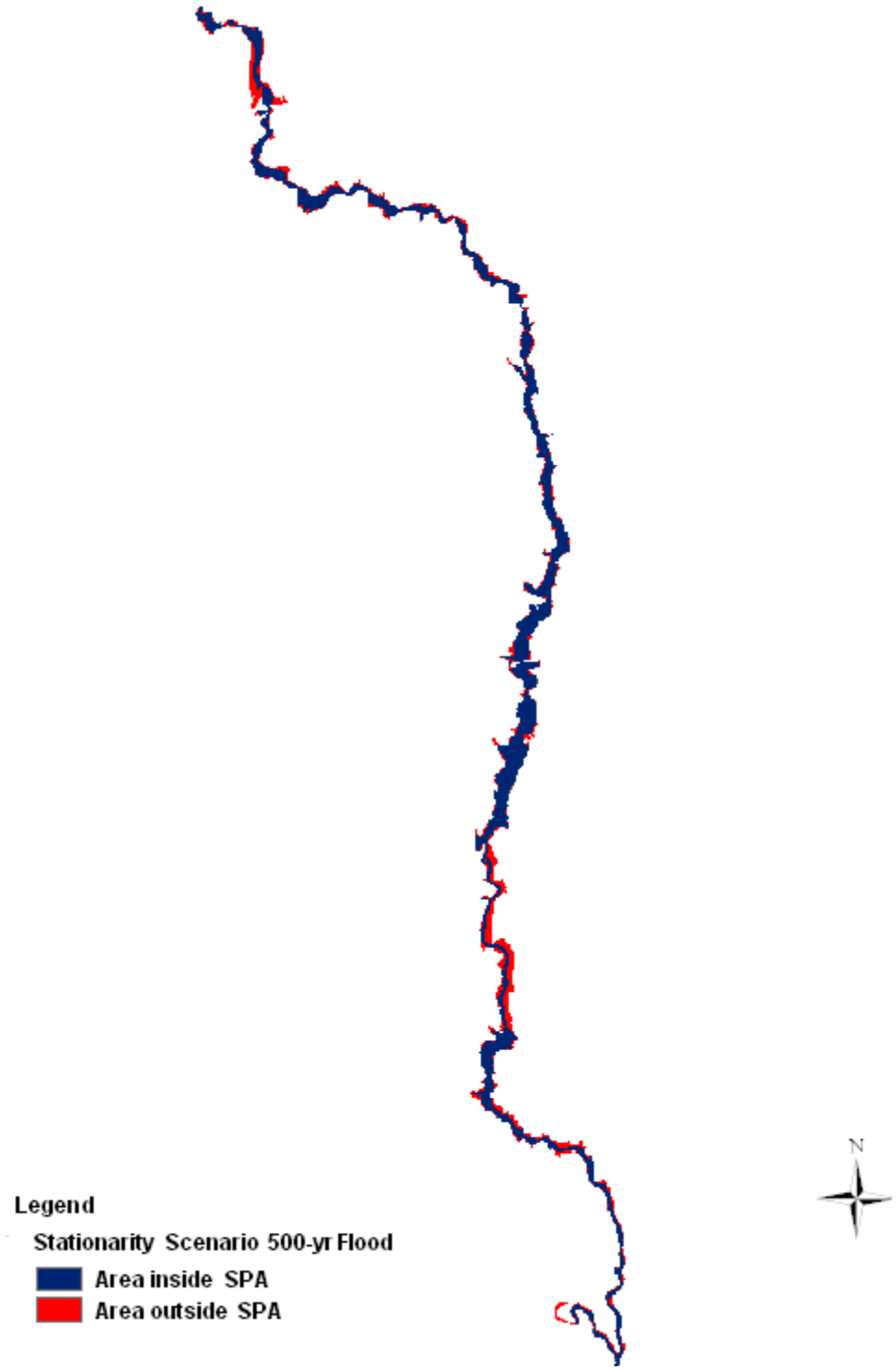

Figure 10-7. Area Within and Outside of SPA for StationarityScenario 500-yr Flood.

Table 10-11. Proportion of Consequences Allocated to Area Inside and Outside SPA for the Best Case 100-yr Flood

Census Block*	Inside	Outside
240276022003004	38%	62%
240276022003008	56%	44%
240276022003010	100%	0%
240276022004000	64%	36%
240276022004001	94%	6%
240276023041000	85%	15%
240276023041005	97%	3%
240276023041006	94%	6%
240276023041012	95%	5%
240276023041019	97%	3%
240276023041021	100%	0%
240276023042010	90%	10%
240276023042015	94%	6%
240276023042016	100%	0%
240276023042017	95%	5%
240276023051000	96%	4%
240276023052001	95%	5%
240276023062014	100%	0%
240276023062015	90%	10%
240276023062016	96%	4%
240276030001005	84%	16%
240276030001006	96%	4%
240276030001007	100%	0%
240276030001008	87%	13%
240276030002000	87%	13%
240276030002001	88%	12%
240276030002016	97%	3%
240276054011003	98%	2%
240276054011004	94%	6%
240276054011005	91%	9%
240276054011007	93%	7%
240276054011009	87%	13%
240276054011010	93%	7%
240276054012000	96%	4%
240276054012002	100%	0%
240276054023000	100%	0%

Census Block*	Inside	Outside
240276054023001	95%	5%
240276054023006	90%	10%
240276054023007	92%	8%
240276054023019	84%	16%
240276054023020	100%	0%
240276056023017	100%	0%
240276056023019	100%	0%
240276056023020	97%	3%
240276066031003	85%	15%
240276066032001	25%	75%
240276066032003	79%	21%
240276066032004	54%	46%
240276067011000	72%	28%
240276067011001	100%	0%
240276067011002	100%	0%
240276067011003	21%	79%
240276067011004	0%	100%
240276067011005	0%	100%
240276067011006	24%	76%
240276067011007	67%	33%
240276067012010	99%	1%
240276067031003	93%	7%
240276068033000	100%	0%
240276068033001	90%	10%
240276068033003	95%	5%
240276068033004	100%	0%
240276068041000	96%	4%
240276068041001	45%	55%
240276068041005	100%	0%
240276068041006	100%	0%
240276068041008	87%	13%
240276068041009	100%	0%
240276068041010	85%	15%
240276069023001	85%	15%
240276069024002	97%	3%
240276069024003	94%	6%
240276069024005	86%	14%

Census Block*	Inside	Outside
240276069024006	86%	14%
240276069024007	100%	0%

*Due to resampling issues in ArcGIS, Census Tracks 240276068041007 and 240276067011023 were not included in the SPA analysis. The consequences were assumed to remain at the 2010 conditions for these census tracks.

Table 10-12. Proportion of Consequences Allocated to Area Inside and Outside SPA for the Best Case 500-yr Flood.

Census Block	Inside	Outside
240276022003004	38%	62%
240276022003008	52%	48%
240276022003010	96%	4%
240276022004000	62%	38%
240276022004001	84%	16%
240276022004002	0%	100%
240276023041000	70%	30%
240276023041005	90%	10%
240276023041006	90%	10%
240276023041012	87%	13%
240276023041019	89%	11%
240276023041020	0%	100%
240276023041021	69%	31%
240276023042010	87%	13%
240276023042011	0%	100%
240276023042015	79%	21%
240276023042016	100%	0%
240276023042017	89%	11%
240276023051000	90%	10%
240276023052001	87%	13%
240276023062014	56%	44%
240276023062015	73%	27%
240276023062016	90%	10%
240276030001005	82%	18%
240276030001006	52%	48%
240276030001007	62%	38%
240276030001008	43%	57%
240276030002000	77%	23%
240276030002001	68%	32%

Census Block	Inside	Outside
240276030002002	0%	100%
240276030002003	0%	100%
240276030002016	84%	16%
240276054011003	92%	8%
240276054011004	91%	9%
240276054011005	90%	10%
240276054011006	100%	0%
240276054011007	91%	9%
240276054011008	79%	21%
240276054011009	49%	51%
240276054011010	68%	32%
240276054012000	86%	14%
240276054012002	47%	53%
240276054012003	0%	100%
240276054013000	0%	100%
240276054023000	90%	10%
240276054023001	72%	28%
240276054023003	0%	100%
240276054023006	78%	22%
240276054023007	77%	23%
240276054023009	0%	100%
240276054023019	56%	44%
240276054023020	100%	0%
240276056023017	77%	23%
240276056023019	19%	81%
240276056023020	83%	17%
240276066031000	0%	100%
240276066031003	62%	38%
240276066032001	24%	76%
240276066032003	79%	21%
240276066032004	56%	44%
240276067011000	56%	44%
240276067011001	50%	50%
240276067011002	86%	14%
240276067011003	20%	80%
240276067011004	0%	100%
240276067011005	0%	100%

Census Block	Inside	Outside
240276067011006	23%	77%
240276067011007	63%	37%
240276067011023	0%	100%
240276067012008	0%	100%
240276067012010	87%	13%
240276067031003	87%	13%
240276067042000	0%	100%
240276068033000	100%	0%
240276068033001	77%	23%
240276068033003	83%	17%
240276068033004	98%	2%
240276068041000	74%	26%
240276068041001	28%	72%
240276068041005	91%	9%
240276068041006	64%	36%
240276068041007	15%	85%
240276068041008	75%	25%
240276068041009	82%	18%
240276068041010	76%	24%
240276069023001	76%	24%
240276069023002	0%	100%
240276069024002	91%	9%
240276069024003	76%	24%
240276069024005	83%	17%
240276069024006	62%	38%
240276069024007	91%	9%

Table 10-13. Proportion of Consequences Allocated to Area Inside and Outside SPA for the Worst Case 100-yr Flood

Census Block*	Inside	Outside
240276022003004	39%	61%
240276022003008	43%	57%
240276022003010	97%	3%
240276022004000	65%	35%
240276022004001	93%	7%
240276023041000	64%	36%
240276023041005	98%	2%

Census Block*	Inside	Outside
240276023041006	89%	11%
240276023041012	93%	7%
240276023041019	97%	3%
240276023041021	100%	0%
240276023042010	90%	10%
240276023042015	93%	7%
240276023042016	83%	17%
240276023042017	98%	2%
240276023051000	95%	5%
240276023052001	84%	16%
240276023062014	100%	0%
240276023062015	86%	14%
240276023062016	93%	7%
240276030001005	85%	15%
240276030001006	57%	43%
240276030001007	67%	33%
240276030001008	85%	15%
240276030002000	86%	14%
240276030002001	78%	22%
240276030002016	97%	3%
240276054011003	99%	1%
240276054011004	94%	6%
240276054011005	94%	6%
240276054011006	100%	0%
240276054011007	97%	3%
240276054011008	78%	22%
240276054011009	88%	12%
240276054011010	87%	13%
240276054012000	97%	3%
240276054012002	100%	0%
240276054023000	96%	4%
240276054023001	86%	14%
240276054023003	0%	100%
240276054023006	89%	11%
240276054023007	88%	12%
240276054023019	78%	22%
240276054023020	100%	0%

Census Block*	Inside	Outside
240276056023017	100%	0%
240276056023019	100%	0%
240276056023020	97%	3%
240276066031003	80%	20%
240276066032001	21%	79%
240276066032003	79%	21%
240276066032004	55%	45%
240276067011000	55%	45%
240276067011001	86%	14%
240276067011002	100%	0%
240276067011003	21%	79%
240276067011004	0%	100%
240276067011005	0%	100%
240276067011006	24%	76%
240276067011007	67%	33%
240276067012010	92%	8%
240276067031003	91%	9%
240276068033000	100%	0%
240276068033001	89%	11%
240276068033003	92%	8%
240276068033004	98%	2%
240276068041000	86%	14%
240276068041001	45%	55%
240276068041005	100%	0%
240276068041006	74%	26%
240276068041007	29%	71%
240276068041008	89%	11%
240276068041009	100%	0%
240276068041010	85%	15%
240276069023001	90%	10%
240276069024002	95%	5%
240276069024003	92%	8%
240276069024005	86%	14%
240276069024006	83%	17%
240276069024007	97%	3%

*Due to resampling issues in ArcGIS, Census Track 240276067011023 was not included in the SPA analysis. The consequences were assumed to remain at the 2010 conditions for this census track.

Table 10-14. Proportion of Consequences Allocated to Area Inside and Outside SPA for the Worst Case 500-yr Flood.

Census Block*	Inside	Outside
240276022003004	29%	71%
240276022003006	0%	100%
240276022003008	44%	56%
240276022003010	95%	5%
240276022004000	67%	33%
240276022004001	83%	17%
240276022004002	0%	100%
240276023041000	56%	44%
240276023041005	87%	13%
240276023041006	85%	15%
240276023041012	86%	14%
240276023041019	87%	13%
240276023041020	0%	100%
240276023041021	69%	31%
240276023042010	81%	19%
240276023042011	0%	100%
240276023042015	77%	23%
240276023042016	100%	0%
240276023042017	88%	12%
240276023051000	89%	11%
240276023052001	67%	33%
240276023052002	0%	100%
240276023062014	56%	44%
240276023062015	73%	27%
240276023062016	89%	11%
240276030001005	83%	17%
240276030001006	72%	28%
240276030001007	94%	6%
240276030001008	43%	57%
240276030002000	76%	24%
240276030002001	64%	36%
240276030002002	0%	100%

Census Block*	Inside	Outside
240276030002003	0%	100%
240276030002015	0%	100%
240276030002016	79%	21%
240276054011003	91%	9%
240276054011004	90%	10%
240276054011005	90%	10%
240276054011006	100%	0%
240276054011007	93%	7%
240276054011008	79%	21%
240276054011009	49%	51%
240276054011010	64%	36%
240276054011011	0%	100%
240276054012000	85%	15%
240276054012002	43%	57%
240276054012003	0%	100%
240276054013000	0%	100%
240276054023000	91%	9%
240276054023001	70%	30%
240276054023003	0%	100%
240276054023006	75%	25%
240276054023007	73%	27%
240276054023009	0%	100%
240276054023019	56%	44%
240276054023020	100%	0%
240276056023017	78%	22%
240276056023019	17%	83%
240276056023020	83%	17%
240276066031003	60%	40%
240276066032001	21%	79%
240276066032003	75%	25%
240276066032004	56%	44%
240276067011000	56%	44%
240276067011001	51%	49%
240276067011002	78%	22%
240276067011003	19%	81%
240276067011004	0%	100%
240276067011005	0%	100%

Census Block*	Inside	Outside
240276067011006	23%	77%
240276067011007	62%	38%
240276067011023	0%	100%
240276067012008	0%	100%
240276067012010	85%	15%
240276067031003	92%	8%
240276067042000	0%	100%
240276068021000	0%	100%
240276068033000	100%	0%
240276068033001	82%	18%
240276068033003	86%	14%
240276068033004	93%	7%
240276068041000	72%	28%
240276068041001	24%	76%
240276068041005	91%	9%
240276068041006	66%	34%
240276068041007	15%	85%
240276068041008	75%	25%
240276068041009	81%	19%
240276068041010	76%	24%
240276068042001	0%	100%
240276069023001	78%	22%
240276069023002	0%	100%
240276069024002	84%	16%
240276069024003	75%	25%
240276069024005	88%	12%
240276069024006	54%	46%
240276069024007	87%	13%

*Due to resampling issues in ArcGIS, Census Track 240276022003006 and 2402760220032000 were not included in the SPA analysis. The consequences were assumed to remain at the 2010 conditions for these census tracks.

11 Works Cited

Allen, M.R. and W.J. Ingram (2002). "Constraints on Future Changes in Climate and the Hydrologic Cycle".*Nature,* 19(12 September): 224-232).

Beighley, R.E., Kargar, M. and Y.He (2009). "Effects of Impervious Area Estimation Methods on Simulated Peak Discharges". *Journal of Hydrologic Engineering*, 14(4):388-398.

Blais, N.C., Nguyen, E.T., Dogan, F., Samant, L., Mifflin, E., and C. Jones (2006". "Managing Future Development Conditions in the National Flood Insurance Program". Prepared under subcontract to the American Institutes for Research as part of the 2001–2006 Evaluation of the National Flood Insurance Program. ABSG Consulting Inc.

Bronstert, A., Niehoff, D., and G. Burger (2002). Effects of Climate and Land-use Change on Storm Runoff Generation: Present Knowledge and Modelling Capabilities. *Hydrologic Processes*, 16:509-529.

Burn, D.H. and M.A. Hag Elnur (2001). "Detection of Hydrologic Trends and Variability". *Journal of Hydrology*, 255:107-122.

Burby, RaymondJ.(2006). "HurricaneKatrina and theParadoxesofGovernment DisasterPolicy:BringingAboutWise Governmental Decisions for Hazardous Areas", Invited Paper Prepared for Publication in the Annals of the American Academy of Political and Social Sciences.

Castellarin, A., Burn, D.H., and A Brath (2000). "Assessing the Effectiveness of Hydrological Similarity Measures for Flood Frequency Analysis". *Journal of*

Hydrology, 241:270-185.

Charlton, R., Fealy, R., Moore, S., Sweeney, J. and C. Murphy (2006). Assessing the Impact of Climate Change on Water Supply and Flood Hazard in Ireland Using Statistical Downscaling and Hydrological Modelling Techniques. *Climatic Change* 74:475-491.

Christensen, J.H., B. Hewitson, A. Busuioc, A. Chen, X. Gao, I. Held, R. Jones, R.K. Kolli, W.-T. Kwon, R. Laprise, V. Magana Rueda, L. Mearns. C.G. Menendez, J. Raisanen, A. Rinke, A. Sarr and P. Whetten, 2007: Regional Climate Projections. In: *Climate Change 2007: The Physical Science Basis. Contribution of Working Group I to the Group Fourth Assessment Report of the Intergovernmental Panel on Climate Change* [Solomon, S., D. Qin, M. Manning, Z. Chen, M. Marquis, K.B. Averyt, M. Tignor and H.L. Miller (eds.)]. Cambridge University Press, Cambridge, United Kingdom and New York, NY, USA.

Cubasch, U., Waskewitz, J., Hegerl, G. and J. Perlwitz (1995). "Regional Climate Changes as Simulated in Time-Slice Experiments". *Climatic Change*, 31:273-304.

Cunderlik, J.M. and T.B.M.J. Ouarda (2006). "Regional Flood-Duration-Frequency Modeling in the Changing Environment". *Journal of Hydrology*, 318:276-291.

Dai, A., Qian, T., K.E. Trenberth, and J.D. Milliman (2009). "Changes in Continental Freshwater Discharge from 1948 to 2004". *Journal of Climate*, 22:2773-2792.

Davis, S.J., Caldeira, K., and Matthews, H.D. (2010). "Future CO2 Emission and Climate change from Existing Infrastructure". *SCIENCE*, 329:1330-1333.

De Michele, C., Montanari, A., and R. Rosso (1998). "The Effects of Non-Stationarity on

the Evaluation of Critical Design Storms". *Water Science Technology*, 37(11):1870193.

De Roo, A., Schmuck, G., Perdigao, V., and J. Thielen (2003). The Influence of Historic Land Use Changes and Future Planned Land Use Scenarios on Floods in the Oder Catchment. *Physics and Chemistry of the Earth*. 28:1291-1300.

Dore, M.I. (2005). "Climate Change and Changes in Global Precipitation Patterns: What do we Know?" *Environmental International*, 31:1167-1181.

Douglas, E.M., Vogel, R.M., and C.N. Kroll (2000). "Trends in Floods and Low Flows in the United States: Impact of Spatial Correlation". *Journal of Hydrology*, 240:90-105.

Douville, H., Chauvin, F., PLanton, S., Royer, J.F., Salas-Melia, D., and S. Tyteca (2002)."Sensitivity of the Hydrological Cycle to Increasing Amounts of Greenhouse Gases and Aerosols". *Climate Dynamic*, 20:45-68.

Dunne, T. and L.B. Leopold (1978).Water in Environmental Planning. W.H. Freeman andCo., San Francsisco.

El Adlouni, S., Ouarda, T.B.M.J., Zhang, X., Roy, R., and B. Bobee (2007). "Generalized Maximum Likeihood Estimators for the Nonstationary Generalized Extreme Value Model". *Water Resources Research,* 43:W03410.

Endreny, T.A. and K.E. Thomas (2009). "Improving Estimates of Simulated Runoff Quality and Quantity Using Road-Enhanced Land Cover Data". *Journal of Hydrologic Engineering*, 14(4):346-351.

Fekete, B.M., Vorosmarty, C.J., Roads, J.O., and C.J. Willmott (2003). "Uncertainties in Precipitation and Their Impacts on Runoff". *Journal of Climate*, 17:294-304.

Department of Homeland Security: Federal Emergency Management Agency (FEMA) (2009). Multi-hazard Loss Estimation Methodology: Flood Model User Manual, Washington, D.C.

Dillow, J.J.A. (1996). "Technique for Estimating Magnitude and Frequency of Peak Flows in Maryland". U.S. Geological Survey Water-Resources Investigations Report 95-4154. Prepared in Cooperation with the Maryland State Highway Administration. Towson.

Fitzpatrick, F.A., Knox, J.C., and H.E. Whitman (1999). Effects of Historical Land-Cover Changes on Flooding and Sedimentation, North Fish Creek, Wisconsin. USGS Water-Resources Investigations Report 99-4083, June.

Frei, C. and C. Schar (2000). "Detection Probability of Trends in Rare Events: Theory and Application to Heavy Precipitation in the Alpine Region". *Journal of Climate*, 14: 1568-1585.

Frey, A.E., Olivera, F., Irish, J.L., Dunkin, L.M., Kaihatu, J.M., Ferreira, C.M., and B.L. Edge(2010). "Potential Impacts of Climate Change on Hurricane Flooding Inundation, Population Affected and Property Damages in Corpus Christi". *Journal of the American Water Resources Association*, 46(5):1049-1059.

GeoLytics, Inc., 2003, Neighborhood Change Database (NCDB), 1970-2000 tract data, East Brunswick, NJ, GeoLytics, Inc.; accessed January 2011 at h*ttp://www.geolytics.com/USCensus,Neighborhood-Change-Database-1970-2000,Products.asp*.

Glick, R.H. (2009). "Impacts of Impervious Cover and Other Factors on Storm-water Quality in Austin, Texas". *Journal of Hydrologic Engineering*, 14(4):316-323.

Goldschalk, D.R. (2006). "Buildout Analysis: A Valuable Planning and Hazard Mitigation Tool". *Zoning Practice: American Planning Association*: 3:2-7.

Groisman, P.Y., Knight, R.W., and T.R. Karl (2001). "Heavy Precipitation and High Streamflow in the Contiguous United States: Trends in the Twentieth Century". *Bull. Amer. Meteor. Soc.*, 82:219-246.

Groisman, P.Y., Knight, R.W., Easterling, D.R., Karl, T.R., Hegerl, G.C., and V.N. Razuvaev (2004)."Trends in Intense Precipitation in the Climate Record". *Journal of Climate*, 18:1326-1350.

Groupe de recherché en hydrologiestatistique (GREHYS) (1996). "Presentaion and Review of Some Methods for Regional Flood Frequency Analysis". *Journal of Hydrology*, 186:63-84.

Gulf and Engineers Consultant (GEC) (2006). "Depth-Damage Relationships for Structures, Contents, and Vehicles and Content-to-Structure Value Ratios (CSVR) in Support of the Donaldsonville to the Gulf, Louisiana, Feasibility Study". Prepared for the United States Corps of Engineers.

Hamlet, A.F. and D.P. Lettenmaier (2007). "Effects of 20th Century Warming and Climate Variability on Flood Risk in the Western U.S.".*Water Resources Research,* 43:W06427.

Hayhoe, K. et al. (2007). "Past and Future Changes in Climate and Hydrologic Indicators in the US Northeast". *Clim. Dyn.*, 28:381-407.

Hennessy, K.J., Gregory, J.M., and J.F.B. Mitchell (1997). "Changes in Daily Precipitation under Enhanced Greenhouse Conditions". *Climate Dynamics*, 13:667-680.

Hegerl, G.C. and S. Solomon (2009).“Risks of Climate Engineering”.*SCIENCE*, 325: 955-956.

Hinkley, D.V. (1969). “Inference about the Intersectionin Two-Phase Regression”. *Biometrika*, 56:495-504.

Huntington, T.G. (2006). “Evidence for Intensification of the Global Water Cycle: Review and Synthesis”. *Journal of Hydrology*, 319:83-95.

Interagency Advisory Committee on Water Data (1982). “Guidelines for Determining Flood Flow Frequency”, *Bulletin17B of the Hydrology Committee*, USGS, Office of Water Data Coordination, Reston, VA, March 1982.

Iorio, J.P., et al., 2004: Effects of Model Resolution and Subgrid Scale Physics on the Simulation of Precipitation in the Continental United States. *Climate Dynamics*, 23:243–258, doi:10.1007/s00382-004-0440-y.

IPCC, 2000: IPCC Special Report on Emissions Scenarios [NebojsaNakicenovic and Rob Swart (eds.)]. Cambridge University Press, UK. pp 570.

IPCC, 2007: Climate Change 2007: Synthesis Report. Contribution of Working Groups I, II, and III to the Fourth Assessment Report of the Intergovernmental Panel on Climate Change [Core Writing Team, Pachauri, R.K. and Reisinger, A. (eds.)]. IPCC, Geneva, Switzerland, 104 pp.

Javelle, P., Ouarda, T.B.M.J., Bobee, B., Galea, G., and J.M. Gresillon (2001). “Development of Regional Flood-Duration-Frequency Curves Based on the Index-Flood Method”. *Journal of Hydrology,* 258:249-259.

Jha, M. Arnold, J.G., Gassman, P.W., Giorgi, F., and R.R. Gu (2006). “Climate Change Sensitivity Assessment on Upper Mississippi River Basin Streamflows using

SWAT". *Journal of American Water Resources Association*, August: 998-1015.

Jones, P.D. Groisman, P. YA., Coughlan, M., Plummer, N., Wang, W-C., and T.R. Karl (1990). "Assessment of Urbanization Effects in Time Series of Surface Air Temperature over Land". *Nature*, 347: 169-172.

Kaplan, S. and B.J. Garrick (1981). "On the Quantitative Definition of Risk". *Risk Analysis*, 1(1):11-27.

Karl, T.R., Knight, R.W., and N. Plummer (1995). "Trends in High-Frequency Climate Variability in the Twentieth Century". *Nature*, 377(21):216-219.

Karl, T.R. and R.W. Knight (1998). "Secular Trends of Precipitation Amount, Frequency, and Intensity in the United States". *Bulletin of the American Meteorological Society*, 79(2): 231-241.

Kauffman, G.J., Belden, A.C., Vonck, K.J., and A.R. Homsey (2009). "Link between Impervious Cover and Base Flow in the Clay Creek Wild and Scenic Watershed in Delaware". *Journal of Hydrologic Engineering*, 14(4):324-334.

Kaufman, D.S., Schenider, D.P, McKay, N.P., Ammann, C.M., Bradley, R.Y., Briffa, K.R., Miller, G.F., Ott-Bliesner, B.L., Overpeck, J.T., and B.M Vinther (2009). "Recent Warming Reverses Long-Term Arctic Cooling". SCIENCE, 325:1236-1239.

Kerr, R.A. (2009). "Both of the World's Ice Sheets May be Shrinking Faster and Faster". *SCIENCE*, 326:217.

Kerr, R.A. (2009). "What Happened to Global Warming? Scientists Say Just Wait a Bit". *SCIENCE*, 326:28-29.

Kerr, R.A. (2010). "El Nino Lends More Confidence to Strong Global Warming".

SCIENCE, 330:1465.

Khaliq, M.N., Ouarda, T.B.M.J., Ondo, J.-C., Gachon, P., and B. Bobee (2006). "Frequency Analysis of a Sequence of Dependent and/or Non-Stationary Hydro-Meteorological Observations: A Review". *Journal of Hydrology. 329:534-552.*

Khaliq, M.N., Ouarda, T.B.M.J, Gachon, P., Sushama, L., and A. St-Hilaire (2009). "Identification of Hydrological Trends in the Presence of Serial and Cross Correlations: A Review of Selected Methods and Their Application to Annual Flow Regimes of Canadian Rivers". *Journal of Hydrology*, 368:117-130.

Kharin, V.V. and F.W. Zwiers (2000). "Changes in the Extremes in an Ensemble of Transient Climate Simulations with a Coupled Atmosphere-Ocean GCM". *Journal of Climate*, 13: 3760:3788.

Kharin, V.V. and F.W. Zwiers (2005). "Estimating Extremes in Transient Climate Change Simulations". *Journal of Climate*, 18:1156-1173.

Kharin, V.V., Zwiers, F.W., Zhang, X. and G.C. Hegerl (2007). Changes in Temperature and Precipitation Extremes in the IPCC Ensembal of Global Coupled Model Simulations". *Journal of Climate*: 20: 1419-1444.

Kiehl, J. (2011). "Lessons from Earth's Past". *SCIENCE*, 331:158-159.

Knowles, N. and D.R. Cayan (2002). Potential Effects of Global Warming on the Sacramento/San Joaquin Watershed and the San Francisco Estuary. *Geophysical Research Letters*, 29(18):38-1-38-4.

Konrad, C.P., Booth, D.B., and S.J. Burges (2005). "Effects of Urban Development in the Puget Lowland, Washington, on InterannualStreamflow Patterns: Consequences

for Channel Form and Streambed Disturbance". *Water Resources Research*, 41(7):W07009.

Koutsoyiannis, D. (2004). "Statistics of Extremes and Estimation of Extreme Rainfall: II. Empirical Investigation of Long Rainfall Records". *Hyrdological Sciences-Journal*, 49(4):591-610.

Kundzewicz, Z.W., and A.J. Robson (2004). "Change Detection in Hydrological Records – a Review of the Methodology".*Hydrological Sciences Journal*, 49(1):7-19.

Kwon, H.-H., Brown, C., and U. Lall (2008). "Climate Informed Flood Frequency Analysis and Prediction in Montana using Hierarchical Bayesian Modeling". *Geophysical Research Letters,* 35:L05404.

Kwon, H.-H., Sivakumar, B., Moon, Y.-I., and B.-S. Kim (2011). "Assessment of Change in Design Flood Frequency under Climate Change using a Multivariate Downscaling Model and a Precipitation-Runoff Model". *Stoch.Environ. Res. Risk Assess*, 25:567-581.

Labat, D., Godderis, Y., Probst, J.L., and J.L. Guyot (2004). "Evidence for Global Runoff Increase Related to Climate Warming". *Advances in Water Resources*, 27: 631-642.

Le Treut, H., R. Somerville, U. Cubasch, Y. Ding, C. Mauritzen, A. Mokssit, T. Peterson and M. Prather, 2007: Historical Overview of Climate Change. In: Climate Change 2007: The Physical Science Basis. Contribution of Working Group I to the Fourth Assessment Report of the Intergovernmental Panel on Climate Change [Solomon, S., D. Qin, M. Manning, Z. Chen, M. Marquis, K.B. Averyt, M. Tignor and H.L. Miller (eds.)]. Cambridge University Press, Cambridge, United

Kingdom and New York, NY, USA.

Leclerc, M. and T.B.M.J. Ouarda (2007). "Non-stationary Regional Flood Frequency Analysis at Ungauged Sites". *Journal of Hydrology*, 343:254-265.

Lettenmaier, D.P., Wood, E.F., and J.R. Wallis (1994)."Hydro-Climatological Trends in the Continental United States, 1948-88".*Journal of Climate*, 7:586-607.

Levy, B. and McCuen,R.H. (1999). "Assessment of Storm Duration for Hydrologic Design". *Journal of Hydrologic Engineering*. ASCE 4(3):209-213.

Lins, H.F., and J.R. Slack (2005)."Seasonal and Regional Characteristics of U.S. Streamflow Trends in the United States from 1940 to 1999".*Physical Geography*, 26(6):489-501.

Lund, R. and J. Reeves (2002). "Detection of Undocumented Changepoints: A Revision of the Two-Phase Regression Model". *Journal of Climate*, 15: 2457-2554.

Mareuil, A., Leconte, R., Brissette, F., and M. Minville (2007). Impacts of Climate Change on the Frequency and Severity of Floods in the Chateauguay River Basin, Canada. *Can. J. Eng*. 34:1048-1060.

Martins, E.S., and J.R. Stedinger (2000). "Generalized Maximum-Likelihood Generalized Extreme-Value Quantile Estimators for Hydrologic Data".*Water Resources Research*, Vol 36(3): 737-744.

Maryland Department of Planning (2009). Maryland State Data Center: Projections. Retrieved from http://planning.maryland.gov/msdc/MD_outlook_map.shtml. December 2010.

Maurer, E.P., L. Brekke, T. Pruitt, and P.B. Duffy (2007). 'Fine-Resolution Climate Projections Enhance Regional Climate Change Impact Studies', *Eos Trans. AGU*,

88 (47), 504.

Maurer, E.P., Breke,L.D., and T. Pruitt (2010). "Contrasting Lumped and Distributed Hydrology Models for Estimating Climate Change in Impacts on California Watersheds". *Journal of the American Water Resources Association*, 46(5): 1024 -1035.

McCuen, R.H. (2005). Hydrologic Analysis and Design: Third Edition. Pearson Prentice Hall,Upper Saddle River.

McCuen, R.H. and W.O. Thomas (1990). "Flood Frequency Analysis Techniques for Urbanizing Watersheds". *American Water Resources Association: Urban Hydrology Symposium Proceedings*:35-46.

Meehl, G.A., Washington, W.M., Santer, B.D., Collins, W.D., Arblaster, J.M., Hu, A., Lawrence, D.M., Teng, H., Buja, L., and W.G. Strand (2006). "Climate Change Projections for the Twenty-First Century and Climate Change Commitment in the CCSM3". *Journal of Climate*, 19:2597-2617.

Meehl, G.A., T.F. Stocker, W.D. Collins, P. Friedlingstein, A.T.,Gaye, J.M. Gregory, A. Kitoh, R. Knutti, J.M. Murphy, A. Noda S.C.B. Raper, I.G. Watterson, A.J. Weaver and Z.-C. Zhao, 2007: Global Climate Projections. In: *Climate Change 2007: The Physical Science Basis. Contribution of Working Group I to the Fourth Assessment Report of the Intergovernmental Panel on Climate Change* [Solomon, S., D. Qin, M. Manning, Z. Chen, M. Marquis, K.B. Averyt, M. Tignor and H.L. Miller (eds.)]. Cambridge University Press, Cambridge, United Kingdom and New York, NY, USA.

Mejia, A.I. and G.E. Moglen (2009). "Spatial Patterns of Urban Development from

Optimization of Flood Peaks and Impervious-Based Measures". *Journal of Hydrologic Engineering*, 14(4):416-424.

Milliman, J.D., Farnsworth, K.L., Jones, P.D., Xu, K.H., and L.C. Smith (2008). "Climatic and Anthropogenic Factors Affecting River Discharge to the Global Ocean, 1951-2000". *Global and Planetary Change,* 62:187-194.

Milly, P.C.D., Dunne, K.A., and A.V. Vecchia (2005). "Global Pattern of Trends in Streamflow and Water Availability in a Changing Climate". *Nature,* 438: 347-350.

Milly, P.C.D., Wetherald, R.T., Dunne, K.A., and T.L. Delworth (2002). "Increasing Risk of Floods in a Changing Climate". *Nature*, 15(31): 513-517.

Milly, P.C.D., Betancourt, J., Falkenmark, M., Hirsch, R.M., Kundzewicz, Z.W., Lettenmaier, D.P, and R.J. Stouffer (2009). "Stationarity is Dead: Whither Water Management?" SCIENCE 319: 573-574.

Moglen, G.E., and D. E. Shivers (2006). "Methods of Adjusting U.S. Geological Survey Rural Regression Peak Discharges in an Urban Setting". *Scientific Investigations Report 2006-5270*.

Morales, A. and Saltzman, H. (2002). "Little Patuxent River: Watershed Restoration Action Strategy". Howard County Department of Public Works Stormwater Management Division.

Moscrip, A.L. and D.R. Montgomery (1997). "Urbanization, Flood Frequency, and Salmon Abundance in Puget Lowland Steams". *Journal of the American Water Resources Association*, 33(6):1289-1297.

Moser, D., Bridges, T., Cone, S., Haimes, Y., Harper, B.K., Shabman, L., and C. Yoe

(2009). White Paper: Transforming the Corps into a Risk Managing Organization.

Moussa, R., Voltz, M., and P. Andrieux (2002). Effects of the Spatial Organization of Agricultural Management on the Hydrological Behaviour of a Farmed Catchment during Flood Events. *Hydrological Processes*, 16:393-412.

Muzik, I. (2002). A First-Order Analysis of the Climate Change Effect on Flood Frequencies in a Subalpine Watershed by Means of a Hydrological Rainfall-Runoff Model. *Journal of Hydrology*, 267:65-73.

Nichols, M.H., Renard, K.G., and H.B. Osborn (2002). "Precipitation Changes from 1956 to 1996 on the Walnut Gulch Experimental Watershed". *Journal of the American Water Resources Association*, 38(1):161-172.

Nijssen, B., O'Donnell, G.M., Lettenmaier, D.P., Lohmann, D., and E.F. Wood (2001). "Predicting the Discharge of Global Rivers". *Journal of Climate*, 14: 3307-3324.

Olsen, J.R. (2006). "Climate Change and Floodplain Management in the United States". *Climate Change,* 76:407-426.

Overpeck, J.T., Meehl, G.A., Bony, S., and D.R. Easterling (2011). "Climate Data Challenges in the 21st Century". *SCIENCE*, 331:700-703.

Peterson, T.C.. Gallo, K.P, Lawrimore, J., Owen, T.W., Huang, A., and D.A. McKittrick (1999). "Global Rural Temperature Trends".*Geophys. Res. Lett.*, 26: 329-332.

Purdy, G. (2010). "ISO 31000:2009- Setting a New Standard for Risk Management". *Risk Analysis*, 30(6):881-886.

Radziejewski, M. and Z.W. Kundsewicz (2004). "Detectability of Changes in Hydrological Records".*Hydrological Sciences*, 49(1):39-53.

Raff, D.A. Pruitt, T. and L.D. Brekke (2009). "A Framework for Assessing Flood Frequency Based on Climate Projection Information". *Hydrol. Earth Syst. Sci. Discussions*, 6:2005-2040.

Randall, D.A., R.A. Wood, S. Bony, R. Colman, T. Fichefet, J. Fyfe, V. Kattsov, A. Pitman, J.Shukla, J. Srinivasan, R.J. Stouffer, A. Sumi and K.E. Taylor, 2007: Climate Models and their Evaluation. In: Climate Change 2007: The Physical Science Basis. Contribution of Working Group I to the Fourth Assessment Report of the Intergovernmental Panel on Climate Change [Solomon, S., D. Qin, M. Manning, Z. Chen, M. Marquis, K.B. Averyt, M.Tignor and H.L. Miller (eds.)]. Cambridge University Press, Cambridge, United Kingdom and New York, NY, USA.

Reed, W.B. (1990). "An Evaluation of the Effects of Changing Land Use on the Urban Flood Frequency and Hydrograph Characteristics of Valley Creek". *American Water Resources Association: Urban Hydrology Symposium Proceedings*:23-31.

Reeves, J., Chen, J., Wang, X., Lund, R., Lund, R., and Q. Lu (2007). "A Review and Comparison of Changepoint Detection Techniques for Climate Data". *Journal of Applied Meteorology and Climatology*, 46:900-915.

Renard, B., Lang, M., and P. Bois (2006). "Statistical Analysis of Extreme Events in a Non-Stationary Context via a Bayesian Framework. Case Study with Peak-Over-Threshold Data". *Stochastic Environmental Research and Risk Assessment*, 21(2):97-112.

Sauer, V.B., Thomas, W.O., Jr., Stricker, V.A., and K.V. Wilson (1981). *Magnitude and Frequency of Urban Floods in the United States*, U.S. Geological Survey,

Reston, VA.

Semenov, V.A. and L. Bengtsson (2002). "Secular Trends in Daily Precipitation Characteristics: Greenhouse Gas Simulation with a Coupled AOGCM". *Climate Dynamics*, 19:123-140.

Sivapalan, M. and J.M Samuel (2009). "Transcending Limitations of Stationarity and the Return Period: Process-Based Approach to Flood Estimation and Risk Assessment". *Hydrological Processes*, 23:1671-1675.

Soil Conservation Services (1986)."Urban Hydrology for Small Watersheds". United States Department of Agriculture. Technical Release 55. Washington, DC.

Stedinger, J. and V.W. Griffis (2008). "Flood Frequency Analysis in the United States: Time to Update". *ASCE Journal of Hydrologic Engineering*, April:199-204.

Stedinger, J., Vogel, R.M., and E. Foufoula-Georgiou (1993). "Frequency Analysis of Extreme Events". In Maidment, D.R. (ed), Handbook of Hydrology, (Chapter 18). McGraw-Hill, inc.: New York.

Strupczewksi, W.G., Singh, V.P. and W. Feluch (2001) "Non-stationary Approach to At-Site Flood Frequency Modelling I. Maximum Likelihood Estimation". *Journal of Hydrology*, 248:123-142.

Sun, Y., S. Solomon, A. Dai, and R. Portmann, 2006: How often does it rain? *Journal of Climate*, 19, 916–934.

Sweet, W.V. and J.W. Geratz (2003). "Bankfull Hydraulic Geometry Relationships and Recurrence Intervals for North Carolina's Coastal Plain". *Journal of American Water Resources Association*, August: 861-871.

Theobald, D.M., Goetz, S.J., Norman, J.B., and P. Jantz (2009). "Watersheds at Risk to

Increased Impervious Surface Cover in the Conterminous United States". *Journal of Hydrologic Engineering*, 14(4):362-368.

Todd, C.E.D., Goss, A.M., Tripathy, D., and J.M. Harbor (2007). "The Effects of Landscape Transformation in a Changing Climate on Local Water Resources". *Physical Geography*, 28(1):21-36.

Trenberth, K.E. (1999). "Conceptual Framework for Changes of Extremes of the Hydrological Cycle with Climate Change". *Climate Change,* 42:327-339.

Trenberth, K.E., P.D. Jones, P. Ambenje, R. Bojariu, D. Easterling, A. Klein Tank, D. Parker, F. Rahimzadeh, J.A. Renwick, M. Rusticucci, B. Soden, and P. Zhai, 2007: Observations: Surface and Atmospheric Climate Change. In: *Climate Change 2007: The physical Science Basis.* Contribution of Working Group I to the Fourth Assessment Report of the Intergovernmental Panel on Climate Change [Solomon, S., D. Qin, M. Manning, Z. Chen, M. Marquis, K.B. Averyt, M. Tignor, and H.L. Miller (eds.)]. Cambridge University Press, United Kingdom and New York, NY USA.

Treusdell, L.E. (1942). "16th Census of the United States, 1940: Population: Second Series: Characteristics of the Population of Maryland". U.S. Government Printing Office, Washington, DC.

United States Army Corps of Engineers (USACE) (2006). "Risk Analysis for Flood Damage Reduction Studies". Regulation No. 1105-2-101, 3 January.

U.S. Department of Commerce Bureau of Census (1961). "1960 Census Population Advance Reports: MD: Report PC(A2)-22". Washington, DC.

United States Army Corps of Engineers (USACE) (2009a). "Performance Evaluation of

the New Orleans and Southeast Louisiana Hurricane Protection System". Final Report of the Interagency Performance Evaluation Task Force.

USACE (2009b). "USACE National Economic Development Procedures Manual Overview: Report 09-R-2". Institute for Water Resources, Alexandria, Virginia.

USGS National Streamflow Information Program (2005). "Trends in the Water Budget of the Mississippi River Basin, 1949-1997". Fact Sheet 2005-3020.

Villarini, G., Smith, J.A., Serinaldi, F., Bales, J., Bates, P.D., and W.F. Krajewski (2009). "Flood Frequency Analysis for Nonstationary Annual Peak Records in an Urban Drainage Basin". *Advances in Water Resources*, 32:1255-1266.

Villarini, G., Serinaldi, F, Smith, J.A., and W.F. Krajewski (2009). "On the Stationarity of Annual Flood Peaks in the Continental United States during the 20th Century". *Water Resources Research*, 45:W08417.

Villarini, G., Smith, J.A., and F. Napolitano (2010). "Nonstationary Modeling of a Long Record of Rainfall and Temperature over Rome". *Advances in Water Resources*, 33(10): 1256-1267.

Wang, X. L. (2003). "Comments on 'Detection of Undocumented Changepoints: A Revision of the Two-Phase Regresion Model'". *Journal of Climate*, 16:3383-3385.

Weggel, J.R. (2011). "Are Floods on the Delaware River Getting Worse?" *ASCE Journal of Hydrologic Engineering*, 263-265.

Wilby, R. L., and T. M. L. Wigley (2002). "Future changes in the distribution of daily precipitation totals across North America." G*eophys. Res. Lett.,* 29, 1135, doi:10.1029/2001GL013048.

Wilks, D.S. (1993). "Comparison of Three-Parameter Probability Distributions for Representing Annual Extreme and Partial Duration Precipitation Series". *Water Resources Research*, 29(10):3543-3549.

Xiong, L. and S. Guo (2004). "Trend Test and Change-Point Detection for the Annual Discharge Series of the Yangtze River at the Yichange Hydrological Station". *Hydrological Sciences,* 49(1):99-111.

Yue, S., Pilon, P., and G. Cavadias (2002). "Power of the Mann-Kendall and Spearman's Rho Tests for Detecting Monotonic Trends in Hydrological Series". *Journal of Hydrology*, 259:254-271.

Yue, S. and P. Pilon (2004). "A comparison of the Power of the t-test, Mann-Kendall, and Bootstrap Tests for Trend Detection". *Hydrological Sciences,* 49(1): 21-39.

Zhang, X., Zwiers, F.W., and G. Li (2004). "Monte Carlo Experiments on the Detection of Trends in Extreme Values". *Journal of Climate*, 17:1945-1952.

"*We acknowledge the modeling groups, the Program for Climate Model Diagnosis and Intercomparison (PCMDI) and the WCRP's Working Group on Coupled Modelling (WGCM) for their roles in making available the WCRP CMIP3 multi-model dataset. Support of this dataset is provided by the Office of Science, U.S. Department of Energy.*"